

The Effect of Turbulent Flow on Corrosion of Mild Steel in High Partial CO₂
Environments

A dissertation presented to
the faculty of
the Russ College of Engineering and Technology of Ohio University

In partial fulfillment
of the requirements for the degree
Doctor of Philosophy

Azmi Mohammed Nor

May 2013

© 2013 Azmi Mohammed Nor. All Rights Reserved.

This dissertation titled
The Effect of Turbulent Flow on Corrosion of Mild Steel in High Partial CO₂
Environments

by

AZMI MOHAMMED NOR

has been approved for
the Department of Chemical and Biomolecular Engineering
and the Russ College of Engineering and Technology by

Srdjan Nestic

Russ Professor of Chemical and Biomolecular Engineering

Dennis Irwin

Dean, Russ College of Engineering and Technology

ABSTRACT

MOHAMMED NOR, AZMI, Ph.D., May 2013, Chemical Engineering

The Effect of Turbulent Flow on Corrosion of Mild Steel in High Partial CO₂ Environments

Director of Dissertation: Srdjan Nestic

The need to develop natural gas hydrocarbon gas fields that have high concentrations of CO₂ necessitates technical evaluation of the feasibility of using carbon steels as infrastructure material particularly as its use would positively impact the economic viability of such development projects. This requires a suitable CO₂ corrosion prediction model. However, the upper pressure limit of existing CO₂ corrosion prediction models is 20 bar, well below the encountered subcritical and supercritical pressures (73.4 bar). Employing existing models for the design of the production assets would lead to over prediction, resulting in overdesign and high costs. A further requirement for the development of a suitable corrosion model for high CO₂ partial pressure environments was the inclusion of the effect of flow. Therefore, this study focused on three parameters that might affect the flow-sensitivity of CO₂ corrosion: CO₂ partial pressure, pH, and temperature.

To accomplish the objectives, two types of flow geometries were used to study flow-sensitive corrosion at elevated CO₂ partial pressure and high temperature environment: rotating cylinder electrode (RCE) and thin-channel flow cell (TCFC). Since TCFC was a new flow apparatus, the mass transfer behavior of TCFC was characterized using limiting current density technique. In the experiment, the limiting

current density of API 5L X-65 carbon steel was measured at various velocities in 1 wt% NaCl electrolyte at pH 3.0 for each of the test temperatures of 30° C and 50° C. The data showed good correlation with the mass transfer correlation of Sleicher and Rouse for a smooth pipeline. This established TCFC as being suitable for study of flow-sensitive corrosion.

In RCE experiments, the effect of pH (pH 3.0 to pH 5.0) was studied at CO₂ partial pressure of 10 bar and temperature of 25° C and 50° C in 1 wt% NaCl electrolyte. The findings indicated that the increase in pH led to the decrease in corrosion rate. Most importantly, the findings revealed that the effect of pH on flow-sensitivity as compared against a mass transfer correlation was not considerable even when the concentration of hydrogen ions was relatively high. This was attributed to the dominant effect of flow-insensitive chemical-reaction controlled hydration of dissolved CO₂ that precedes the direct reduction of carbonic acid. The effect of temperature (25° C, 50° C, and 80° C) at CO₂ partial pressure of 10 and 80 bar and at pH 3.0 and pH 4.0 showed that the increase in temperature considerably accelerated CO₂ corrosion rates. However, the increase in temperature even at 80° C did not seem to significantly enhance the flow-sensitivity of CO₂ corrosion. This again may be attributed to the dominance of direct reduction of carbonic acid that was limited by the slow hydration of aqueous CO₂. The effect of increasing CO₂ partial pressure (10, 40, and 80 bar) as carried out at pH 3.0 and 50° C was to enhance CO₂ corrosion rate due to the increase in the direct reduction of carbonic acid as its concentration increased. However, the increase was not linear and became relatively smaller as the CO₂ partial pressure increased further probably due to the

saturation of adsorbed carbonic acid on the steel surface. In fact, in the RCE experiments, the corrosion rate decreased at high CO₂ partial pressure and temperature (80 bar and 80° C). However, this was more due to the formation of protective iron carbonate layers, resulting from the change in water chemistry. Nevertheless, the TCFC experiments with a larger volume of test solution produced more realistic results with no iron carbonate layer formation at 80 bar and 80° C test conditions. Even in the absence of iron carbonate layers in the TCFC, the flow-sensitivity of CO₂ corrosion at elevated CO₂ partial pressure was still relatively low due to the dominance of flow-insensitive hydration of aqueous CO₂. Notwithstanding this, the fact that the corrosion rates at low temperature (25° C) in the RCE and TCFC with similar mass transfer coefficients correlated well indicated that CO₂ corrosion was geometry-independent.

DEDICATION

To

My parents, Bedah Bt. Mohamed and the late Mohammed Nor Abu Bakar,

My parents-in-law, Rosnah Bt Mohd Aris and Md Deris Ali

My beloved wife, Misma Annita, my four beloved children

and all other family members

For their constant support and love

ACKNOWLEDGMENTS

I would like to express my sincere gratitude and indebtedness to my academic supervisor, Prof. Srdjan Nestic for his invaluable supervision, advice, and guidance throughout my PhD program. He was always willing to entertain my queries and to make my difficult questions clarified. I greatly appreciate his tremendous moral support when ‘matters’ got tough. He was unflinchingly determined to seeing the project proceed and complete as planned despite some unnecessary resistance.

I would like to extend my appreciation to Prof. Howard D. Dewald, Prof. Jeffrey J. Rack, Prof. Dusan Sormaz, and Dr. David Young for serving on my PhD committee and the valuable feedbacks on my dissertation.

I am also grateful to the Project Leader, Mr. Marc Singer for his assistance and valuable inputs during the execution of the project. I would also like to extend my appreciation to Dr. David Young for his valuable advice and patience in improving my dissertation and Dr. Yoon-Seok Choi for his technical help in overcoming ‘hiccups’ in experimental work and technical feedbacks on the results.

I would also like to thank Mr. Albert Schubert, Mr. Bruce Brown, Mr. Daniel Cain, Mr. Phil Bullington who were dedicated in ensuring the experiments were successfully executed. Special thanks go to Mr. Cody Shafer and Mr. Steven Upton, who dedicatedly and untiringly attended to any experimental problem related to equipment. The latter’s deep commitment helped ensure that the TCFC experiments could be completed successfully.

I was also lucky to have received great assistance from my two colleagues, Mr. Firdaus Suhor and Mr. Mohd Farid Mohamed, who together shared sweet and bitter memories in the course of the project execution. Deep appreciation also goes to Dr. Sa'adan Mat, the initiator of the project, and Datuk Dr. Zainal Abidin Hj Kasim, the then Rector of Universiti Teknologi PETRONAS, for providing invaluable moral and management support to us. A special appreciation to PETRONAS Management, especially, Mr. Mohd Hasni Hashim and Mrs. Rozilah Kamarudin, who were supportive and kind enough to provide me an opportunity to return to Ohio University to complete my PhD while undertaking the work here.

Above all, I am also greatly indebted to my families, especially my mother, my parents-in law, and wife, for their prayer, constant support, encouragement, and understanding that motivated me to finish the work. I also owe my four children, namely, Mohammed Aqil, Nur Afiqah, Muhammad Afiq and Nur Atiqah for the little time I spent with them.

Last but not least, I would also like to thank my friends at ICMT who, one way or another, have benefitted me through their friendship and discussion.

TABLE OF CONTENTS

	Page
Abstract.....	3
Dedication.....	6
Acknowledgments.....	7
TABLE OF CONTENTS.....	9
List of Tables	11
List of Figures.....	12
Chapter 1: Introduction.....	17
Chapter 2: Phase Behavior of Carbon Dioxide.....	21
Chapter 3: Overview of CO ₂ Corrosion.....	25
3.1 Chemical reactions.....	25
3.1.1 Aqueous water chemistry model.....	32
3.1.2 The Effect of water chemistry on CO ₂ corrosion.....	36
3.2 Electrochemical reactions	39
3.2.1 Cathodic reactions.....	40
3.2.2 Anodic reactions	50
3.2.3 Mass transport.....	53
3.3 Influential factors.....	56
3.3.1 Environment.....	56
3.3.2 Metallurgy.....	64
3.3.3 Microstructure.....	69
3.3.4 Corrosion product layers.....	70
3.3.5 Flow	73
3.4 CO ₂ corrosion models.....	98
3.4.1 Empirical models	98
3.4.2 Mechanistic models	100
3.4.3 Semi-empirical model.....	101
Chapter 4.0: Research Objectives and Work Strategy.....	103
4.1 Research objectives.....	103

	10
4.2	Work strategy..... 103
4.3	Published papers 104
Chapter 5.0: Experimental Details 106	
5.1	Introduction..... 106
5.2	Mass transfer characterization of thin channel flow cell (TCFC)..... 106
5.2.1	Experimental execution 107
5.2.2	Results and discussion 118
5.3	High pressure-high temperature rotating cylinder electrode 124
5.3.1	Experimental execution 125
5.3.2	Results and discussion 137
5.4	High pressure-high temperature (HPHT) thin channel flow cell (TCFC) 166
5.4.1	Experimental execution 166
5.4.2	Results and discussion 176
Chapter 6.0: Modeling 188	
6.1	Effect of CO ₂ partial pressure..... 188
6.1.1	CO ₂ corrosion rate..... 188
6.1.2	Flow-sensitivity..... 191
6.2	The effect of temperature..... 193
6.3	The effect of pH 193
6.4	Anodic reaction..... 195
6.5	Validation of the model 195
Chapter 7.0: Conclusions and Future Work..... 198	
7.1	Conclusions..... 198
7.2	Future work..... 199
References..... 201	

LIST OF TABLES

	Page
Table 1: Comparison of physical properties among different phases of CO ₂ [14]	22
Table 2: The empirical equations for the equilibrium constants.....	30
Table 3: The equilibrium constants for high partial pressure of CO ₂	32
Table 4: The physical properties of water and Sc numbers at 30° C and 50° C for mass transfer characterization.....	111
Table 5: <i>Re</i> numbers at various liquid velocities for mass transfer characterization.....	112
Table 6: Chemical composition (in wt%) of X65 carbon steels (balance Fe)	114
Table 7: The physical properties of water and the Reynolds numbers	127
Table 8: The test matrix for the HPHT RCE experiments.....	128
Table 9: CO ₂ phases and the autogeneous pH covered in the test matrix.....	129
Table 10: The corresponding TCFC linear liquid velocity calculated from the RCE peripheral velocity	170
Table 11: The corresponding Reynolds numbers for the TCFC linear liquid velocities	171
Table 12: The key experimental conditions in the TCFC experiments	171

LIST OF FIGURES

	Page
Figure 1: Comparison of the mole fraction of dissolved CO ₂ (xCO ₂) in water between a model and experimental data at 25° C. [15].....	20
Figure 2: The phase diagram of pure CO ₂ [20].....	21
Figure 3: The critical curve of CO ₂ -water system [26]	24
Figure 4: Concentration of carbonic as a function of pH for an open system at pCO ₂ =1bar and 25 °C.....	34
Figure 5: Concentration of carbonic as a function of pH for closed systems at pCO ₂ =1bar and 25° C.....	35
Figure 6: The dissolution of iron carbonate (siderite) in NaCl solution as a function of pH [1].....	39
Figure 7: The variation of cathodic limiting current densities with velocities in a N ₂ -purged solution of pH 4 and 22° C showing flow-sensitivity [51]	43
Figure 8: The variation of cathodic limiting current densities with velocities in a CO ₂ -purged solution of pH 4 and 22° C showing less flow-sensitivity [51].....	43
Figure 9: Diffusion of hydrogen ions and carbonic acid through the diffusion boundary layer and hydration of aqueous CO ₂ in the bulk and within the boundary layer [57]	47
Figure 10: Limiting current density for a CO ₂ and an HCl solution at pH4, 22° C measured potentiostatically using a rotating cylinder electrode [51]	55
Figure 11: The solubility of ferrous ions as a function of temperature in pure-distilled water at pCO ₂ =1bar for corroding steel (□) and solid iron carbonate (■) [71].....	59
Figure 12: Corrosion rate as a function of pressure at 40 °C and autogeneous pH [12]..	63
Figure 13: The corrosion rate of carbon steels at two different concentrations of Ni, namely, 1.45 wt% and 3.35 wt%, and at three different pH values: pH 4, pH 5, and pH 6. The steels with the Ni addition are indicated in circles [89].....	68
Figure 14: The effects of flow on corrosion rate [17].....	75
Figure 15: The diffusion boundary layer resides within the viscous laminar sub-layer [115].....	78
Figure 16: Low pressure thin-channel flow cell	107
Figure 17: The flow diagram of the low pressure TCFC [147].....	108
Figure 18: A schematic flow channel of the low-pressure TCFC	108
Figure 19: The electrochemical probe used in the mass transfer characterization experiment.....	113

Figure 20: Cathodic polarization curves at three different liquid velocities, pH 3.0, and 30° C showing the limiting current region.....	116
Figure 21: Cathodic polarization curves at three different liquid velocities, pH 3.0, and 50° C showing the limiting current region.....	117
Figure 22: Limiting current densities for ascending (A) and descending (D) velocities at pH 3.0 and 30° C determined potentiostatically at -950 mV (Ag/AgCl).....	118
Figure 23: Limiting current densities as a function of liquid velocities at 30° C and pH 3.0	120
Figure 24: Limiting current densities as a function of liquid velocities at 50° C and pH 3.0	120
Figure 25: Mass transfer correlation at 30° C and various liquid velocities. Note that $y = (Sh - 5)Sc^{0.33}$ and $x = Re^{0.88}$	121
Figure 26: Mass transfer correlation at 50° C and various liquid velocities.....	122
Figure 27: A 7.5-liter high pressure and high temperature rotating cylinder electrode autoclave for flow study at ICMT.....	125
Figure 28: Rotating cylinder lid equipped with a rotating shaft and a pressure balance compartment	126
Figure 29: Specimen for HPHT rotating cylinder electrode.....	131
Figure 30: An experimental set up for HPHT RCE experiments	132
Figure 31: The open-circuit potential measured prior to LPR measurements at pCO ₂ =10 bar, pH 4.0, and 25° C.....	134
Figure 32: Nyquist plot for pCO ₂ =80bar, T=25° C; pH=3.0	138
Figure 33: Data cross validation for pCO ₂ =10 bar; T=50° C; pH=4.0 at 500 rpm.....	139
Figure 34: Data cross validation for pCO ₂ =10 bar; T=50° C; pH=5.0 at 500 rpm.....	140
Figure 35: Data cross validation for pCO ₂ =40 bar; T=50° C; pH=3.0 at 0 rpm.....	140
Figure 36: Data cross validation for pCO ₂ =80 bar; T=50° C; pH=3.0 at 0 rpm.....	141
Figure 37: Comparison of corrosion rate from LPR tests between pH 3.0 and pH 4.0 at pCO ₂ =10 bar and 25° C	142
Figure 38: Comparison of corrosion rate from LPR tests among pH 3.0, pH4.0, and pH 5.0 at pCO ₂ =10 bar and 50° C.....	143
Figure 39: Cathodic polarization curves at various velocities; pCO ₂ =10bar, pH 3.0 and	144
Figure 40: Cathodic polarization curves at various velocities; pCO ₂ =10 bar, pH 4.0 and 25° C.....	145

Figure 41: Cathodic polarization curves at various velocities; pCO ₂ =10 bar, pH 4.0 and	146
Figure 42: Comparison of corrosion rates between pH3.0 and pH4.0 at pCO ₂ =10bar, 25° C, and 500 RPM.....	147
Figure 43: Comparison of anodic curves between pH 3.0 and pH 4.0; pCO ₂ =10 bar and	148
Figure 44: Comparison of corrosion rate from LPR tests between 25° C and 50° C at pCO ₂ =10 bar and pH3.0.....	150
Figure 45: Comparison of corrosion rate from LPR tests between 25° C and 50° C at pCO ₂ =10 bar and pH4.0.....	150
Figure 46: Comparison of corrosion rate from LPR tests between 25° C, 50° C, and 80° C at pCO ₂ =80 bar and pH3.0.....	151
Figure 47: Cathodic polarization curves at various velocities at pCO ₂ =10 bar, pH 3.0 and 25° C.....	152
Figure 48: Cathodic polarization curves at various velocities at pCO ₂ =10 bar, pH 4.0 and 50° C.....	152
Figure 49: Comparison of anodic curves between 25° C and 50° C at pCO ₂ =10bar, pH 4.0, and stagnant conditions.....	154
Figure 50: Comparison of corrosion rate from LPR tests among pCO ₂ of 10 bar, 40 bar, and 80 bar at 50° C and pH 3.0.	155
Figure 51: Surface analysis at pCO ₂ =80 bar, pH=3.2 and T=80° C showing iron carbonate formed on the substrate	156
Figure 52: An XRD spectrum for the specimen exposed at pCO ₂ =80 bar, pH 3.2, and T=80° C.....	157
Figure 53: Comparison of anodic curves between pCO ₂ of 10 bar and 40 bar, and pH 3.0, and 50° C.....	159
Figure 54: Surface analysis at pCO ₂ =10 bars, pH=3.0 and T=25° C, suggesting iron carbide layers formed on the substrate.....	160
Figure 55: Surface analysis at pCO ₂ =10 bars, pH=4.0 and T=25° C suggesting iron carbide layers formed on the substrate.....	161
Figure 56: Surface analysis at pCO ₂ =10 bars, pH=5.0 and T=50° C suggesting iron carbide layers formed on the substrate.....	162
Figure 57: Surface analysis after the removal of iron carbide layers indicating general corrosion. The pit-like defect in (b) might have been due to an inclusion.	163
Figure 58: Corrosion rate and corrosion potentials over time with pCO ₂ =80 bar and at 80° C, pH 3.2, and 1000 RPM	164

Figure 59: Surface analysis at $p\text{CO}_2=80$ bar, $\text{pH}=3.2$ and $T=80^\circ\text{C}$, showing the increase in the protectiveness of iron carbonate layers formed on the substrate over a long exposure period under a flowing condition	165
Figure 60: High pressure and high temperature thin channel flow cell.....	167
Figure 61: The three-probe LPR probe used to measure corrosion rates <i>in-situ</i>	173
Figure 62: The weight loss coupon used in the experiment.....	174
Figure 63: Data cross validation for $p\text{CO}_2=10$ bar; $T=25^\circ\text{C}$; $\text{pH}=3.4$ at 8 m/s.....	176
Figure 64: Comparison of the corrosion rates from LPR measurement as a function of liquid velocity between a Rotating Cylinder Electrode (RCE) and a Thin Channel Flow Cell (TCFC) at $p\text{CO}_2$ of 10 bar, 25°C , and pH 3.4 on the basis of equivalent velocity.	177
Figure 65: Comparison of the corrosion rates from LPR measurement as a function of liquid velocity between a Rotating Cylinder Electrode (RCE) and a Thin Channel Flow Cell (TCFC) at $p\text{CO}_2$ of 80 bar, 25°C , and pH 3.0 on the basis of equivalent velocity.	178
Figure 66: Comparison of the corrosion rates from LPR measurement as a function of liquid velocity between a Rotating Cylinder Electrode (RCE) and a Thin Channel Flow Cell (TCFC) at $p\text{CO}_2$ of 80 bar, 80°C , and pH 3.2 on the basis of equivalent velocity.	179
Figure 67: A surface image and elemental analysis of the corrosion product layer obtained using EDX, suggesting the presence of cementite (iron carbide) with some minor alloying elements; steel sample exposed to water saturated with $p\text{CO}_2=10$ bar, at 25°C , and pH 3.4 for 24 h.....	181
Figure 68: A surface image and elemental analysis of the corrosion product layer obtained using EDX, suggesting the presence of cementite (iron carbide) with some minor alloying elements; steel sample exposed to water saturated with $p\text{CO}_2=80$ bar, at 25°C , and pH 3.0 for 24 h.....	182
Figure 69: A surface image and elemental analysis of the corrosion product layer obtained using EDX, suggesting the presence of cementite (iron carbide) and siderite (iron carbonate); steel sample exposed to water saturated with $p\text{CO}_2=80$ bar, at 80°C , and pH 3.2 for 24 h.....	183
Figure 70: Surface image after the removal of corrosion product layer indicating general corrosion. Steel specimen was exposed to CO_2 -saturated solution with $p\text{CO}_2=10$ bar, at pH 3.4 and 25°C	185
Figure 71: Surface image after the removal of corrosion product layer indicating general corrosion. Steel specimen was exposed to CO_2 -saturated solution with $p\text{CO}_2=80$ bar, at pH 3.0 and 25°C	186
Figure 72: Surface image after the removal of corrosion product layer indicating general corrosion. Steel specimen was exposed to CO_2 -saturated solution with $p\text{CO}_2=80$ bar, at pH 3.0 and 80°C	186

- Figure 73: The change in carbonic acid concentration as a function of CO₂ partial pressure at 25° C as modeled by the custom-built water chemistry model [15]..... 189
- Figure 74: The fractional surface coverage as a function of CO₂ partial pressure to account for the effect of adsorbed carbonic acid on CO₂ corrosion rate. 191
- Figure 75: Comparison of corrosion rates between Supercorp[®] and the TCFC data 196
- Figure 76: A comparison of Supercorp[®] with Multicorp[®] for PETRONAS CO₂ transport pipeline (32"). The modeling was for 40° C and 2.2 m/s fluid velocity 197

CHAPTER 1: INTRODUCTION

Carbon dioxide (CO₂) is not corrosive when it is dry. However, when it dissolves in water, it becomes corrosive due to a chemical generation of reducible species such as carbonic acid and related hydrogen ions that promote electrochemical reactions between a metal surface and electrolyte [1]. This corrosion phenomenon known as CO₂ corrosion or “sweet” corrosion is a major problem in the oil and gas industry. CO₂ is naturally present in oil and gas fields [2] and mild steel, the dominant metal used in the oil and gas industry due to its cost effectiveness, is susceptible to CO₂ corrosion [3]. The first study on CO₂ corrosion related to the oil and gas industry can be traced back to an extensive study carried out by the American Petroleum Institute in the years leading up to 1925 [4]. Since then, studies on CO₂ corrosion have made extensive progress [5]. Nevertheless, the study of CO₂ corrosion has largely focused on low CO₂ partial pressure which falls in the range of 1-20 bars [6]. CO₂ corrosion problems have increased as oil and gas exploration/production goes into marginal and harsher fields such as deep-water and stranded gas fields [7]. While about 90 percent of petroleum reservoirs have less than one mole percent of CO₂ content [2], stranded hydrocarbon gas fields could have a significantly higher CO₂ content [8]; for example, Natuna D-Alpha in Indonesia has 70 mole percent of CO₂ out of 240 trillion cubic feet (tcf) of gas. High CO₂ content of more than 50 mole percent mostly originates from thermal decomposition of carbonate minerals [2] in which the general reaction is: $MCO_{3(crystal)} \rightarrow MO_{(crystal)} + CO_2 \uparrow$ [9].

Like Indonesia, Malaysia also has non-developed hydrocarbon gas reserves located in high CO₂ fields estimated at 38 trillion cubic feet (tcf) [8]; the concentration of

CO₂ is estimated to be as high as 89 mole percent. At the outset, the development of these fields would call for the use of expensive corrosion resistant alloys (CRA) due to possible high CO₂ corrosion. This would potentially render the project development costs untenable. It must also be noted that the use of CRA such as stainless steels does not guarantee their technical and economic feasibility when a maximum allowable corrosion rate of 0.1 mm/yr is considered [10]. An alternative approach would be to evaluate the technical feasibility of using carbon steels. Unlike transportation and sequestration of supercritical CO₂, where the amount of water is normally negligible or comes from condensation, field development has to consider the presence of formation water which has the potential of containing multiple and potentially corrosive species such as sulfate, chloride, and sulfide [11]. Evaluating the technical feasibility of carbon steel in such corrosive environments poses a new challenge as the validity domain of the existing corrosion prediction models is limited to 20 bars of CO₂ partial pressure [6]. Using the existing models to predict the corrosion rate of carbon steel beyond the validity domain would result in their over prediction [10, 12]; a comparison between a model corrosion rate and experimental corrosion rate suggests an over prediction factor of about five times [13]. This would consequently rule out the possibility of opening up an operational window for the economic use of carbon steel. Therefore, there is a need to study and model the corrosion behavior of carbon steel in high mole percent CO₂ environments including at supercritical CO₂ conditions (74 bars and 31° C) [14]; the aim would be to develop a corrosion prediction model for high pressure CO₂ corrosion which would provide operational windows for the economic use of carbon steel.

The envisaged prediction model is mechanistic in nature, comprising three modules: water-chemistry, electrochemistry, and flow. Each module was carried out by a different researcher. A water chemistry model for high CO₂ partial pressure is essential so as to incorporate the non-ideality of the gas and solution [1, 15]. The current models mostly make use of Henry's law in modeling the solubility of CO₂ in water [3], and this may partly contribute to the over-prediction of corrosion rate due to over prediction of the amount of dissolved CO₂, hence carbonic species concentrations as shown by **Figure 1** below [15]. The electrochemistry model addresses the possible precipitation of corrosion product layers at a low autogeneous bulk pH (pH < 4) and their possible influence on corrosion rate; it also looks into corrosion rates in CO₂-saturated water and water saturated CO₂-rich phase [16]. The effect of flow will also be incorporated into the model as it has the possible effects of increasing the corrosion rate by increasing the mass transfer rates of the corrosive species to the pipe wall and challenging the protectiveness of the corrosion product films [17, 18]. This is in fact the primary objective of the present work: to evaluate the effects of flow in high concentration CO₂ environments at elevated pressures of pCO₂, pH values and temperatures.

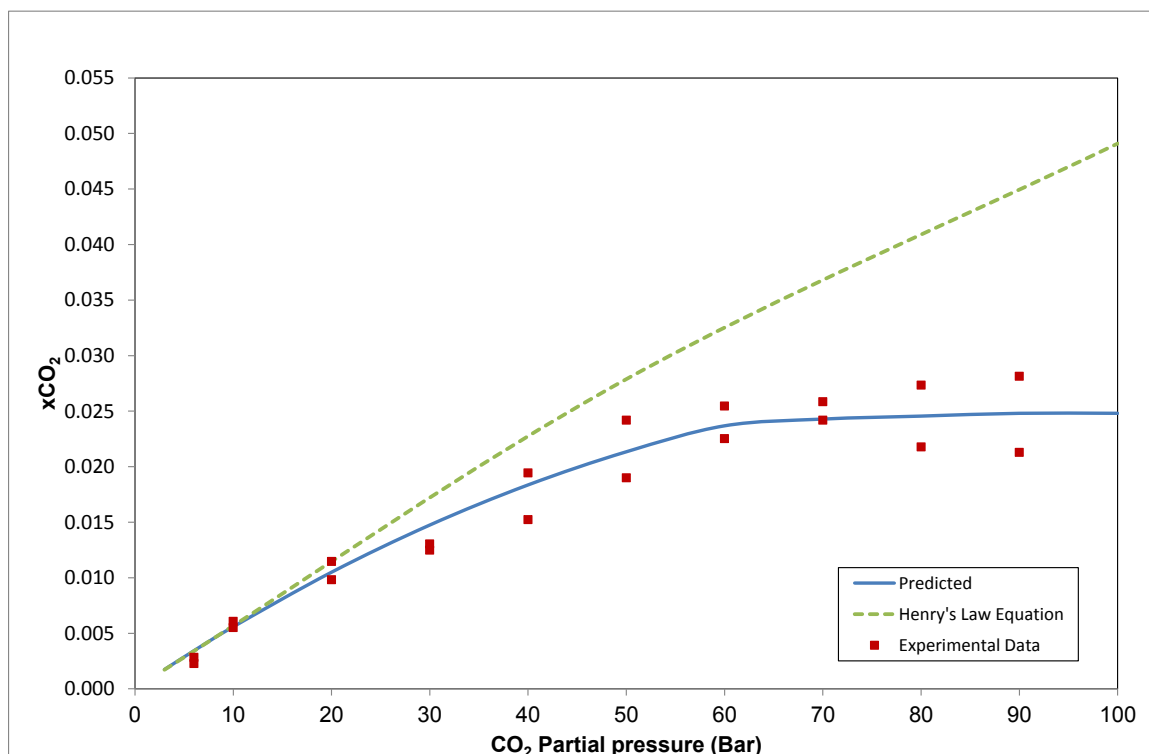


Figure 1: Comparison of the mole fraction of dissolved CO₂ (x_{CO_2}) in water between a model and experimental data at 25° C. [15]

In the present study, the hydrodynamic effects on CO₂ corrosion were first evaluated using a high pressure and high temperature (HPHT) rotating cylinder electrode (RCE) and then HPHT thin channel flow cell (TCFC). For the RCE experiments, corrosion rates were measured via weight loss and electrochemical methods at various pH values (3-5), temperatures (25-50° C), near critical and supercritical CO₂ partial pressures (10-80 bar) and at equivalent fluid velocities from 0 to 1.5 m/s. TCFC experiments involved repeating some parts of the same test matrix, albeit at a higher equivalent velocity range. This allows the prediction of corrosion rate in the TCFC loop using RCE through the similarity solution method [19].

CHAPTER 2: PHASE BEHAVIOR OF CARBON DIOXIDE

Since the experimental conditions involved a different range of pressures and temperatures, it is pertinent to understand the phase behavior of carbon dioxide in its pure state and in CO₂-water binary mixtures. Such understanding helps shed light on the test conditions encountered and how they may have affected corrosion rates. **Figure 2** below shows that pure CO₂ could exist in four phases: gas, liquid, solid, and supercritical fluid [20]:

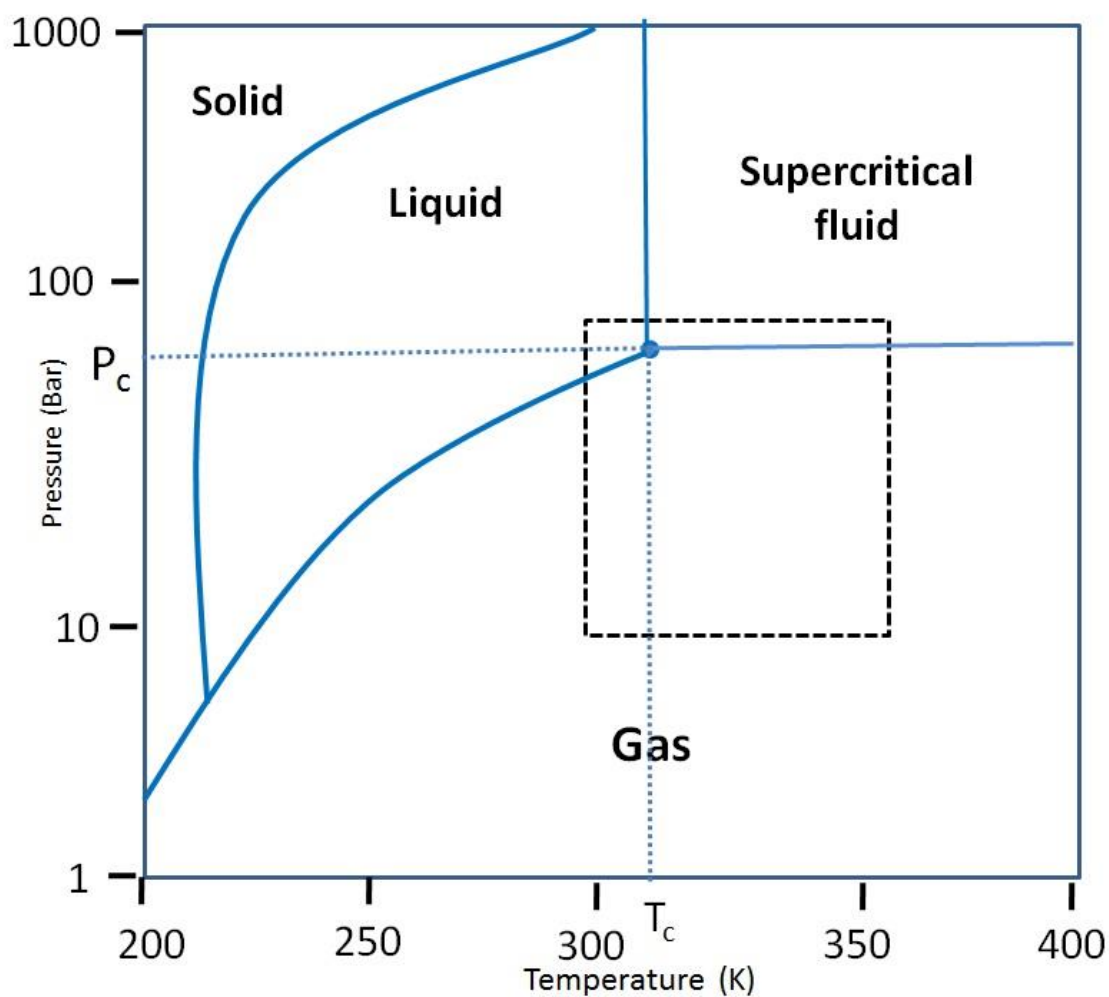


Figure 2: The phase diagram of pure CO₂ [20].

At normal atmospheric pressure and temperature, CO₂ only exists as gas [21]. The figure above also indicates that solid CO₂ could turn directly into gas, a process called sublimation that takes place at low temperatures and pressures. The reverse process occurs around these conditions where gaseous CO₂ converts directly to a solid. Gaseous and liquid CO₂ are colorless whilst its solid phase is snow-like white [22]. It co-exists as gas, liquid, and solid at about 5.2 bars and 217 K [21]. However, as the pressure and temperature increase along the vapor-liquid line, a single CO₂ phase that is neither liquid nor gas will exist, beginning at a critical point: 74 bars and 304 K. This phase is termed a supercritical fluid; as shown by **Table 1**, supercritical CO₂ has a density approaching that of a liquid, but viscosity similar to that of a gas; moreover, diffusivity in supercritical CO₂ is higher than in the liquid phase [14, 23]:

Table 1: Comparison of physical properties among different phases of CO₂ [14]

	CO ₂		Naphthalene in CO ₂
	Density ρ (kg/m ³)	Viscosity η (μ Pa.s)	Diffusion Coefficient D (m ² /s)
Gas, 313K, 1 bar	2	16	5.1×10^{-6}
Supercritical, 313K, 100 bar	632	17	1.4×10^{-8}
Liquid, 300K, 500 bar	1029	133	8.7×10^{-9}

It is to be noted that once CO₂ reaches its critical temperature, increasing its pressure cannot turn it into a liquid [23, 24]. Moreover, once CO₂ reaches its critical pressure, increasing its temperature will not turn it into gas [23, 24].

In this study, the test matrix encompassed the gas, liquid, and supercritical phases of CO₂ as shown by the dotted rectangle in **Figure 2** above. In relation to this, it must be pointed out that in this study, supercritical CO₂ refers to the CO₂-rich phase only at the pressures and temperatures of interest, particularly 80 bars-50° C and 80 bars-80° C, the mixture in the water-rich phase does not reach supercritical phase [10, 25, 26]. The reason is that it will take a much higher pressure for the aqueous CO₂-water system (water-rich phase) to become supercritical; this is especially true when the volume of water is large. For example, referring to the critical curve in **Figure 3** below, five mole percent of dissolved CO₂ in the binary system will require about 250 bars of total pressure [26]; since vapor pressure even at 80° C (~0.5 bar) is negligible compared to the partial pressure of CO₂, it could then be said that an experiment at five mole percent of CO₂ will require about 250 bars of pCO₂:

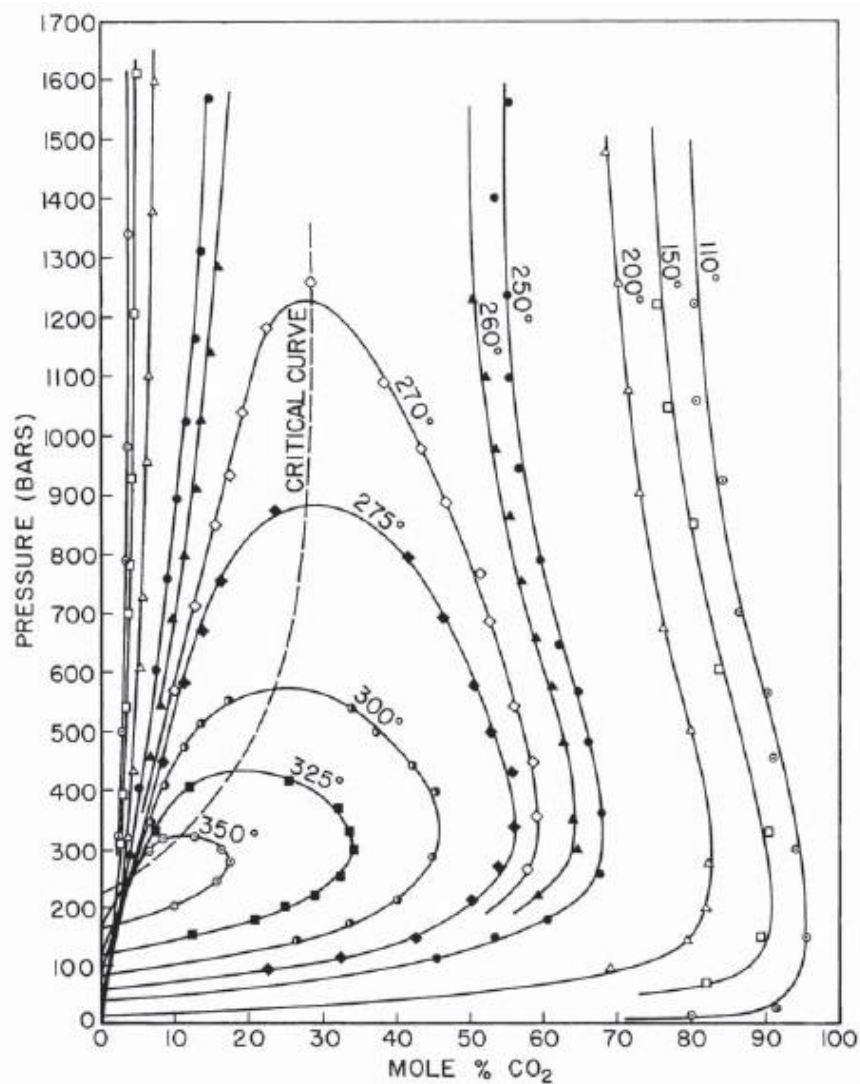


Figure 3: The critical curve of CO₂-water system [26]

Of the physical properties stated in **Table 1** above, density plays a significant role in corrosion; this is because it influences the solubility of solutes such as water vapor in the CO₂-rich phase [24, 27]. This in turn affects corrosion of carbon steel in the CO₂-rich phase [28]. On the other hand, solubility of gaseous CO₂ in water influences corrosion of carbon steel in the water-rich phase *via* the water chemistry of the solution.

CHAPTER 3: OVERVIEW OF CO₂ CORROSION

Prediction of CO₂ corrosion entails understanding of its mechanism and the factors that affect it. Mechanistically, CO₂ corrosion involves three simultaneous processes: chemical reactions, electrochemical reactions and mass transport [29]:

3.1 Chemical reactions

Chemical reactions that occur homogeneously start with the dissolution of gaseous carbon dioxide (CO₂) in water:



For low partial pressure of CO₂ (pCO₂), the solubility of CO_{2(g)} in water is governed by Henry's law in which the temperature-dependent solubility constant, K_{sol} , is defined as [30, 31]:

$$K_{sol} = \frac{C_{CO_2}}{pCO_2} \quad (2)$$

where C_{CO_2} corresponds to the concentration of dissolved CO₂ while pCO₂ refers to the concentration of CO₂ in the gas phase termed as partial pressure of CO₂. Henry's constant is then defined as $K_H = \frac{1}{K_{sol}}$. For example, at 25 °C and pCO₂ of 1 bar, $K_{sol} = 3.12 \times 10^{-2} \frac{M}{bar}$, giving the concentration of aqueous CO₂ of $3.10 \times 10^{-2} M$. Henry's

law is, however, valid for low $p\text{CO}_2$ in which the amount of solute is small [24]. For high $p\text{CO}_2$, its solubility in water is governed by the following relation [27]:

$$K_{sol} = \frac{m_{\text{CO}_2}}{p\text{CO}_2} \quad (3)$$

where m_{CO_2} is in molal. **Equation (3)** is similar to **equation (2)** except that dissolved CO_2 in **equation (2)** is given in molar. m_{CO_2} is calculated by the following equation which comes from the equation for the calculation of mole fraction of aqueous CO_2 in water, x_{CO_2} :

$$m_{\text{CO}_2} = \frac{55.508 \times x_{\text{CO}_2}}{(1 - x_{\text{CO}_2})} \quad (4)$$

where the constant 55.508 is the molality of water, and x_{CO_2} corresponds to mole fraction of CO_2 dissolved in water; x_{CO_2} is calculated using the following relation [27]:

$$x_{\text{CO}_2} = B(1 - y_{\text{H}_2\text{O}}) \quad (5)$$

while $y_{\text{H}_2\text{O}}$, the mole fraction of water in the CO_2 -rich phase, is calculated as follows:

$$y_{\text{H}_2\text{O}} = \frac{(1 - B)}{\left(\frac{1}{A} - B\right)} \quad (6)$$

where A and B are defined as follows:

$$A = \frac{K_{H_2O}^o}{\phi_{H_2O} P_{tot}} \exp\left(\frac{(P - P^0)\bar{V}_{H_2O}}{RT}\right) \quad (7)$$

$$B = \frac{\phi_{CO_2} P_{tot}}{55.508 K_{CO_2(g)}^o} \exp\left(-\frac{(P - P^0)\bar{V}_{CO_2}}{RT}\right) \quad (8)$$

where ϕ_{H_2O} and ϕ_{CO_2} refer to the fugacity coefficients solved using the Redlich-Kwong equation of states, P_{tot} corresponds to the total pressure of the system in bar, R is the gas constant, P^0 is a reference pressure at 1 bar obtained from the literature, \bar{V}_{H_2O} and \bar{V}_{CO_2} are the average partial molar volumes obtained from the literature, and $K_{H_2O}^o$ and $K_{CO_2(g)}^o$ are the true equilibrium constants at a reference pressure of 1 bar which are calculated as follows:

$$\log(K^o) = a + bT + cT^2 + dT^3 \quad (9)$$

where T is temperature in Celsius, and a, b, and c are regression constants. The in-house water-chemistry model developed as part of this research work [15] makes use of the above equations for modeling the solubility of gaseous CO₂ in water, *i.e.*, CO_{2(aq)}. In the model, the gas phase is taken to be non-ideal while the solution is assumed to be ideal (activity coefficient=1) as no salt addition is considered [27].

The dissolved or aqueous CO₂ will then hydrate, forming carbonic acid:



The corresponding equilibrium constant for hydration is defined as follows:

$$K_{hy} = \frac{c_{H_2CO_3}}{c_{CO_2}} \quad (11)$$

The equilibrium constant for hydration only changes slightly with temperature within the range of interest (20 to 100° C) and does not depend on pressure [32]. At 25° C, $K_{hy} = 2.58 \times 10^{-3}$, and its pressure independence means the value is applicable for both low and elevated CO₂ partial pressures [15, 32]. It is worth noting that the dehydration rate constant is much higher than the hydration rate constant; for example, at 25° C, while the former is 19.2 s⁻¹, the latter is 4.37 x10⁻²s⁻¹. This indicates that less than 1% of dissolved CO₂ turns into carbonic acid [33].

Carbonic acid further weakly dissociates into bicarbonate and hydrogen ions:



The equation for the equilibrium constant of the reaction is given as follows:

$$K_{ca} = \frac{c_{H^+} c_{HCO_3^-}}{c_{H_2CO_3}} \quad (13)$$

K_{ca} is pressure and temperature dependent. At 25° C and 1 bar pCO₂, $K_{ca} = 1.7 \times 10^{-4}M$. Bicarbonate ions then dissociate into carbonate and hydrogen ions:



Its equilibrium constant, K_{bi} , is defined as:

$$K_{bi} = \frac{C_{H^+}C_{CO_3^{2-}}}{C_{HCO_3^-}} \quad (15)$$

K_{bi} depends on temperature and ionic strength. At 25 °C and 1 bar pCO₂, $K_{bi} = 4.94 \times 10^{-11}M$. Another source of hydrogen ion comes from dissociation of water [34]:



The equilibrium constant, K_{wa} , is defined as follows:

$$K_{wa} = C_{H^+}C_{OH^-} \quad (17)$$

Table 2 below lists the empirical equations for calculating the above equilibrium constants at low pCO₂:

Table 2: The empirical equations for the equilibrium constants

Chemical Reactions	Equilibrium Constants
Dissolution of gaseous CO ₂ in water [30]	$K_{sol} = \frac{14.5}{1.00258} \times 10^{-(2.27+5.65 \times 10^{-3} T_f - 8.06 \times 10^{-6} T_f^2 + 0.075 I)}$ molar/bar
Hydration of aqueous CO ₂ [32]	2.58×10^{-3}
Dissociation of carbonic acid[30]	$K_{ca} = 387.6 \times 10^{-\left(6.41 - 1.594 \times 10^{-3} T_f + 3.52 \times 10^{-6} T_f^2 - 3.07 \times 10^{-5} p - 0.4772 I^{\frac{1}{2}} + 0.11807 I\right)}$ molar
Dissociation of bicarbonate ions[30]	$K_{bi} = 10^{-(10.61 - 4.97 \times 10^{-3} T_f + 1.331 \times 10^{-5} T_f^2 - 2.624 \times 10^{-5} p - 1.66 I^{\frac{1}{2}} + 0.34661 I)}$ molar
Dissociation of water [35]	$K_{wa} = 10^{-(29.3868 - 0.0737549 T_k + 7.47881 \times 10^{-5} T_k^2)}$ molar ²

In the above equations, T_f refers to the temperature in Fahrenheit while T_k corresponds to the temperature in Kelvin, p refers to the partial pressure of CO₂ in bar, and I is the ionic strength (molar) which can be calculated as follows:

$$I = \frac{1}{2} \sum_i c_i z_i^2 \quad (18)$$

where c_i refers to the concentration of species i and z_i the oxidation state of the species involved in the reaction.

Table 3 below shows the equations for the equilibrium constants for high partial pressure of CO_2 for which a pH model has been based on; experimentally validated in another related work [15]:

Table 3: The equilibrium constants for high partial pressure of CO₂

Chemical Reactions	Equilibrium Constants
Dissolution of gaseous CO ₂ in water [15]	$K_{sol} = \frac{m_{CO_2}}{p_{CO_2}}$ molar/bar
Hydration of aqueous CO ₂ [32]	2.58×10^{-3}
Dissociation of carbonic acid[36]	$\ln K_{ca} =$ $233.5159304 - 11974.38348 \times T^{-1} - 36.50633536 \ln T +$ $(-45.08004597 \times T^{-1} + 2131.318848 \times T^{-2} + 6.714256299 \times$ $T^{-1} \ln T)(P - P_s) + (0.008393915212 \times T^{-1} - 0.4015441404 \times$ $T^{-2} - 0.00124018735 \times T^{-1})(P - P_s)^2$ molar
Dissociation of bicarbonate ions[36]	$\ln K_{bi} = -151.1815202 - 0.088695577 \times T - 1362.259146 \times$ $T^{-1} + 27.79798156 \ln T - (29.51448102 \times T^{-1} + 1389.015354 \times$ $T^{-2} + 4.419625804 \times T^{-1} \ln T)(P - P_s) + (0.003219993525 \times$ $T^{-1} - 0.1644471261 \times T^{-2} - 0.0004736672395 \times T^{-1} \ln T)(P -$ $P_s)^2$ molar
Dissociation of water [36]	$\log K_{wa} = -4.098 - 3245.2 \times T^{-1} + 2.2362 \times 10^{-5} \times T^{-2}$ $- 3.984 \times 10^7 \times T^{-3}$ $+ (13.957 - 1262.3 \times T^{-1} + 8.5641 \times 10^5$ $\times T^2) \log \rho_{H_2O}$

3.1.1 Aqueous water chemistry model

Knowing the equilibrium constants, the above homogeneous chemical reactions could be used to model the pH and carbonic species concentrations. To do that, an electro-neutrality equation needs to be taken into account so that the number of unknown

species, namely aqueous CO₂, hydrogen ions, hydroxyl ions, carbonic acid, bicarbonate ions and carbonate ions, satisfy charge balance based upon their known, and inter-related equilibria [34]. The electro-neutrality equation is given as follows:

$$C_{H^+} = C_{OH^-} + C_{HCO_3^-} + C_{CO_3^{2-}} \quad (19)$$

The pH model developed based on the above equations is applicable for an open system in which pCO₂ is known and constant; this is true when the amount of gaseous CO₂ is much larger relative to that of water, and it could be simulated in a laboratory experiment by continuous purging of gaseous CO₂. As such, for a closed-system in which the amount of gaseous CO₂ is limited, pCO₂ is no longer constant as gaseous CO₂ dissolves into water and chemically reacts as described earlier; an additional equation is thus required to account for an additional unknown: pCO₂. Since the initial amount of gaseous CO₂ introduced into the closed system is known and constant, it means that the total amount of carbonic species (in moles) is conserved. Accordingly, an equation that reflects the conservation of the total amount of carbonic species is added to account for the changing of pCO₂ [31, 34]:

$$m_{CO_2(g)} + m_{CO_2(aq)} + m_{H_2CO_3} + m_{HCO_3^-} + m_{CO_3^{2-}} = n \quad (20)$$

where n refers to a constant molar quantity of gaseous CO_2 initially introduced into the closed-system. At low partial pressure of CO_2 , n (in mole) is calculated using an equation of state for an ideal gas as follows:

$$n = \frac{p\text{CO}_2V}{RT} \quad (21)$$

Employing the open system model yields a distribution of carbonic species in equilibrium as a function of pH at 1bar, 25 °C as shown in **Figure 4** below:

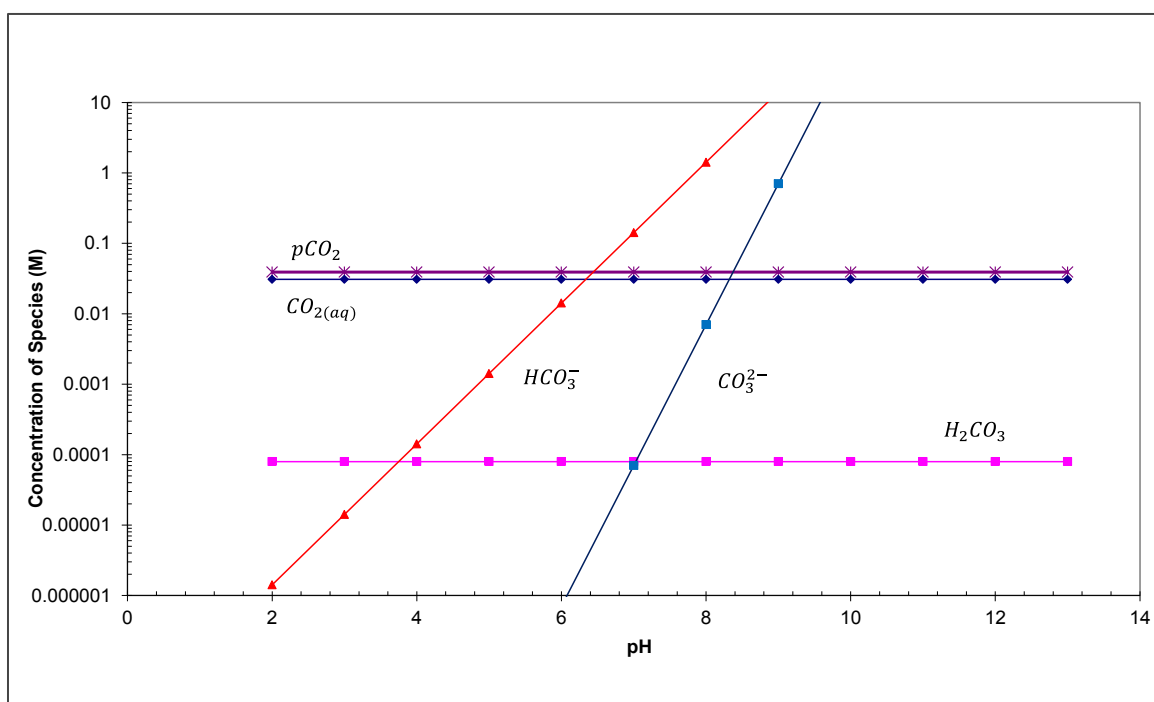


Figure 4: Concentration of carbonic as a function of pH for an open system at $p\text{CO}_2=1$ bar and 25 °C.

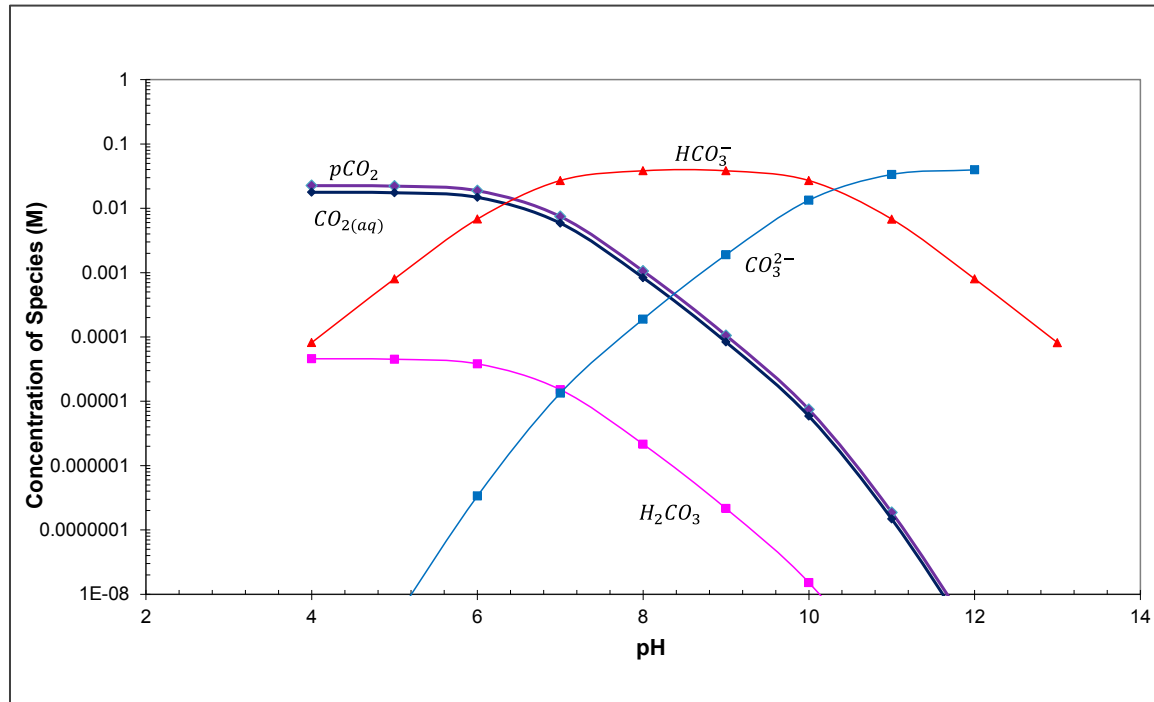


Figure 5: Concentration of carbonic as a function of pH for closed systems at $pCO_2=1$ bar and $25^\circ C$.

Figure 5 above, on the other hand, shows the concentration of carbonic species in equilibrium as a function of pH for closed systems:

It is important to note that the presence of ferrous ions from the dissolution of carbon steel could lead to an increase in pH as it disturbs the electro-neutrality of the ionic species given in **equation (19)**. This fact is important as the pH of the test solution tends to change over time, particularly for a small volume autoclave or glass cell [3, 4, 37].

It must also be noted that all the chemical reactions given earlier are in equilibrium, for otherwise a stable pH is not possible. The chemical equilibrium which satisfies the following Gibbs free energy equation [38] will, however, be disturbed once

carbon steel is introduced into the solution due to electrochemical reactions between the reducible species and the steel surface [39]:

$$\Delta G^{\circ} = -RT \ln K \quad (22)$$

where ΔG° is the change in Gibb free energy at standard conditions (25 °C and 1 atm), R is the gas constant, T is temperature in Kelvin, and K is the equilibrium constant.

3.1.2 *The Effect of water chemistry on CO₂ corrosion*

Water and its chemical compositions are of paramount importance in corrosion as water serves as electrolytic path as well as influences the pH and the formation of films through dissolved species. Like other types of aqueous corrosion, CO₂ corrosion requires the presence of water to effect corrosion process since water acts as an electrolyte that allows the movement of chemical species in-between anode and cathode to complete an electrical circuit [38]. In CO₂ corrosion, water is further required for the hydration of aqueous CO₂ that will not only provide the reducible carbonic species, namely carbonic acid and bicarbonate, but also determine the pH of the solution [40] as dissolved CO₂ acidifies it [41, 42](see §3.1.1). pH of the solution is important as it indicates the concentration of the free hydrogen ions involved in the cathodic reactions as reflected by **equation (26)**; the lower the pH is, the more corrosive the solution is and vice versa [42, 43]. However, unlike in strong acid solution, the change in corrosion rate in CO₂-saturated solution is not proportional to the change in pH as the limiting current density is partly under the chemical reaction-control that is not dependent on pH [44]. Apart from

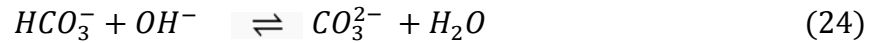
cathodic reactions, it also influences the anodic reactions at pH lower than 4 in which the increase in pH increases the anodic dissolution (see § 3.2.2) [18, 45].

It must be noted that solution pH also depends on the sources of water; that is, either formation water or condensation water [1]. The formation water normally contains various ions such as ferrous, chloride, sulfate, carbonate and bicarbonate ions [11]; the presence of bicarbonate and ferrous ions will help increase the pH, hence reduce the corrosion rate due to the decrease in the reduction of hydrogen ions [1, 18]. On the other hand, condensed water does not contain extraneous ions [11]. As such, its pH, when saturated with aqueous CO₂, will be lower than that of formation water, making it more corrosive. It is also more corrosive because condensed water allows more dissolution of iron as compared to formation water that already has some dissolved ferrous ions [42]. That is why an autogeneous pH of CO₂-saturated solution usually falls between pH 3 to pH 4 while atypical pH value in the field is between pH 4-6 due to the presence of other dissolved species [44].

Another significance of pH is that it influences the formation of ferrous carbonate layers by affecting the super saturation (S) of ferrous carbonate [46] defined as follows:

$$S = \frac{C_{Fe^{2+}}C_{CO_3^{2-}}}{K_{sp}} \quad (23)$$

where K_{sp} is the solubility product of ferrous carbonate (siderite). As shown by **Figure 4**, the increase in pH or hydroxyl ions leads to the increase in carbonate concentration due the following reaction [41]:



This in turn increases ferrous carbonate concentration in the solution as reflected by **equation (23)** which leads to precipitation of ferrous carbonate on steel surface [43]. The equation also suggests that at low pH in which saturation is not achieved ($S < 1$) due to low concentration of ferrous or carbonate ions, any ferrous carbonate formed may dissolve [47]. For this reason, an increase in pH helps prevent the removal of ferrous carbonate by chemical dissolution [18, 47]. This is shown by **Figure 6** below that indicates the decrease in the solubility of ferrous carbonate, as reflected by the decrease in ferrous ion concentration, as pH increases [1, 48]. Thus, an increase from pH 4 to pH 5 reduces the solubility of iron carbonate five times while an increase from pH 5 to pH 6 reduces its solubility hundred times [1, 18].

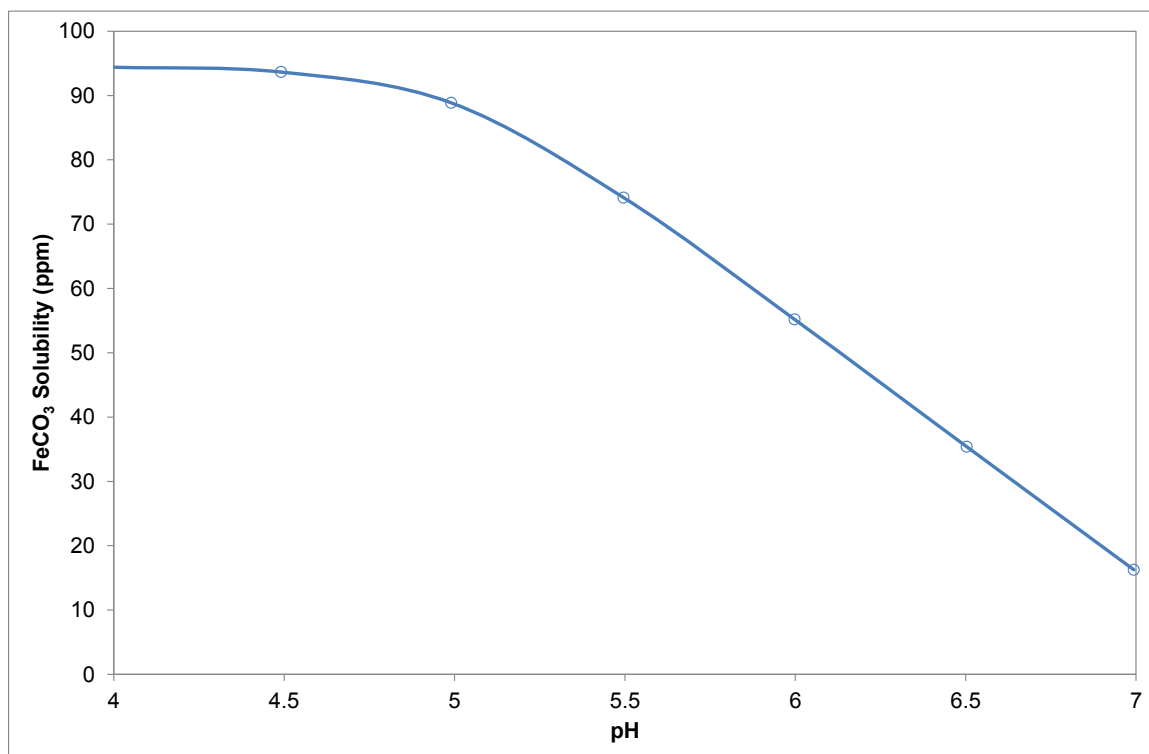
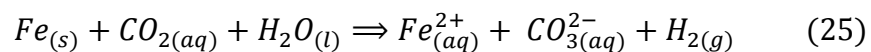


Figure 6: The dissolution of iron carbonate (siderite) in NaCl solution as a function of pH [1]

3.2 Electrochemical reactions

The information on the distribution of carbonic species as elucidated in Section 3.1 is vital as the reducible species are involved in electrochemical reactions that lead to corrosion of carbon steel. The overall reaction of the dissolution of carbon steel in CO₂ environment is [43]:



The above overall reaction actually consists of two simultaneous electrochemical reactions that take place on the steel surface: cathodic and anodic reactions:

3.2.1 Cathodic reactions

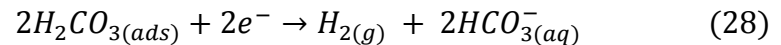
Hydrogen ions produced in the chemical reactions participate in the electrochemical reactions by being reduced at the cathodic sites, evolving hydrogen gas in two steps:



and

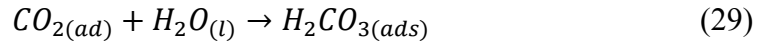


While carbonic acid dissociation provides a source of hydrogen ions, it itself is directly reduced on the steel surface; that is, carbonic acid is adsorbed on the surface, followed by its heterogeneous dissociation and reduction [5, 29]:

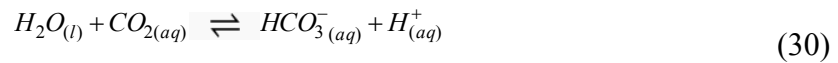


There are three different steps proposed as the rate determining step (RDS) in the direct reduction of carbonic acid: purely electrochemical, chemical reaction and chemical-mass transport. DeWaard and Milliams [49] proposed that the RDS is the release of hydrogen from the *adsorbed* carbonic acid as given in **equation (28)**; they also suggested that adsorbed bicarbonate would then combine with hydrogen ions to reproduce carbonic acid. Schmitt and Rothmann [50], however, proposed that the RDS is the slow chemical

reaction of the hydration of *adsorbed* aqueous CO₂ given in **equation (29)**, i.e., a heterogeneous reaction:



Similarly, Nescic [51] also proposed the hydration of dissolved aqueous CO₂ as the RDS, albeit the hydration reaction is homogeneous: taking place within the bulk and reaction boundary layer. The hydration process is homogeneous because it has been observed that different metals such as platinum and iron produce the same cathodic limiting current densities; heterogeneous hydration would lead to different cathodic limiting current densities on different metals as each metal would adsorb CO₂ differently [52]. Regardless of the mechanism, the theories agree that the fact that CO₂ corrosion involves principally two cathodic reduction reactions makes it more corrosive than strong acid at the same pH [49, 53]. Remita and co-workers [54], however, attribute the higher corrosion rates in the CO₂ environment to the buffering effect of CO₂; that is, buffering lowers and stabilizes the surface pH by providing additional sources of hydrogen ions at the interface:



As such, they contend that the direct reduction of carbonic acid plays no role in causing the corrosion rate in CO₂-containing electrolyte to be higher than that in strong acid of the same pH. This was because CO₂-purged solution yielded a lower surface pH than did the N₂-purged solution as measured on a gold electrode. The direct reduction of molecular carbonic acid, on the other hand, would lead to the increase in surface pH due to the generation of bicarbonate ions on the steel surface per **equation (28)**. Linter and Burstein [55], who agreed with Remita, reject the direct reduction mechanism on the ground that hydrogen evolution by the direct reduction of carbonic acid and bicarbonate would require a much more negative over-potential than would hydrogen ion reduction at the same pH: -0.622V for carbonic acid reduction and -0.856V for bicarbonate reduction compared to -0.481V for hydrogen ion reduction as measured against a saturated calomel electrode at pH 4. Nevertheless, the buffering effect mechanism may not be able to explain why CO₂ corrosion is not as flow sensitive as strong acid corrosion. That is, hydrogen ions, if considered as the only possible reducible species in CO₂ corrosion, should make CO₂-corrosion sensitive to flow [1, 51, 56]. Moreover, even if it is assumed that the buffering effect enriches the concentration of hydrogen ions near the metal surface, hydrogen ions still need to diffuse through the boundary layer, hence flow will have some bearing on the rate of hydrogen ion transport, hence CO₂ corrosion rate [57]. A comparison between **Figure 7** and **Figure 8** below illustrates the difference in corrosion rates between N₂-purged and CO₂-purged solutions at the same pH; while **Figure 7** clearly shows flow sensitivity, **Figure 8** suggests a relatively low flow-sensitivity [51]:

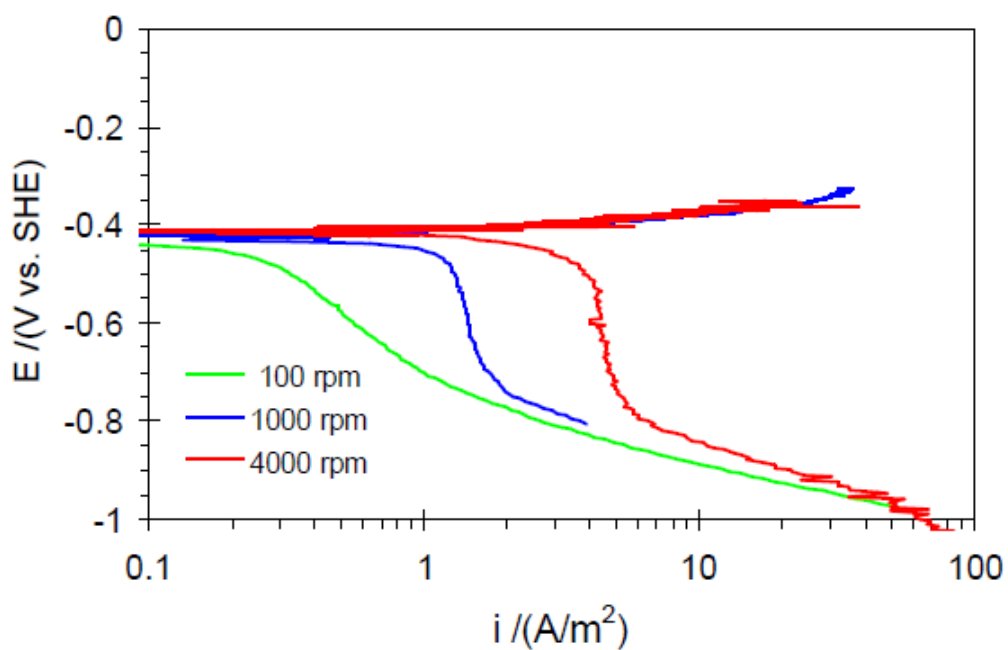


Figure 7: The variation of cathodic limiting current densities with velocities in a N_2 -purged solution of pH 4 and $22^\circ C$ showing flow-sensitivity [51]

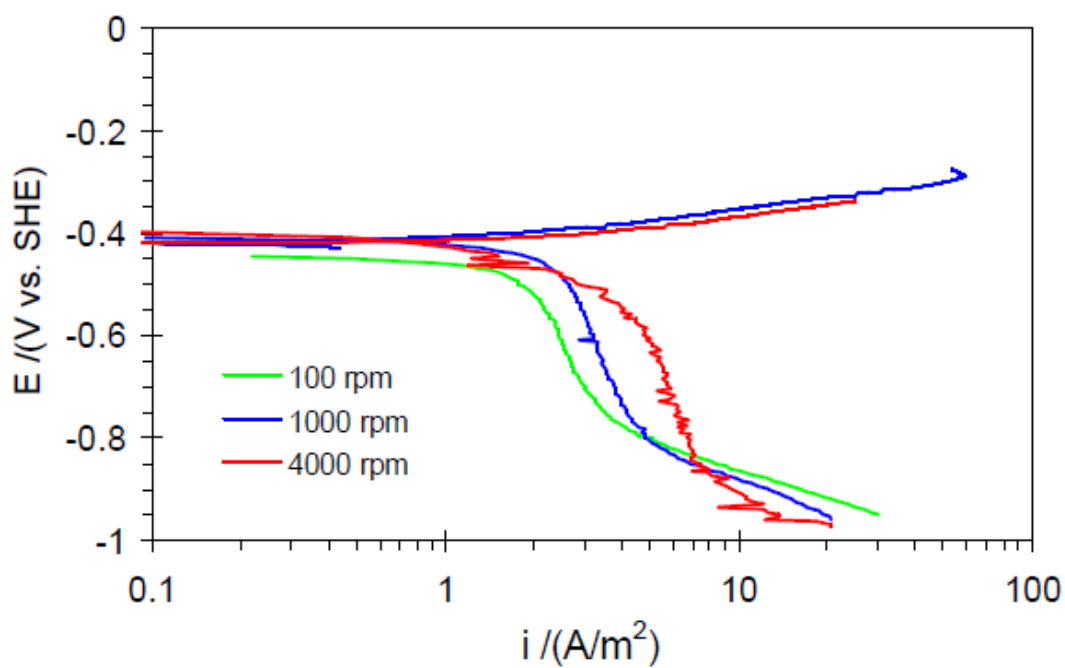
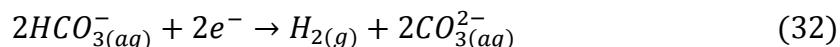


Figure 8: The variation of cathodic limiting current densities with velocities in a CO_2 -purged solution of pH 4 and $22^\circ C$ showing less flow-sensitivity [51]

Additionally, if hydrogen ions were the only reducible species in CO₂-corrosion, its limiting current density should decrease in proportion to the increase in pH. This is because the limiting current density of N₂-purged solution changes proportionally with the change in pH [44]. This suggests the role of chemical-reaction controlled limiting current density. In this regard, the direct reduction mechanism seems to be able to explain the flow insensitivity of CO₂ corrosion by attributing it to the slow hydration of aqueous CO₂.

The additional cathodic reaction of bicarbonate reduction as proposed in the direct reduction mechanism comes into play at pH values higher than 5 [29]:



Nevertheless, it is argued that the direct reduction of bicarbonate has negligible effects on corrosion rates [29]. Despite this fact, Zhang and co-workers [58] suggest that the reduction of bicarbonate slows down the decrease in corrosion rate which results from the increase in pH.

It is important to note that all the above cathodic species which are reduced at the metal surface could yield either charge-transfer cathodic current density or limiting cathodic current density, depending on the rate of mass transport of the species to the metal surface or the rate of charge-transfer reactions at the metal surface. This will then determine whether the total cathodic current density will come mainly from charge-transfer reaction or the rate of mass transport:

$$i_{c(total)} = \frac{1}{i_{c(charge)}} + \frac{1}{i_{c(mass)}} \quad (33)$$

Equation (33) indicates that a high charge-transfer (reaction) will cause the total cathodic current density to arise largely from the rate of mass transport and *vice versa*. Consequently, this will determine whether the resultant corrosion rate would be under charge-transfer control, mixed-transfer control, or mass-transfer control.

3.2.1.1 Charge-transfer cathodic current density

Charge-transfer cathodic current density is calculated by the following Tafel equation [43]:

$$i_{c_j} = i_{c_j}^o \times 10^{\left(\frac{-E - E_{rev_j}}{b_{c_j}}\right)} \quad (34)$$

where i_{c_j} is the cathodic current density of reducible species j , E is the corresponding potential of interest, $i_{c_j}^o$ is its exchange current density, E_{rev_j} is its corresponding reversible potential, and b_{c_j} is its Tafel coefficient or slope. $i_{c_j}^o$ could be calculated as follows:

$$i_{c_j}^o = i_o^{ref} e^{-\frac{\Delta H}{R} \left(\frac{1}{T_K} - \frac{1}{T_{Kref}} \right)} \quad (35)$$

As for the reversible potential, it is calculated as:

$$E_{rev_j} = -\frac{2.303R(T_K)}{nF}pH \quad (36)$$

The equation for the Tafel coefficient is defined as:

$$b_{c_j} = \frac{2.303R(T_K)}{0.5F} \quad (37)$$

Another source of cathodic species comes from water, abundantly present near the metal and cathodically reduced at the surface by the following reaction:



The direct reduction of water occurs when the steel surface is negatively polarized to the reversible potential of water [43, 59], and it requires a relatively large overvoltage [42]:

$$E_{rev_{H^+/H_2}} = -\frac{2.303R(T_K)}{2F}pH \quad (39)$$

As water near the surface is not depleted, the cathodic reaction is only under charge transfer-control [43, 55].

3.2.1.2 Limiting cathodic current density

The direct reduction mechanism postulates two types of limiting current density in CO₂ corrosion [43, 50, 57]:

1. That arising from the mass transport of species to the metal surface *via* the diffusion boundary layer: i_{lim}^d
2. That arising due to the slow hydration of aqueous CO_2 : i_{lim}^c

The first type involves the reduction of hydrogen ions while the second type involves the reduction of carbonic acid as illustrated in **Figure 9** below:

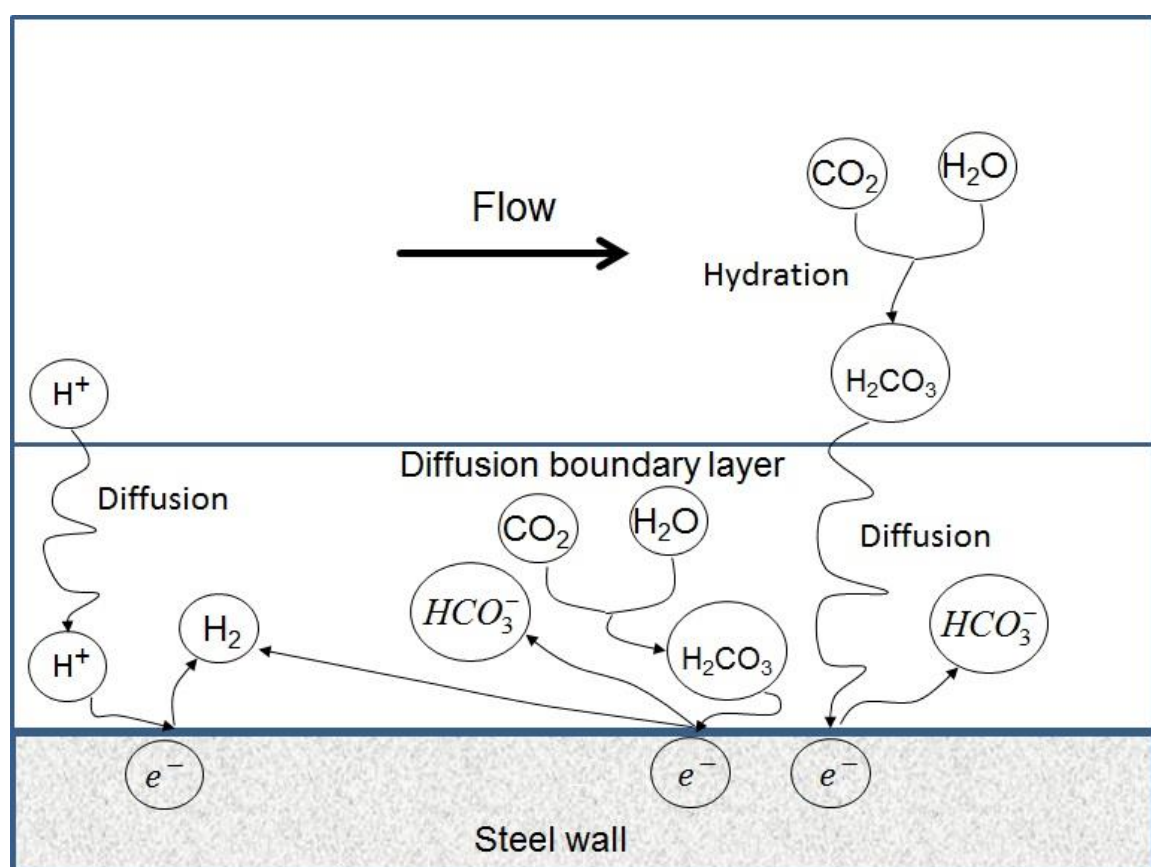


Figure 9: Diffusion of hydrogen ions and carbonic acid through the diffusion boundary layer and hydration of aqueous CO_2 in the bulk and within the boundary layer [57]

The first type limiting current density is derived from Fick's first law under steady-state diffusion [60-62]:

$$J = \frac{i}{nF} = -D \left(\frac{C_b - C_s}{\delta_d} \right) \quad (40)$$

where J is the flux of the species transported normally or perpendicularly to the surface given in $\left(\frac{\text{mol}}{\text{m}^2 \cdot \text{s}}\right)$, C_b and C_s are the concentrations of the species in the bulk solution and near the metal surface (Molar), respectively, D is the diffusion coefficient $\left(\frac{\text{m}^2}{\text{s}}\right)$, δ_d is the thickness of the diffusion boundary layer (m), n is the number of moles exchanged per mole of species participating in the reaction, i is the current density arising from mass transport to the surface $\left(\frac{\text{A}}{\text{m}^2}\right)$, and F is Faraday constant $\left(96500 \frac{\text{C}}{\text{mole}}\right)$.

The limiting current density (i_{lim}) then arises when high charge transfer reaction rates at the metal surface deplete the concentration near the surface to zero; the rate of cathodic reduction on the metal surface therefore depends on the mass transport rate of the species to the surface. In this case, **equation (40)** becomes [60]:

$$i_{lim}^d = nF \frac{D}{\delta_d} C_b \quad (41)$$

or

$$i_{lim}^d = nF k_m C_b \quad (42)$$

where $k_m = \frac{D}{\delta_d}$ is the mass transfer coefficient which depends on the geometry, velocity, and physical properties of the fluid [61, 62] *via* Sherwood number (see § 3.3.5), and C_b is the bulk concentration of the reducible species.

The second type of limiting current density is derived from Fick's laws, but with an additional term that accounts for the ratio between diffusion boundary layer (δ_d) and reaction boundary layer (δ_r) [51, 57]:

$$\xi = \frac{\delta_{d(H_2CO_3)}}{\delta_{r(H_2CO_3)}} \quad (43)$$

in which the reaction boundary layer is defined as:

$$\delta_{r(H_2CO_3)} = \sqrt{\frac{D_{(H_2CO_3)}}{k_b}} \quad (44)$$

where k_b is the reaction rate constant of the dehydration reaction (backward reaction) of **equation (10)**. It also assumes a first-order chemical reaction of **equation (10)** and a steady-state condition [51]. So, the chemical reaction-controlled limiting current density is given as [51, 57]:

$$i_{lim}^c = k_m F C_{H_2CO_3} \xi \coth \xi \quad (45)$$

In this regard, the slow chemical reaction of the hydration of dissolved CO_2 is assumed to take place in both bulk solution and reaction boundary layer as illustrated in **Figure 9**; the latter resides within the diffusion boundary layer, particularly for a stagnant condition when δ_d is much larger than δ_r [51, 57]. However, the ratio between the two boundary

layers could be affected by fluid flow; at a high velocity, the thickness of the diffusion boundary layer would reduce in which case ξ would be less than 1 [51, 57].

3.2.2 Anodic reactions

Correspondingly, at the anodic sites, iron will oxidatively dissolve as follows:

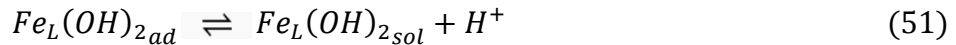
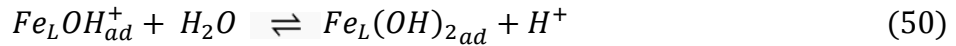
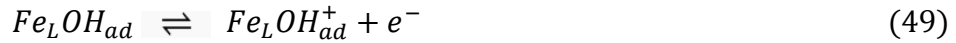
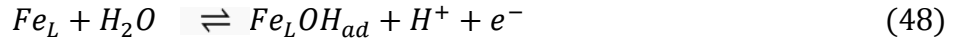


The equation that describes the rate of the above anodic reaction is given as follows [45]:

$$i_a = \kappa(C_{OH^-})^{a1}(pCO_2)^{a2}10^{\frac{E}{b_a}} \quad (47)$$

where κ is the reaction rate constant, C_{OH^-} is the concentration of the hydroxyl ions, $a1$ and $a2$ are reaction orders, E is potential, and b_a is Tafel coefficient or slope. For CO_2 corrosion, the dependence of anodic reaction on pH varies with pH range. The anodic reaction is pH dependent at pH less than 4 as $a1$ is equal to two; at this instance, anodic current density increases as the pH increases [63]. Moreover, at this pH range, the anodic current density would exhibit the same behavior regardless of whether the environment is hydrochloric acid solution or CO_2 -dissolved solution as long as both solutions are at the same pH [63]; in fact, the types of anions do not seem to make any significant difference in the anodic current density [55]. However, the anodic reaction becomes less pH dependent at pH values between 4 and 5 as the reaction order ($a1$) falls between one and two, and is no longer pH dependent at pH higher than 5 as the reaction order becomes

zero [45]. This behavior is possibly related to the fact that hydroxyl ions serve as a catalyst to the iron dissolution process via the following mechanism where Fe_L is defined as the adsorption of CO_2 at the Fe surface (or $FeCO_{2(ad)}$) [45]:



As the concentration of hydroxyl ions adsorbed on the surface increases, the dissolution of iron initially increases until it reaches a saturation point at which the further increase in pH or hydroxyl ion concentration does not lead to any further increase in anodic reaction rate [45, 64]. At pH lower than 4, the rate determining step is the desorption process given in **equation (51)** due to a higher charge transfer rate in **equation (49)** [45, 53]. On the other hand, when the pH is above 5, the rate determining step is the charge transfer reaction described by **equation (49)** [44, 53]. Recall that Fe_L in the above equations was described as the adsorption of CO_2 on iron surface: $Fe_L = FeCO_{2(ad)}$. In this regard, the effect of CO_2 on the anodic reaction does not depend on pH as experimentally observed [45]. The reaction order with respect to pCO_2 (a_2) is given as follows [45]:

$$pCO_2 < 0.01 \text{ bar}$$

$$a_2 = 0$$

$$\begin{array}{ll} 0.01\text{bar} < p\text{CO}_2 < 1 \text{ bar} & a_2=1 \\ p\text{CO}_2 > 1 \text{ bar} & a_2=0 \end{array}$$

Moreover, the anodic reaction of carbon steel is under charge transfer control from its corrosion potential (E_{corr}) up to 200 mV more positive than E_{corr} [5, 29]. Further anodic polarization of carbon steel in a CO_2 -saturated environment would enhance the anodic dissolution due to the disruption of the formation of a thin-oxide passive film [55]. This is supported by the fact that reverse and forward scans produced overlapping anodic polarization curves suggesting that the formed film could re-dissolve, hence was not protective [65]. As for being within the 200 mV range, the anodic current density exhibits Tafel behavior and could be described as follows [43]:

$$i_a = i_a^0 \times 10^{\left(\frac{E-E_{rev}}{b_a}\right)} \quad (53)$$

where i_a^0 refers to anodic exchange current density, and E_{rev} is the reversible potential of the anodic reaction defined as follows[57]:

$$E_{rev_{\text{Fe}^{2+}/\text{Fe}}} = E_{rev_{\text{Fe}^{2+}/\text{Fe}}}^o + \frac{2.303R(T_K)}{2F} \log C_{\text{Fe}^{2+}} \quad (54)$$

where $E_{rev_{\text{Fe}^{2+}/\text{Fe}}}^o$ refers to the standard redox potential of ferrous iron which can be calculated from the electrochemical equilibrium Gibb's free energy [59]:

$$E_{rev_{Fe^{2+}/Fe}}^o = -\frac{\Delta G}{2F} \quad (55)$$

At standard conditions of 25° C and 1 atm, it is given as -0.44 V with respect to the standard hydrogen electrode [59]. As for the Tafel coefficient, it is as follows:

$$b_{c_j} = \frac{2.303R(T_K)}{1.5F} \quad (56)$$

The exchange current density depends not only on pH and pCO₂ as noted in **equation (47)** above, but also on temperature through the following relationship [43]:

$$i_a^o = i_o^{ref} e^{\frac{\Delta H}{R} \left(\frac{1}{T_K} - \frac{1}{T_{Kref}} \right)} \quad (57)$$

where i_o^{ref} is a reference exchange current density, ΔH is the enthalpy of activation, T_K and T_{Kref} are the temperature of interest and the reference temperature in Kelvin, respectively. As a charge-transfer controlled reaction, anodic current density is not flow-dependent [55, 66].

3.2.3 Mass transport

The rates of the above electrochemical reactions are dependent on the mass transport rates of the reducible species towards and of oxidized metal ions away from the metal surface. The mass transport involved in CO₂ corrosion normally occurs *via*

molecular diffusion and convection; mass transport due to electro-migration is negligible in spontaneous corrosion as the local anodes and cathodes are on the same metal surface [31] and the presence of highly conductive supporting electrolytes such as sodium chloride [61]. Molecular diffusion occurs within a diffusion boundary layer as a result of concentration gradient while convective mass transport arises due to the flow of solution over a metal surface.

The reduction of hydrogen ions in **equation (26)** produced *via* reactions (12), (14) and (16) is limited by the mass transport of hydrogen ions to the metal surface [50]. This fact is evident in strong acid in which the hydrogen evolution rate is limited by the rate of hydrogen ion transport to the surface [56]. Some studies [29, 50] have also suggested that the direct reduction of carbonic acid also has a diffusion-limiting current component. However, since its chemical-reaction rate (hydration of dissolved CO₂) is much slower than its diffusion rate, the former becomes the rate determining step. **Figure 10** below shows the existence of a diffusion-limiting current component of carbonic acid reduction in which the gap between the two curves widens with the increased rotational speed, indicating slight flow sensitivity of carbonic acid as reflected by **equation (45)** [51].

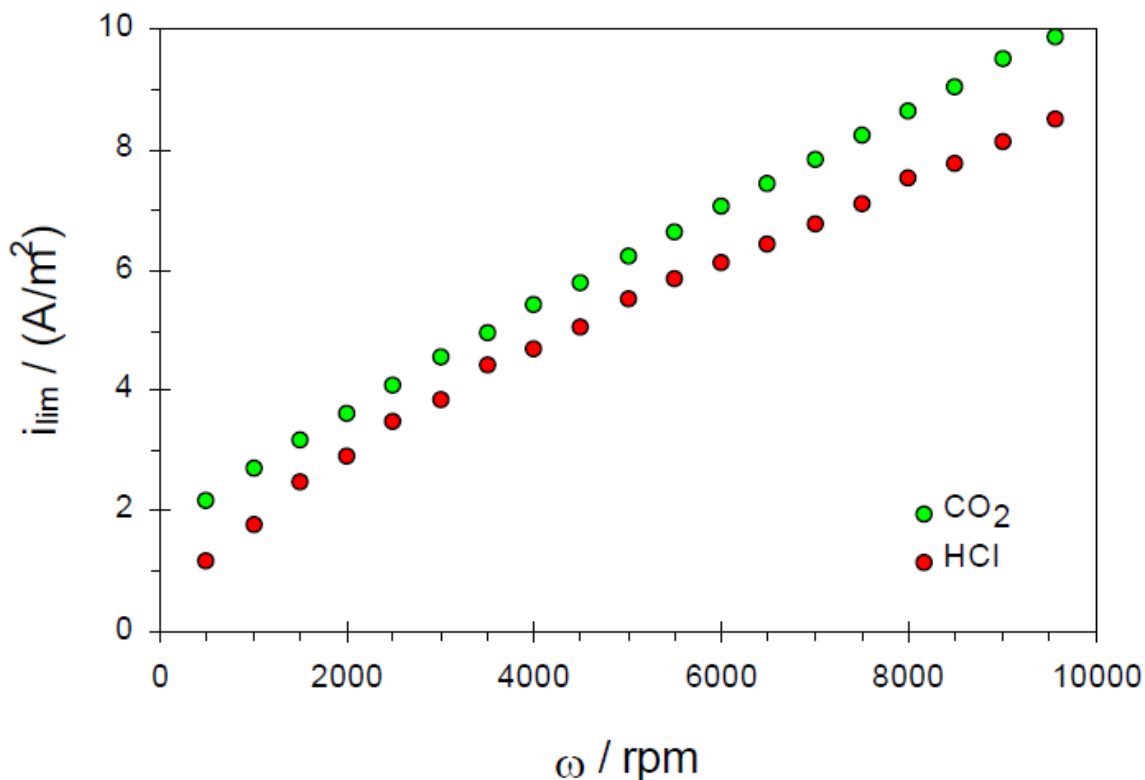


Figure 10: Limiting current density for a CO_2 and an HCl solution at pH4, 22° C measured potentiostatically using a rotating cylinder electrode [51]

With the hydration of aqueous CO_2 being the slowest step in the reduction of carbonic acid, the flow-sensitivity of CO_2 corrosion of mild steel comes largely from the mass transport of hydrogen ions [44]. As such, the sensitivity of CO_2 corrosion to flow can be clearly observed at pH values lower than 4 where the concentration of hydrogen ions is relatively high [29, 34]. The increase in pH reduces the hydrogen ion concentration and makes carbonic acid reduction dominant; this results in the corrosion rate being less flow sensitive [18, 57]. The decrease in flow-sensitivity also occurs when CO_2 partial pressure is increased. The work by Wang and co-workers [67] indicates that the increase in cathodic limiting current density from a low velocity to a higher velocity at 3 bar could be observed while there seemed to be a negligible increase in cathodic

limiting current density with increased velocity at 10 bar [67]. The flow sensitivity of CO₂ corrosion is governed by the interplay between mass transport processes and flow; that is, this requires knowledge of the interrelationship between mass transport processes and hydrodynamics as is discussed below in section **3.3.5**.

3.3 Influential factors

The chemical and electrochemical reactions along with the mass transport of the species involved in CO₂ corrosion are influenced by several interrelated factors [7]. These factors can be categorized into environment, metallurgy, corrosion product layers, and flow [1]:

3.3.1 Environment

The environmental factors consist of temperature and CO₂ partial pressure, each is described in the following sections:

3.3.1.1 Temperature

Temperature influences CO₂-corrosion by affecting the solubility of gaseous CO₂, the diffusion as well as the mass transfer coefficients of reducible species, the rates of chemical and electrochemical reactions, and the formation of iron carbonate. The increase in temperature will decrease the amount of carbon dioxide that dissolves in water [27] due to the decrease in solubility and the increase in the partial pressure of water vapor that lowers the pCO₂. For low pCO₂, the decrease in solubility is reflected by the solubility constant (K_{sol}) in **Table 2** while for high pCO₂, the temperature affects the CO₂ solubility constant given by **equation (3)** via the two coefficients given in **equations (7) and (8)**: A and B. The decrease in dissolved CO₂ will lead to a relatively

higher autogeneous pH or lesser concentration of hydrogen ions, hence a relatively lower corrosion rate. However, since the difference in autogeneous pH values due to temperature differences is minimal, the contribution to the change in corrosion rate due to the change in autogeneous pH is probably insignificant. For example, the pH at 10 bar, 25° C is 3.43 while the pH at 10 bar 50° C is 3.50 [68].

The significant contribution comes from the increase in the kinetics of chemical and electrochemical reactions which lead to the increase in corrosion rate for film-free conditions [1, 43], surpassing the contribution from pH change. For chemical reactions, the increase in temperature will increase the reaction rate constant (k) in accordance with Arrhenius equation [69]:

$$k(T) = k(T_0)e^{\frac{E}{R}\left(\frac{1}{T_0} - \frac{1}{T}\right)} \quad (58)$$

where $k(T_0)$ is the reaction rate constant at a reference temperature, T_0 (K), and E is the activation energy (J/mol). Similarly, as shown by **equation (57)**, Arrhenius equation also governs the charge transfer reaction rate *via* the exchange current density [44]; this is understandable since exchange current density essentially corresponds to the rate of chemical reactions, but with an additional factor to account for the effect of potentials (concentration of electrons) [70]. Moreover, temperature dependence of electrochemical reactions also comes via the diffusion coefficient (D) and mass transfer coefficient (K_m); the Stokes-Einstein equation reflects the temperature dependence of D while the temperature effect on K_m also comes *via* the effect on viscosity (see §3.3.5) [44].

Consequently, the influence on charge transfer and mass transfer rates could have a bearing on the rate determining step. For example, it was observed that at 20° C, the corrosion rate was initially not flow-sensitive as it was under charge-transfer control. However, when the temperature was raised to 60° C, the corrosion rate became flow-sensitive; this suggests that the corrosion rate at 60° C was under mass-transfer control. The reason the rate determining step switched to mass-transfer control was that the charge-transfer rate increased much more than the mass-transfer rate with the increase in temperature [52].

The most significant effect of temperature, however, is on the formation of iron carbonate layers in which temperature influences the solubility and growth of the corrosion product layers. In this regard, it has been observed that at temperature of about 80° C, corrosion rate will instead decrease with temperature [1, 71]. This is attributed to the formation of protective iron carbonate layers. As shown by **Figure 11** below, the increase in temperature reduces the solubility of iron carbonate as reflected by the decreased concentrations of ferrous ions in the solution [71]:

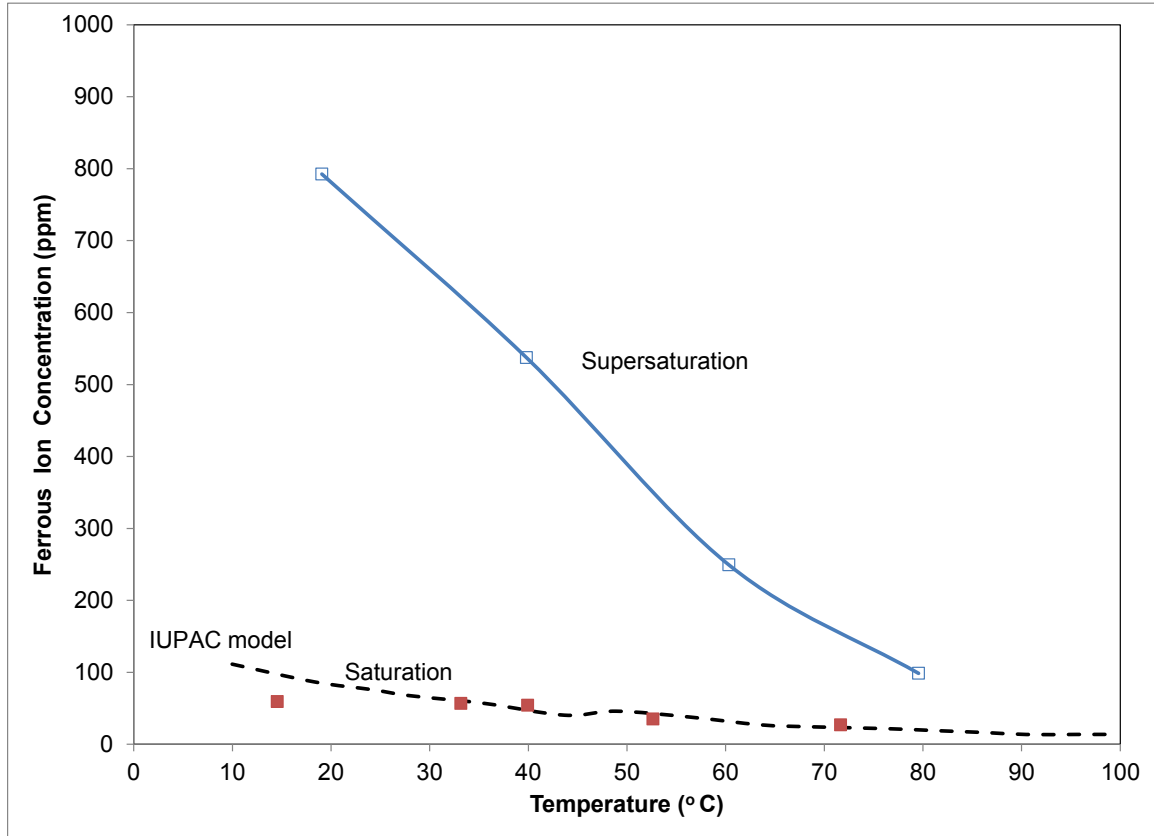


Figure 11: The solubility of ferrous ions as a function of temperature in pure-distilled water at $p\text{CO}_2=1\text{bar}$ for corroding steel (\square) and solid iron carbonate (\blacksquare) [71]

This means that the solubility product (K_{sp}) given in **equation (56)** will become small as the temperature increases. This facilitates the solution in reaching super saturation (S) with respect to FeCO_3 , hence its growth on the metal surface at a higher temperature.

The temperature-dependent K_{sp} is given as follows [72]:

$$\log K_{sp} = -59.3498 - 0.041377T_K - \frac{2.1963}{T_K} + 24.5724\log T_K + 2.518I^{0.5}0.657I \quad (59)$$

where T_K is temperature in Kelvin, and I is ionic strength in molar.

Another role of temperature in iron carbonate layer formation is to accelerate the kinetics of layer growth defined as [73]:

$$R_{gr} = k_{gr}(S - 1)^2 \quad (60)$$

where R_{gr} is the rate of layer growth, k_{gr} is the growth rate constant, and S is supersaturation. Temperature affects the growth rate by influencing the growth rate constant; a higher temperature will lead to a rapid precipitation of iron carbonate due to a higher k_{gr} [73, 74]. That is why any iron carbonate layer formed at a relatively low temperature (<60° C), despite a high concentration of ferrous ions (high supersaturation), was not fully protective [71, 75]. Even at 60° C, the iron carbonate layer formed could only reduce the corrosion rate minimally [71]. Only when the temperature reached 80° C did the formed iron carbonate layer become dense and protective, reducing the corrosion rate considerably [71]. In this regard, supersaturation alone is insufficient to ensure the formation of a protective iron carbonate layer; it also requires a more rapid kinetics of layer growth which could only be achieved at a higher temperature [71, 76]. At a low temperature, layer growth is slow and the layer formed is most likely not uniform, possibly leading to pitting [76, 77]. On the other hand, at high temperature, the layer grows at a faster rate and is continuous over the metal surface [76, 77]. This is probably because, at temperatures below 80° C, the corrosion rate that is relatively higher than the film growth rate undermines the layer formation; consequently, the iron carbonate layer, if formed, will be porous while above 80° C, the opposite is true [73]. The relative

competition between corrosion rate (CR) and film growth rate is termed scaling tendency (ST) and described by the following equation [73]:

$$ST = \frac{R_{gr}}{CR} \quad (61)$$

3.3.1.2 CO₂ Partial Pressure

CO₂ partial pressure (pCO_2) signifies the concentration of CO₂ in the gas phase [69]. It is defined as the product of the mole fraction (y_{CO_2}) in the gas phase and the total pressure of the system (P):

$$pCO_2 = y_{CO_2}P \quad (62)$$

It influences CO₂ corrosion rate through the concentration of gaseous CO₂ that dissolves in the aqueous phase; the increase in pCO_2 thus increases the solubility of gaseous CO₂ as elucidated in **Section 3.1** [1]. At a relatively high pressure, non-ideality of gas that arises due to molecular interactions must be taken into account. In this case, fugacity, instead of pressure, is used. Fugacity is related to pressure by the following relationship [78]:

$$f_{CO_2} = \phi pCO_2 \quad (63)$$

where ϕ is the fugacity coefficient.

It must be further noted that at low pCO_2 , the solubility of CO₂ in aqueous solution obeys Henry's law in which the concentration of aqueous CO₂ will increase

linearly with $p\text{CO}_2$; this is valid for relatively small amounts of solute (in this case, dissolved CO_2). However, at a relatively high $p\text{CO}_2$, the CO_2 solubility will no longer increase linearly due to the non-ideality of the CO_2 gas (see **Figure 1**) [3, 7]. Moreover, at low $p\text{CO}_2$, an infinite dilution assumption is valid while at a relatively high $p\text{CO}_2$, activity instead of concentration needs to be taken into account due to non-ideal solution behavior that arises from the increase in the concentration of solutes [7]. This factor leads to the non-linearity of corrosion rate with $p\text{CO}_2$ [79].

When there is no corrosion layer formation on the steel surface, the increase in CO_2 partial pressure will increase CO_2 -corrosion rate. This is partly due to the decrease in pH following the increase in the concentration of dissolved CO_2 [7]. Nevertheless, the corrosion rate will also increase even at a constant pH due to the increase in carbonic acid concentration, hence carbonic acid reduction in accordance with **equation (28)** [43]. Dugstad and co-workers found that the corrosion rate increased proportionally to $p\text{CO}_2$ by a power of 0.7 at $p\text{CO}_2$ of below 5 bar [18] while Videm and co-workers found the corrosion rate to be proportional to $p\text{CO}_2$ by a power of 0.5 to 0.8 [42]. On the other hand, Seiersten found that the corrosion rate decreased with the increase in $p\text{CO}_2$ as shown by **Figure 12** below [12]:

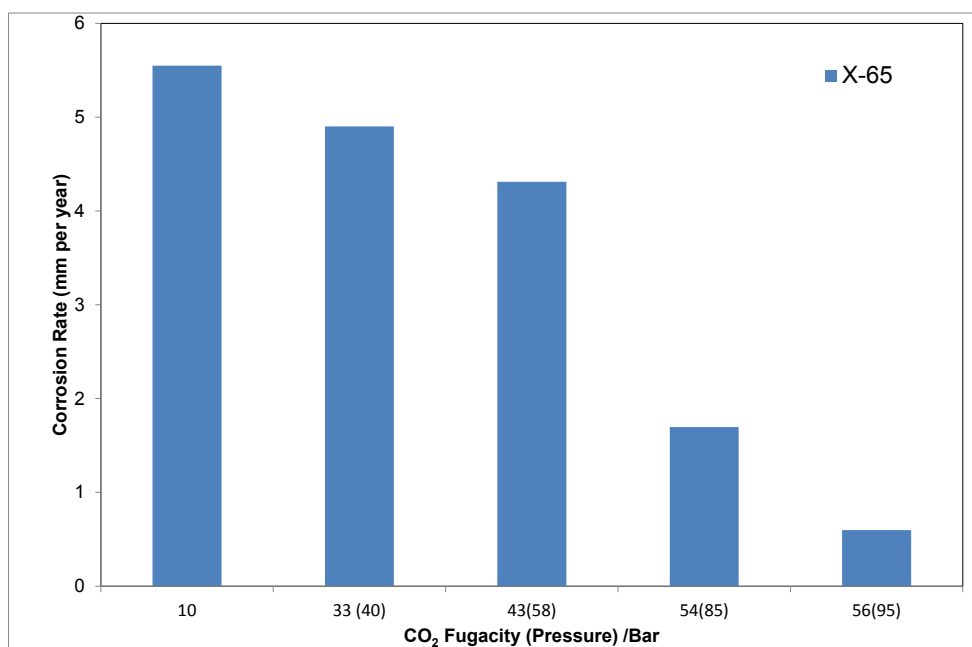


Figure 12: Corrosion rate as a function of pressure at 40 °C and autogeneous pH [12]

The decrease was despite the fact that the corrosion product layer that formed was not particularly protective. However, it is possible that the decrease might have been due to a change in water chemistry, particularly its pH. This was because the experiment was conducted in a 2.2-L stagnant autoclave for a longer duration (1 to 2 weeks) [12]. As the $p\text{CO}_2$ increased, the corrosion rate initially increased. However, due to a small volume of test solution, a higher initial corrosion made the solution quickly saturated with ferrous ion. This led to an increase in pH, hence a decrease in corrosion rate. Videm and Dugstad observed that an increase of ferrous ion concentration close to its solubility limit led to two-orders of magnitude reduction in corrosion rate [42]. However, Moiseeva suggests that it is possible for corrosion rate to decrease with the increase in $p\text{CO}_2$. This occurs once $p\text{CO}_2$ reaches a threshold value beyond which hydrogen evolution will impede the cathodic process [41].

Under conditions conducive for the formation of protective iron carbonate layers ($T > 80^\circ \text{C}$ and relatively high pH), the increase in $p\text{CO}_2$ could lead to a decrease in corrosion rate due to the increase in carbonate ion concentrations that help increase the super-saturation [5, 46]. This is particularly true when the $p\text{CO}_2$ reaches a supercritical level. Lin and co-workers found that the iron carbonate films formed on carbon steel exposed to supercritical-saturated water were more compact and had finer grain sizes that helped reduce porosity, hence corrosion rate [80].

3.3.2 Metallurgy

The severity of CO_2 corrosion arising from the interaction between the environment and metal surface partly depends on the metallurgy of the metal surface. Metallurgical effects arise from chemical compositions (micro-alloying) and micro structures [81]:

3.3.2.1 Chemical compositions

Since carbon steel corrodes markedly in CO_2 -environments, especially under non-film forming conditions, there have been some attempts to further improve its CO_2 -corrosion resistance by introducing alloying elements such as chromium, nickel, and copper. The main alloying element is chromium while other elements are also added in much smaller concentrations so as to improve further the properties of Cr-alloyed carbon steel [82]. For example, vanadium is added to maintain Cr in solid solution rather than exist as chromium carbide [83].

3.3.2.1.1 Chromium

Chromium is the most widely used alloying element typically added to steel in the range of 0.5 to 3.0 wt% [7]. The maximum amount of Cr is typically limited to 3.0 wt% so as to balance the corrosion resistance and the economics of material selection [83]. As a rule of thumb, the CO₂ corrosion rate of carbon steel would decrease with the increased chromium content [84]. At the same time, the temperature at which corrosion rate reaches a maximum would also increase [84]. This indicates that Cr improves the corrosion resistance of carbon steel by enhancing the protectiveness and persistence of corrosion product [85]. This is consistent with the observation that Cr-alloyed carbon steel did not suffer mesa attack or pitting under flowing conditions [85-87]; Cr content as low as 0.5 wt% could prevent mesa attack in a high flow condition [85, 88]. In fact, at 0.5 wt% Cr, the protective layer that was intentionally scratched would reform, thus preventing localized corrosion [85]. Dugstad and co-workers [89] found that flow affected CO₂ corrosion rate differently at different concentrations of chromium; while corrosion rate continuously increased with the increase in velocity at 0.5 wt% Cr, at Cr content of 1.02 wt% and higher, the magnitude of corrosion rate was not only lower than that of 0.5 wt% Cr, but also reached a maximum. This could suggest the increase in the strength of corrosion product layers with the increase in Cr content. Ikeda et al. [84] observed that while carbon steel substrate could not form corrosion product layers when the fluid velocity reached a critical velocity at which fluid erosion comes into play, the presence of 2 wt% chromium enabled the formation of protective layers. Similarly, while iron carbonate layers formed at temperatures lower than 70° C are normally not

protective, the presence of 0.5 wt% Cr allows the formation of protective iron carbonate layers [85].

Surface analysis indicates that corrosion product layers contain a much higher Cr content than does the bulk steel [84, 87, 89]. XRD analysis of corrosion product layers of 3 wt% Cr carbon steel indicates the presence of mainly iron carbonate in the outer layer and of chromium oxide and iron carbonate in the inner layer [87]; the presence of chromium oxide suggests passivation is responsible for reducing the corrosion rate [82, 83, 87]. Furthermore, the reduction of corrosion rate could also be due to the corrosion product layers being more adherent and continuous as observed in 3 wt% Cr carbon steel [82]. It must be noted that the concentration of alloying elements in the corrosion product layers comes mainly from the bulk metal rather than due to the precipitation from the aqueous environment [89]. Ikeda found that the beneficial effect of Cr would be observed when the concentration of Cr in the corrosion product layers was at least 11 wt% [84]. This means that Cr must remain in solid solution with the iron rather than be present as chromium carbide which would make it less available for formation of chromium oxide passive layers [82, 83]. To ensure Cr is in a substitutional solid solution with iron, other alloying elements that have more affinity to form carbides such as vanadium, molybdenum, and niobium have been added [83]. Dugstad and co-workers [86, 89] found that the presence of Cr could also surpass the effect of microstructure; they found that carbon steels of different microstructures exhibited the same corrosion behavior in the presence of Cr: the corrosion rate decreased with the increase in Cr content. The drawback of Cr-rich corrosion product layers is that it reduces the

effectiveness of corrosion inhibitor by reducing the adsorption effectiveness of the inhibitor on the steel surface [90].

3.3.2.1.2 *Nickel*

The addition of Ni helps increase the toughness and strength of carbon steel [91]. In terms of CO₂ corrosion, Kimura and co-workers [85] determined that the addition of Ni up to 0.5 wt % in 0.5 wt % Cr-alloyed carbon steel did not produce any significant effect on the corrosion rate of carbon steel subject to 1 bar CO₂-saturated solution with a velocity of 1 m/s, at pH 4 to 5, and 50 °C. Dugstad and co-workers [89], on the other hand, observed an increase in corrosion rate with the addition of Ni from 1.45 wt% to 3.35 wt% at pH 4 to pH 6, 60° C, 2 bar pCO₂, and a liquid velocity of 0.1 m/s to 13 m/s. However, based on **Figure 13** below, it is difficult to draw such conclusions as the two carbon steels identified as steel 14 and 17 which had different Ni concentrations also had different concentrations of chromium: 0.4 wt% and 1.4 wt% Cr. It was possible that steel 17 had a lower corrosion rate because of a higher Cr content instead of a lower Ni content (confounding effect).

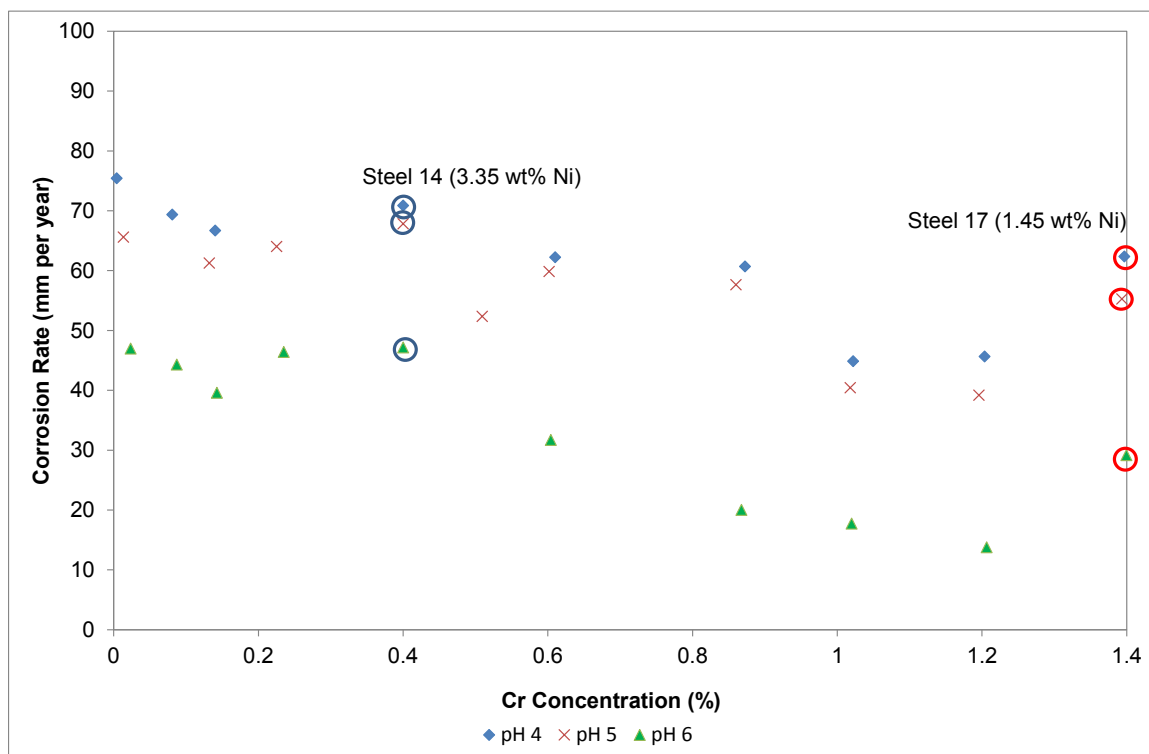


Figure 13: The corrosion rate of carbon steels at two different concentrations of Ni, namely, 1.45 wt% and 3.35 wt%, and at three different pH values: pH 4, pH 5, and pH 6. The steels with the Ni addition are indicated in circles [89].

3.3.2.1.3 Copper

The addition of Cu in carbon steels helps to improve strength through precipitation hardening and corrosion resistance, particularly to atmospheric and marine corrosion [91, 92]. However, exposure to CO₂-containing solution leads to an increase in corrosion rate of carbon steels [85, 89, 93]. The presence of 0.5 wt% Cu increases the corrosion rate of carbon steel by one and a half times. Nevertheless, with the addition of 0.5 wt% Cr, the corrosion rate of 0.2 wt% Cu-alloyed carbon steel does not show any significant increase [85]. The possible reason for the increase in corrosion rate is that Cu enhances the rate of hydrolysis of CO₂, leading to a higher concentration of carbonic acid [93].

3.3.3 *Microstructure*

The microstructure of carbon steel depends on the chemical composition and heat treatment [91, 94]. Among its microstructures are ferrite, pearlite, martensite, and austenite. Normally as-received carbon steel has a ferritic-pearlitic microstructure. Microstructure influences CO₂ corrosion through its un-oxidized cementite (Fe₃C) layer that forms part of the original steel matrix of the steel. Iron carbide could accelerate corrosion rate by galvanic coupling to the underneath steel and also influence the protectiveness of iron carbonate layers formed [81, 95]. For ferritic-pearlite, in non-film forming conditions, dissolution of ferrite will expose its lamellar and porous cementite on the steel surface, creating cavities; this results in a galvanic coupling between the exposed cementite and underneath ferrite [1]. As more layers of cementite are exposed to the environment due to the dissolution of iron, corrosion rate would initially increase due to the increase in cathodic areas [86, 90, 95]. On the other hand, if turbulent flow could remove the outer cementite layers, the corrosion rate could be reduced due to the reduction in the size of cathodic sites [86, 95, 96]. This was why Dugstad and co-workers [86] found the corrosion rate at a higher velocity (6.8 m/s) was lower than that of a lower velocity (4.1 m/s). In film forming conditions, the galvanic coupling will lead to the formation of non-protective iron carbonate layer when internal acidification precedes the supersaturation of iron carbonate in the matrix [7, 97]; internal acidification results from the depletion of the buffering ions, namely bicarbonate, within the lamellar matrix due to electro-migration [95, 98]. On the other hand, when supersaturation is achieved prior to the internal acidification, the iron carbonate layer formed will be protective [95].

In a stagnant condition or at a relatively low flow rate, cementite could help iron carbonate reach supersaturation locally within the cementite matrix by increasing the local ferrous ion concentration trapped inside the cavities and reducing the diffusion rate of ferrous ions to the bulk solution [89, 94].

The iron carbonate layers that form within the cementite cavities will have stronger adhesion as the cavities serve as porous surfaces that anchor the iron carbonate layers [1, 94, 99]. While this normally happens on ferritic-pearlitic carbon steel due to the presence of a network of cementite lamellae, such condition is less likely to happen to martensitic carbon steel. This is because martensitic carbon steel has more carbons in solid solution rather than in cementite [1, 94]. This reduces the number of cavities that help increase the saturation locally and that serve as the anchoring points [1, 94]. Palacios and Shadley [94] found that the iron carbonate layers that formed on normalized API N-80 carbon steel were more protective than that on API N-80 martensitic carbon steels.

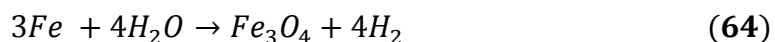
3.3.4 *Corrosion product layers*

It is clear from the earlier sections that in CO₂ corrosion processes, several types of corrosion product layers, namely iron carbonate (siderite, FeCO₃), cementite (Fe₃C) and magnetite (Fe₃O₄), could form depending on the environmental conditions. Of these, iron carbonate plays the most significant role in reducing corrosion rate if the layer formed is compact and strongly adheres to the substrate [100, 101]. Cementite, becoming dominant at the surface due to oxidative dissolution of ferrite, will be the main corrosion product layer formed at a temperature lower than 40° C [71, 102], low pH (pH ≤ 4.5)

[100], and low $p\text{CO}_2$ (<5 bar) [102]; this is consistent with “non-film forming conditions” with respect to iron carbonate formation. At these environmental conditions, corrosion products contain only little iron carbonate [71]. This is because of its high solubility, slow deposition rate at a low temperature [72, 73] and a low concentration of carbonate at a low pH and $p\text{CO}_2$. At 25° C, its solubility product (K_{sp}) is 2.88×10^{-11} [103]. As such, a pH value of 6.5 is required to form iron carbonate as the main corrosion product, but with poor adhesion to the substrate and high porosity [104]. Consequently, corrosion of carbon steel leaves behind an undissolved skeletal network of cathodic cementite on the steel surface (see §3.3.3). At a higher temperature (above 80° C), high pH (above pH 5.5), and high $p\text{CO}_2$, iron carbonate will be the dominant corrosion product layer as its solubility is low and its growth rate is high at elevated temperature, and the concentration of carbonate and ferrous ions is high at elevated $p\text{CO}_2$ [5, 71, 100]; higher pH also yields elevated concentration of carbonate. According to Schmitt, at 110° C (and 60 bar), magnetite (Fe_3O_4) may start to form underneath the iron carbonate layer [5, 102]. At 130° C, a thin passive layer of magnetite and hematite formed underneath the iron carbonate layer [102]. Tanupabrungsun found that at a much higher temperature (200-250° C), magnetite was the only corrosion product layer formed on API 5L X65 carbon steel exposed to $p\text{CO}_2$ of 1-2.5 bar in 1 wt% NaCl electrolyte [105]. On the other hand, Lin and co-workers found that at 200° C, iron carbonate was the main corrosion product layer formed on N80, P110, and J55 carbon steels subject to $p\text{CO}_2$ of 14 bar and 20 bar. Similarly, Ikeda and co-workers [84] also found iron carbonate as the only corrosion product formed on pure iron exposed to a 5 wt% NaCl electrolyte at 200° C and 250° C

and $p\text{CO}_2$ of 30 bar. The difference of corrosion products observed between the work of Tanupabrungsun and the works of Lin and Ikeda could be due to the difference in $p\text{CO}_2$; in the latter work, a higher $p\text{CO}_2$ produced a higher concentration of carbonate and bicarbonate ions that helped form iron carbonate; a higher temperature accelerated the growth rate of iron carbonate [102].

The types of corrosion product layers formed on the steel substrate could influence CO_2 corrosion rate and the types of corrosion: general or localized [102]. The formation of cementite will accelerate the general corrosion rate of carbon steel *via* galvanic coupling between the cementite and the steel substrate (see §3.3.3) [89]. The formation of protective iron carbonate can reduce uniform corrosion rate by acting like a barrier coating that separates the reactive carbon steel from the aggressive aqueous CO_2 environment; this helps slow down the diffusion of corrosive species to the substrate [46]. It also reduces the dissolution of steel by forming electrical resistant, insulating paths between anodic and cathodic sites [46]. Nevertheless, the formation of iron carbonate could be a precursor to localized corrosion [106]. This occurs in a process that initiates when the steel substrate becomes completely covered by iron carbonate and essentially passivates due to the increase in local pH underneath the iron carbonate layer [106]; the increase in local pH likely results from the reduction of hydrogen ions and molecular carbonic acid (see **equation (26)**) and the restricted molecular diffusion of ferrous ions to the bulk solution. This leads to the formation of magnetite (Fe_3O_4) which has been hypothesized to occur as a thin layer at the boundaries between FeCO_3 crystals and the steel [107] and forms according to the following reaction [102, 107]:



Consequently, the potential of the steel surface underneath the corrosion product layers becomes more positive [106]. When part of the iron carbonate is removed either mechanically [108] or chemically [47], it leads to local depassivation as the local pH changes due to the exposure of the local solution to the bulk solution [106]. This makes the exposed substrate anodic as its potential is more negative. A difference in potential leads to galvanic coupling, resulting in localized corrosion [106]. When the resultant localized corrosion arises due to the partial removal of iron carbonate by flow, the attack is known as mesa corrosion. The exposed substrate will have a table-like attack with a deep, flat-bottom surface being surrounded by intact iron carbonate layers [109]. Without the corrosion product layer, the exposed substrate experiences high localized corrosion enhanced by flow through the increase in mass transfer rate of corrosive species to the surface [109, 110]. However, in the areas where corrosion product layers are intact, the layers could reduce the flow-sensitivity of CO₂ corrosion by increasing the mass-transfer resistance of the reducible species to the metal surface [102, 110].

3.3.5 *Flow*

Since corrosion is a surface-related degradation process, the flow of fluid media over a metal surface could decrease or increase the corrosion rate of the metal [111]. Under particular circumstances, fluid flow will help decrease corrosion rate when it removes solid materials from the metal surface. This is because deposition of solids can

generate environments that lead to crevice and pitting corrosion. Deposited solid can additionally become a settling ground for planktonic sulfate reducing bacteria (SRB) that can initiate H₂S corrosion [112]. For a passive metal, flow helps form passive films by increasing its cathodic limiting current density to a critical current density where the corrosion current density will decrease due to formation of a protective, oxide-type thin film [60]. However, the most marked effect of flow is to enhance corrosion [111]. In CO₂ corrosion, flow has been observed to increase corrosion rate except when it helps remove cathodic iron carbide layer that can establish galvanic cells between itself and the anodic steel surface [113]. For a single-phase flow, there are two ways by which flow can accelerate corrosion rate: increasing mass transport rate and removing protective corrosion product layers [29, 46]:

3.3.5.1 Effect on mass transport

Flow accelerates corrosion rate when it is under mass transport control which occurs when the charge transfer rate is so high that the concentration of the reactants at the metal surface is depleted [110]. Consequently, any increase in velocity will increase the mass transport rate, hence the corrosion rates, until the charge-transfer reaction becomes the rate determining step; the further increase in velocity has no further effects on corrosion rates as shown in **Figure 14** below [17]:

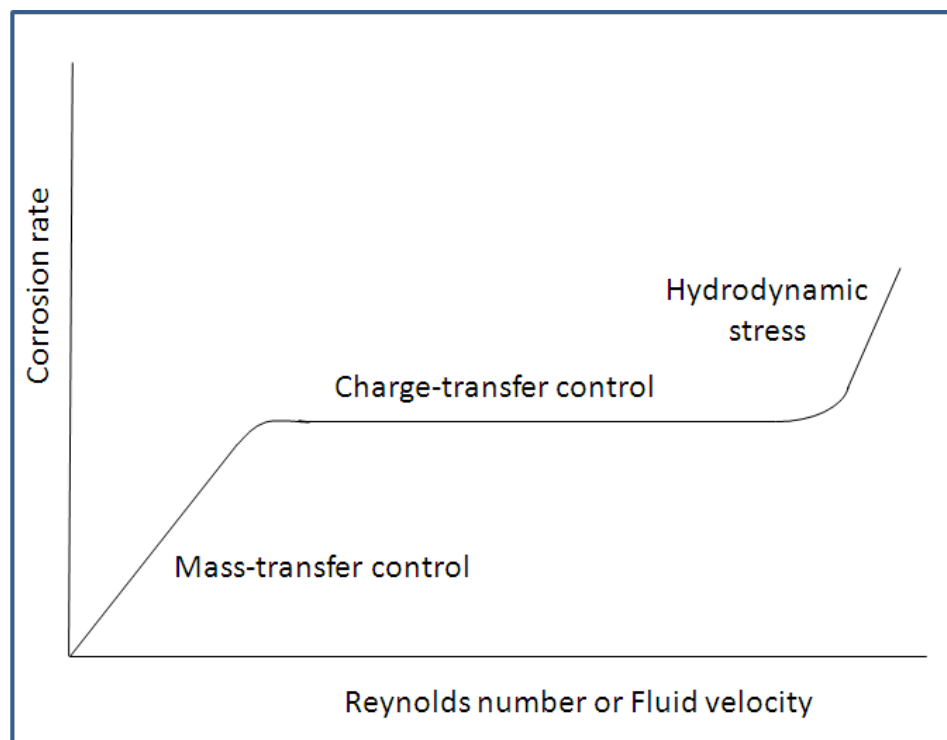


Figure 14: The effects of flow on corrosion rate [17]

The increase in corrosion rate with velocity is pronounced in a film-free condition [18]. This is because there is no mass-transfer resistance of the reactants to the metal surface. To understand better how flow accelerates corrosion rate, it is imperative to understand the modes of mass transport involved: molecular diffusion and convection.

3.3.5.1.1 *Diffusive mass transport*

Near the metal surface, there exists a concentration gradient which drives ions or molecules from a high concentration region to diffuse into a low concentration region, hence the gradient is established. For cathodic sites, the high concentration region corresponds to the bulk solution. Within this diffusion boundary layer (assuming electro-migration is negligible due to the presence of highly conductive supporting electrolyte) [17], mass transport of reacting species will be mainly due to molecular diffusion [112].

For stagnant solution, Fick's first law for steady-state conditions defines the flux (J) of species ($\frac{mol}{m^2s}$) diffusing perpendicularly to the electrode through the diffusion boundary layer as follows [60]:

$$J = \frac{i}{nF} = -D \times \frac{\Delta C}{\delta} \quad (65)$$

where

n is the number of electrons exchanged in the reactions

F is Faraday constant = $96500 \frac{C}{mol}$

I is current density ($\frac{A}{m^2}$)

D is diffusion coefficient ($\frac{m^2}{s}$)

ΔC is the concentration difference between the surface and the bulk solution normal to the electrode

δ is diffusion boundary layer (m)

The negative sign in **equation (65)** indicates that the molecular diffusion mass transport occurs from a high concentration to a low concentration. For cathodically-controlled limiting current density:

$$\Delta C = C_b - C_s \quad (66)$$

where

C_b is bulk concentration ($\frac{mol}{m^3}$)

C_s is surface concentration ($\frac{mol}{m^3}$)

Since diffusion coefficients in liquids are small, the corrosion rate in stagnant solution is relatively small [112]. The corrosion rate increases when the solution is in flowing conditions. This is because convection enhances mass transport rate of the reacting species to or of the corrosion products from the surface.

3.3.5.1.2 Convective mass transport

Convective mass transport entails the transport of the species due to flow itself [112]. The effects of flow on mass transport rate are coupled by inter-relating the hydrodynamic dimensionless parameters to a mass transport dimensionless parameter. The hydrodynamic parameters are the Reynolds number (Re) and Schmidt number (Sc) defined as follows [17]:

$$Re = \frac{VL}{\nu} = \frac{\rho VL}{\mu} \quad (67)$$

$$Sc = \frac{\nu}{D} \quad (68)$$

where:

V is velocity of the fluid (m/s)

L is the characteristic length of the hydrodynamic system (m)

ν is kinematic viscosity of the fluid (m^2/s)

ρ is density of the fluid (kg/m^3)

μ is dynamic viscosity of the fluid (kg/m.s)

D is Diffusion coefficient (m^2/s)

Reynolds number signifies the ratio between the inertial force and viscous force while the Schmidt number signifies the ratio between molecular momentum transport and molecular diffusion mass transport [112]. It indicates the relative thickness of the diffusion boundary layer; that is, a high Schmidt number (Sc) suggests a thin diffusion boundary layer [44, 60]. A high Sc number also indicates that convective mass transport is more dominant than molecular diffusion mass transport [61]. The position of diffusion boundary layer within the hydrodynamic boundary layer is shown by **Figure 15** below. The velocity gradient shown in the figure is caused by non-slip condition at the wall which retards the fluid flow. This causes the turbulent flow to diminish as it gets closer to the wall until the flow becomes steady where layers of fluid run in parallel and the velocity reaches zero at the wall [60, 114]. It is within this laminar hydrodynamic boundary layer resides the diffusion boundary layer [61].

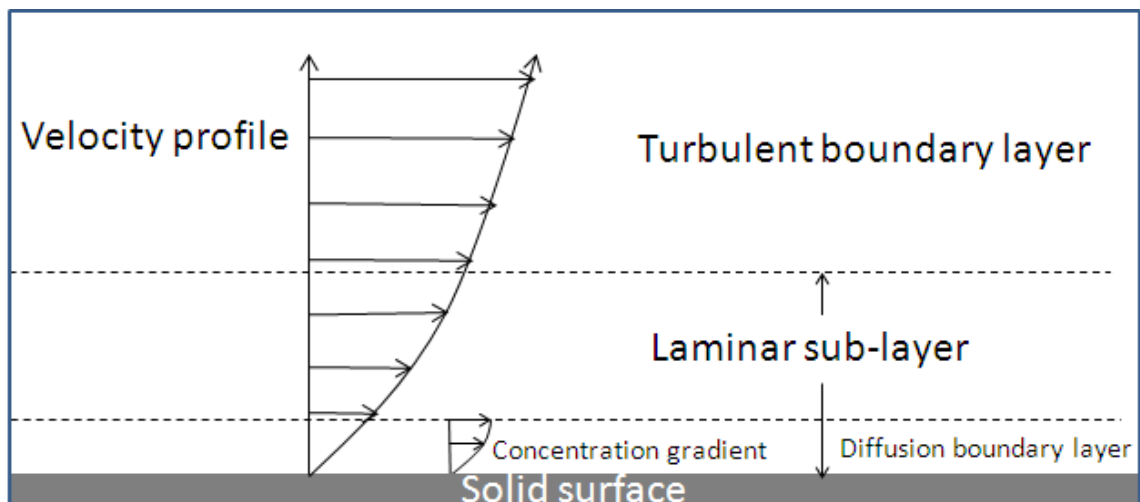


Figure 15: The diffusion boundary layer resides within the viscous laminar sub-layer [115]

The mass transport parameter is the mass transfer correlation: Sherwood number (Sh). It signifies the ratio between convective mass transport and molecular diffusion mass transport and is defined as follows:

$$Sh = \frac{K_m L}{D} = a(Re^x)(Sc^y) \quad (69)$$

where:

K_m is mass transfer coefficient (m/s)

L is characteristic length (m)

a, x, y are constants

These three constants are geometry dependent and need to be determined empirically; they are normally available in the open literature for heat and mass transfer studies. For a rotating cylinder electrode, the mass transfer correlation commonly used is Eisenberg's correlation [116]:

$$Sh = 0.079(Re^{0.7})(Sc^{0.36}) \quad (70)$$

For a cylindrical specimen [117],

$$Re = \frac{\omega d_c^2}{2\nu} \quad (71)$$

where:

ω is angular velocity (rad/s)

d_c is diameter of the cylindrical specimen (m)

ν is kinematic viscosity (kg/m.s)

Equations (67) to (69) indicate that the mass transfer coefficient (K_m) is dependent on velocity, geometry, and liquid physical properties such as viscosity and density. For corrosion rates under purely mass transfer control, the relationship between the mass transfer coefficient and limiting current density is given as below:

$$i_{lim} = nFC_bK_m \quad (72)$$

where:

n is number of electrons transferred for a single half-cell reaction

F is Faraday constant=96500 C/mol

C_b is bulk concentration of the reducible species (Molar)

Comparison of **equation (69)** with Fick's first law of diffusion as given in **equation (41)** reveals that the mass transfer coefficient corresponds to [51, 57]:

$$K_m = \frac{D}{\delta} \quad (73)$$

Equation (73) indicates that the increase in velocity at a certain temperature (constant diffusion coefficient) leads to the increase in mass transfer coefficient due to the thinning of the diffusion boundary layer (δ); that is, for turbulent flow, eddy diffusivities penetrate

further into the mass transfer boundary layer with the increase in velocity [31, 118]. It must be noted that the limiting current density as given in **equation (69)** provides the cathodic current density as contributed to purely by mass-transfer controlled cathodic reaction. The total cathodic current density ($i_{c(\text{total})}$), taking into account the cathodic current density from charge-transfer rates (i_{ct}), is then given by **equation (33)** [29, 60].

3.3.5.2 Effects on corrosion product layers

As mentioned earlier, when the local concentration of ferrous and carbonate ions at the metal surface exceed super-saturation level, ferrous carbonate will form on the metal surface. The formation of protective layer leads to reduction in corrosion rates by increasing the mass transfer resistance and preventing metal dissolution [119]. Flow can however affect the layer by interfering with the supersaturation level or removing the layer [5, 46]. It interferes with the supersaturation level by enhancing the transport rate of hydrogen ions to the metal surface and the transport rate of ferrous ions from the surface to the bulk [120]. The interference leads to the formation of porous iron carbonate layers [99].

As for mechanical removal, it is proposed to be due to shear stress. **Figure 14** shows that as velocity increases further, hydrodynamic stress will come into play. This onset of accelerated corrosion is therefore not attributable to electrochemical corrosion phenomena. The possible cause is then hypothesized to be due to fluid shear stress acting on the film or layer surface. The wall shear stress (τ_w) arises due to velocity gradient $\left(\frac{\partial U}{\partial y}\right)$ or molecular momentum transport perpendicular to the flow direction [114, 121].

For Newtonian fluids, the wall shear stress is related to velocity gradient as follows [114, 121]:

$$\tau_w = \mu \left(\frac{\partial U}{\partial y} \right)_{y=0} \quad (74)$$

U is the mean velocity $\left(\frac{m}{s}\right)$ parallel to the pipe wall.

It is therefore suggested that layer removal occurs when the wall shear stress exceeds the adhesion strength of the layer [122]. However, some studies have shown that shear stress *alone* cannot remove the layer because while shear stress falls in the range of 10 to 100 Pa, the adhesion strength is of the order of MPa [108, 123]. Ruzic [119] suggests that the removal of the ferrous carbonate layer in a single-phase flow is due to the joint action of chemical dissolution and mechanical removal of ferrous carbonate layers. Regardless of the mechanism, any removal of the layers will expose the metal surface to the aggressive environment, hence corrosion. In one-phase flow, hydrodynamic stress only removes the surface layer and does not directly damage the substrate mechanically [112].

3.3.5.3 Studies on the effect of flow on CO₂ corrosion

Like early studies of other corrosion mechanisms [61], the effect of flow on CO₂ corrosion was unaccounted for since CO₂ corrosion was deemed to be mainly under charge-transfer control [50, 52]. For example, the early CO₂ corrosion model developed by de-Waard and Milliams did not include the flow effect [3, 124] which would lead to underestimation of the CO₂ corrosion rate [52, 125]. The possible reason for the

oversight on flow effect was that the earlier studies were carried out at a low temperature in which the charge-transfer reaction rate was probably lower than the mass transport rate [52, 102].

The effect of flow on CO₂ corrosion is more clearly observed at a low pH (pH <5) since the concentration of hydrogen ions is higher at a low pCO₂, thus making the effect of chemical reaction (the hydration of aqueous CO₂) less dominant than that of the mass transport of hydrogen ions [120], and at higher temperature due to the dominant increase in charge-transfer reaction rate [52]. The first two factors relate to the fact that flow-sensitivity of CO₂ corrosion arises mainly from the transport of hydrogen ions [120]. The studies in low and high pCO₂ below illustrate some attempts to characterize the effect of flow on CO₂ corrosion in terms of pH, pCO₂, temperature, and corrosion product layers.

3.3.5.3.1 *Flow studies in low CO₂ partial pressure (pCO₂ ≤ 20 bar)*

Schmitt and Rothmann(1977) studied the cathodic limiting-current density component on carbon steel and platinum in a CO₂-saturated 0.5 M Na₂SO₄ solution at 0.67 bar pCO₂, 25° C and pH 4.2 using a rotating disc electrode (RDE). Their results showed that the cathodic limiting current density increased with the increase in the rotational speed. However, the cathodic limiting current density measured was higher than that assumed to be purely due to the diffusion of hydrogen ions alone. Such assumption had to be ruled out based on the fact that the plot of limiting current density *versus* the square root of angular velocity did not pass through the origin. As such, they attributed the additional cathodic limiting current density to the diffusion of undissociated molecular carbonic acid and the slow chemical reaction of the hydration of aqueous CO₂

adsorbed on the metal surface as given in **equation (27)**. However, their assumption on heterogeneous hydration may conflict with their data that showed similar cathodic limiting current density on both steel and platinum [52, 126]. It is unclear how they arrived at the conclusion that CO₂ corrosion rate was under charge-transfer control on the basis of cathodic limiting current density alone; no comparison with measured corrosion rate was made. In fact, the fact that the cathodic limiting current density increased with flow may probably suggest a flow-sensitive corrosion rate [52], especially considering the anodic reaction of carbon steel is independent of flow [44]. Furthermore, it should be noted that cathodic limiting current density could be observed at such a low test temperature probably because of the relatively low pCO₂ [52] in which the mass transport of hydrogen ions is more dominant than the hydration of dissolved CO₂ [120]. Finally, the use of RDE means that the study was only applicable to laminar flow while the flow pattern in the field is mostly turbulent [112]. It must be noted that under laminar flow in which the mass transport rate is lower than that of turbulent flow, flow-sensitivity is more easily observable [127].

Eriksud and Sontvedt [52] studied the effect of flow on CO₂ corrosion of API X52 carbon steel at 1 to 2 bar pCO₂, 20° C and 60° C, pH 3.9, and various velocities in a CO₂-saturated 4 wt% NaCl solution using a flow loop. Their work highlighted the effect of temperature on the flow-sensitivity of CO₂ corrosion. They found that CO₂ corrosion was not flow-sensitive at a low temperature (20° C) as the rate-determining step was the charge-transfer reaction; this was deduced from the fact that the measured corrosion current density was lower than the cathodic limiting current density. Unlike that

observed by Schmitt and Rothmann, their flow pattern was turbulent and produced higher mass transport rate than the laminar flow, making the corrosion rate under charge-transfer reaction control more likely. However, in a way, their results helped confirm the conclusion by Schmitt and Rothmann on charge-transfer control of CO₂ corrosion rate at a low temperature as discussed above. When temperature increased to 60° C, they found that CO₂ corrosion became more flow-sensitive; this is because the increase in temperature increased the charge-transfer rate more than the mass-transfer rate. The fact that the corrosion rate was equal to the cathodic limiting current density established that CO₂ corrosion rate was under mass-transport control.

Herce and co-workers [128] studied the effect of a single-phase flow on AISI 1018 carbon steel over a range of temperatures (30, 50, 80, and 115° C), pH values (pH 4, 5, and 6), pCO₂ (2, 10, 20 psi), and velocities expressed as fluid wall shear stress (1-400 N/m²) using a pipe flow loop. They assumed that the corrosion rate in N₂-purged and CO₂-solutions to be about the same, thus concluding that CO₂ corrosion was mainly due to reduction of hydrogen ions. They reduced the effect of pCO₂ and temperature to water chemistry, specifically hydrogen ion concentrations. In this way, they could relate the effect of flow in terms of hydrogen ion concentrations or pH. However, it must be noted that their results showed a gap in corrosion rates *versus* shear stress between both types of solution, similar to the one shown in **Figure 9**, suggesting that their assumption was incorrect; that is, they neglected the contribution from the carbonic acid reduction to the corrosion rates [50]. This would make their model predict a lower corrosion rate.

Kvarekvål [129] investigated the relationship between corrosion current density and cathodic limiting current density in a single-phase flow of 3 wt% NaCl solution saturated with CO₂ at various pCO₂ (0.58 bar to 1 bar), pH values (pH 3.8 to 6.5), temperatures (25 to 90° C), and velocities (0.25 to 2.5 m/s) in the absence and presence of small amounts of H₂S using a flow loop. His results suggested that the flow-sensitivity of CO₂ corrosion decreased as pH increased; the cathodic polarization curves exhibited Tafel behavior at pH 5.5 and higher which could probably be due to the dominance of direct water reduction cathodic current density (under charge-transfer control) [44]. Moreover, flow sensitivity was observed at all the test temperatures, including at 25° C and higher at higher temperatures at a test pH of about 4. He attributed the flow-sensitivity at 25° C to the presence of iron carbide that increased the surface area, resulting in the increase in the magnitude of the charge-transfer reaction. His findings showed that flow-sensitive corrosion current density as governed by mass-transport control differed minimally from the the cathodic limiting current density. The corrosion current density governed by purely mass-transport control should be equal to the cathodic limiting current density. The difference between the two in his results could have arisen from the use of Pt to measure the cathodic limiting current density and the use of carbon steel for corrosion measurements; the carbon steel surface was subject to corrosion. Additionally, his work did not study the effect of pCO₂ on the flow-sensitivity of CO₂ corrosion as the variation in pCO₂ was essentially due to the variation in the test temperature.

Nesic and co-workers [110] studied the effect of a single-phase flow on CO₂ corrosion of API X65 carbon steel exposed to 1 wt% NaCl solution saturated with CO₂ at 1 bar pCO₂ in two different flow geometries: straight pipe (SP) and rotating cylinder electrode (RCE). The electrolyte was set at pH values of 4, 5, and 6 while the temperature was set at 20° C. To ensure similar mass transfer rate in both flow geometries, they used equivalent velocity derived by equating the mass transfer correlations and shear stress of both flow geometries. At equivalent velocity, the liquid shear stress of each apparatus was similar. Furthermore, to ensure the specimens were exposed to the same water chemistry, the experiments in SP and RCE were run concurrently in the same loop. Their results indicated the flow-sensitivity of CO₂ corrosion rate in both flow geometries increased as the pH decreased due to the increase in hydrogen ion concentrations, and that their corrosion rates were close to each other, proving that corrosion rate was geometry-independent. Also important was that flow-sensitivity of CO₂ corrosion could be observed even at 20° C; this finding contradicted the results of Eriksud and Sontvedt mentioned earlier even though both works were also carried out at about the same pH. The possible cause for the difference was that the work of Eriksud and Sontvedt simulated slug flow which has higher turbulent diffusivities.

The reason for the above difference is supported by a research conducted by Silva and co-workers, [130] who studied the effect of flow on the corrosion behavior of four different grades of API 5L carbon steels: X52, X60, X65, and X70. They were exposed to a 3 wt% NaCl electrolyte saturated with 0.7 bar CO₂ at pH 3.9 and 20° C. They used a rotating cylinder electrode (RCE) to simulate a turbulent flow at various rotational speeds

up to 10,000 rpm. They observed that the anodic polarization curves of all steel grades did not change with velocity as reflected by the relatively constant anodic Tafel coefficient with velocity; this suggested that the anodic reaction of the dissolution of iron in CO₂ corrosion was under charge-transfer control. They also observed the increase in the cathodic limiting current density with the increase in velocity, suggesting a flow-sensitive corrosion. Comparison of cathodic limiting current density with corrosion rate, as measured by linear polarization resistance (LPR) technique, showed a good agreement. This confirmed that the corrosion behavior of the four carbon steel grades at 20° C was indeed flow-sensitive; that is, similar to the finding of Nescic and co-workers described above. It must also be noted that like Nescic and co-workers, they also observed flow-independent cathodic limiting current density component from the plot of limiting current *versus* (velocity)^{0.7} based on Eisenberg's correlation where the intercept did not go through the origin. The limiting current was attributed to the slow hydration of dissolved CO₂ as hypothesized by Schmitt and Rothmann [50].

While the above works focused on the effect of flow on CO₂ corrosion rate in terms of enhanced mass-transport, some works also studied the effect of flow on corrosion product layers. There are two ways by which flow could affect the corrosion product layers [46]:

- Mechanical removal of formed and hitherto protective iron carbonate
- Interference with the formation of protective iron carbonate layers

These two mechanisms are discussed below:

Ruzic and co-workers [108] studied the effect of a single-phase undisturbed flow on the mechanical removal of iron carbonate that was artificially pre-deposited on 1020 mild steel in 1 wt% NaCl and at pH 6.9 and 80° C. Hydrodynamic shear stress was simulated using a rotating cylinder electrode (RCE) flow apparatus at two rotational speeds: 7000 and 10000 rpm corresponding to 4.40 m/s and 6.28 m/s, respectively. LPR was used to monitor the FeCO₃ removal process in which the specimen would be recovered from the glass cell, for subsequent characterization, once a stable corrosion rate was achieved. They found that there was an initiation time of about four to eleven hours, depending on the types of pre-grown iron carbonate layers, for the mechanical removal of the iron carbonate to take place. As reflected by corrosion rates over time, the higher the velocity, the less time it took to initiate the removal process and the higher the corrosion rate. The removal was localized rather than uniform. Since the calculated shear stress (about 470 Pa maximum) was much lower than the adhesion strength of the iron carbonate layers (ranging from 1 MPa to 30 MPa), they concluded that liquid shear stress alone was not sufficient to cause the local mechanical removal of the iron carbonate layers. Instead, they proposed the removal process was initiated by the fatigue of the iron carbonate layers that resulted from locally fluctuating wall shear stress, pressure, and velocity imparted mainly by turbulent Taylor vortices (TTV). Consequently, the layers would be separated, leading to cracking by centrifugal force. Cracking further led to an increased local turbulent intensity that eventually caused the removal of the layer. The last stage is similar to the mechanism of erosion-corrosion [131]. The proposed mechanism of the mechanical removal of the iron carbonate layer suggests that it may

probably be unique to RCE and may not be applicable to a straight pipe flow where TTV and centrifugal force are missing.

For this reason, Yang and co-workers [123] studied, using a thin-channel flow cell (TCFC), the effect of a single-phase flow on iron carbonate layers pre-deposited on X52 carbon steel exposed to 1 wt% NaCl at pH 6.6 and 80° C. The method used to deposit iron carbonate layers was similar to that of Ruzic and co-workers above. Yang and co-workers employed a tensile machine to measure the cohesion and adhesion strength of the layers; the tests indicated that the adhesion strength of the layers was larger than 10 MPa. On the other hand, the calculated wall shear stress produced by the liquid flow was 20 Pa (velocity was not given). Like the work of Ruzic and co-workers, the present results also indicated that wall shear stress could not mechanically remove the layers. More importantly, surface analysis using SEM indicated no damage to the layers. This helps show that the mechanical removal observed by Ruzic and co-workers was probably unique to RCE. Nevertheless, the different types of carbon steel might have also contributed to the difference.

Gao and co-workers examined the effect of flow on the mechanical properties of iron carbonate layers on API X65 carbon steel using a hydrodynamic high pressure-high temperature (HPHT) autoclave; the flow geometry was not indicated as to whether it was a rotating cylinder electrode or some other geometric configurations. The steel specimens were exposed to artificial formation water saturated at three different CO₂ partial pressures (1, 3 and 10 bars) and at 65° C, but with no information of solution pH given. Iron carbonate layers were allowed to develop on the steel surfaces while the

surfaces were independently subject to three different liquid velocities for 240 hours: 0, 0.5, and 1 m/s. They also measured the mechanical properties of the layers after the exposure: adhesion strength by tensile test, Young's modulus (E) by nano-indentation, layer fracture toughness (K_{IC}) by Vickers' indentation, and interfacial fracture toughness (K'_{IC}) by tensile test using a single-notched specimen. Their data indicated that flow produced iron carbonate layers, with poorly-packed grain boundaries, that were more porous than the layers produced at static conditions. Consequently, the specimens with flow-produced iron carbonate layers had corrosion rates higher than that for stagnant-produced iron carbonate layer specimens. Higher corrosion rate helped produce thicker, yet still non-protective layers. This was because of the higher concentration of ferrous ions available, but flow prevented the voids created from being-filled. Moreover, the increase in velocity also reduced the interfacial fracture toughness of the layers as the surface profile produced by corrosion prior to the layer formation was smoother, and corrosion reaction products were partly removed from the steel surface, leading to limited iron carbonate crystal growth. The low interfacial fracture toughness (a measure of resistance to crack propagation at the interface between the layer and steel surface) of deposited layers increased the localized corrosion rate; cracks were initiated at voids that formed between the layers and the substrate. It is hard to evaluate the validity of their results as no indication of pH or iron carbonate supersaturation was given, and no information on the flow geometry was provided. There was also no photographic evidence for locally removed layers. What is clear was that the test temperature would not be conducive to the growth of protective iron carbonate layers (see § 4.3); that was

why the formed layers contained voids that served as crack initiation points when subject to flow. It would be worthwhile to run the same experiments at a higher temperature and pH where protective iron carbonate layers would form to see whether such layer failures would occur. The study should also account the effects of microstructures on the mechanical properties of iron carbonate layers.

Dugstad [99] studied the effect of a single-phase flow regime in a flow loop on iron carbonate layers formed under flowing conditions at various velocities (0 to 7 m/s), temperatures (40, 60, 80, and 120° C), pCO₂ (1.8 to 2.6 bar), and pH (5.5 and 6.0). Carbon steels with ferritic-pearlitic and martensitic microstructures were used as the substrates. The results indicated that the specimens exposed at 40 and 60° C at low supersaturation values, 1-3 times, developed non-protective iron carbonate layers, thus the corrosion rates remained high throughout the exposure. Increasing the temperature to 80° C enhanced the protectiveness of the layers, but the specimens were subject to mesa attack on the areas where the layers were removed by flow. At 120° C, the protectiveness of the layer improved further, and no mesa attack was observed.

When the supersaturation was increased to between 10 and 100 times, the layers formed at 40 and 60° C grew thicker with greater precipitation, but were still porous resulting in higher corrosion rates. Increasing the temperature to 80° C enhanced the protectiveness of the layers, thus reducing the corrosion rates and preventing the specimens from undergoing mesa attack except when the velocity was increased to 4.1 and 6.8 m/s.

Thus, his results indicated that flow could interfere with the protectiveness of iron carbonate layers formed by affecting the local supersaturation. This was substantiated further by the fact that the layers formed became more protective due to a greater heterogeneous precipitation occurring close at the metal surface. This reduced the corrosion rate significantly when the flowing conditions were brought to stagnant conditions for two to five days. Higher temperature helped increase the scaling tendency which is a competition between growth rate and corrosion rate [46, 73].

3.3.5.2.1 *Flow studies in high CO₂ partial pressure ($pCO_2 \geq 20$ bar)¹*

Literature on the effect of flow in high CO₂ partial pressure is sparse; few studies address the flow effect in near critical CO₂ environments. Despite the wide interest in CO₂ transport in carbon capture and storage (CCS) and enhanced oil recovery (EOR), almost all studies in CO₂ corrosion at supercritical CO₂ were carried out in stagnant conditions [77, 80, 132-136]. Although one study [137] simulated the effects of velocity on supercritical CO₂ corrosion, the focus of the study was more on the effects of crude oils/water mixtures on super-critical CO₂ corrosion at one particular velocity: 1 m/s. They did not study the hydrodynamic and mass transfer effects on corrosion. For this reason, the literature review here only focuses on the effect of flow in near critical CO₂ environments.

Denpo and Ogawa [19] studied the effect of flow on corrosion of N80 carbon steel, typically used as a casing material downhole, and stainless steel at various CO₂ partial pressures (1, 10, and 40 bar), dissolved oxygen concentrations (10 to 5000 ppb)

¹ The content of this section was published in the co-authored paper of reference [166]. Reproduced with permission from NACE International, Houston, TX. All rights reserved. Paper 11242 presented at CORROSION/2011, Houston, Texas. © NACE International 2011.

and velocities using a flow loop (2 m/s to 17 m/s) and a rotating cylinder electrode (0.1 m/s to 1 m/s); the test temperature was set at 80° C. The test pH was not stated, but was most probably at autogeneous pH: 4.24 at 1 bar, 3.62 at 10 bar and 3.32 at 40 bar as calculated using an in-house model [68]. The work employed weight loss specimens for the corrosion rate measurement in the flow loop and electrochemical tests for the measurements of the corrosion rate and determination of the corrosion mechanism under the influence of flow. They found no formation of protective films on all carbon steel specimens for the pipe flow at the velocity ranges studied. They also observed that the corrosion rate of carbon steel increased with the increase of velocity with the power law of 0.6; the corrosion rate also increased with the increase in dissolved oxygen concentration. By setting the mass transfer rates of pipe and RCE equal, they were able to relate the RCE linear velocity to pipe linear velocity which would yield a similar corrosion rate. It is interesting that the work indicates the flow sensitivity of CO₂ corrosion even at high CO₂ partial pressure. However, this sensitivity was observed probably because the autogeneous pH studied corresponded to the relatively high hydrogen ion concentration which would give a dominant mass transport process [44]. The work did not address the effect of flow on corrosion as a function of pH. Nor did the work study the effect of flow on corrosion rate as a function of temperature. More importantly, the presence of dissolved oxygen might have increased the effect of mass transport, thus possibly contributing to the flow sensitivity observed.

Dugstad and co-workers [18] studied the corrosion of carbon steel at various CO₂ partial pressures (0.5 bar to 21 bar), temperatures (20 to 90° C), pH values (4-6), and flow

velocities (0.1 m/s to 13 m/s). They observed that the corrosion rate increased with the increase in flow at low pH, but the corrosion rate became less sensitive to flow as the pH increased; this was due to lower hydrogen ion concentration and the dominance of carbonic acid reduction at a high pH. They also found that the effect of flow on corrosion rate was more observable at higher temperature. Nevertheless, the given mechanism by which flow affects corrosion rate was unclear. While the authors attributed the removal of iron carbide by flow at 20 to 40° C as the cause of observed *decrease* in corrosion rate with concomitant lessening of galvanic effects, they also attributed the flow-induced removal of iron carbide as the reason for the *increase* in corrosion rate at a higher temperature due to its role in effecting mass transfer resistance. They also ruled out the possibility of interrelating hydrodynamics to mass transport from the data obtained in evaluating the effects of flow [18].

Hara and co-workers [138] studied the effect of flow on carbon steel (N80), low alloy steel, and stainless steels using an autoclave equipped for solution circulation with an external test section; static experiments were run in the autoclave while flow experiments were run in the external test section. The experiments were carried out in non-film forming conditions at various CO₂ partial pressures (4 to 40 bar), temperatures (45 to 180° C), and velocities (2 m/s to 17 m/s). Corrosion rate was determined from weight loss. Their results suggested that the corrosion rate of carbon steel and low alloy carbon steel was under mass transfer control and was proportional to Re number with 0.83th power law: $Re^{0.83}$. They also found that the corrosion rate increased with the increase in temperature. This work is useful as its data analyses related the corrosion

rates and the hydrodynamic parameters. The analyses, however, only considered the reduction of hydrogen ions and neglected the contribution of carbonic acid reduction to the total cathodic current density, yet the Sh number calculated from weight loss must have incorporated the direct reduction of carbonic acid. Without electrochemical measurements, particularly from potentiodynamic sweeps, it is hard to deduce that the corrosion rate came mainly from hydrogen ion reduction; the order of magnitude of the change in corrosion rate is much larger when carbonic acid reduction is also considered [65]. At 40 bar, the observed effect of flow was most probably because the test pH was at autogeneous pH: 3.47[68]; at this pH, the hydrogen ion concentration was relatively high. Moreover, the effect of flow at 40 bar was restricted to 120° C where diffusion coefficients are relatively high. It may be worthwhile to determine whether the flow effect could be similarly observed at a lower temperature corresponding to the field temperature. The work also did not address the flow effect on CO₂ corrosion as a function of pH as it was most probably carried out at autogeneous pH [138].

Wang and co-workers [67] studied the effects of velocity (0.2 m/s, 1 m/s, and 2 m/s) and CO₂ partial pressure (3, 10 and 20 bar) at pH 5 and 60° C on corrosion rate of API 5L X-65 carbon steel in a single-phase flow using a high pressure flow loop. They found that flow did not affect the anodic reaction at these three CO₂ partial pressures as it was under charge transfer control. They also observed that the cathodic limiting current density became less flow-sensitive with the increase in CO₂ partial pressure although its value increased with the increase in CO₂ partial pressure; this was probably because at such high CO₂ partial pressures, the cathodic limiting current density came largely from

the slow chemical reaction of the hydration of dissolved CO₂ into carbonic acid (**equation (43)**). It must be noted that the study focused on a single pH (pH 5) where the effects of flow even in low CO₂ partial pressure are less dominant [44]. It would be interesting to know if the same observation is applicable at a lower pH, particularly at pH less than 4 in which hydrogen ion concentration is relatively higher. Likewise, the scope of the study could be expanded to see the effect of flow on corrosion rate at various temperatures and at much higher CO₂ partial pressures [67].

Wu and co-workers [139] investigated the effect of flow on API 5L X-65 carbon steel exposed to simulated formation water saturated with pure CO₂ and CO₂/H₂S at pCO₂ of 4.4 bar, 90° C and various velocities (1, 2, and 3 m/s) using autoclaves. Their results suggested that corrosion rate in pure CO₂ system increased with velocity, and iron carbonate was partially removed, leading to mesa attack. It is possible that the flow-sensitivity could be observed since the test was carried out at pCO₂ of less than 5 bar [120] and at a high-temperature where mass-transport rate of hydrogen ions could still be relatively significant [52]. The study, however, did not account for the variation of temperature, pH, and pCO₂ on flow-sensitivity. It is interesting to know whether such flow-sensitivity could be observed at a higher pCO₂, particularly for a supercritical CO₂ phase (CO₂-rich phase).

The above review indicates that no study on the effect of flow has been carried out in the presence of supercritical CO₂. As for the near-critical CO₂ phase, the highest pCO₂ was at 40 bar, but the study was limited to the autogeneous pH. It is therefore the aim of the present work to fill this gap by looking into the effect of flow on CO₂

corrosion at near-critical and supercritical CO₂ as a function of pH and temperature, the outcome of which would be used to model CO₂ corrosion in near-critical and supercritical CO₂ environments.

3.4 CO₂ corrosion models

CO₂ corrosion models are employed in oil and gas industry as a prediction tool, particularly during the design stage. It is used to determine the corrosion allowance, corrosion control and monitoring strategy (such as inhibitor availability and position of corrosion probes), level of risks for risk-based inspection, and life-cycle costs. The underlying aim of such modeling is to evaluate the suitability of carbon steel as opposed to more expensive corrosion resistant alloys in production environments [3]. There are several CO₂ corrosion models available in the industry such as Multicorp[®], Electronic Corrosion Engineer[®] (ECE), Hydrocorr[®], and Norsork. Nyborg [140, 141] evaluated the strength of several CO₂ corrosion models based on features relating to pH calculation, the effect of iron carbonate layer, fluid flow, H₂S, top-of-the line corrosion, and acetic acid. He also compared the predicted corrosion rates from various models against the field data [142]. All of the CO₂ corrosion models available in the literature fall under one of these categories: empirical, mechanistic, or semi-empirical. The classification is based on the extent the models are grounded in theory [113].

3.4.1 Empirical models

Empirical models ignore the underlying physico-chemical laws. The models are based on curve-fitting of experimental data [113] or on an artificial neural network (ANN) trained to capture the underlying non-linear relationship between various

influencing parameters and CO₂ corrosion rate [143]. This approach renders the theoretical understanding on the interaction among parameters difficult since ANN only serves as a 'black box' that captures and generalizes the input-output relationship. Furthermore, the validity domain of the empirical models is limited to the ranges of the parameters specified in the experiments or monitored in the field. In this regard, the models can interpolate corrosion rate well, particularly when the database is huge and reliable, but extrapolate it poorly [113]. Another drawback is that the addition of a new parameter in the models may require extensive experimental work, and its effect can only be introduced to an existing model by a correction factor [44]. The use of several correction factors will overshadow the ways the parameters interact to affect corrosion rate [45, 125]. In the case of ANN-based models, the ANN has to be retrained using a new set of experimental data. Nevertheless, an empirical model may be required to fill in the gap in the mechanistic understanding of an underlying process [143]. An example of an empirical model is the one developed by Nestic and Vrhovac [143] using the experimental database from the Institute for Energy Technology (IFE) in Norway. They used 308 data sets to train a three-layer ANN while 20 data sets were used for validation of the model to check whether the trained ANN generalized or memorized. The input comprised temperature, pCO₂, velocity and pH while the output was corrosion rate. The model was compared against one mechanistic model and two semi-empirical models which were calibrated against the same database. The results indicated the superiority of the ANN model over these models.

3.4.2 *Mechanistic models*

Mechanistic models are based on the theoretical understanding of physico-chemical phenomena that take place during CO₂ corrosion such as the solubility of CO₂ in water and the distribution of generated carbonic species, the transport of other chemical species, and the electrochemical reactions on the steel surface [113]. The related coefficients and dimensionless numbers employed such as Henry's law coefficient, mass transfer coefficient, and *Sc* number have clear physical meanings [113]. The models allow a mechanistic understanding on how the interaction among influencing parameters affects CO₂ corrosion. For example, they can inter-relate the effect of pH and flow on corrosion rates; that is, a low pH leads to a more flow-sensitive corrosion due to a higher transport of hydrogen ions. It is more convenient to incorporate the effects of a new factor such as a higher pCO₂ into the existing models [44]. This is because a mechanistic model normally comprises several sub-models such as water chemistry model, flow model, and electrochemistry model that can be modified or enhanced independently. Not only do the models interpolate, but extrapolate more reliably as well [113]. There are a few mechanistic models available in the literature such as the ones developed by Gray and co-workers [40], Nesic and co-workers [44, 73, 74, 144], Pots [57], and Dayalan and co-workers [145]. Basically, these mechanistic CO₂ corrosion models consist of chemical, transport, and electrochemical models which form the basic structures of mechanistic models.

3.4.3 Semi-empirical model

The models combine the features of both empirical and mechanistic models discussed above. Regressions of experimental data or ANN models are coupled to the mechanistic models when the theoretical understanding on some parts of the corrosion process remains unclear. An example of an earlier semi-empirical model is the de-Waard Milliams model [124]. The model was developed by curve-fitting of experimental corrosion rate at a given temperature and pCO_2 . In this regard, the model relates CO_2 corrosion rate, V_{corr} (mm/yr) to pCO_2 (bar) and T (K) only [3, 146]:

$$\log(V_{corr}) = 7.96 - \frac{2320}{273+T} - 0.00555T + 0.67\log(pCO_2) \quad (75)$$

The model assumes the cathodic reduction reaction comes mainly from the direct reduction of carbonic acid, and that the corrosion rate is fully under charge-transfer control [3]. As such, flow effect is not accounted for except in the revised model by incorporating a resistance model that relates corrosion rate to charge-transfer controlled corrosion rate (V_{ct}) and to mass-transfer controlled corrosion rate (V_{mt}) [3]:

$$V_{corr} = \frac{1}{\frac{1}{V_{ct}} + \frac{1}{V_{mt}}} \quad (76)$$

It must be noted that all the prediction models above are only valid for pCO_2 of 20 bars [6]. It has been proven experimentally that these models would over predict the

corrosion rate when used beyond $p\text{CO}_2$ of 20 bar [6, 10, 16]. One possible reason is that all of them use Henry's law to account for the solubility of gaseous CO_2 in water, neglecting the non-ideality of gas at higher $p\text{CO}_2$ [15]. This makes the models predict higher solubility of gaseous CO_2 in the aqueous phase.

CHAPTER 4.0: RESEARCH OBJECTIVES AND WORK STRATEGY

4.1 Research objectives

The above literature review on flow studies points out that there are some gaps that need to be closed in studying the effect of flow on CO₂ corrosion in high pCO₂ environment, particularly at supercritical CO₂ conditions. In line with this finding, the objectives of this study are set as follows:

- Determine the effect of flow on CO₂ corrosion at near critical CO₂ environments (10 and 40 bar CO₂ partial pressure) and supercritical CO₂ environments (80 bar CO₂ partial pressure).
- Study the effect of flow on CO₂ corrosion as function of pH (3, 4, 5) in high pressure CO₂ environments
- Study the effect of flow on CO₂ corrosion as function of temperature (25° C and 50° C) in high pressure CO₂ environments
- Establish a relationship between a rotating cylinder electrode and a high pressure and high temperature thin channel flow cell (HPHT-TCFC) apparatus in predicting the corrosion rate using a similarity solution method.

It must be noted that all the above supercritical conditions refer only to CO₂-rich phase as it will require a much higher pressure to attain supercritical conditions for H₂O-CO₂ binary mixture [26].

4.2 Work strategy

The study on the effect of a single-phase flow employed two different flow geometries: high pressure-high temperature (HPHT) rotating cylinder electrode and

HPHT thin-channel flow cell (TCFC). The underlying aim was to demonstrate flow-geometry independent corrosion rate. Since the thin-channel flow cell (TCFC) was a new flow apparatus, its mass transfer behavior had to be characterized first. This was to allow the determination of the power law upon which corrosion rate under purely mass transfer control is dependent on velocity. The information would be used to assess the magnitude of change in CO₂ corrosion rate with respect to flow [117]. The flow effect was first studied using a high pressure and high temperature 7.5-L rotating cylinder electrode autoclave, followed by the HPHT-TCFC for selected parts of the test matrix. A correlation between the two different flow geometries was established so as to allow the prediction of corrosion rate in a large-scale system (TCFC) using a small scale system (RCE). TCFC was also used to validate the prediction model experimentally

4.3 Published papers

Portions of the work presented in this dissertation were published in the following co-authored papers:

- M. F. Mohamed, A. Mohammed Nor, M. F. Suhor, M. Singer, Y. S. Choi and S. Nestic, "Water chemistry for corrosion prediction in high-pressure CO₂ environments," in *Corrosion/2011*, 2011, Paper 11375.
- A. Mohammed Nor, M. F. Suhor, M. F. Mohamed, M. Singer, S. Nestic. "Corrosion of carbon steel in high CO₂ environment: Flow effect," in *Corrosion/2011*, 2011, Paper 11242.

- A. Mohammed Nor, M. F. Suhor, M. F. Mohamed, M. Singer, S. Nestic. “Corrosion of carbon steel in high CO₂ environment: The effect of high flow rate,” in *Corrosion/2012*, 2012, Paper C2012-0001683.
- M. F. Suhor, M. F. Mohamed, A. Mohammed Nor, M. Singer, S. Nestic. “Corrosion of mild steel in high CO₂ environment: Effect of the FeCO₃ layer,” in *Corrosion/2012*, 2012, Paper C2012-0001434.

CHAPTER 5.0: EXPERIMENTAL DETAILS

5.1 Introduction

The study on the effect of flow on CO₂ corrosion in high pCO₂ environment involved three different flow apparatus: a low pressure thin channel flow cell (TCFC), a high pressure-high temperature (HPHT) rotating cylinder electrode (RCE), and a HPHT thin-channel flow cell (TCFC). The low pressure TCFC was used to characterize the mass-transfer behavior of the channel flow so as to identify a suitable mass-transfer correlation (*Sh* number). The HPHT RCE was employed to study the flow-sensitivity of CO₂ corrosion at various pCO₂, temperature, and pH. RCE was however limited by the maximum velocity it could produce: 1 m/s. To enable the study at a higher flow rate, HPHT TCFC was used. It was also used to validate the model experimentally.

5.2 Mass transfer characterization of thin channel flow cell (TCFC)

The study on the effect of flow on corrosion requires that the flow apparatus has a well-defined hydrodynamic and mass transfer behavior [61, 62]. This is important in establishing that the observed flow-sensitive corrosion is due to mass-transfer control and not due to hydrodynamic shear stress and in determining the power law upon which corrosion rate under purely mass transfer control varies with velocity [117]. The most important reason is to enable a correlation between two different flow geometries such as rotating cylinder electrode in the laboratory and pipe in the field [117]. In this work, the results from the high-pressure and high-temperature (HPHT) TCFC would be correlated with the results from HPHT rotating cylinder electrode (RCE) so as to establish geometry-independent corrosion rates. As such, characterizing the mass transfer

behavior of TCFC was essential for this new flow equipment as no mass-transfer correlation (Sh number) had been identified to reflect its mass-transfer behavior.

5.2.1 Experimental execution

5.2.1.1 Experimental apparatus

A low pressure thin channel flow cell, as shown in **Figure 16** below, was used in this work to establish a suitable mass transfer correlation for this new apparatus and for the HPHT-TCFC which was being assembled at that time:

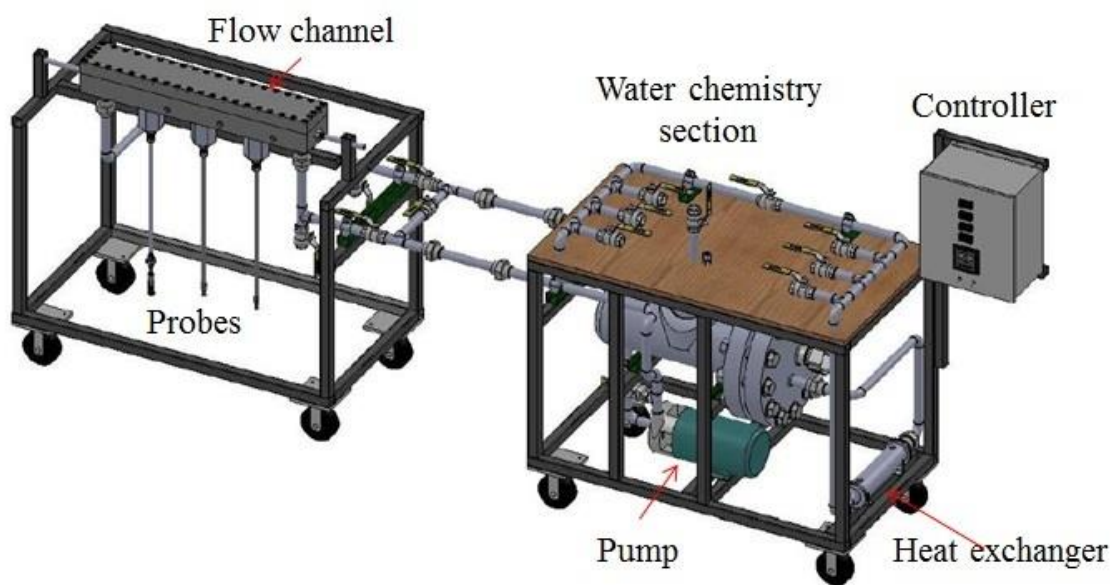


Figure 16: Low pressure thin-channel flow cell

Figure 17 shows the flow diagram of the TCFC system while **Figure 18** shows the flow channel and the probes.

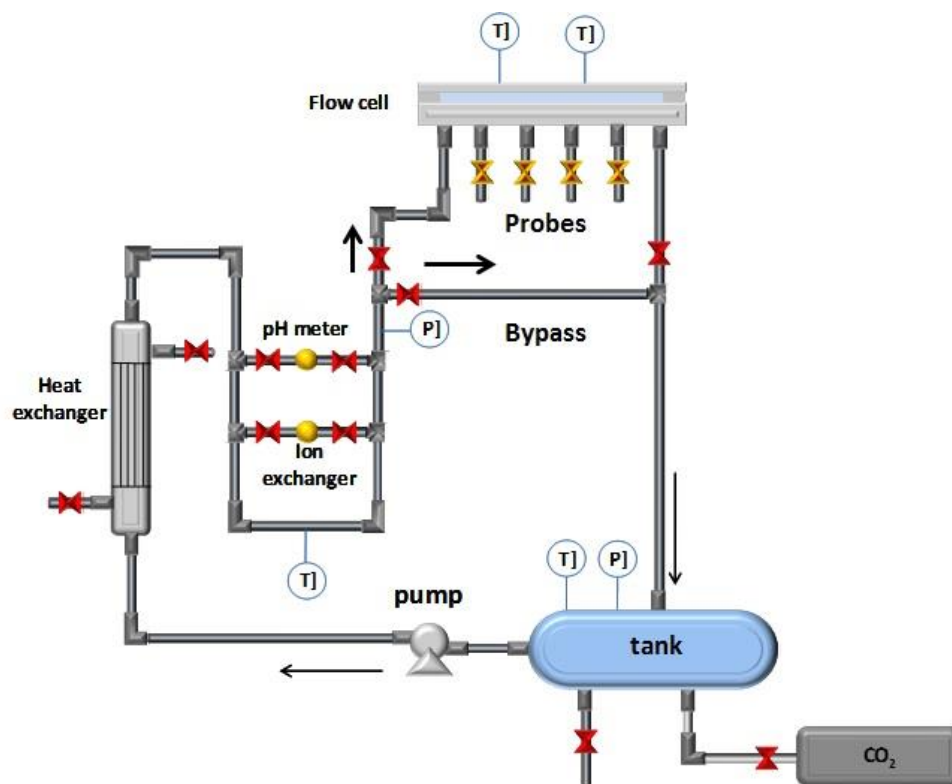


Figure 17: The flow diagram of the low pressure TCFC [147]

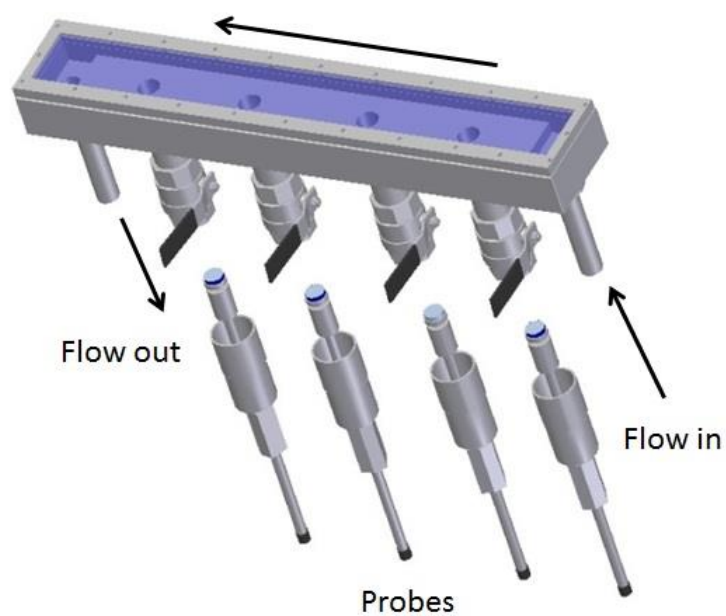


Figure 18: A schematic flow channel of the low-pressure TCFC

The results from the low pressure TCFC were expected to be applicable for the HPHT TCFC. This is because liquid is incompressible. As such, the difference in operating/test pressure will not affect the liquid properties such as density and viscosity which are more temperature dependent.

The TCFC was designed to study the effect of a fully-developed single-phase turbulent flow on corrosion. The width of the channel (100 mm) is much larger than its thickness or height (3 mm) so as to ensure that there will be no edge effect and the velocity gradient will be in the height direction only; that is, the momentum and mass transport will only be one dimensional. The entrance length is set at 100 mm which ensures that the hydrodynamic and the diffusion boundary layer will be uniform over the specimens. The TCFC system has a ratio of liquid volume to specimen surface area of 650 mL/cm^2 which will help minimize the change in water chemistry due to corrosion and can accommodate four different types of probes in a single experiment: LPR, potentiodynamic scan, weight loss, and electrochemical quartz crystal microbalance (EQCM). It has two sections: a water chemistry section that allows pH adjustment and a test section, the flow channel. The test solution contained in a 20-liter vessel is first circulated through the bypass while the water chemistry is being adjusted and then introduced into the flow channel once the desired water chemistry had been achieved. A centrifugal pump is used to circulate the test solution in the loop. The temperature of the test solution can be adjusted using a heat exchanger by adjusting the flow rate of the cooling water [148].

5.2.1.2 Experimental parameters

Table 4 shows the physical properties of water and the corresponding Schmidt numbers (Sc) calculated at 30° C and 50° C using the following equations [44]:

$$\mu = \mu_{ref} \times 10^{\frac{1.327(20-T_C) - 0.00105(20-T_C)^2}{T_K + 105}} \quad (77)$$

where

T_K is the absolute temperature of the test solution (K)

T_C is the temperature of the test solution (° C)

and

$$D_{H^+} = D_{H_{ref}^+} \times \frac{T_K}{T_{ref}} \times \frac{\mu}{\mu_{ref}} \quad (78)$$

where

D_{H^+} is the diffusion coefficient of hydrogen ions (m²/s)

$D_{H_{ref}^+}$ is the diffusion coefficient of hydrogen ions at a reference temperature (m²/s)

T_{ref} is reference temperature (° C)

μ_{ref} is reference water dynamic viscosity at T_{ref} (kg/m.s)

As for water density required for the calculation of kinematic viscosity, it was calculated as follows:

$$\rho = 1152.3 - 0.5516(T_K) \quad (79)$$

The value of the reference viscosity was obtained from reference [44] at the reference temperature of 20° C: $\mu_{ref} = 1.002 \times 10^{-3}$ kg/m.s. On the other hand, the value of the reference diffusion coefficient for hydrogen ions was obtained from reference [70] at the reference temperature of 25° C: $D_{H_{ref}^+} = 9.312 \times 10^{-9}$ m²/s.

Table 4: The physical properties of water and Sc numbers at 30° C and 50° C for mass transfer characterization

Temperature (°C)	μ of water (kg/m.s)	ρ of water (kg/m ³)	ν (m ² /s)	D (m ² /s)	Sc
30	0.000898	997	8.01×10^{-7}	1.06×10^{-8}	76
50	0.000559	987	5.57×10^{-7}	1.64×10^{-8}	34

Re numbers (hence *Sh* numbers) were varied by changing the volumetric flow rates of the test solution to give the test matrix as given in **Table 5**:

Table 5: *Re* numbers at various liquid velocities for mass transfer characterization

GPM	Velocity (m/s)	Re Numbers	
		30 ° C	50 ° C
3	0.6	2284	3288
4	0.8	3781	5442
6	1.3	4647	6689
8	1.7	6144	8843
10	2.1	7877	11338
12	2.5	9452	13605
14	2.9	11028	15873
16	3.4	12603	18140
18	3.6	14021	20181
20	4.2	15754	22675

It must be noted that the calculation of Reynolds number made use of the height of the flow channel instead of the hydraulic diameter [149].

5.2.1.3 Experimental methods

a) Test solution

The test solution was a 1 wt% NaCl electrolyte so as to factor out the effects of migration. It was prepared by dissolving 200.0 g of NaCl in deionized water. Following Nestic and co-workers [44], the test solution was set at pH 3.0 so as to ensure that the test

environment fully corresponded to mass-transfer control. This was achieved by adding 20 ml of 1 M HCl and making up the volume of the solution to 20 L.

If the pH increased once the solution was circulated in the TCFC, HCl diluted with the test solution was injected at the water chemistry section until the pH reached 3 ± 0.05 . The test solution was de-aerated with N_2 until the dissolved oxygen level reached about 5 ppb or lower as measured by a colorimetric method using CHEMets[®] ampoules. This would help ensure that the limiting current densities obtained during the experiment were mainly from hydrogen ion reduction. The solution was continuously bubbled with N_2 during the experiment, and the pressure was maintained at 1 bar using N_2 .

b) Test specimen

To measure the limiting current densities, a probe as shown in **Figure 19** was used. The probe consisted of three metallic rings electrically separated by epoxy; the center and outer rings were made of stainless steels while the middle ring was made of API 5L X-65 carbon steel:



Figure 19: The electrochemical probe used in the mass transfer characterization experiment.

The chemical composition of the carbon steel is given in **Table 6** below:

Table 6: Chemical composition (in wt%) of X65 carbon steels (balance Fe)

C	Mn	Si	P	Cr	Cu	Ni	Mo	Al
0.065	1.54	0.25	0.013	0.001	0.05	0.04	0.007	0.041

In the experiment, the middle ring which had an area of 0.95 cm^2 was used as the working electrode while the center ring was used as the counter electrode. This special probe ensured that the counter and working electrodes would not be grounded since the TCFC body was already grounded; initial attempts of using the body of the TCFC and later the outer ring of the probe as the counter electrode resulted in cathodic polarization curves in which the limiting current behavior and the water reduction current density were not observable since the potentiostat/galvanostat allows only one cell (the apparatus) to be grounded [150]. An external Ag/AgCl reference electrode connected to the solution *via* salt bridge with a porous plug at the end was used to measure the potential of the carbon steel working electrode. Prior to the electrochemical measurements, working electrodes were polished using 400-grit, followed by 600-grit silicon carbide abrasive papers, then washed with isopropanol alcohol and dried using a heat gun.

c) Test procedure

Prior to introducing the test solution into the TCFC system, the whole system was purged with N_2 four to five times and then closed; the pressure was held slightly higher

than the atmospheric pressure. This was found to accelerate the de-aeration of the test solution when introduced into the system. This step also helped remove any residual water in the system. 16-L of the test solution was then transferred to the TCFC system; the balance was used to make up the 16-L volume, if necessary. The pump circulated the test solution around the TCFC system bypassing the flow channel which was separated from the rest of the system. The test solution was then de-aerated with N_2 until the dissolved oxygen level was reduced to 5ppb or lower. The pH of the test solution was measured and adjusted by injecting de-aerated HCl solution at the water chemistry section until it reached $pH\ 3 \pm 0.05$. Once the desired water chemistry had been achieved, the probe was flush-mounted on the flow channel. Flush mounting ensured that the diffusion boundary layer would be uniform over the probe surface. With the probe valves closed, the flow channel was then purged with N_2 a few times. To avoid a sudden surge in pressure, the flow outlet was opened first, followed by the flow inlet. The bypass piping was then closed to ensure the test solution would flow through the flow channel. The solution was continuously bubbled with N_2 during the experiment, and the pressure was maintained at 1 bar using N_2 . The experiment was carried out at two test temperatures, namely 30°C and 50°C , corresponding to two different viscosities and diffusion coefficients (see **Table 4**).

d) Electrochemical measurements

A Gamry Reference 600 Potentiostat/Galvanostat was used for the electrochemical measurements. An external Ag/AgCl reference electrode connected to the solution *via* a salt bridge with a porous wooden plug at the end was used to measure

the potential of the carbon steel working electrode. At the start of the experiment, the open-circuit potentials of the working electrode were first measured until they became stable; it normally took about 10-30 minutes. Potentiodynamic sweeps were carried out at three different velocities so as to obtain the current plateau (limiting current density) as shown by **Figure 20** and **Figure 21** below:

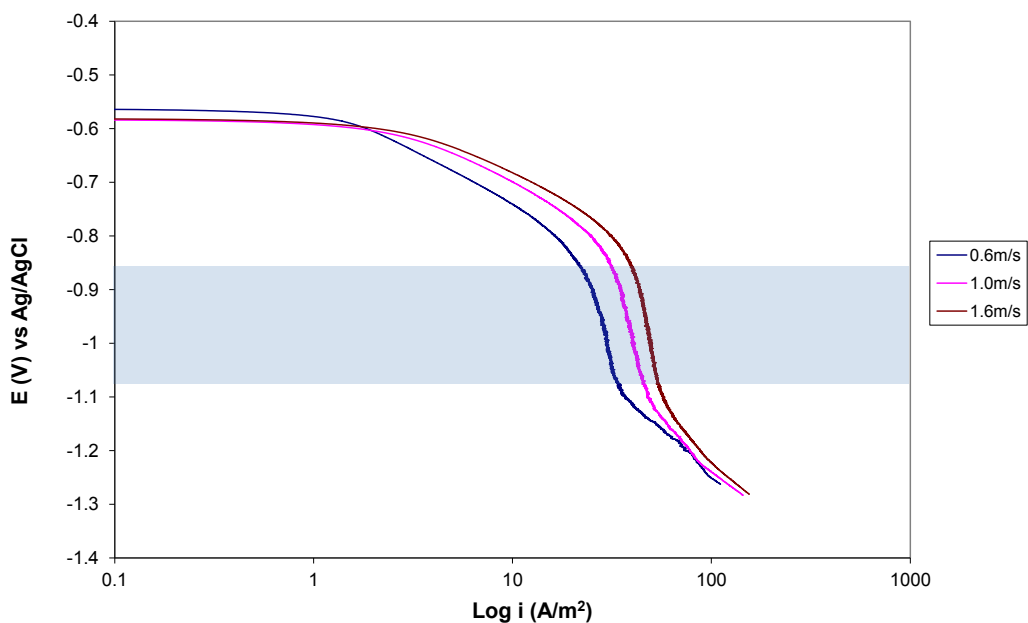


Figure 20: Cathodic polarization curves at three different liquid velocities, pH 3.0, and 30° C showing the limiting current region.

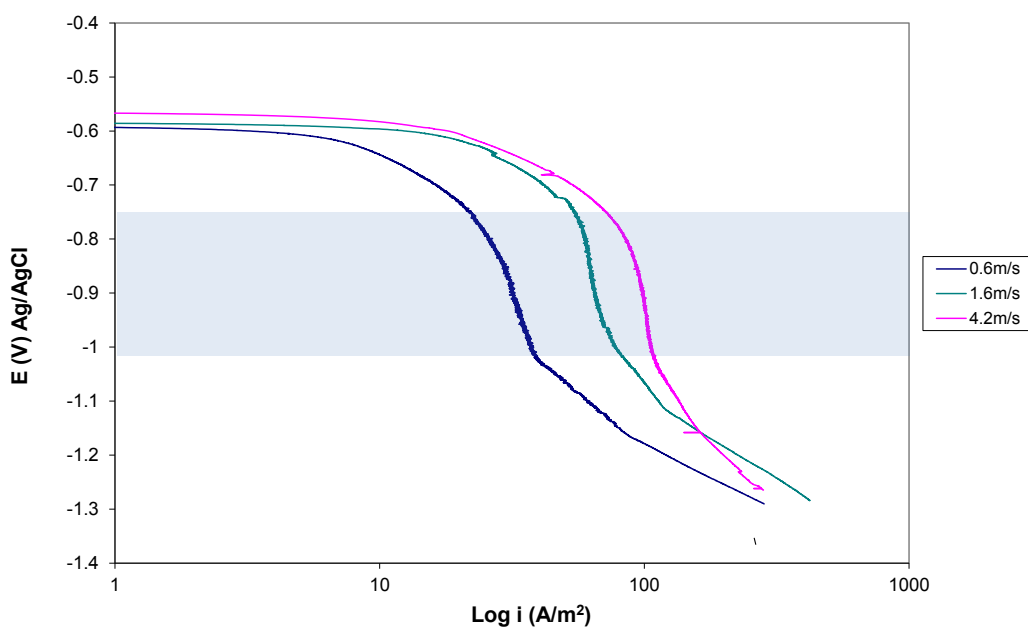


Figure 21: Cathodic polarization curves at three different liquid velocities, pH 3.0, and 50° C showing the limiting current region.

This would help determine a single potential at the current plateau region applicable for all the velocities. For this purpose, the specimen was cathodically swept from an open-circuit potential to a potential 700 mV more negative at a scan rate of 0.2 mV/s. Once the potential at the current plateau region was identified, the specimen would be potentiostatically polarized at the potential (*vs.* Ag/AgCl) in ascending order of velocities given in **Table 5**. Based on **Figure 20** and **Figure 21** above, the potentials at the current density plateau region were taken as -950 mV and -900 mV, respectively (Ag/AgCl). The potentiostatic measurements were carried out for two minutes at each velocity; this was to allow the current densities to be stable before moving to the next velocity. At each new velocity, the solution temperature was readjusted to the desired temperature by

adjusting the cooling water flow rate. To ensure the consistency of the current densities, the potentiostatic sweep would then be repeated, but in descending order of velocities. **Figure 22** gives an example of potentiostatically measured current densities measured at ascending and descending order for two velocities:

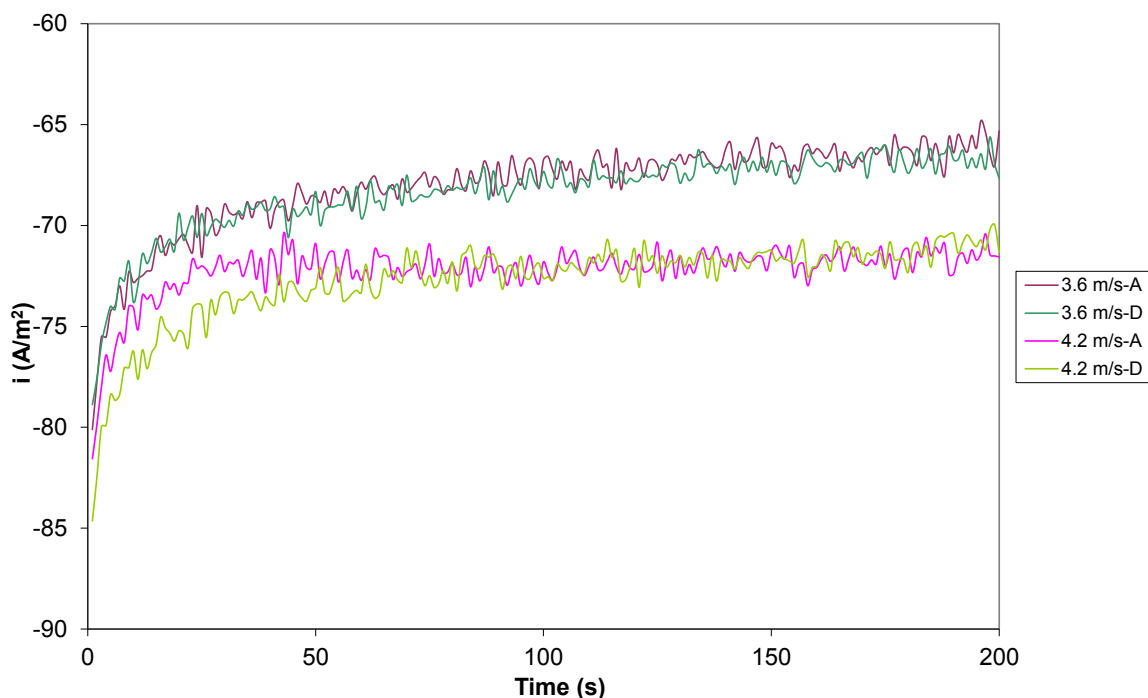


Figure 22: Limiting current densities for ascending (A) and descending (D) velocities at pH 3.0 and 30° C determined potentiostatically at -950 mV (Ag/AgCl)

The above figure shows that the limiting current densities measured in ascending and descending orders were consistent; that is, there was little difference in water chemistry, temperature, or steel surface to have caused inconsistencies.

5.2.2 Results and discussion

Figure 20 and **Figure 21** shown above indicate that the limiting current potential plateau at 50° C (-750 mV to -1010 mV) was relatively larger than that at 30° C (-850 mV

to -1040 mV). This could be due to the higher charge-transfer rate at 50° C which made the cathodic reaction under mass transport control. This was further evidenced from the fact that it took a relatively lower negative potential (starting at -760 mV) for the mixed controlled region at 50° C to reach the limiting current region as compared to that at 30° C (starting at -850 mV).

Figure 23 and **Figure 24** show the plots of limiting current densities versus velocities for ascending (forward) and descending (reverse) velocities at 30° C and 50° C, respectively. The limiting current densities were first corrected by subtracting out the current densities due to water reduction. The limiting current densities were then converted to mass transfer coefficients (k_m) using **equation (69)**. **Figure 23** and **Figure 24** suggest that the limiting current densities (hence the mass transfer coefficients) increase with the increase in velocities. This is due to the thinning of the mass boundary layer as the flow became turbulent: the turbulent eddies penetrated further into the sub-viscous layer as velocities increased [46, 118].

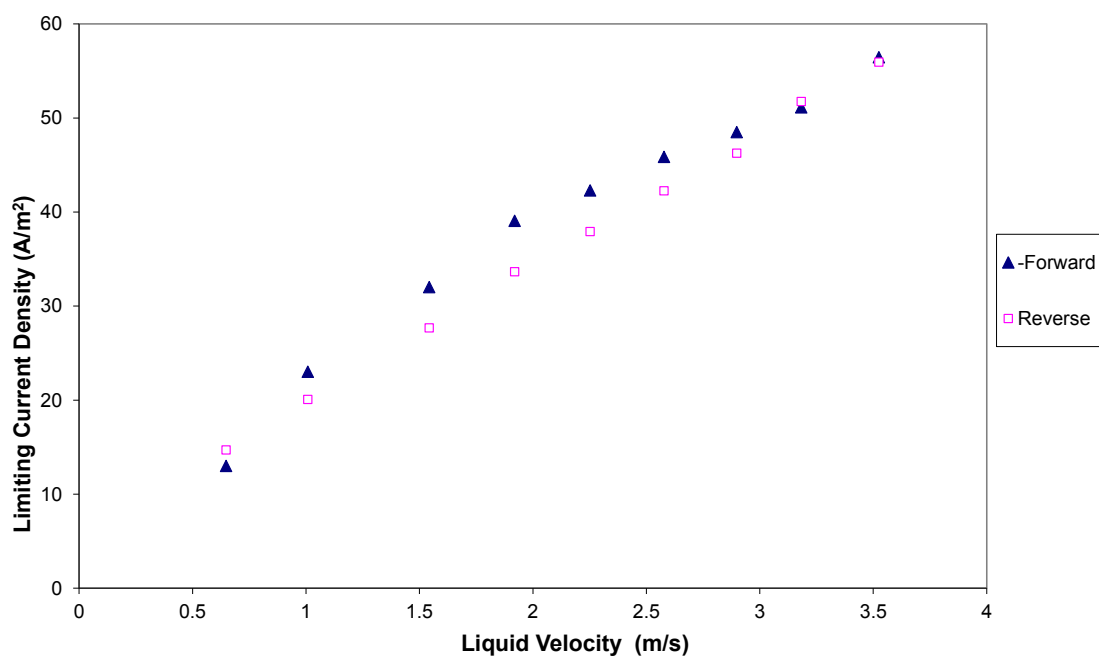


Figure 23: Limiting current densities as a function of liquid velocities at 30° C and pH 3.0

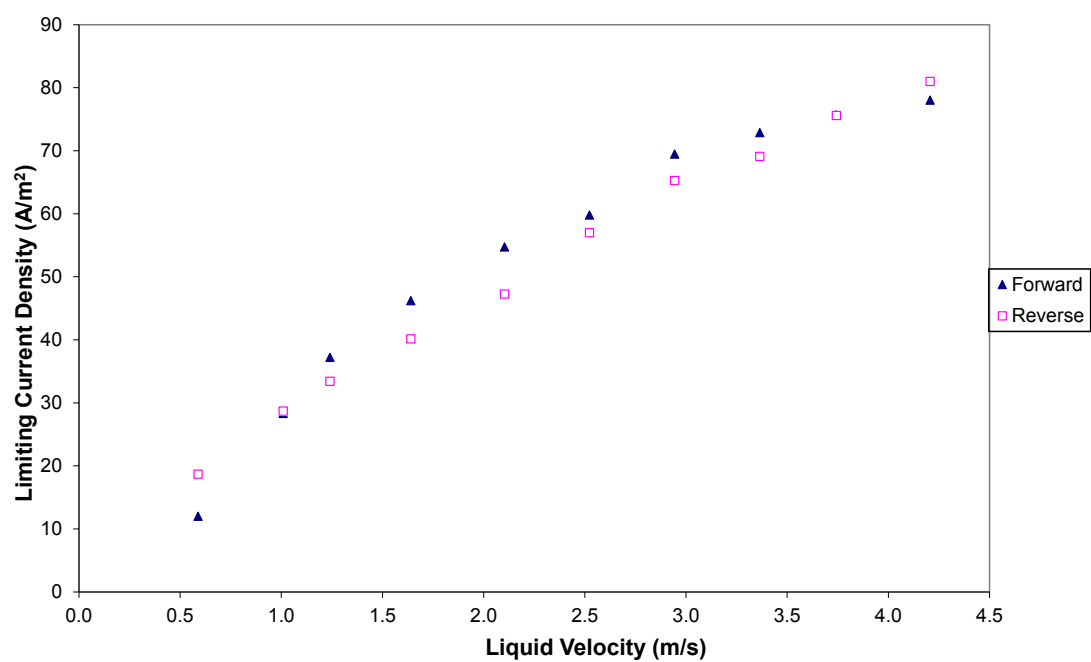


Figure 24: Limiting current densities as a function of liquid velocities at 50° C and pH 3.0

Using **equation (71)**, k_m values were then converted to Sh numbers. **Figure 25** and **Figure 26** show the results of experimental Sh numbers plotted against the theoretical Sh numbers as a function of Re^a . The theoretical Sh numbers were calculated using the correlation of Sleicher and Rouse for smooth pipeline as given below [151]:

$$Sh = 5 + 0.015 Re^a Sc^b \quad (80)$$

where

$$a = 0.88 - \frac{0.24}{(4 + Sc)} \quad (81)$$

$$b = \frac{1}{3} + 0.5 \exp(-0.6Sc) \quad (82)$$

The correlation is valid for $0.1 < Sc < 10^4$ and $10^4 < Re < 10^6$.

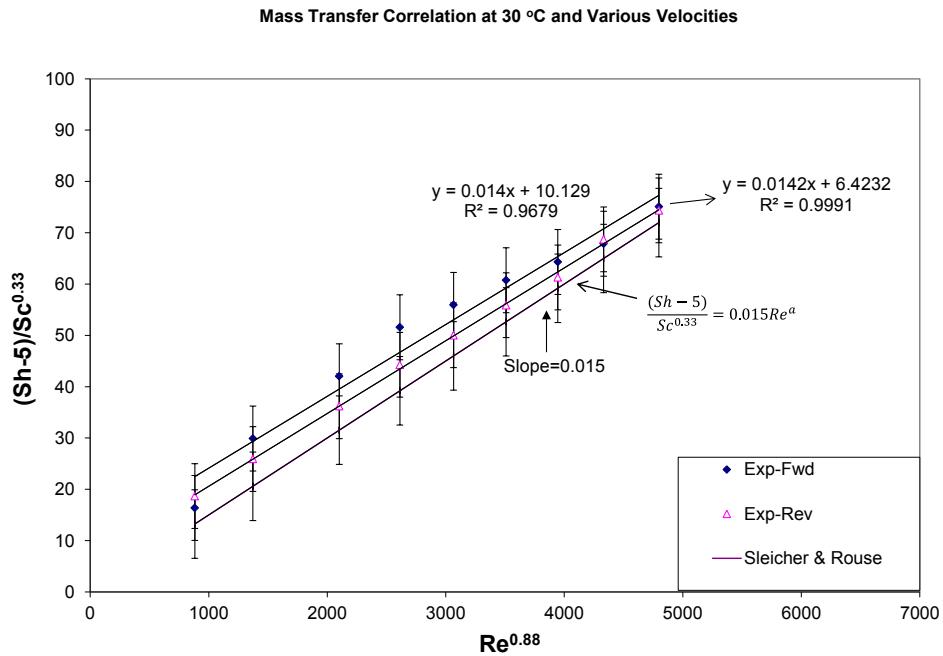


Figure 25: Mass transfer correlation at 30° C and various liquid velocities. Note that $y = \frac{(Sh-5)}{Sc^{0.33}}$ and $x = Re^{0.88}$

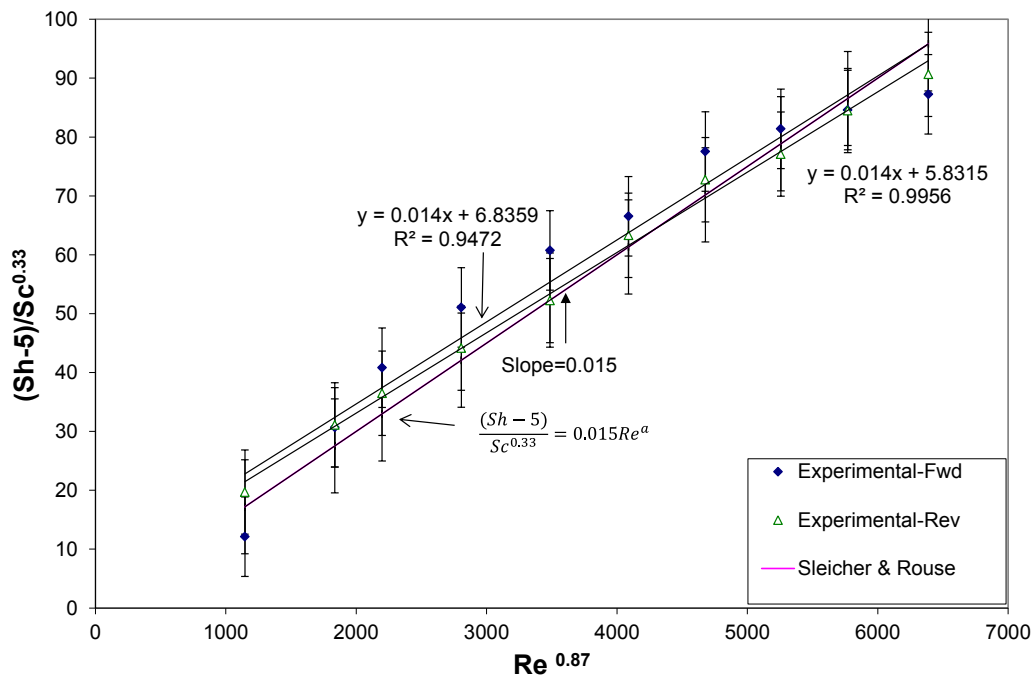


Figure 26: Mass transfer correlation at 50° C and various liquid velocities. Note that $y = \frac{(Sh-5)}{Sc^{0.33}}$ and $x = Re^{0.88}$

The comparison shows that the experimental data at two temperatures seem to correlate well with the data from the Sleicher and Rouse correlation (about 7% to 15% average errors) bearing in mind that the Sleicher and Rouse correlation itself has an associated error of 10% [151]. It is interesting to note that the relatively close correlation was observed despite the fact that some of the Re numbers in the experiment were below 10^4 . Applying linear regression on the data at 30° C and 50° C yielded a correlation coefficient of determination (R^2) of more than 95% and a slope of 0.014 for both. High R^2 indicates that both data sets have a high degree of best-fit to the regression models. More importantly, the slope value of 0.014 is close to the slope of the Sleicher and Rouse

correlation which is 0.015. This suggests that the corrosion rates at pH 3.0 were under mass transfer control.

More importantly, the fact that the experimental and theoretical slopes correlate well suggests that the mass transfer correlation for TCFC follows the heat transfer correlation of the Sleicher and Rouse intended for smooth pipeline in which Nu is replaced with Sh and Pr with Sc for use as mass transfer correlation [152]; Nu is defined as follows:

$$Nu = \frac{hL}{\kappa} \quad (83)$$

where:

Nu is Nusselt number

h is the convection heat transfer coefficient ($\text{W}/\text{m}^2\cdot\text{K}$)

κ is thermal conductivity ($\text{W}/\text{m}\cdot\text{K}$)

L is characteristic length (m)

and

$$Pr = \frac{\nu}{\alpha} \quad (84)$$

where

$$\alpha = \frac{\kappa}{c_p\rho} \quad (85)$$

Where α , C_p , and ρ are thermal diffusivity (m^2/s), heat capacity ($\text{J}/\text{kg}\cdot\text{K}$), and density (kg/m^3), respectively.

The good correlation between experimental data and the Sleicher and Rouse model also affirms that the corrosion process could be used to establish or validate a mass transfer correlation [110, 153]. This correlation further indicates that the power law with which corrosion rates depend on velocity varies with temperature through **equations (68), (79), and (81)**. This allows the correlation to account for the change in fluid properties such as viscosity and density as a result of temperature changes [151]. Most important is that the work proves that the TCFC has well-defined hydrodynamic and mass transfer behavior and could be used to study the effects of flow on corrosion due to mass transfer control.

5.3 High pressure-high temperature rotating cylinder electrode²

Rotating cylinder electrode has been used extensively in the study of single-phase flow-sensitive corrosion since it can reach turbulent flow regime at a relatively low Reynolds number ($Re > 200$); that is, at a relatively low rotational speed or velocity. Another advantage is that it also has a well-defined hydrodynamic and mass transfer behavior. Its mass transfer correlation is given by Eisenberg's correlation as shown in **equation (70)**. Unlike the rotating disc electrode, it has an equipotential over the specimen surface, producing a uniform corrosion [62]. The principle operation of RCE is that the fluid flows due to the rotation of the specimen as a result of no-slip condition [117]: a shear-driven flow. As such, it does not require the use of a pump to move the fluid. This makes it relatively simple to run RCE, particularly for glass cell experiment

² Portions of the content of this section were published in the co-authored paper of reference [166]

as compared to the flow loop. The volume of liquid that it requires is also much smaller than that of flow loop, making it relatively cheaper to run experiments by RCE [117].

5.3.1 Experimental execution

5.3.1.1 Experimental apparatus

HPHT rotating cylinder electrode autoclave as shown in **Figure 27** consists of a 7.5 liter pressure vessel and a lid attached with a rotating assembly:

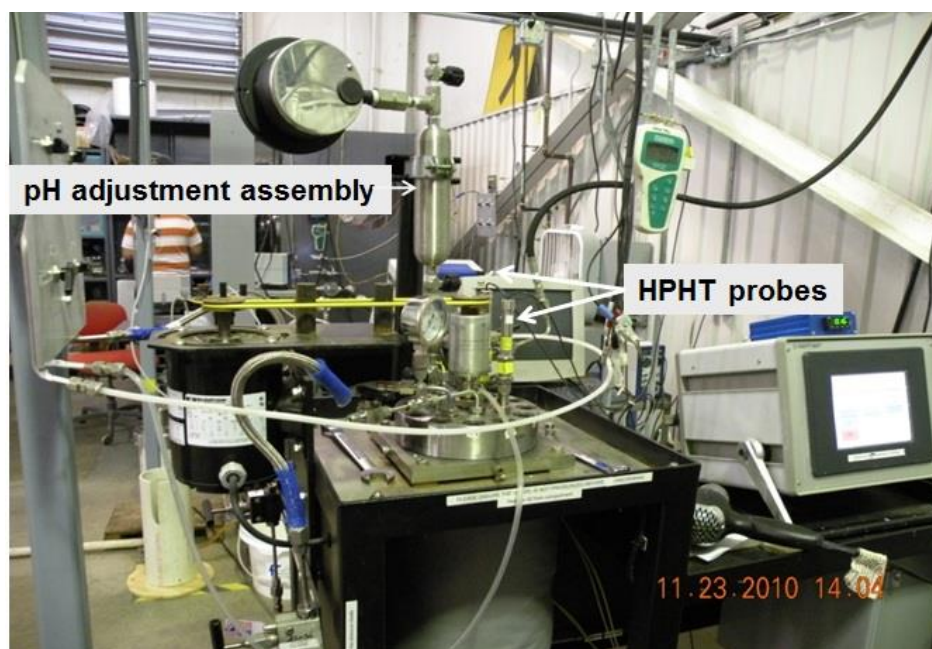


Figure 27: A 7.5-liter high pressure and high temperature rotating cylinder electrode autoclave for flow study at ICMT

The autoclave is made of 316-stainless steel and designed for a maximum working pressure (MAWP) of 350 bar (about 5000 psi). It is also equipped with 3 heating bands and can withstand a maximum working temperature of 300 °C. The RCE has a maximum rotation speed of 1650 RPM. The lid has the following ports for probes: pH probe, Ag/AgCl reference electrode, and counter electrode. As shown by **Figure 28**, the counter

electrode is attached to the shaft, driven by a magnetic drive that is cooled down by cooling water so as to avoid the motor from stalling. The lid is also equipped with gas inlet and outlet. To prevent the ingress of corrosive gas from the test vessel into the electrical compartment attached to the lid, the compartment needs to be pressurized using N_2 at a slightly higher pressure than that of the vessel.

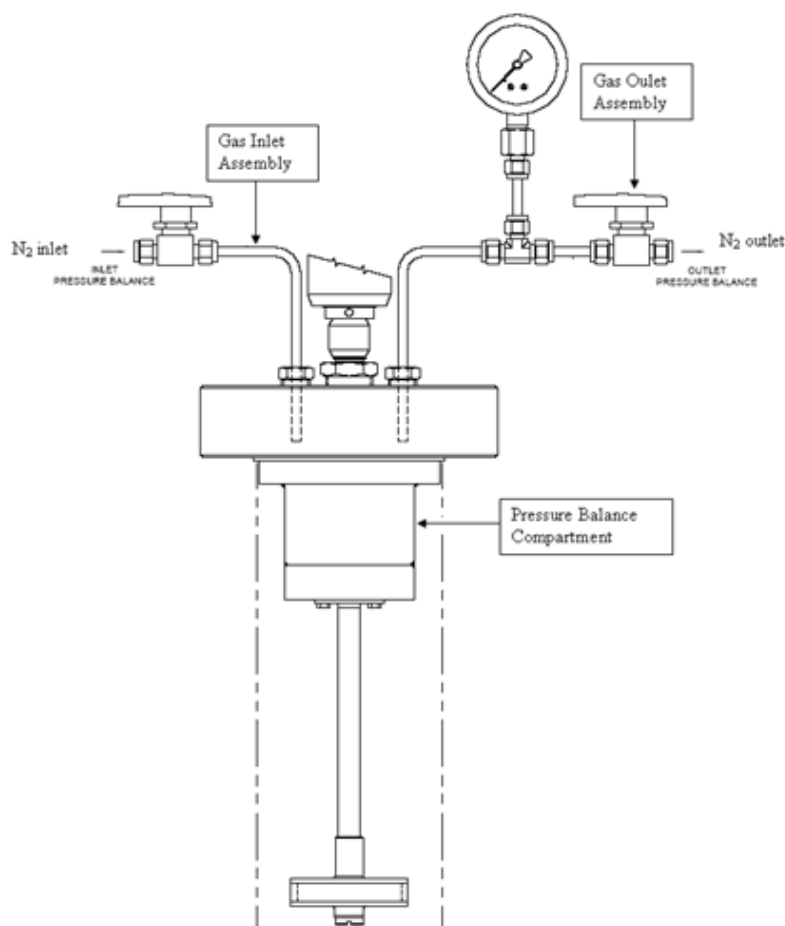


Figure 28: Rotating cylinder lid equipped with a rotating shaft and a pressure balance compartment

For pH adjustment, a 300 mL Monel cylinder was mounted on the lid port as shown in **Figure 27** above. The autoclave is equipped with the following safety features: a rupture disc, an automatic over temperature shut-off, an over-pressure shut-off, and a casing that encloses the rotating belt. The rotational speed of the specimen and the temperature of the test solution are controlled from a digital control panel that also monitors the pressure inside the vessel. For pH and electrochemical measurements, high pressure and high temperature (HPHT) glass pH probe and Ag/AgCl reference electrode probe were used; a platinized niobium electrode served as the counter electrode in a three-electrode electrochemical set up.

5.3.1.2 Experimental parameters

Table 7 shows the physical properties of water and the corresponding Reynolds numbers calculated for the three angular velocities, namely 100, 500, and 1000 rpm at the three test temperatures:

Table 7: The physical properties of water and the Reynolds numbers

Temperature (° C)	ρ of water (kg/m ³)	μ of water (kg/m.s)	Reynolds numbers		
			100 rpm	500 rpm	1000 rpm
25	1000	0.000891	2350	11800	23500
50	987	0.000559	3760	18800	37600
80	972	0.000357	5690	28500	56900

The corresponding peripheral velocities were 0.1, 0.5, and 1 m/s as calculated by the following equation:

$$V = \omega d_C \quad (86)$$

where:

V is peripheral velocity (m/s)

ω is angular velocity (rad/s)

d_C is the diameter of the cylindrical specimen (m)

The above table shows that the flow regime simulated in the experiments was turbulence as $Re > 200$. **Table 8** shows the test matrix for the HPHT RCE experiments:

Table 8: The test matrix for the HPHT RCE experiments

Parameter	Description
Test Solution	1 wt% NaCl
pH	3.0, 4.0, 5.0
Temperature	25° C, 50° C, 80° C ⁽¹⁾
pCO ₂	10, 40, 80 bar
Flow Conditions	Turbulent (Re >200)
Rotational Speed	0, 100, 500, 1000 RPM
Peripheral Velocity	0, 0.1, 0.5, 1 m/s

(1) Only at autogeneous pH

The matrix specified pH 3.0 as the lowest pH since it corresponded to the autogenous pH at 80 bar-25° C which could be expected in the field conditions for CO₂ transport pipeline where free water comes mainly from condensation [154]. Moreover, based on the studies at low pCO₂, pH 3.0 exhibits the highest flow-sensitivity due to it being the condition with the highest concentration of hydrogen ions. On the other hand, pH 5.0 was specified since that is the highest pH at which flow-sensitive CO₂ corrosion is still observed, albeit at a low pCO₂ [44, 129]. The maximum test temperature was set at 80° C since this is the temperature at which formation of protective iron carbonate layer is normally observed albeit at high pH for a low pCO₂. However, a parallel work [16] indicated that protective iron carbonate layers formed in stagnant conditions at 80 bar-80° C even at pH 3.2. Inclusion of this condition in the test matrix helped to verify whether such iron carbonate could still form under flowing conditions.

Based on the pCO₂-temperature matrix, the experiments covered three phases of CO₂ as given by the table below:

Table 9: CO₂ phases and the autogenous pH covered in the test matrix

pCO ₂ (bar)	Temperature (° C)		
	25	50	80
10	Gaseous (pH 3.4)	Gaseous (pH 3.5)	
40		Gaseous (pH 3.2)	
80	Liquid (pH 3.0)	Supercritical (pH 3.1)	Supercritical (pH 3.2)

The autogenous pH values shown in brackets were calculated by an in-house model [15]. The pH values were used to determine whether the test solution was fully saturated at a given test condition.

5.3.1.3 Experimental methods

a) Test solution

Like mass transfer characterization tests, the test solution used in RCE experiments was a 1 wt% NaCl electrolyte prepared by dissolving 200.0 g of NaCl in de-ionized water and making up the volume of the solution to 20 liters. Prior to transferring the test solution into the vessel, it was de-aerated and saturated with CO₂ at ambient conditions in an air tight container for at least four hours, a procedure that was found to accelerate the saturation at higher pCO₂. Without this procedure, it took longer than 30 minutes to saturate the test solution at the elevated pCO₂. Once the test solution had reached the autogenous pH at the desired temperature and pCO₂, the pH of the test solution was adjusted to pH 3.0, 4.0, or 5.0 ±0.1 by injecting de-aerated 1M HCl or 1M NaOH solution into the vessel.

b) Test specimen

Figure 29 shows the test specimen that was machined from a retrieved line pipe of API 5L X-65 carbon steel into a cylinder with an outside diameter of 2 cm and a length of 2 cm:



Figure 29: Specimen for HPHT rotating cylinder electrode

The dimension yielded a total exposed surface area of 15.96 cm^2 . Its chemical composition is given in **Table 6** (see § 5.2.1.3). A banana jack was soldered to the specimen to allow for an electrical contact with the wire inside the rotating shaft so as to allow for electrochemical measurements. Great care was taken to ensure that the specimen would not make any electrical contact with the shaft when mounted. For this reason, checks on electrical shorting between the specimen and the shaft were made after the mounting. Prior to exposure to the test solution, the specimen was polished first with 400 then 600 grit silicon carbide abrasive papers. It was subsequently rinsed with de-ionized water, washed with iso-propanol, and finally dried using a heat gun.

c) Test procedure

Figure 30 below shows the experimental set up of the HPHT RCE:

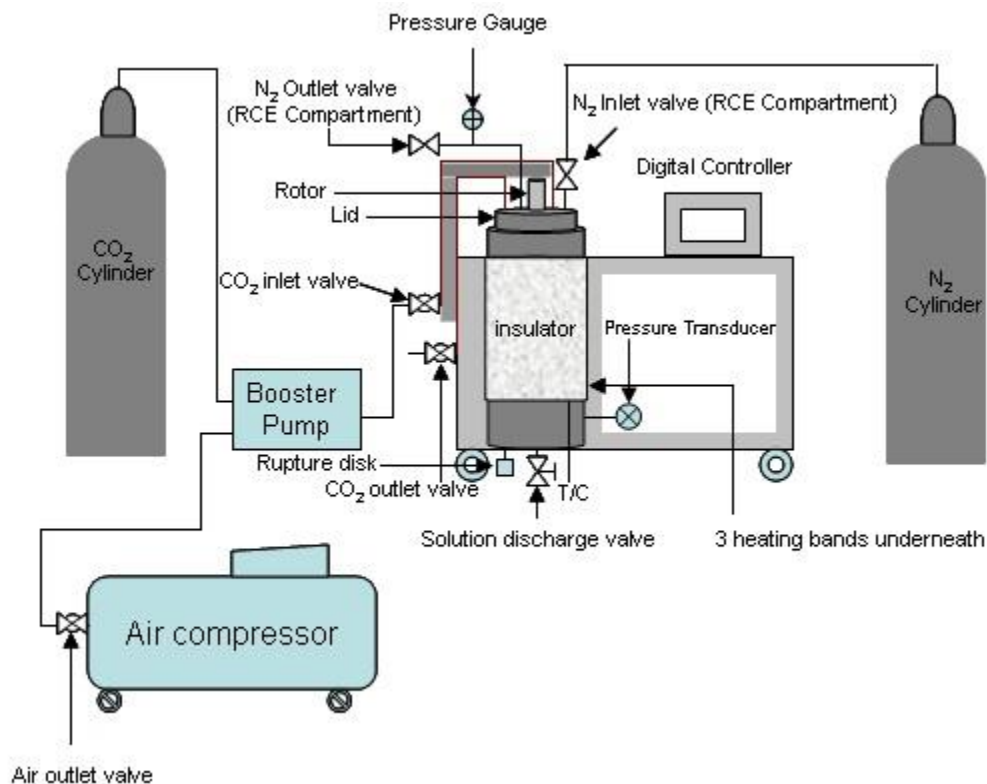


Figure 30: An experimental set up for HPHT RCE experiments

After the lid was mounted on the vessel, and the probes and pH adjustment assembly were installed, the vessel was purged with CO_2 gas at 30 psi for at least fifteen minutes, and all the valves were then closed; the vessel pressure was maintained slightly higher than the atmospheric pressure. After that, the pressure balancing compartment was pressurized using N_2 at a pressure slightly higher than the test pressure. Five liters of the test solution was then transferred to the vessel via the solution discharge valve by pumping it using CO_2 gas. The test solution was then heated to the desired test temperature. It was more convenient to heat the solution first and then pressurize the vessel as this step helped to avoid over pressure. The transferred solution was gradually saturated with CO_2 in multiple stages. An air-driven booster pump was used to increase

the CO₂ partial pressure (pCO₂) since CO₂ from the supply line was limited to about 16 bar. pH was monitored to ensure that the pH of the test solution at each stage reached autogenous pH. It was important to let the CO₂ outlet valve open slightly during the saturation process so as to ensure gaseous CO₂ would dissolve into the test solution: a similar procedure to glass cell experiments. Earlier in the experiments, raising the pressure to the desired pCO₂ with the outlet valve closed led to a relatively low corrosion rate (in the order of 0.001 mm/yr). Finally, the vessel was pressurized to the desired pCO₂, making sure that the pCO₂ reading was stable as it took some time to reach equilibrium and that the autogenous pH at the desired pCO₂ was achieved. Since the vapor pressure at the highest test temperature of 80° C is small (0.5 bar), the total pressure was assumed to correspond to the CO₂ partial pressure. Finally, the pH of the solution was adjusted to pH 3.0, 4.0 or 5.0 ± 0.1 by adding either de-aerated 1M NaOH or 0.2 M HCl using the pH adjustment assembly. To inject the NaOH or HCl solution, the cylinder was pressurized using N₂ to a pressure slightly higher than that of the vessel, and the needle valve to the vessel was gradually opened to release the solution until the pH was fully adjusted. Initially, the pH adjustment assembly was made with a stainless steel cylinder. However, it was observed that the cylinder corroded due to its interaction with HCl solution; this caused some inhibitive effects on the corrosion rate (about 0.5 mm/yr at 10 bar, 50° C, and pH 3); the inhibition might have come from one of its alloying elements: molybdenum [155].

With the desired pH established, the specimen was set at the desired rotational speed. Although the RCE was designed to have a maximum rotational speed of 1750

rpm, it was observed that the shaft was wobbling when the speed was set at 1500 rpm, leading to collection of noisy data. For this reason, the maximum speed set for the experiments was at 1000 rpm.

d) Electrochemical measurements

A Gamry Reference 600 Potentiostat/Galvanostat was used for the electrochemical measurements. A high pressure and high temperature (HPHT) Ag/AgCl probe and a platinized niobium electrode were used as the reference and counter electrodes, respectively. Open-circuit potential (OCP) was first measured until it became stable as shown in **Figure 31** below:

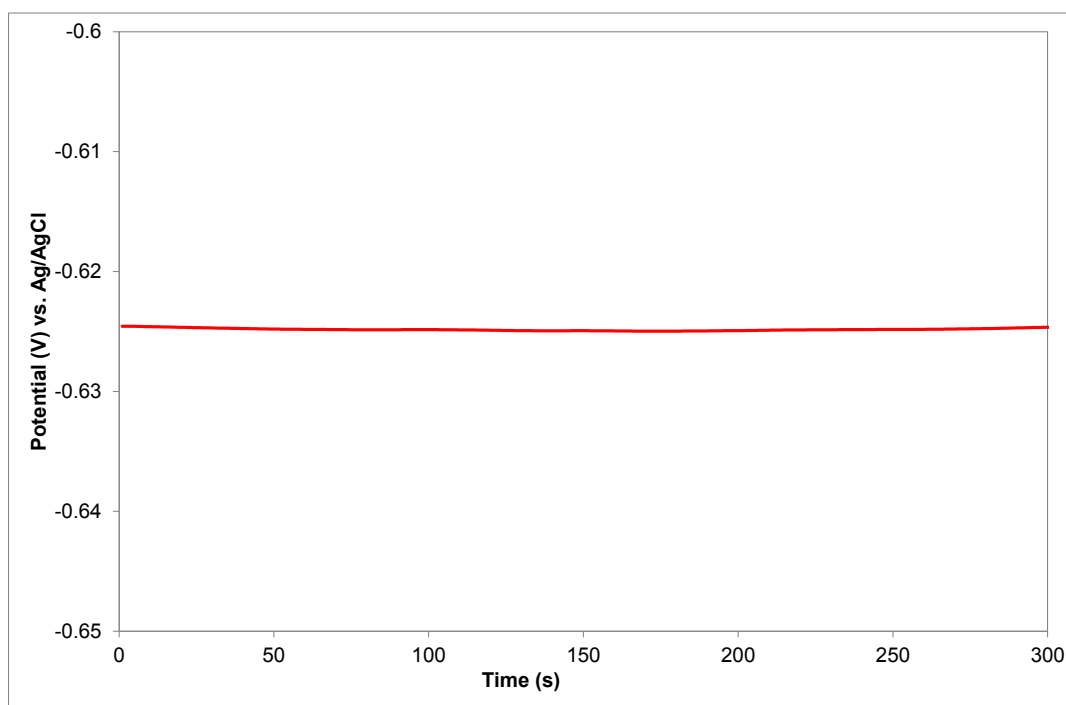


Figure 31: The open-circuit potential measured prior to LPR measurements at $p\text{CO}_2=10$ bar, pH 4.0, and 25°C

This was important so as to ensure a correct reading of linear polarization measurement as a large fluctuation in OCP, especially at values larger than the applied potential for LPR measurement, would yield inaccurate polarization resistance (R_p) values. The specimen potential was polarized at ± 5 mV with respect to the OCP and at a scan rate of 0.125 mV/s. LPR measurements were carried out twice at each velocity given in the test matrix, and LPR was measured first in an ascending order and then in a descending order. Prior to each LPR measurement, OCP was measured for five minutes to ensure that the potential of the specimen would return to its original reading and be stable.

Once LPR measurements were completed, EIS was carried out to measure the solution resistance for correction of R_p values obtained from LPR measurements and for subtraction of IR drop from potentiodynamic data. EIS was carried out in the frequency range of 100kHz to 1mHz with an applied AC potential of ± 5 mV. After that, the specimen was negatively polarized from 0 to -700 mV with respect to OCP at each specified velocity at a scan rate of 0.125 mV/s. Finally, the specimen was positively polarized from 0 to 300 mV with respect to OCP at 0 rpm. A positive potentiodynamic sweep was finally carried out at a stagnant condition as it could contaminate the test solution with ferrous ions and change the specimen surface [44].

e) Weight loss/iron count

To cross-validate the corrosion rates from LPR experiments, corrosion rates were also determined from weight loss and iron count. For weight loss tests, the specimen was set at 500 RPM and left for 24 hours. At the end of weight loss tests, the test solution was sampled and analyzed for iron count using spectrophotometer. The values

of weight loss and iron count were converted to corrosion rate by the following respective equations for weight loss corrosion rate and iron count:

Weight loss [156]

$$\text{Corrosion rate } \left(\frac{\text{mm}}{\text{yr}}\right) = \frac{(8.74 \times 10^4) \times W}{(A \times T \times D)} \quad (87)$$

where

W is mass loss (g)

A is surface area of the specimen (m^2)

T is exposure duration (hours)

D is density of the carbon steel (g/m^3)

Iron count

1. Convert the concentration of ferrous ions into mass loss

$$W = [Fe^{2+}] \times Vol \quad (88)$$

where:

$[Fe^{2+}]$ is Concentration of ferrous ions (mg/L)

$Vol.$ is Volume of the test solution (L)

2. Substitute W into the above corrosion rate formula for weight loss

f) Surface analysis technique

SEM/EDX was used to analyze the morphology and the elemental compositions of the specimen surface including that of corrosion product layers such as cementite (Fe_3C) and siderite (FeCO_3) upon completion of the experiments. Further characterization of the surface layers was conducted by X-ray diffraction (XRD) techniques on some specimens. The steel surface was re-examined after the layers were removed using Clarke solution [157]

5.3.2 Results and discussion

For the calculation of corrosion rates from LPR data, the values of polarization resistance (R_p) in Ohm were first corrected for solution resistance (R_s) obtained from EIS results. Uncorrected R_p values would yield significantly lower corrosion rates since R_p and R_s were of the same order of magnitude. **Figure 32** shows a Nyquist plot for EIS measurement at a typical test condition. The two time constants suggest two different controlling mechanisms: charge transfer at the higher frequencies and mass transfer/chemical-reaction control at the lower frequencies.

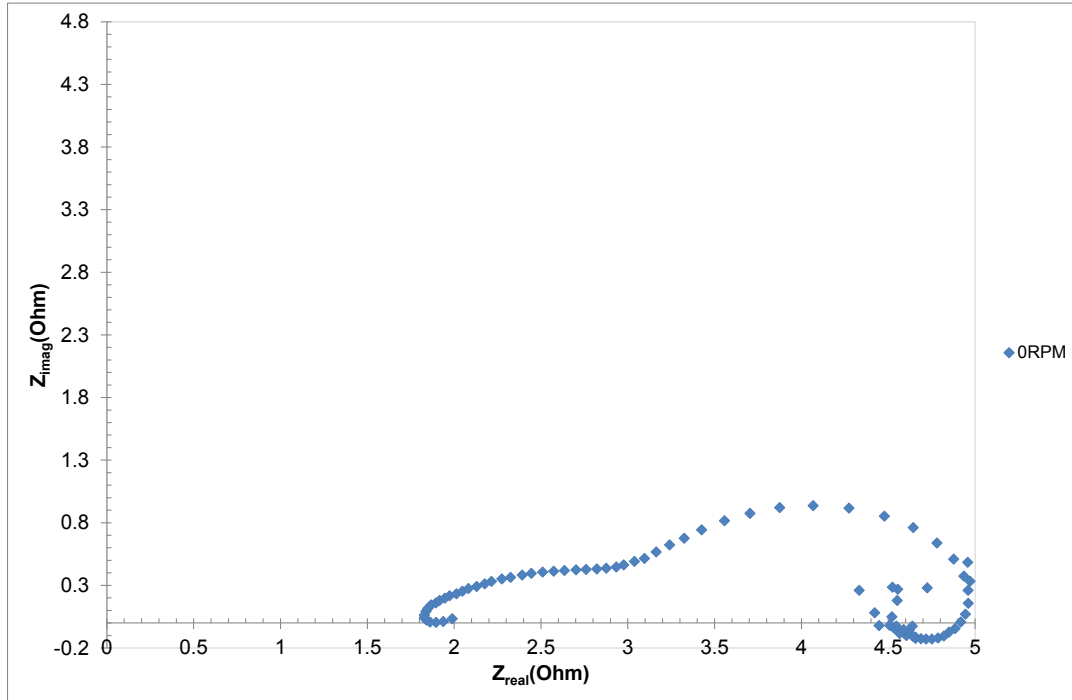


Figure 32: Nyquist plot for $p\text{CO}_2=80\text{bar}$, $T=25^\circ\text{C}$; $\text{pH}=3.0$

Stern-Geary coefficient (**B** value) of 0.026 V [158, 159] was then used to calculate the corrosion current (**I**) given in Amperes [159, 160]:

$$I = \frac{B}{R_p} \quad (89)$$

Corrosion current density obtained by normalizing **I** with the surface area was then multiplied with a factor 1.15, which is valid for carbon steel, to convert it to corrosion rate (mm/yr) [110]. As stated earlier, the LPR data were cross-validated against weight loss and iron count data. **Figure 33** to **Figure 36** show the cross-validation results for the selected test conditions:

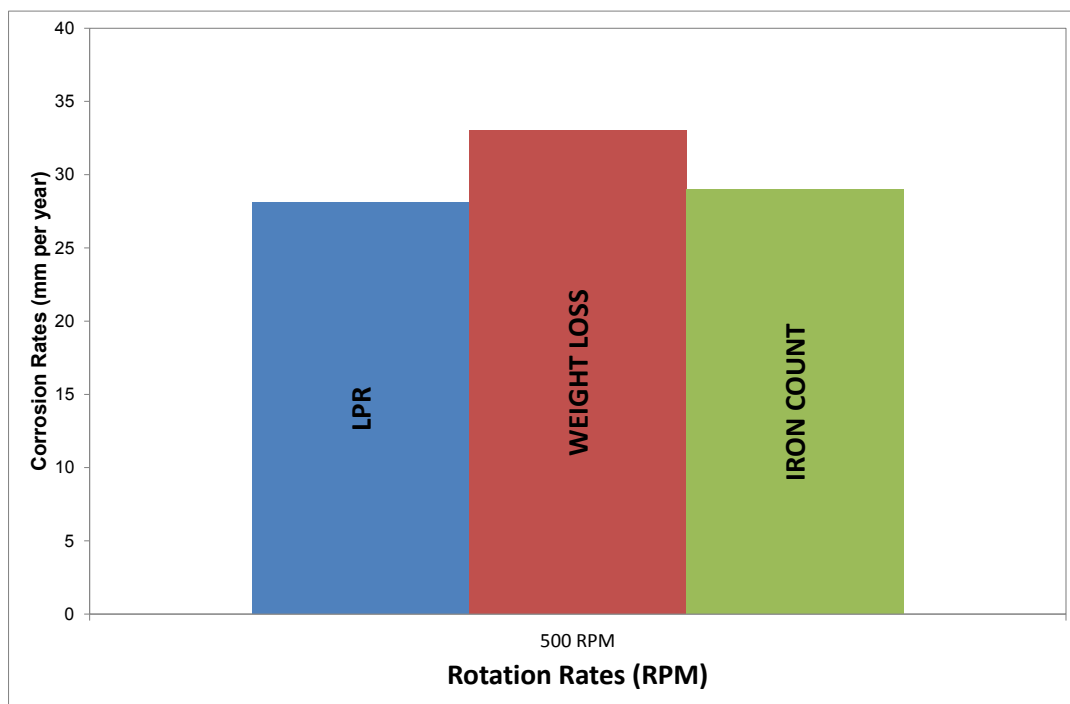


Figure 33: Data cross validation for $p\text{CO}_2=10$ bar; $T=50^\circ\text{C}$; $\text{pH}=4.0$ at 500 rpm

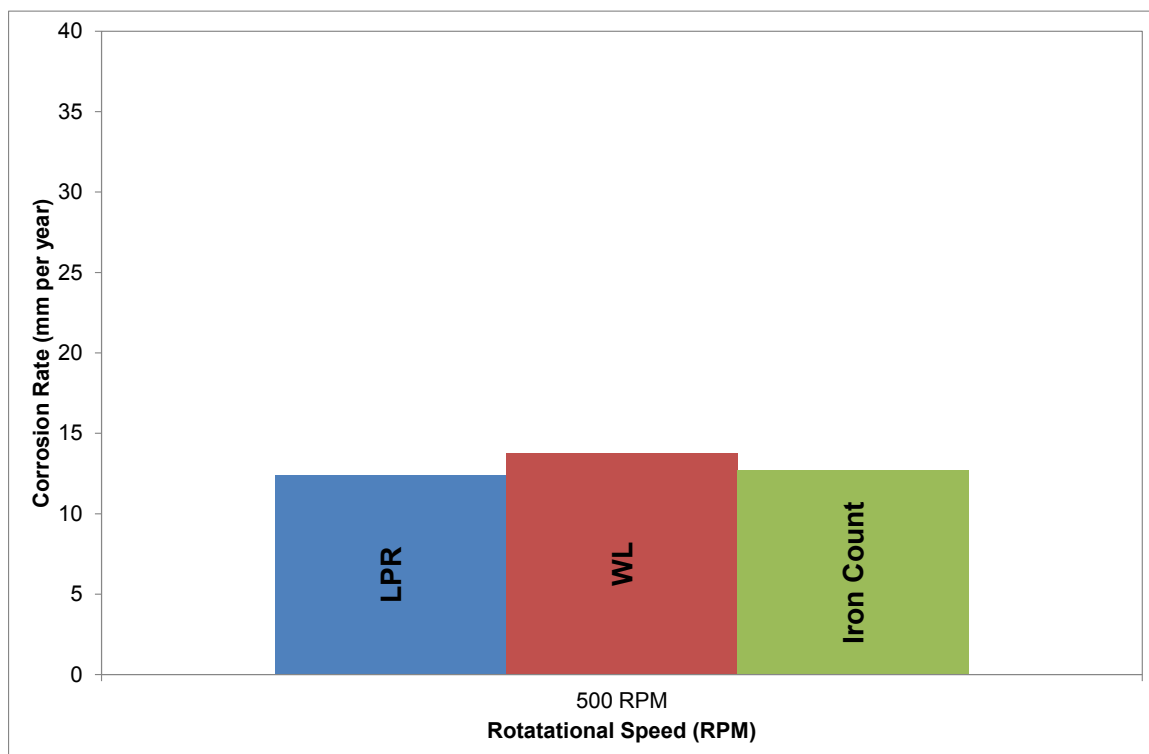


Figure 34: Data cross validation for $p\text{CO}_2=10$ bar; $T=50^\circ\text{C}$; $\text{pH}=5.0$ at 500 rpm

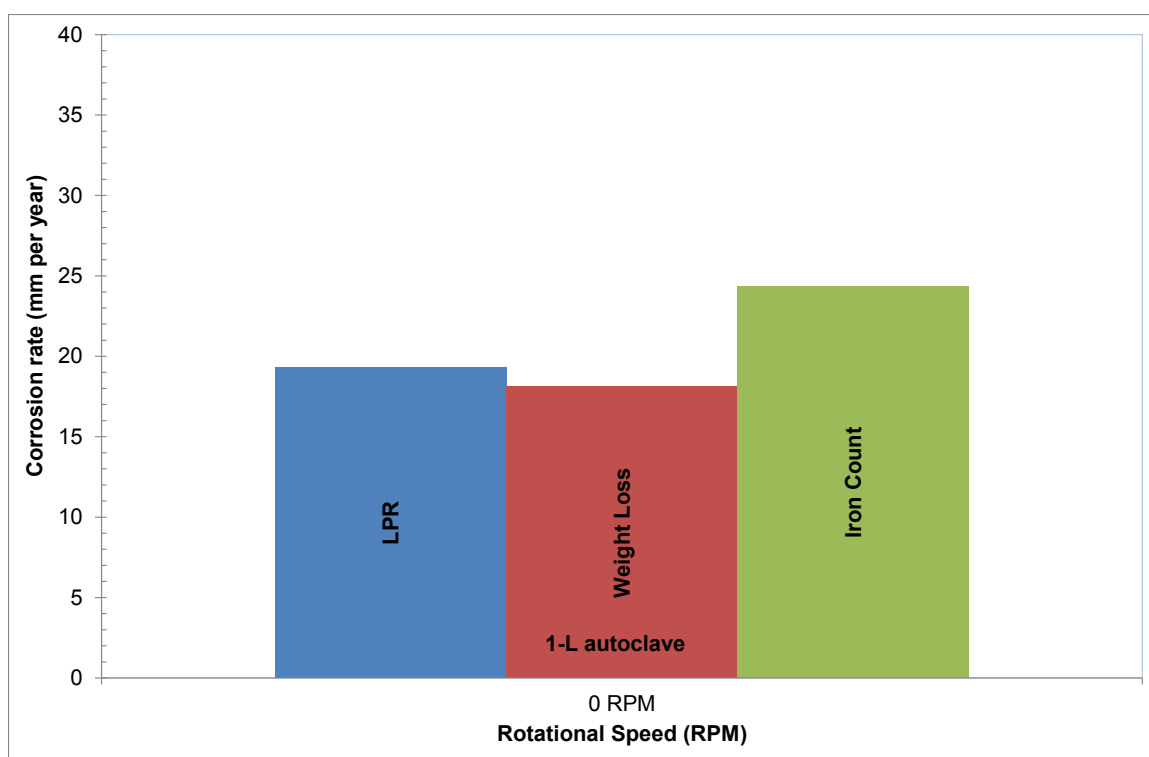


Figure 35: Data cross validation for $p\text{CO}_2=40$ bar; $T=50^\circ\text{C}$; $\text{pH}=3.0$ at 0 rpm

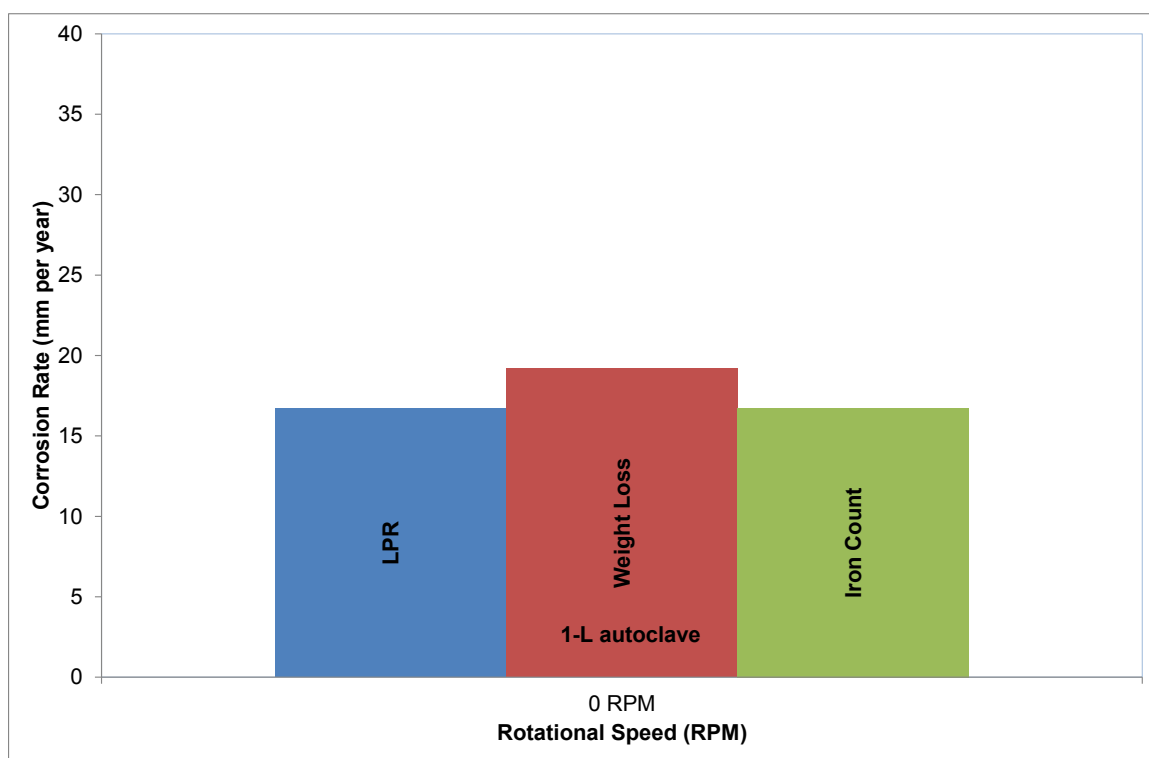


Figure 36: Data cross validation for $p\text{CO}_2=80$ bar; $T=50^\circ\text{C}$; $\text{pH}=3.0$ at 0 rpm

The fact that some of the LPR data were closely-correlated with the weight loss and iron count data indicates that the use of $B=0.026$ V was reasonable. It also suggests that the corrosion rate was not purely under charge-transfer control as proposed by Schmitt and Rothman [50], but there was an influence from cathodic limiting current (mass transfer); charge-transfer control would correspond to a B value of 0.01 V (assuming $b_a=40\text{mV/decade}$ and $b_c=120\text{mV/decade}$) [43, 66].

The experimental results are analysed in terms of pH effect, temperature effect, and $p\text{CO}_2$ effect on the flow-sensitivity of CO_2 corrosion as follows.

5.3.2.1 The effect of pH

Figure 37 and **Figure 38** below show the effect of pH on the flow-sensitivity of CO₂ corrosion at pCO₂ of 10 bar and two temperatures: 25° C and 50° C:

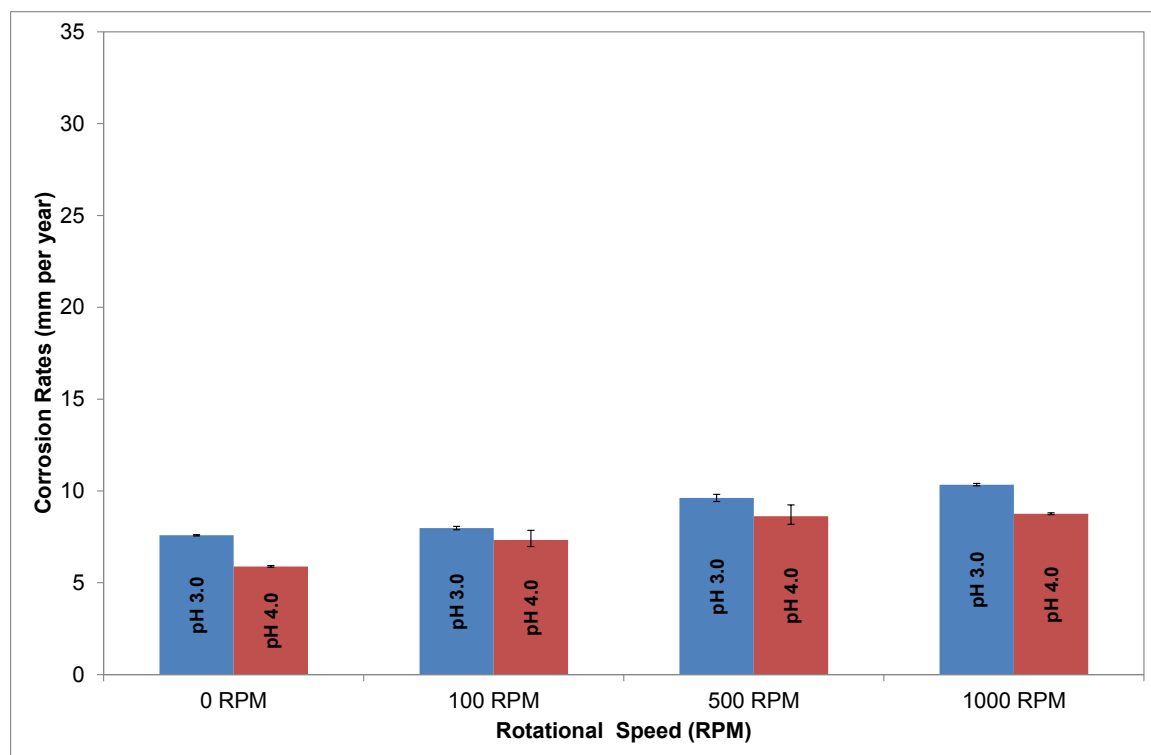


Figure 37: Comparison of corrosion rate from LPR tests between pH 3.0 and pH 4.0 at pCO₂=10 bar and 25° C

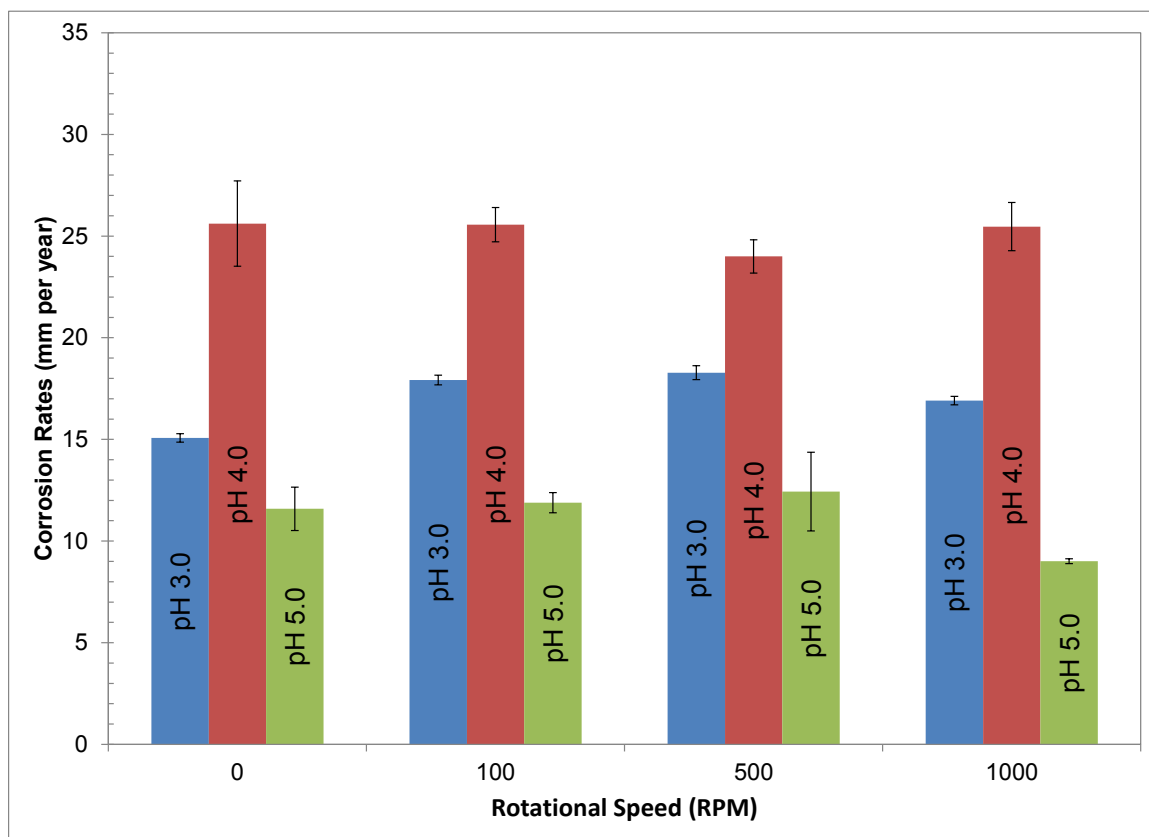


Figure 38: Comparison of corrosion rate from LPR tests among pH 3.0, pH4.0, and pH 5.0 at $p\text{CO}_2=10$ bar and 50°C

Figure 37 and **Figure 38** above indicate that generally, the corrosion rate decreased as pH increased. This trend is similar to what other workers have observed at low $p\text{CO}_2$ [18, 44, 110, 128]. This is because cathodic reduction of hydrogen ions contributed partly to the total cathodic current density; hence, the decrease in hydrogen ion concentration reduces the total cathodic current density and subsequently corrosion rate. However, at 50°C , the corrosion rate seemed to increase as the pH increased from pH 3.0 to pH 4.0, and then decreased again at pH 5.0 with the corrosion rates being the lowest. The same behaviour was observed even when the test was repeated. It is not certain what might have caused this deviation. **Figure 33** shows that even the weight loss

and iron count data obtained separately from the LPR experiments indicate relatively higher corrosion rates.

More importantly, **Figure 37** and **Figure 38** show that flow sensitivity was only minimal at the three pH values. Even at pH 3.0, in which the concentration of hydrogen ions was relatively significant, the flow sensitivity was not pronounced. This was also true for 50° C at which the increase in charge transfer reaction was supposed to have increased flow-sensitivity [52]. The low flow-sensitivity is also evidenced for each pH from the potentiodynamic results shown in the figures below:

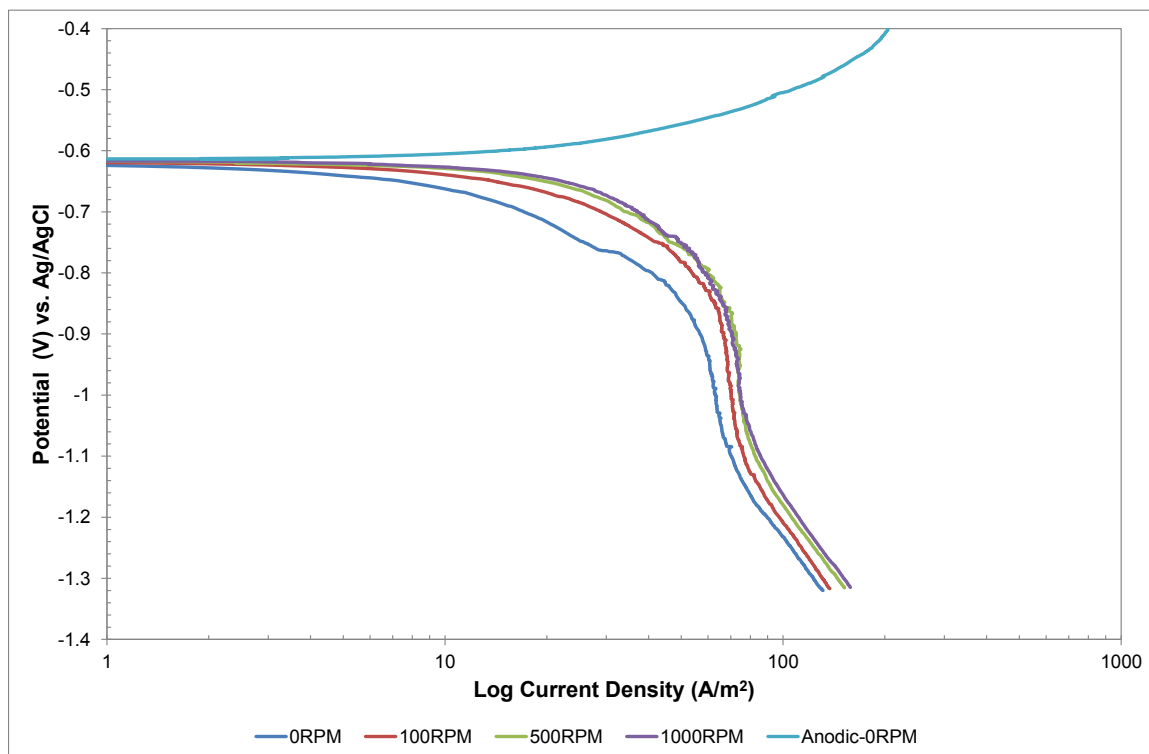


Figure 39: Cathodic polarization curves at various velocities; $p\text{CO}_2=10\text{bar}$, pH 3.0 and 25° C

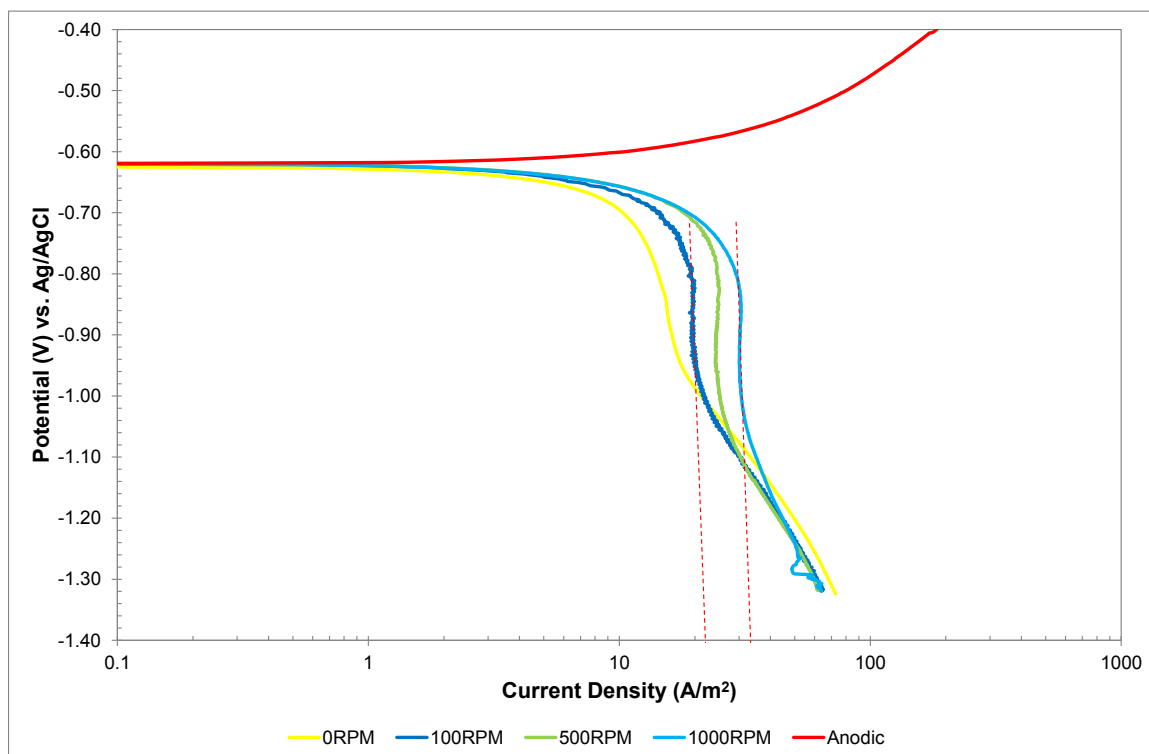


Figure 40: Cathodic polarization curves at various velocities; $p\text{CO}_2=10$ bar, pH 4.0 and 25°C

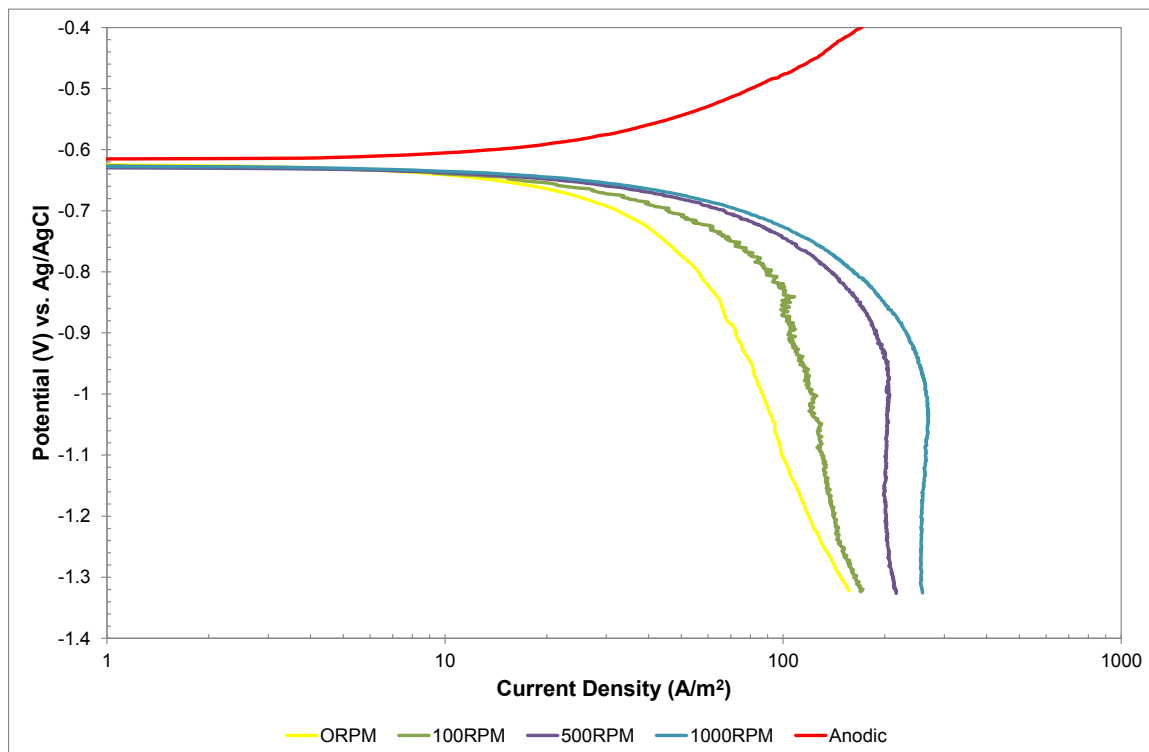


Figure 41: Cathodic polarization curves at various velocities; $p\text{CO}_2=10$ bar, pH 4.0 and 50°C

It is clear from the figures above that unlike in strong acid, the flow sensitivity of CO_2 corrosion is not proportional to the power law of the velocity. Based on Eisenberg's correlation where $i_{lim} \propto \omega^{0.7}$, a tenfold increase (100 RPM to 1000 RPM) in rotational speed at each pH would increase the corrosion rate by five times if a full mass transfer control were assumed. However, LPR and potentiodynamic results indicate only slight increase in corrosion rate with velocity at each of the three pH values. **Figure 41**, for example, suggests an increase of limiting current density by a factor of 1.5 instead of 5 for the tenfold increase in rotational speed. The reason for the slight flow sensitivity is that the cathodic limiting current density was dominated largely by the chemically

controlled cathodic reduction of H_2CO_3 [44, 50]. Further evidence for this is shown in

Figure 42 below:

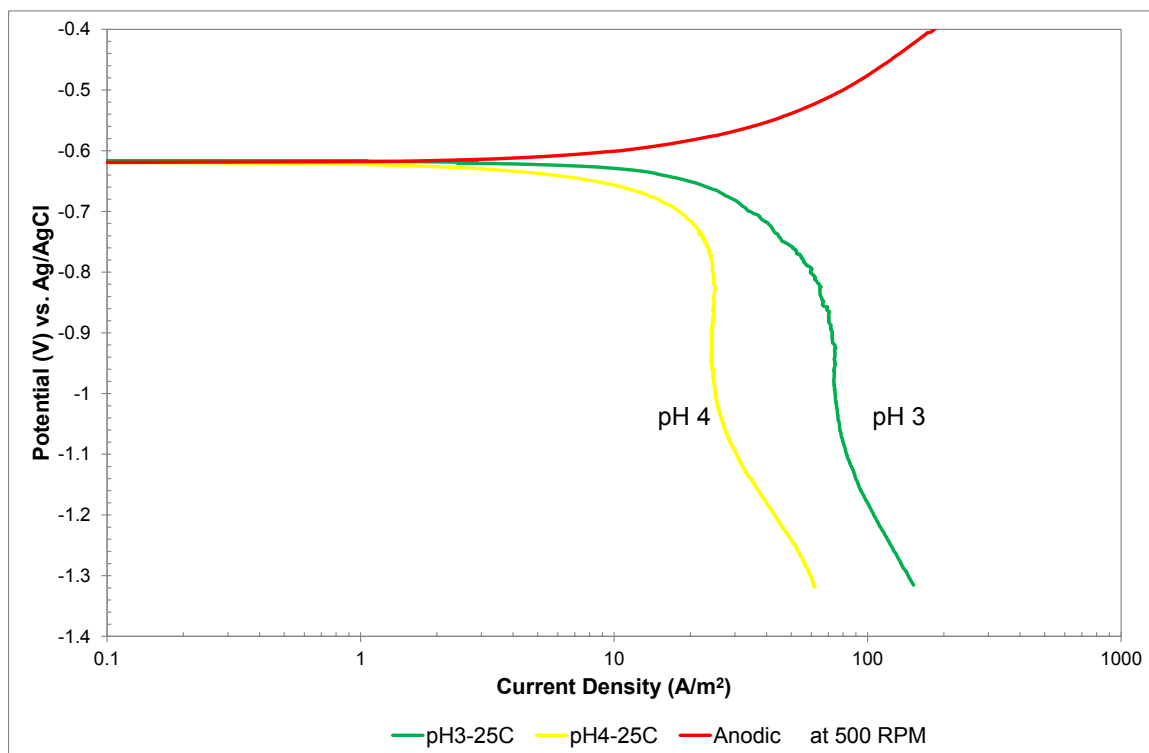


Figure 42: Comparison of corrosion rates between pH3.0 and pH4.0 at $p\text{CO}_2=10\text{bar}$, 25°C , and 500 RPM

The above figure indicates that the decrease in limiting current density with the increase in pH from 3.0 to 4.0 was only by about a factor of three. If the mass-transport came purely from hydrogen ions, the limiting current density would reduce proportionally by a factor of 10 [44]. It is interesting to note that while some significant flow-sensitivity could still be observed at pH 4.0 for $p\text{CO}_2$ of 1bar [110, 129], only slight flow-sensitivity was observed at pH3.0 for $p\text{CO}_2$ of 10 bars. This could again indicate the dominance of H_2CO_3 concentration in the contribution to the total cathodic density. It

must be noted that at 1 bar and 25° C, the concentration of H_2CO_3 is 8.23×10^{-5} M while at 10 bar and 25° C, the concentration of H_2CO_3 is 8.5×10^{-4} M, a tenfold increase in H_2CO_3 concentration [15]. Thus, while the contribution of hydrogen ions on cathodic limiting current density at low pCO_2 was still significant at pH 4.0 and lower, the increase in H_2CO_3 concentration at pCO_2 of 10 bar at the same pH range relatively reduced the contribution from hydrogen ions. Since flow sensitivity arises from the transport of hydrogen ions, the reduction resulted in the decrease in flow-sensitivity.

It is also important to see whether pH affected the anodic reaction rate. **Figure 43** below shows the effect of pH on anodic reaction measured at stagnant conditions:

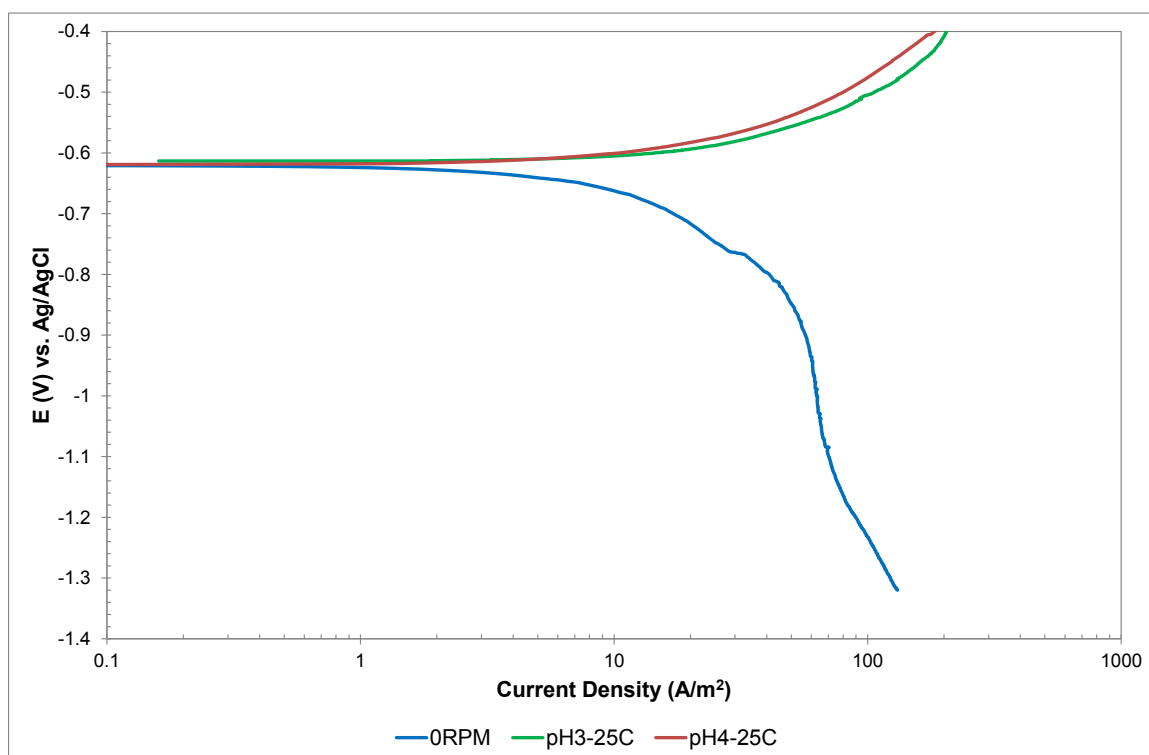


Figure 43: Comparison of anodic curves between pH 3.0 and pH 4.0; $\text{pCO}_2=10$ bar and 25° C

The figure suggests that the change in pH did not have any large effect on the anodic reaction. Some studies at low $p\text{CO}_2$ suggested that the rate of anodic reaction would increase with pH up to pH 4.0. This was due to the increase in the adsorption of hydroxyl ions that act as a catalyst. Above pH 4, the increase in pH did not increase the anodic reaction further as the surface was saturated with hydroxyl ions [45, 63]. The fact that there was only small effect by pH suggests that the steel surface was already saturated with adsorbed hydroxyl ions that led to no further catalytic effect. It might be possible that at a higher $p\text{CO}_2$, CO_2 was also adsorbed on the surface, making it more quickly saturated at pH values below 4 [45]. Since the effect of pH on the flow-sensitivity of CO_2 corrosion at $p\text{CO}_2$ of 10 bar was not that significant even at pH 3.0, no further tests on pH effect were carried out at higher $p\text{CO}_2$.

5.3.2.1 The effect of temperature

Figure 44, **Figure 45**, and **Figure 46** below show the effect of temperature on the flow-sensitivity of CO_2 corrosion at $p\text{CO}_2$ of 10 bar and 80 bar at pH 3.0. The figures show that corrosion rates increased with the increase of temperature. This was probably due to the increase in the kinetics of chemical and electrochemical reactions.

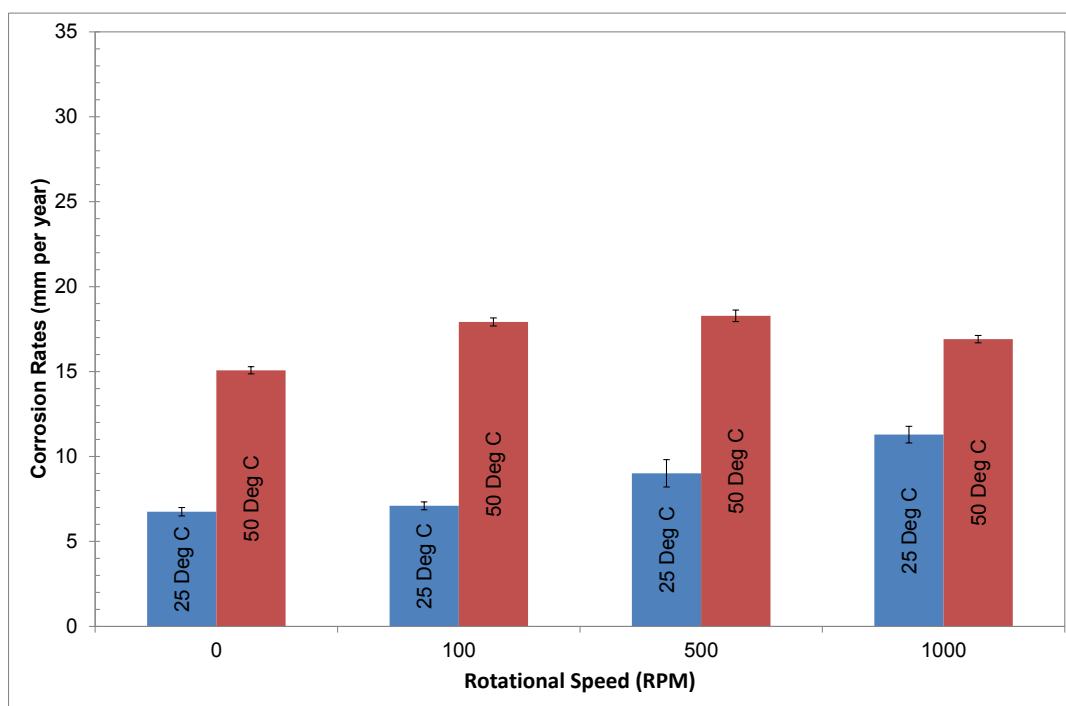


Figure 44: Comparison of corrosion rate from LPR tests between 25° C and 50° C at $p\text{CO}_2=10$ bar and pH3.0

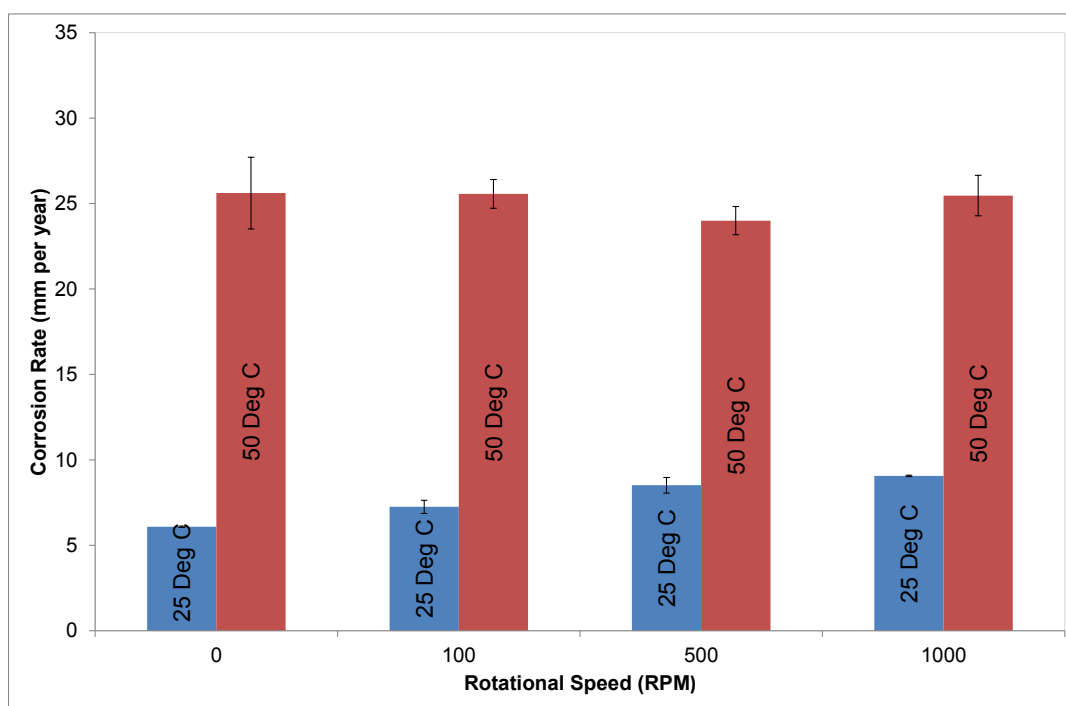


Figure 45: Comparison of corrosion rate from LPR tests between 25° C and 50° C at $p\text{CO}_2=10$ bar and pH4.0

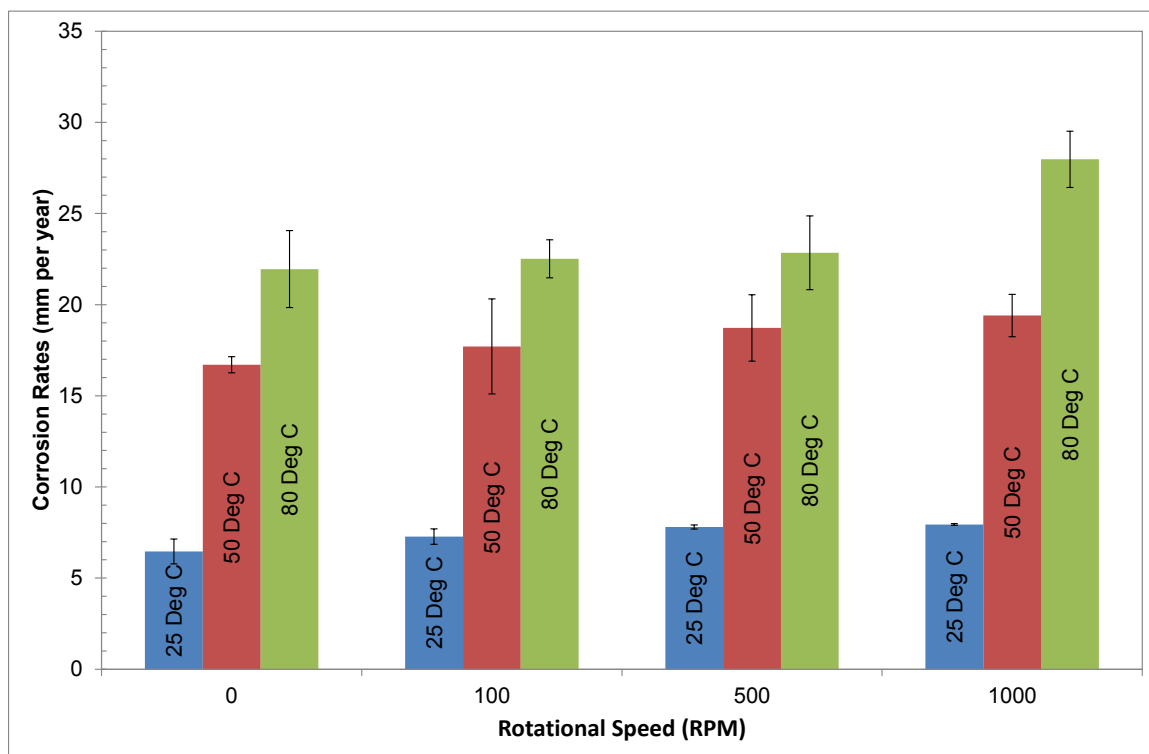


Figure 46: Comparison of corrosion rate from LPR tests between 25° C, 50° C, and 80° C at $p\text{CO}_2=80$ bar and $\text{pH}3.0$

However, at each temperature, there seemed to be slight flow sensitivity as the corrosion rate only increased minimally with the rotational speed. Even at 80° C at which charge-transfer rate was expected to be higher, flow-sensitivity was not pronounced. A similar trend could be observed from the potentiodynamic results shown in the figures below:

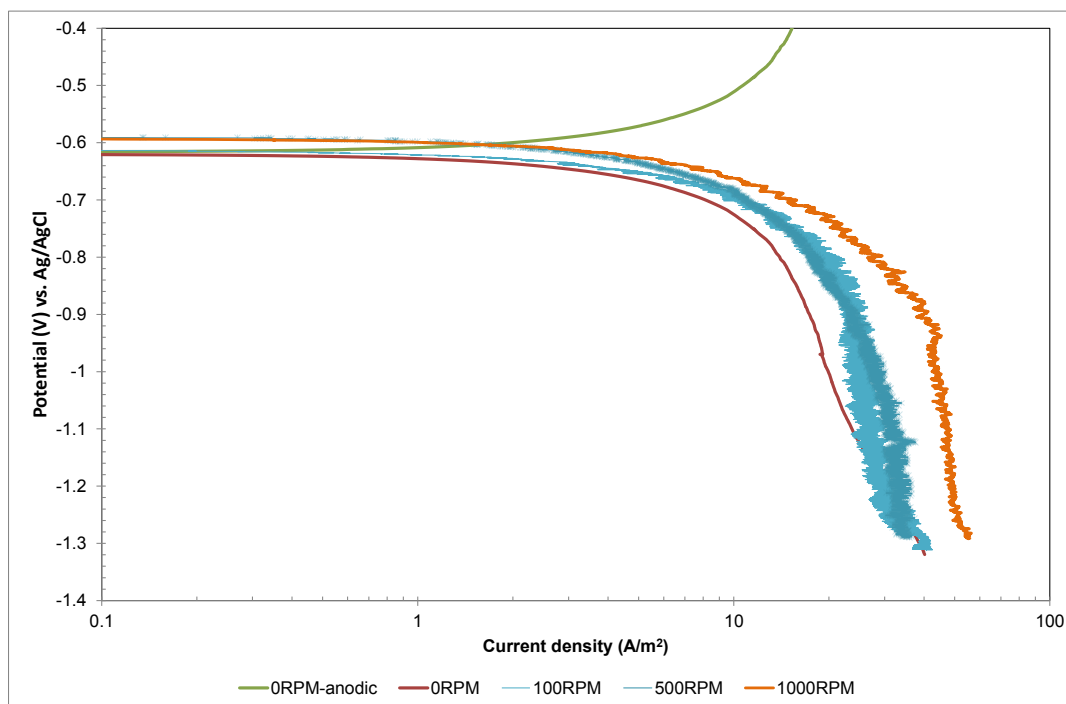


Figure 47: Cathodic polarization curves at various velocities at $p\text{CO}_2=10$ bar, pH 3.0 and 25°C

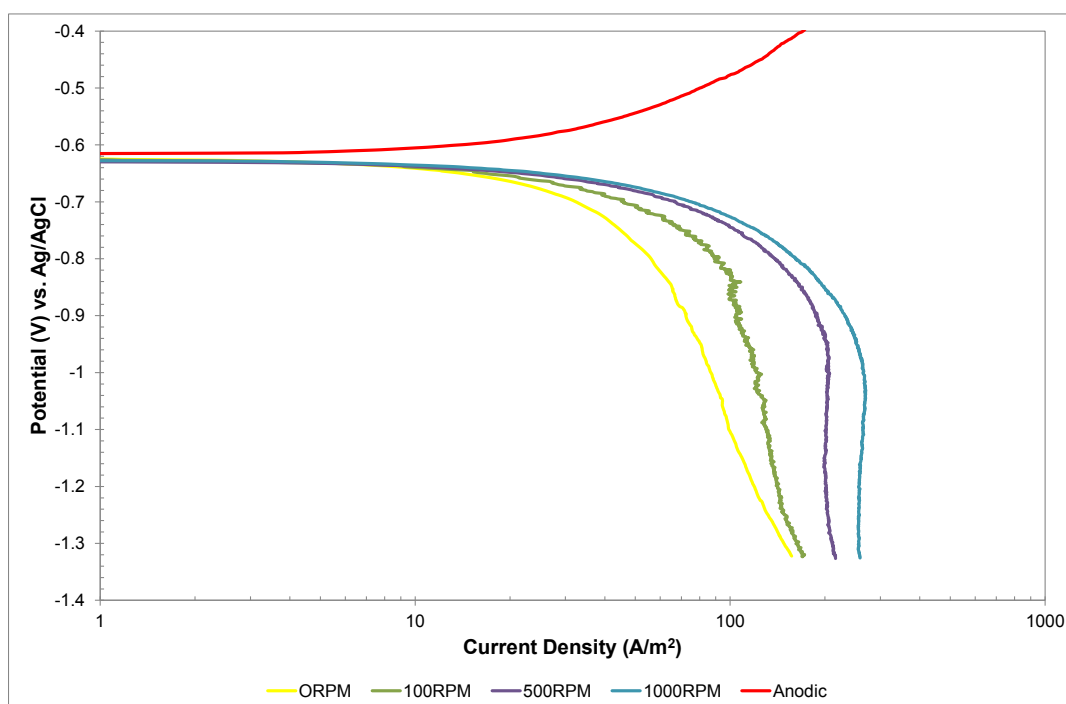


Figure 48: Cathodic polarization curves at various velocities at $p\text{CO}_2=10$ bar, pH 4.0 and 50°C

If corrosion rates were assumed to be fully under mass-transfer control, Eisenberg's correlation would predict an increase in corrosion rates by a factor of 3 when the rotational speed increased from 100 RPM to 500 RPM. **Figure 48**, on the other hand, indicates an increase of corrosion rate by a factor of about 1.3. In this regard, temperature might have increased the chemical reaction rate including the homogeneous hydration of dissolved CO_2 as well as the mass transfer and charge-transfer rates as evidenced from the increase in corrosion rates. Nevertheless, at high pCO_2 in which the reduction of H_2CO_3 could be dominant, the increase was not sufficient enough to make the mass-transport rate of hydrogen ions even at pH 3.0 and 80°C as the rate determining step as observed in HCl solution. Instead, the hydration of dissolved CO_2 could still be the rate determining step.

Figure 49 below shows the effect of temperature on anodic reaction measured at stagnant conditions:

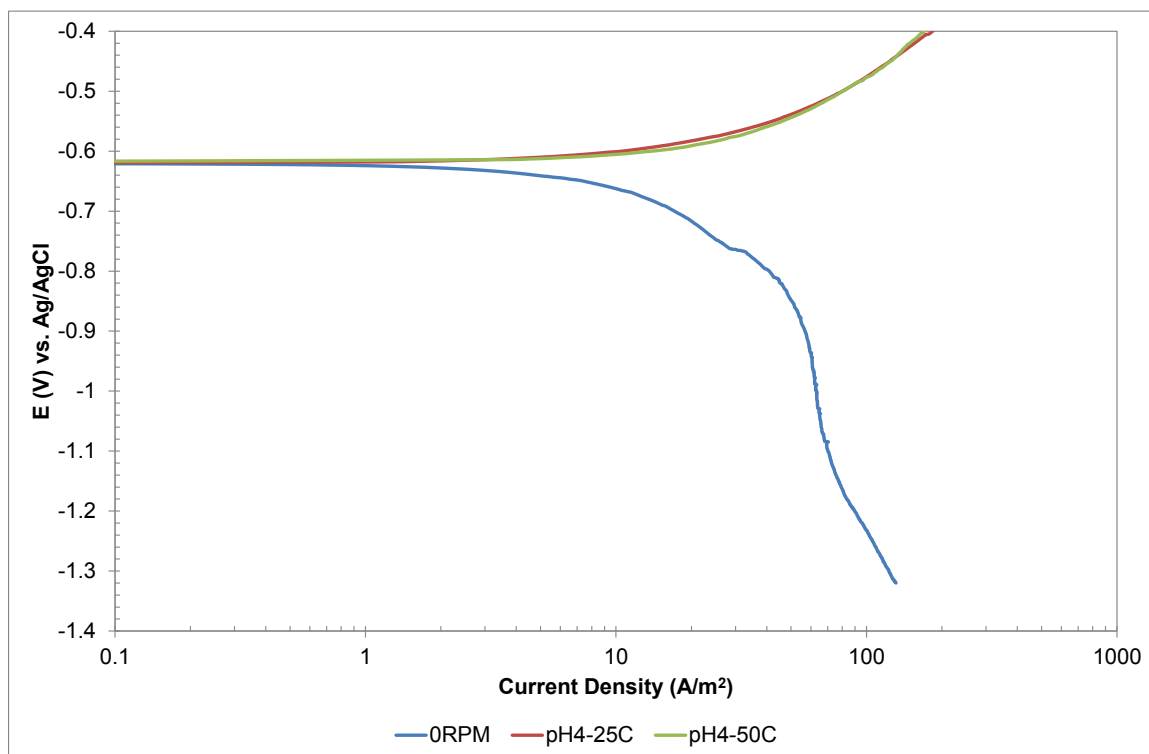


Figure 49: Comparison of anodic curves between 25° C and 50° C at $p\text{CO}_2=10\text{bar}$, pH 4.0, and stagnant conditions

The figure suggests that the change in temperature did not have any effect on the anodic reaction [44]. This seems to contradict **equation (57)** which predicts temperature dependence. Gray and co-workers also observed a temperature-dependent anodic reaction at 25° C and 60° C [40]. However, Nesic and co-workers also found a non-temperature dependence of anodic reaction at low $p\text{CO}_2$ [44]. It is not clear why the anodic reaction also exhibited such behaviour at high $p\text{CO}_2$ [44].

5.3.2.2 The effect of CO_2 partial pressure

Figure 50 below shows the effect of $p\text{CO}_2$ at pH3.0 and 50° C:

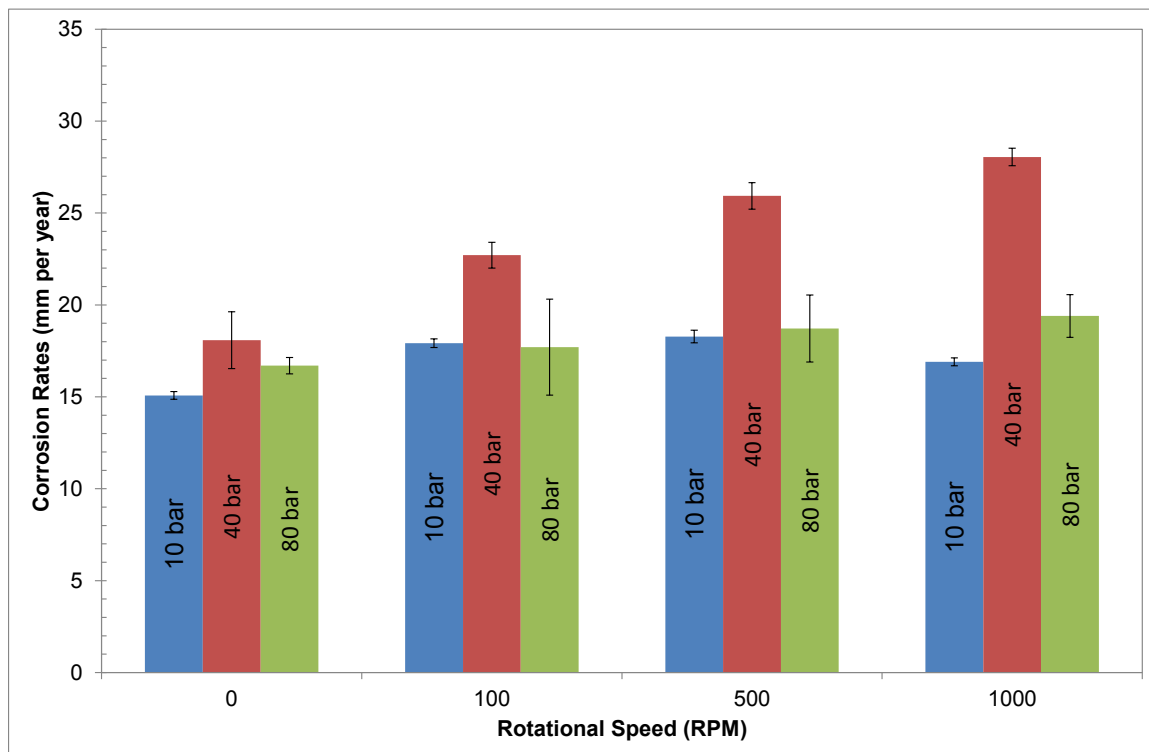


Figure 50: Comparison of corrosion rate from LPR tests among $p\text{CO}_2$ of 10 bar, 40 bar, and 80 bar at 50°C and $\text{pH } 3.0$.

The figure reveals that corrosion rate increased as $p\text{CO}_2$ increased from 10 bar to 40 bar at each rotational speed. This could be due to the increase in the H_2CO_3 concentration which increased the cathodic current density of H_2CO_3 reduction [40, 44, 67]. However, as noted by Dugstad and co-workers, above 5 bar, corrosion rate did not increase considerably with the increase in $p\text{CO}_2$ [18]. The figure further indicates that the corrosion rate decreased as $p\text{CO}_2$ was increased to 80 bar. This was most probably due to the formation of iron carbonate layer at high temperature as shown in **Figure 51** [43]:

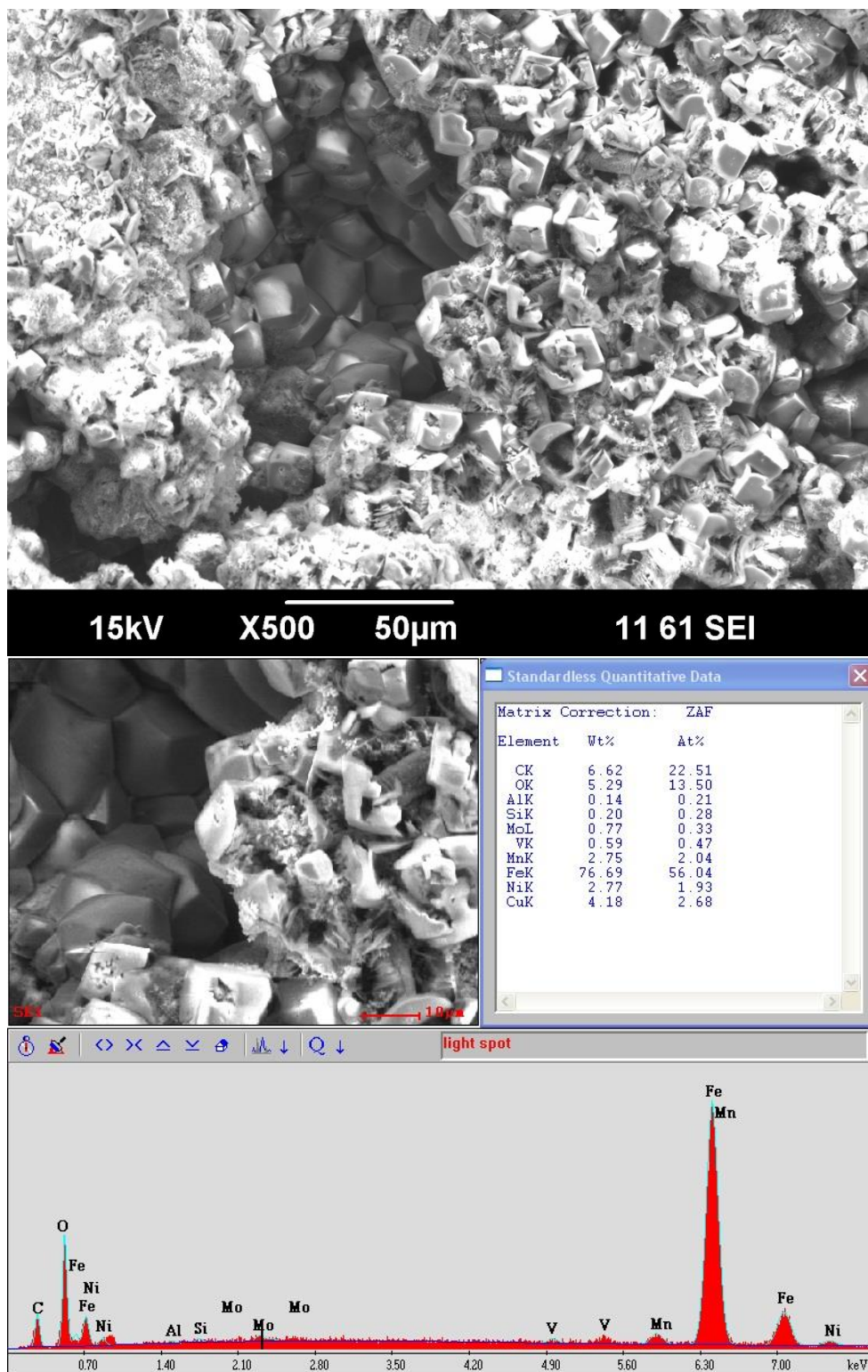


Figure 51: Surface analysis at $p\text{CO}_2=80$ bar, $\text{pH}=3.2$ and $T=80^\circ\text{C}$ showing iron carbonate formed on the substrate

As shown by **Figure 52**, an XRD spectrum verified further that the corrosion product layer that formed under this condition was iron carbonate:

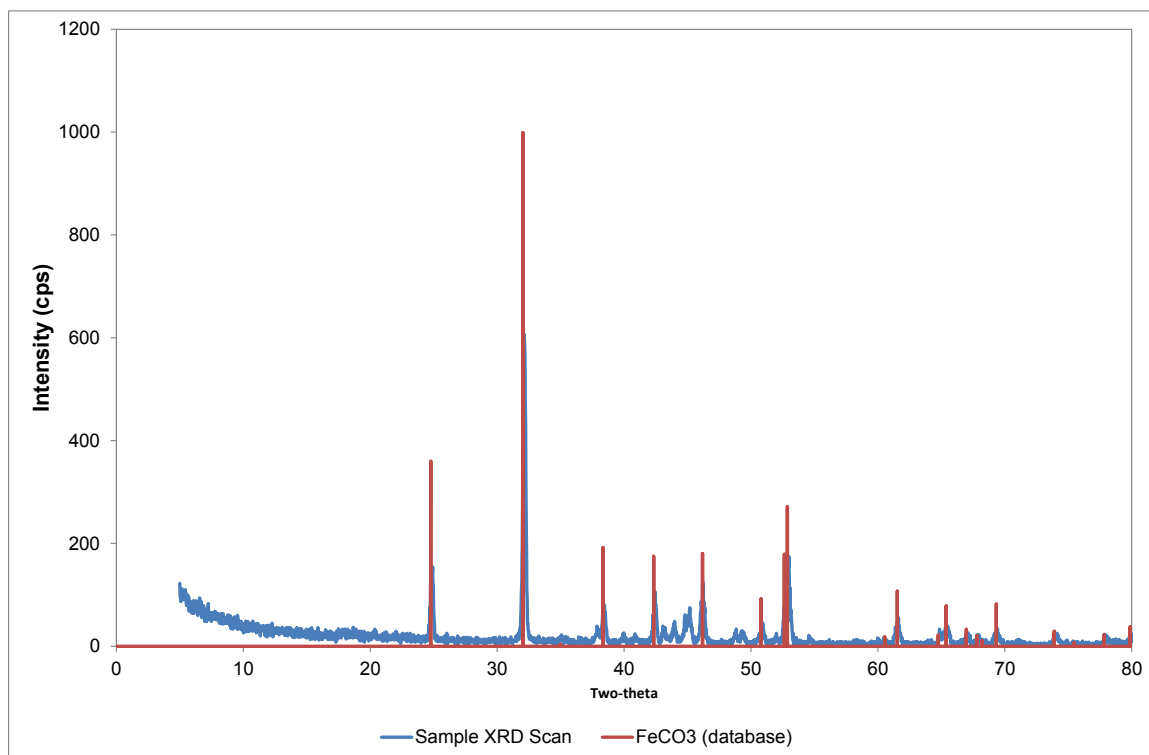


Figure 52: An XRD spectrum for the specimen exposed at $p\text{CO}_2=80$ bar, pH 3.2, and $T=80^\circ\text{C}$.

This also explains why the corrosion rate at 80 bar did not vary with velocity significantly. There was also only slight flow sensitivity at 10 bar. On the other hand, there seemed to be some flow-sensitivity at 40 bar although the factor of increase in corrosion rate with rotational speed did not indicate a fully mass-transfer control. For example, an increase in rotational speed from 100 RPM to 500 RPM only increased the corrosion rate by a factor of 1.13 instead of 3 as predicted by Eisenberg's correlation. Hara also observed a similar trend at 40 bar in which corrosion rate obeyed an

exponential power of 0.83 with respect to velocity, albeit at a much higher temperature (120° C) [138]. It must be noted that Nesic and co-workers observed flow sensitivity that obeyed the power law of 0.7 with respect to velocity at pCO₂ of 1 bar (pH 4.0 and 20° C) [44]. This suggests that while the increase in pCO₂ helped increase corrosion rate by increasing cathodic reduction of H₂CO₃, it also made the chemical step of hydration of dissolved CO₂ that precedes the cathodic reduction more dominant, leading to the reduction in flow-sensitivity. Wang and co-workers also found slight flow sensitivity at pCO₂ of 10 bar and 40 bar (pH 5.0 and 60° C) [67]. This means that at high pCO₂, even a relatively high temperature (50° C) and a low pH (pH 3.0) could not increase the flow-sensitivity of CO₂ corrosion rate.

It is also important to see whether pCO₂ affected the anodic reaction rate. **Figure 53** below shows the effect of pCO₂ on anodic reaction measured at stagnant conditions. The figure indicates that there was only a minimal effect of pCO₂ on the anodic polarization curves. This could probably be due to the fact that the pH was lower than pH 4.2. According to Videm, for pH below 4.2, the anodic dissolution behaviour in CO₂-purged solution was the same as the one in N₂-purged solution [63]. However, no data at higher pH are available to ascertain the slight effect of pCO₂ on anodic reactions. The possible reason, as observed by Linter and Burstein, was that dissolved CO₂ did not affect the anodic reaction within the active dissolution region. Its role only appeared in a passive region by deactivating the film through the formation of a dissolved complex of iron [55].

This may then be true even at elevated $p\text{CO}_2$. This is supported by the work of Nestic and co-workers that found that the reaction order of $p\text{CO}_2$ given in **equation (47)** was zero at $p\text{CO}_2$ higher than 1 bar [45].

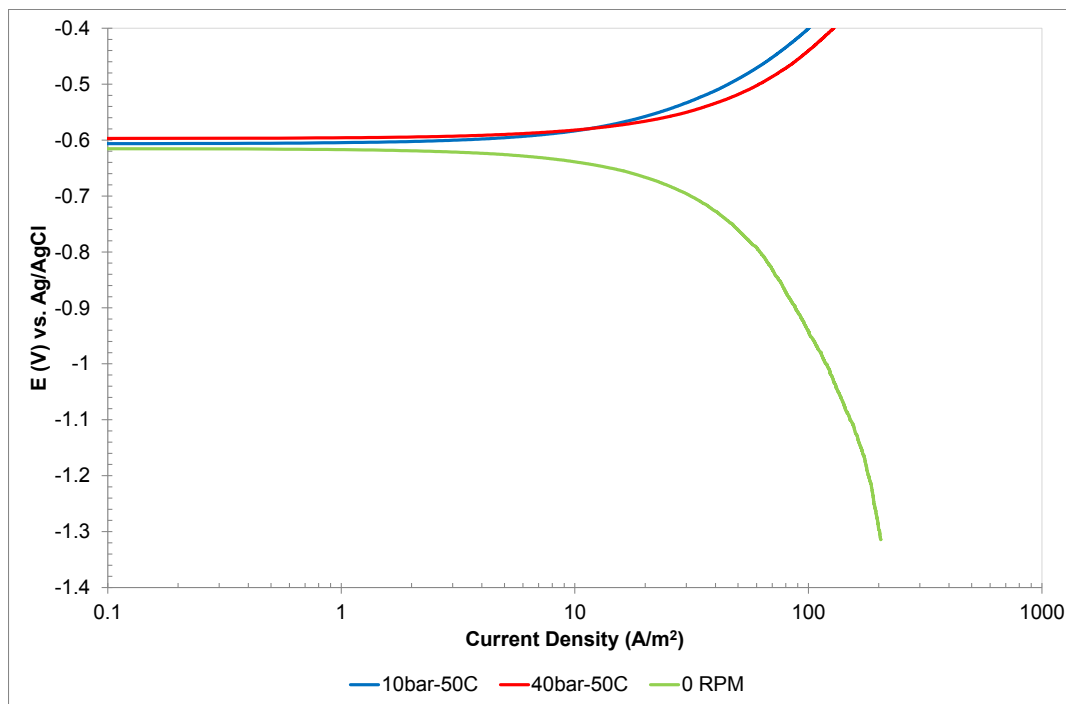


Figure 53: Comparison of anodic curves between $p\text{CO}_2$ of 10 bar and 40 bar, and pH 3.0, and 50° C

5.3.2.3 Surface analysis

Surface analyses using SEM/EDAX indicate that the slight flow-sensitivity observed was mostly due to the corrosion rate being dominated by the slow hydration of dissolved CO_2 rather than the presence of iron carbonate. The corrosion products formed at the test conditions were found to be mainly iron carbide with residual alloying elements, similar to what has been reported in the literature [89]. Except for 80 bar-80° C, the test conditions could be considered as non-layer forming with respect to iron

carbonate as the temperature was below 80° C and the pH was below 5.5. This is shown in **Figure 54** to **Figure 56**:

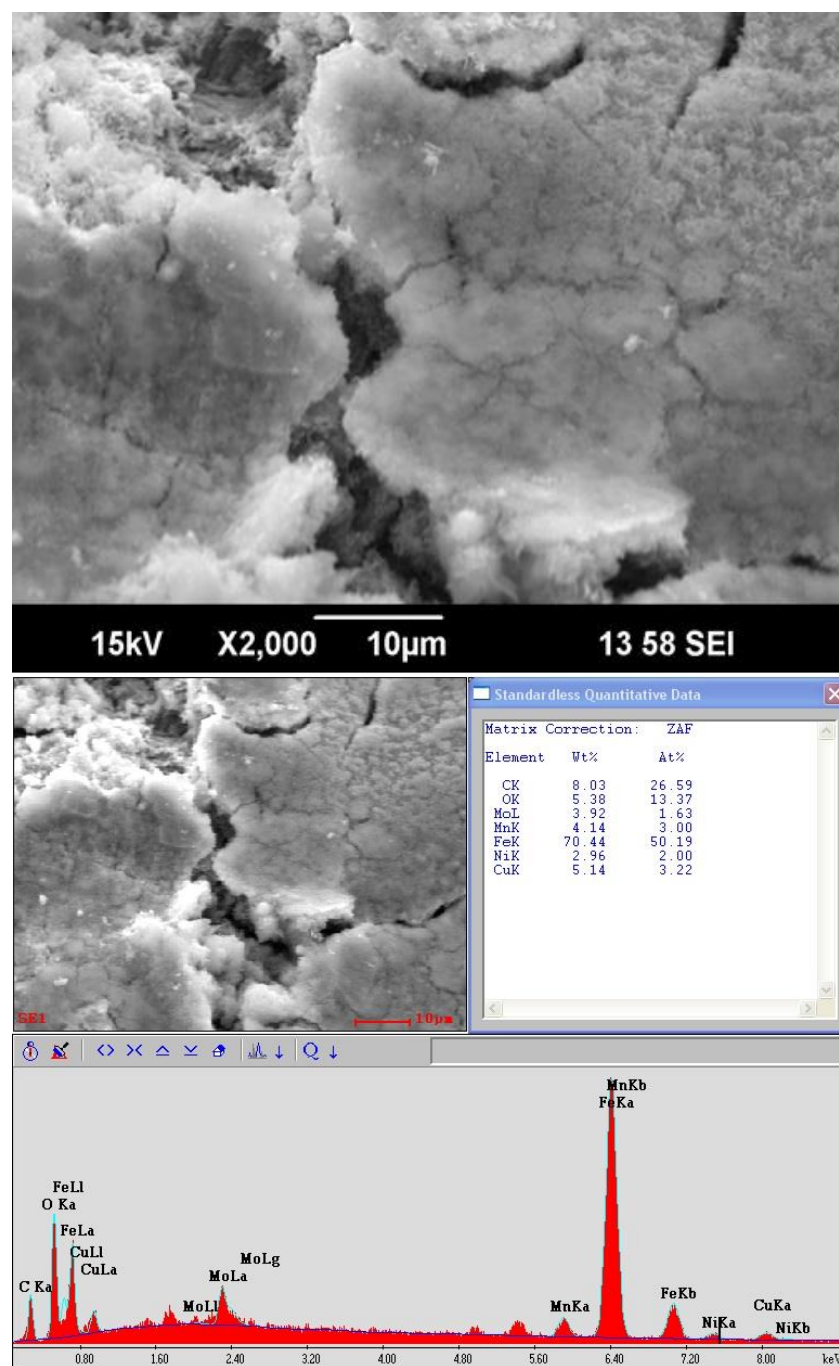


Figure 54: Surface analysis at $p\text{CO}_2=10$ bars, $\text{pH}=3.0$ and $T=25^\circ\text{C}$, suggesting iron carbide layers formed on the substrate

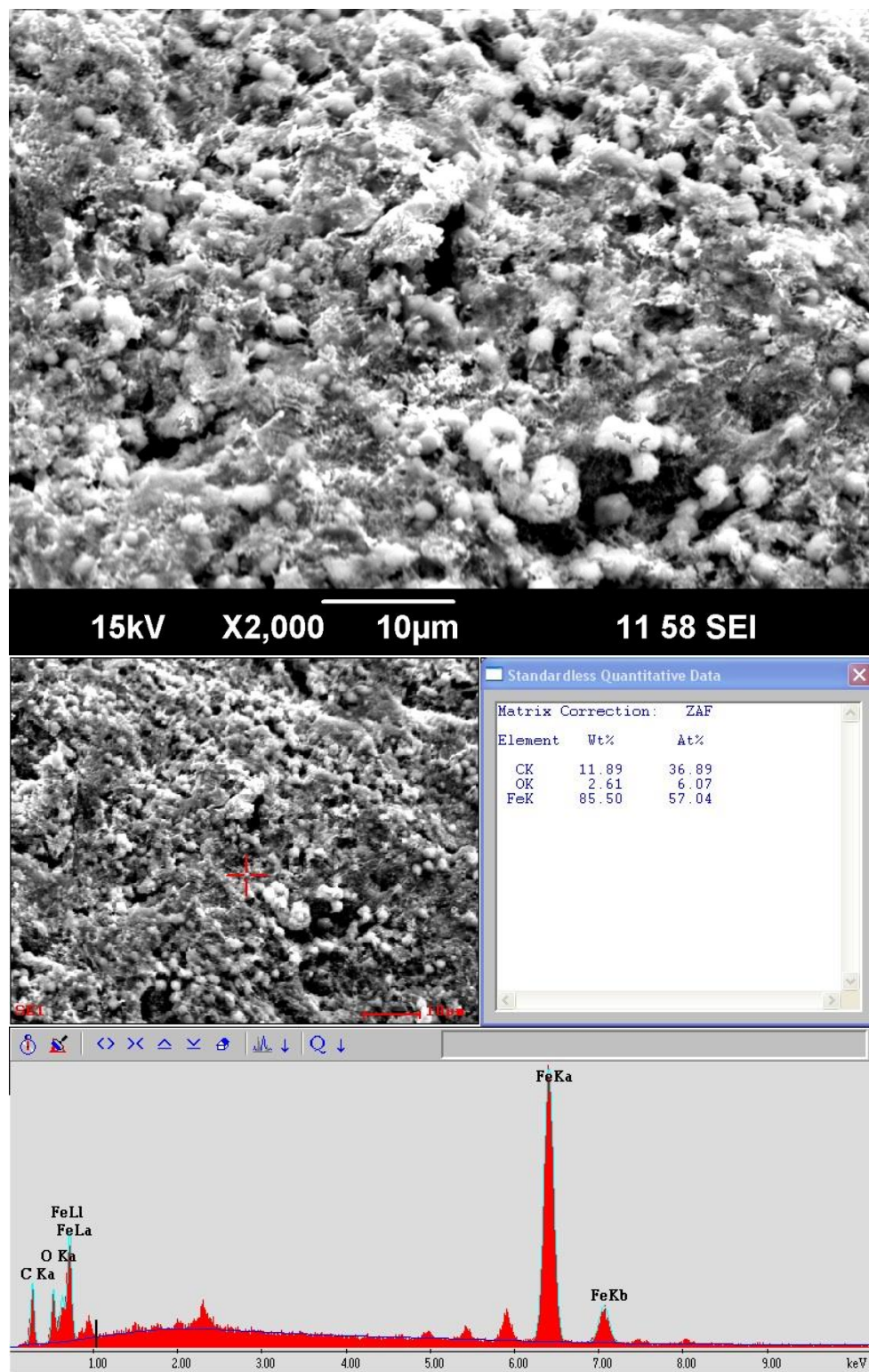


Figure 55: Surface analysis at $p\text{CO}_2=10$ bars, $\text{pH}=4.0$ and $T=25^\circ\text{C}$ suggesting iron carbide layers formed on the substrate

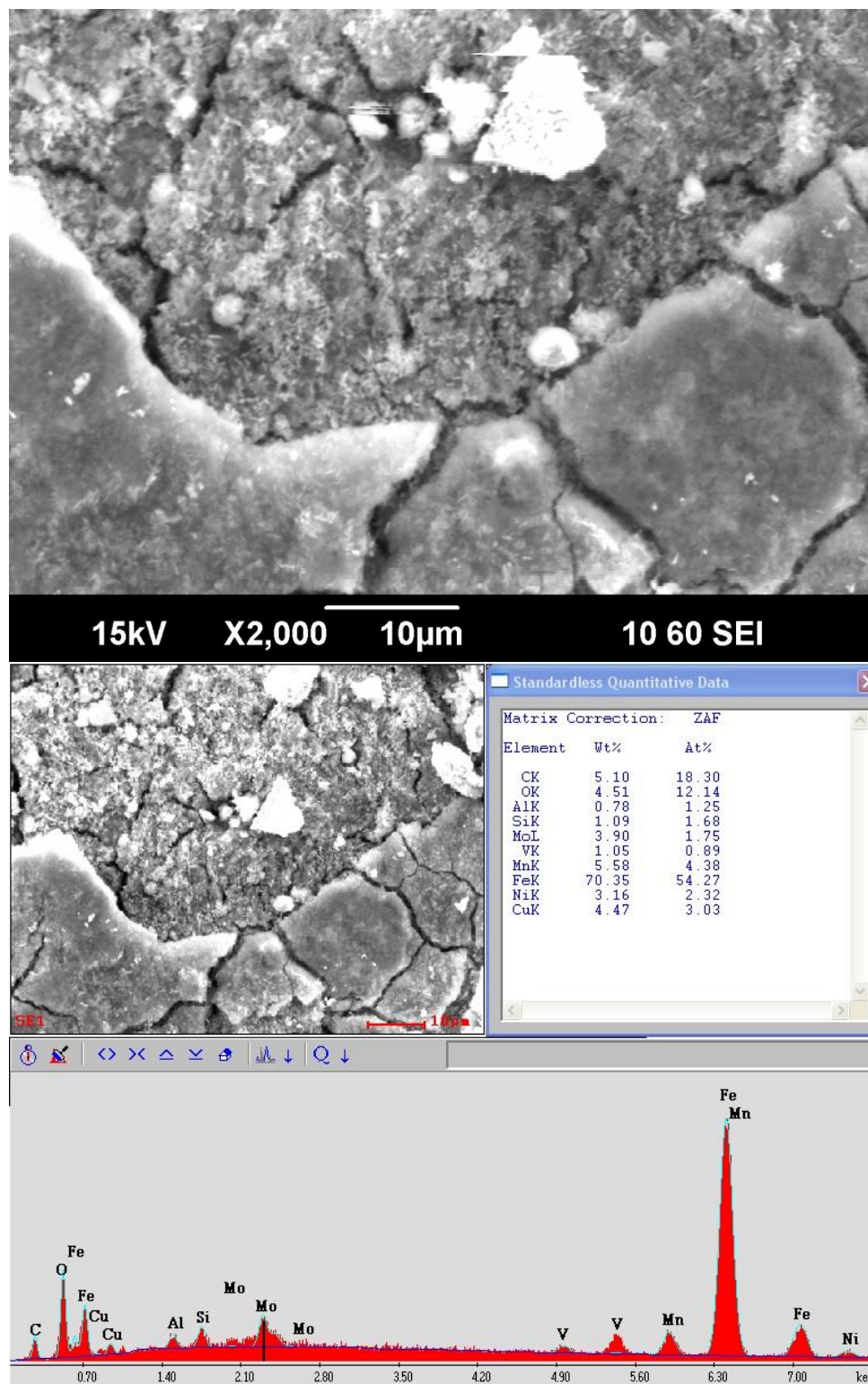


Figure 56: Surface analysis at $p\text{CO}_2=10$ bars, $\text{pH}=5.0$ and $T=50^\circ\text{C}$ suggesting iron carbide layers formed on the substrate.

The iron carbide layers were porous, loosely adherent, and non-protective. The fact that no iron carbonate layers formed on the surface rules out the possibility of low flow sensitivity being due to the formation of protective iron carbonate layers [46, 100]. This also helps explain why the corrosion rate measured by LPR closely correlated with that measured by weight loss and iron count (Fe^{2+} concentration). **Figure 57** shows that the substrate underneath the iron carbide layer only experienced general corrosion:

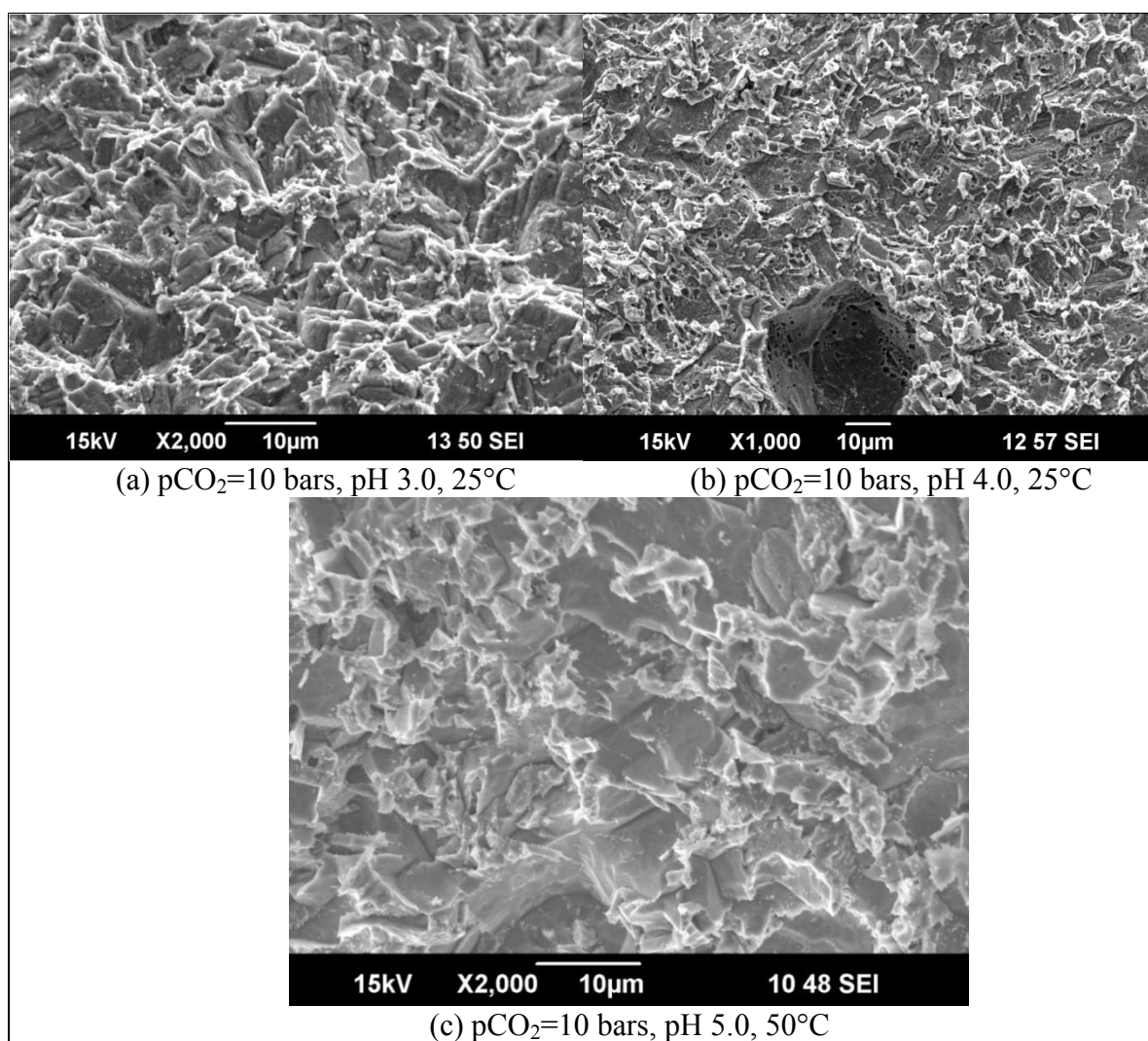


Figure 57: Surface analysis after the removal of iron carbide layers indicating general corrosion. The pit-like defect in (b) might have been due to an inclusion.

It must be noted that the above comparison was for a short-term exposure in which the experiments were run for 24 hours. It is known that coupled with high pH, iron carbonate layers could form at temperatures of 80° C and higher where it possesses a more favorable formation kinetics and a lower solubility. For this reason, a long-term exposure experiment was conducted at 80 bar, 80° C, and pH 3.2 for 100 hours where the specimen was rotated at 1000 RPM to ascertain further whether the protective layers could continue forming at pH 3.2 under a flowing condition. **Figure 51** shown earlier indicates the protective iron carbonate layers formed at the given test condition and helped reduce the corrosion rate significantly. **Figure 58** shows the corresponding corrosion rates and potential over time for the long-term exposure experiment.

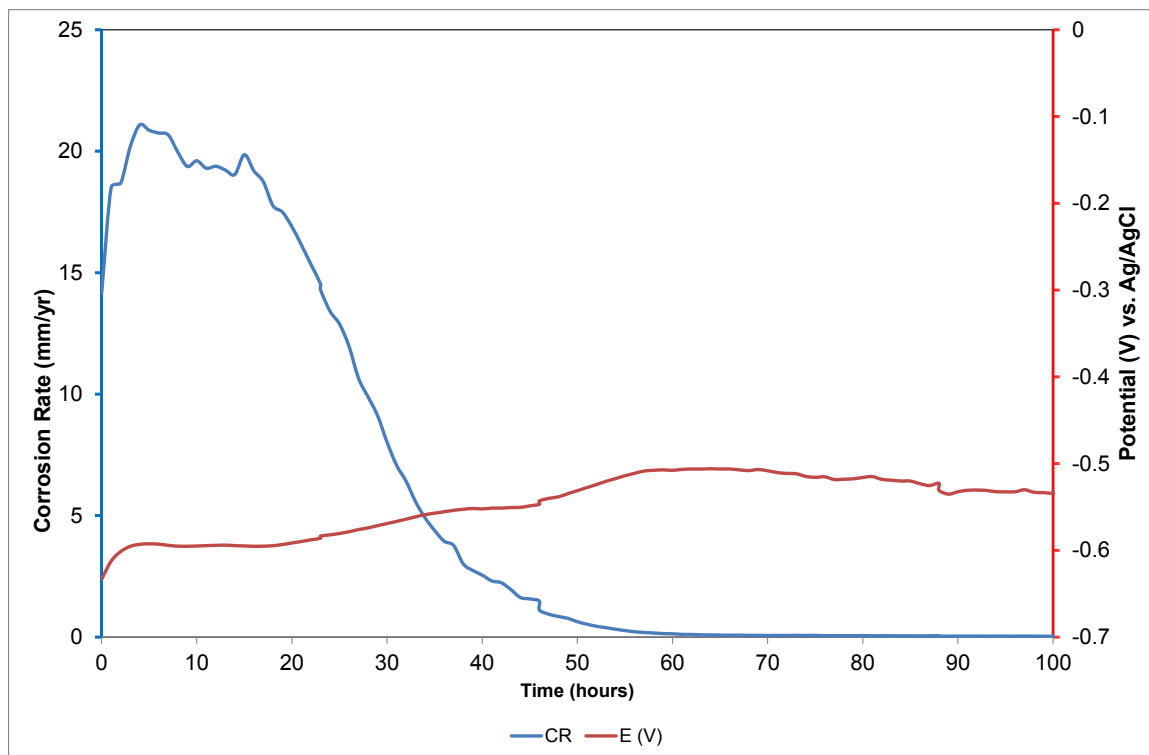


Figure 58: Corrosion rate and corrosion potentials over time with $p\text{CO}_2=80$ bar and at 80° C, pH 3.2, and 1000 RPM

Figure 58 above reveals that the long-term exposure experiment at the specified test condition led to a significant decrease in corrosion rate over time. **Figure 59** reveals that the decrease occurred concurrently with the growth of the protective iron carbonate layers over time:

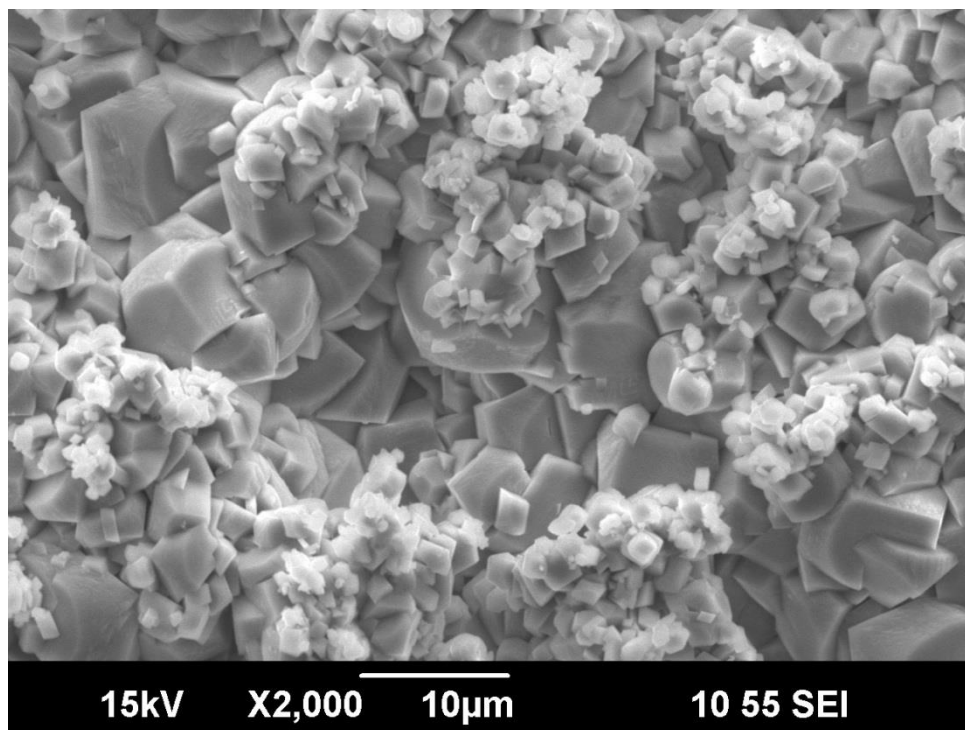


Figure 59: Surface analysis at $p\text{CO}_2=80$ bar, $\text{pH}=3.2$ and $T=80^\circ\text{C}$, showing the increase in the protectiveness of iron carbonate layers formed on the substrate over a long exposure period under a flowing condition

Note that this occurred despite the flowing condition. It is interesting to note that the potential became nobler over time possibly due to the formation of a passive layer from the increase in local pH near the surface [106]. The effect of flow on the formation of protective carbonate layers was verified further using the HPHT TCFC, as is discussed in the next section.

5.4 High pressure-high temperature (HPHT) thin channel flow cell (TCFC)³

The experiments carried out using the HPHT RCE were limited by the maximum velocity it could produce, and the volume of test solution that it could contain. Another important drawback of the RCE is the presence of centrifugal forces that could disrupt the formation of corrosion product layers at the specimen surfaces [110]. A thin-channel flow cell was designed to overcome these problems. In this study, a HPHT TCFC was employed to further verify the flow sensitivity of the RCE results and to establish that the effect of flow on CO₂ corrosion rate was geometry-independent.

5.4.1 *Experimental execution*

5.4.1.1 *Experimental apparatus*

Figure 60 shows a schematic of the HPHT TCFC. It was designed to study the effect of single phase turbulent flow on the corrosion of carbon steel under high CO₂ partial pressure. It could be operated at a maximum pressure of 2000 psi. The main components of the apparatus consisted of a flow channel, a process pressure vessel for the test solution, a heat exchanger, and a gear pump housed in a pressure vessel. The dimensions of the flow channel were the same as for the low pressure TCFC which ensured that the hydrodynamic and mass boundary layers over the specimen were fully-developed (see §5.2.1.1). The HPHT TCFC reaches turbulent flow at $Re > 2800$ [161]. Moreover, the channel could accommodate three different probes simultaneously and was equipped with heaters and thermocouples to reach the desired test temperature. As for the process vessel, it had a volume of 40 liters, but the total solution for the whole TCFC system was 70 liters. In the experiments, the vessel was not completely filled with the

³ Portions of the content of this section were published in the co-authored paper of reference [167]

test solution so as to allow for a “gas cap” that maintained $p\text{CO}_2$ on the top of the process vessel. The CO_2 can be either gas, liquid or supercritical depending on the conditions (temperature/pressure). The 40-L process vessel was equipped with a heater to bring the test solution to the desired temperature up to 95°C . To accelerate CO_2 saturation, a stainless steel sparger was installed inside the bottom of the vessel. The vessel also had three glass sapphire windows that allowed for visual observation.

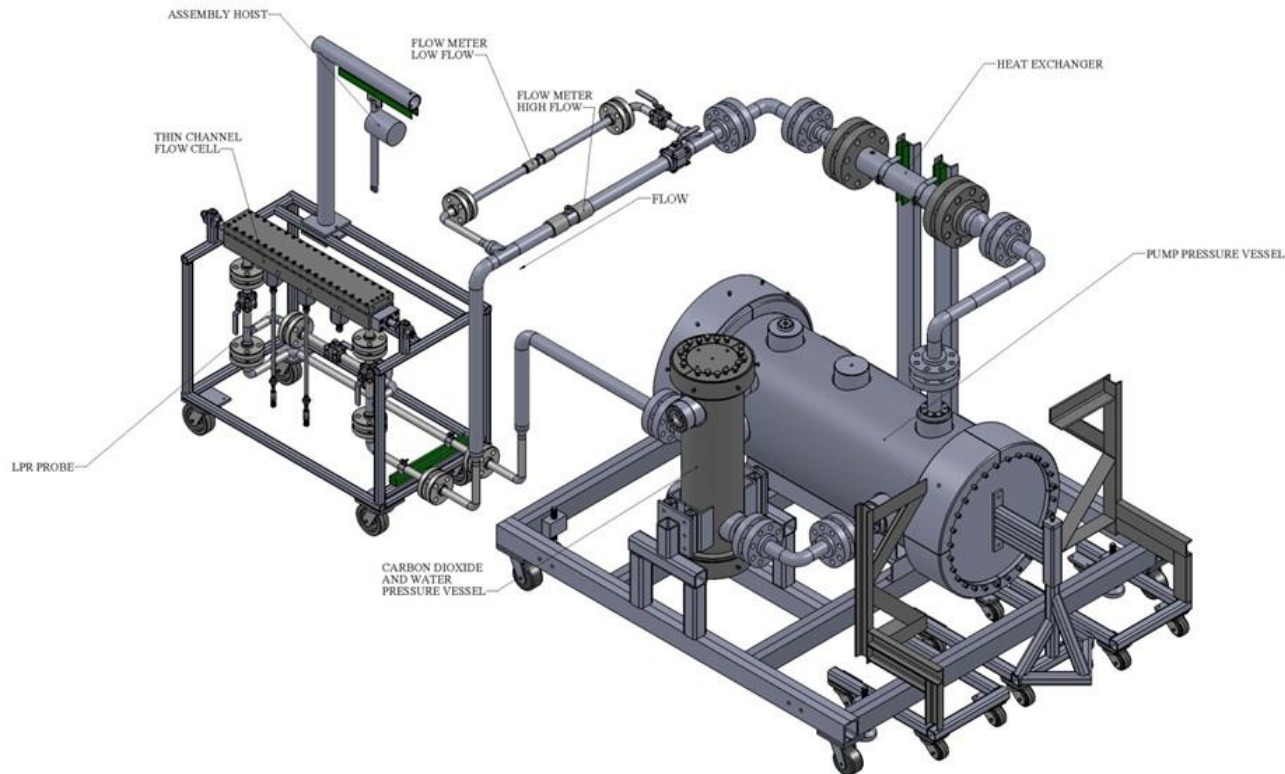


Figure 60: High pressure and high temperature thin channel flow cell.

The liquid pump was designed to deliver 50 gallons per minute (GPM) of test solution. The velocity range that it could produce was 0.23 m/s to 15 m/s. The pump only allowed the circulation of the aqueous phase that was saturated with CO_2 , but not the

CO₂ phase alone. A heat exchanger was used to bring down the solution temperature due to it being increased as the pumping operated. To achieve high pressure, the apparatus was equipped with a set of booster pumps that used solenoid valves to permit automatic pressure control. This was important as the pressure inside the pump vessel had to be adjusted automatically so that the differential pressure at the gear pump seal was maintained below 150 psi to avoid leakage into the vessel pump while the gear pump was circulating the test solution. The TCFC was equipped with a bypass piping system that allowed the water chemistry to be adjusted prior to exposing specimens to the test solution. The materials of the wetted parts were made of 316-stainless steel. As for safety, the apparatus was equipped with the following safety features: rupture discs, an automatic over temperature shut-off, and an over-pressure shut-off.

5.4.1.2 Experimental parameters

To develop the test matrix, it was first necessary to determine the equivalent velocity in the TCFC. To do this, the corrosion rate in both systems was assumed to be under purely mass transfer control [110, 162, 163]. This allowed the mass transfer coefficients of the RCE and TCFC to be equated. For RCE, solving Eisenberg's mass transfer correlation (Sh_c) given in **equation (70)** for the mass transfer coefficient (K_c) yields [116]:

$$K_c = 0.0791 Re_c^{0.7} Sc^{0.356} \frac{D}{d_c} \quad (90)$$

where:

$Sh_c = \frac{k_c d_c}{D}$ is the Sherwood number for the RCE

k_c is the mass transfer coefficient for the RCE in $\left(\frac{m}{s}\right)$

d_c is the diameter of the cylindrical specimen in (m)

D is the diffusion coefficient in $\left(\frac{m^2}{s}\right)$

$Re_c = \frac{V_c d_c}{\nu}$ is the Reynolds number for the RCE

V_c is the peripheral velocity of the cylindrical specimen in $\left(\frac{m}{s}\right)$

ν is the kinematic viscosity of water in $\left(\frac{m^2}{s}\right)$

$Sc = \frac{\nu}{D}$ is the Schmidt number

As for TCFC, solving the Sleicher and Rouse's mass transfer correlation (Sh_T) given in **equation (80)** (see §5.2.2) for the mass transfer coefficient (K_T) yields [151]:

$$K_T = (5 + 0.015 Re_T^a Sc^b) \frac{D}{d_H} \quad (91)$$

where:

$Sh_T = \frac{k_T h}{D}$ is the Sherwood number for the the TCFC

k_T is the mass transfer coefficient for the TCFC in $\left(\frac{m}{s}\right)$

h is the height of the TCFC

$Re_T = \frac{V_T h}{\nu}$ is the Reynolds number for the TCFC

V_T is the linear velocity of the liquid in the TCFC in $\left(\frac{m}{s}\right)$

a, b are empirical constants defined by **equations (81)** and **(82)**

Equating **equations (90)** and **(91)** and solving for TCFC velocity yield:

$$V_T = \frac{v}{\left(0.015 \frac{1}{a} Sc \frac{b}{h^a}\right)} \left(0.0791 Re_c^{0.7} Sc^{0.356} \frac{d_H}{d_C}\right)^{\frac{1}{a}} \quad (92)$$

Equation (92) thus gives the corresponding TCFC equivalent liquid velocities at 25° C, 50° C, and 80° C as follows in **Table 10**:

Table 10: The corresponding TCFC linear liquid velocity calculated from the RCE peripheral velocity

	RCE Peripheral Velocity / (m/s)	TCFC Linear Velocity / (m/s)
1	0	0
2	0.1	0.2
3	0.5	0.8
4	1.0	1.5
5	-	8

The TCFC linear liquid velocities at the three temperatures were set at the same values given in the above table because their differences were less than 10 percent while the pump could not produce stable volumetric flow rates. Additionally, the experiments excluded the second row of the equivalent velocities since the lowest volumetric flow

rate of the pump was 1.1 GPM (0.23 m/s) and the Reynolds number were less than 2800 as shown in **Table 11**:

Table 11: The corresponding Reynolds numbers for the TCFC linear liquid velocities

Temperature (° C)	ρ of water (kg/m ³)	μ of water (kg/m.s)	Reynolds numbers		
			0.2 m/s	0.8 m/s	1.5 m/s
25	1000	0.000891	750	3200	5700
50	987	0.000559	980	4200	7600
80	972	0.000357	1400	6300	11300

The experimental conditions at which the above TCFC linear liquid velocities were applied are shown in **Table 12**:

Table 12: The key experimental conditions in the TCFC experiments

CO ₂ Partial Pressure (bar)	Temperature	
	25° C	80° C
10	Gaseous CO ₂ , water pH 3.4	
80	Liquid CO ₂ , water pH 3.0	Supercritical CO ₂ , water pH 3.2

5.4.1.3 Experimental methods

a) Test solution

The test solution used in HPHT TCFC experiments was a 1wt% NaCl electrolyte prepared by dissolving 600 g of NaCl in de-ionized water and making up the total volume of the solution to 60 liters. Once transferred into the TCFC system, the test solution was circulated at a low pressure and purged with CO₂ gas until the concentration of dissolved oxygen as measured by a colorimetric method using CHEMets[®] ampoules reached a low level (normally less than 5 ppb).

b) Test specimens

Two types of probes were used to determine the corrosion rate: linear polarization resistance (LPR) and weight loss probes. As shown by **Figure 61**, the LPR probe consisted of three concentric steel elements electrically separated by epoxy: the center element and the outer ring were made out of 316 stainless steel while the middle ring was made of API 5L X-65 carbon steel machined from a retrieved line pipe. The center element served as a reference electrode while the outer ring served as the counter electrode. The total exposed surface area of the carbon steel ring was 0.95 cm².

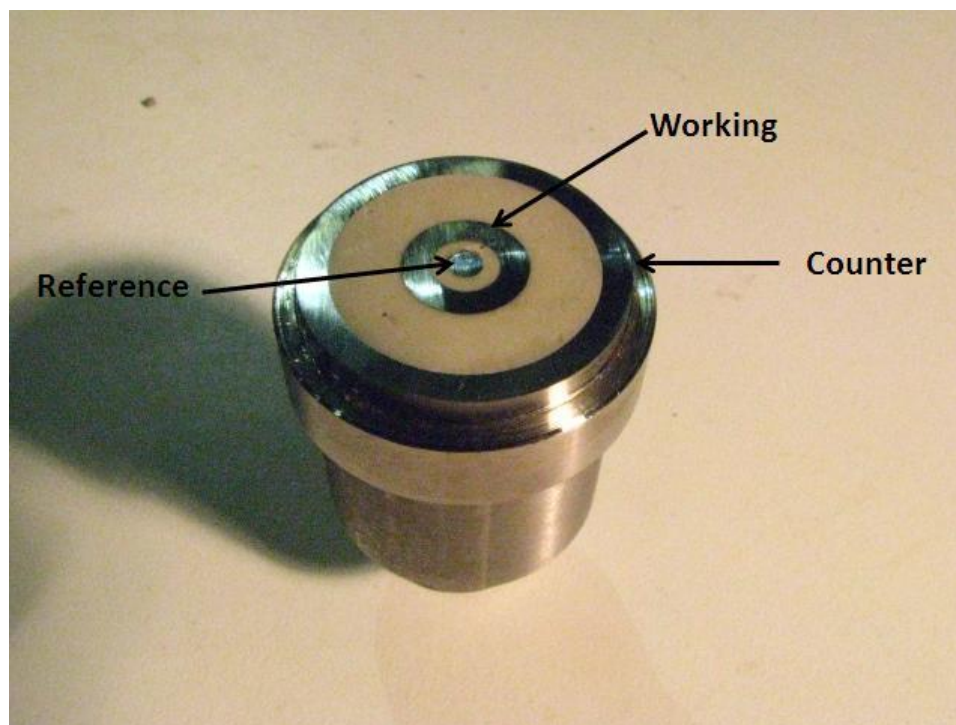


Figure 61: The three-probe LPR probe used to measure corrosion rates *in-situ*

Figure 62 shows the weight loss specimen used to measure the time-averaged corrosion rate and for validation with LPR measurements. To avoid any electrical contact that could lead to galvanic corrosion between the specimen and the probe holder, the bottom and the side of the specimen were coated with Xylan paint. The coated specimen was baked at 300° F for 30 minutes and then recoated since it was found that a single coat could not effectively insulate the specimen from the holder. Once installed on the probe holder, a check to ensure no electrical contact between the probe and holder was made. Prior to exposure, the LPR and weight loss specimens were subject to the same surface preparation as in RCE experiments. Their chemical composition is given in **Table 6** (see §5.3.1.3).

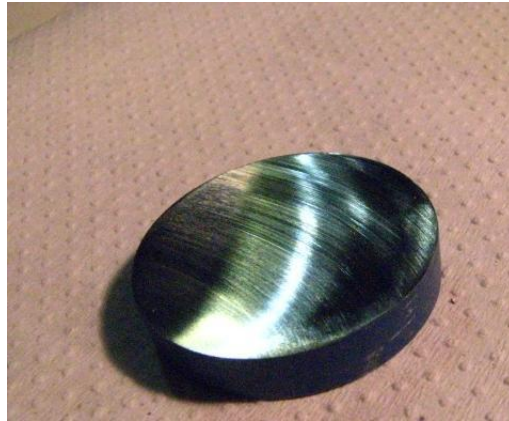


Figure 62: The weight loss coupon used in the experiment.

c) Test procedure

Once the LPR and weight loss coupons were flush-mounted inside the flow channel, the entire TCFC system was purged with N_2 at 100 psi five times. This was to remove any residual water and help accelerate the de-aeration process. In the final purge, the entire system was pressurized with N_2 to the desired pressure. The inlet and outlet valves to the flow channel were subsequently closed while N_2 was discharged from the rest of the system. This was to protect the specimens from corrosion and to avoid a sudden burst in pressure when the test solution was introduced into the flow channel section.

Sixty liters of test solution was then pumped into the process vessel and circulated around the TCFC system so as to remove any bubbles entrained in the solution along the piping. The test solution was purged with CO_2 with the outlet valve of the pressure vessel being slightly opened. The dissolved oxygen level in the test solution was periodically checked using CHEMets[®] ampoules until the concentration of dissolved oxygen reached a low level. Once this was achieved, the test solution was heated to

about 10° C lower than the desired temperature. This was to avoid over-temperature occurring when the pressure was later increased. Once the pressure of the entire TCFC system was increased to the desired CO₂ partial pressure, and the temperature reached the desired value, the test solution was purged with CO₂ until it reached the autogeneous pH given in **Table 12**. Achievement of autogeneous pH, the natural self-generating pH for carbonic acid in the test electrolyte, indicated that the test solution had been fully saturated with dissolved CO₂. The test solution was then introduced into the flow section by initially opening the outlet valve and then the inlet valve so as to avoid back pressure. Corrosion measurements were then started. The procedure for electrochemical measurements was similar to the one described for the HPHT RCE except that there was no potentiodynamic sweep measurement carried out (see § 5.3.1.3). Measurement was carried out twice at each velocity which was varied first in ascending order (0 m/s to 8 m/s) and then in descending order (8 m/s to 0 m/s). It must be noted that since an attempt to simulate stagnant conditions at 80° C led to erratic LPR readings which might have been due to the formation of bubbles in the flow channel, a small flow rate was applied. As for weight loss measurement, the specimen was exposed for at least 24 hours at the equivalent velocity of 8 m/s. At the end of the experiment, the test solution was sampled and analyzed using a spectrometer for determination of ferrous ion concentration (iron count). The corrosion rates measured with weight loss and iron count were cross-validated against the corrosion rate from LPR.

5.4.2 Results and discussion

Figure 63 shows the comparison of corrosion rates obtained by LPR, weight loss, and iron count measurements:

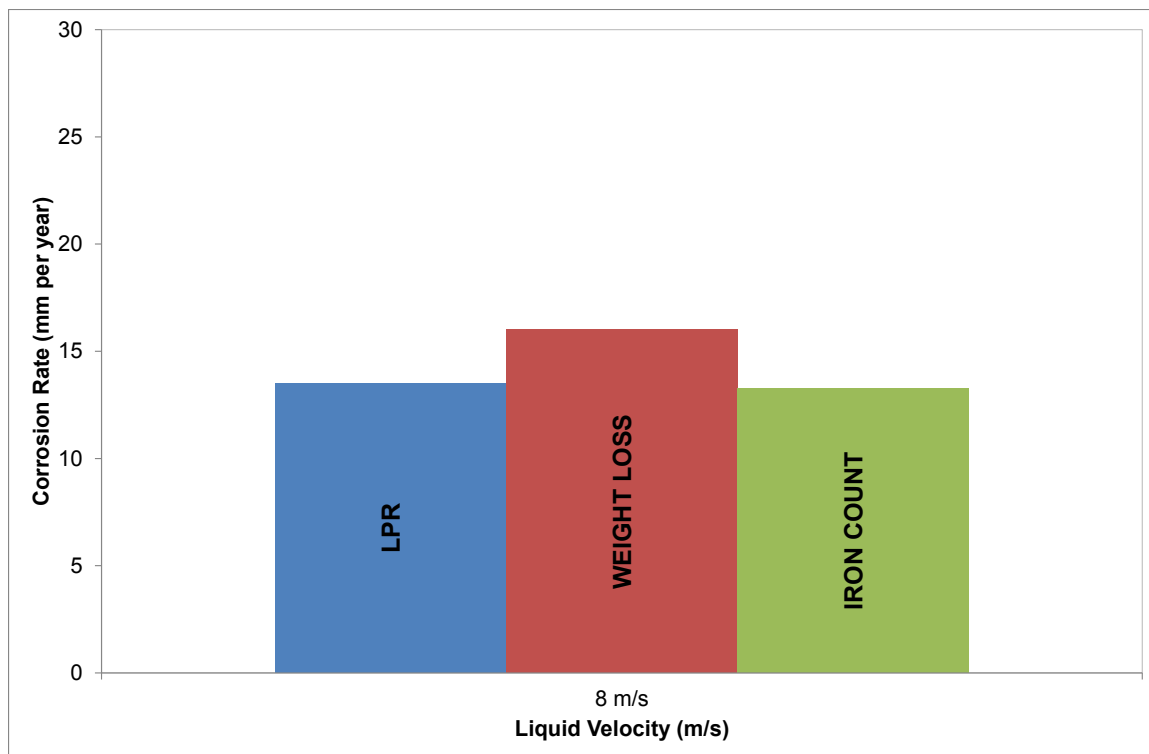


Figure 63: Data cross validation for $p\text{CO}_2=10$ bar; $T=25^\circ\text{C}$; $\text{pH}=3.4$ at 8 m/s.

The figure indicates that the corrosion rates closely correlated with each other. This proves that the Stern-Geary coefficient of 0.026 V used earlier to calculate corrosion rate from LPR measurement in the RCE experiment was also applicable for TCFC experiments. The possible reason for the good correlation was that the test condition was non-layer forming. The value again suggests that the corrosion rate was under mass-transfer control. **Figure 64** to **Figure 66** show the comparison of corrosion rates as a function of velocity obtained from LPR measurement between the RCE and TCFC on the

basis of equivalent velocity. The corrosion rates were calculated using the Stern-Geary coefficient of 0.026 V. It should be noted that the corrosion rate at 8 m/s in **Figure 66** was unavailable as the TCFC system leaked when the tests were attempted twice at this more extreme condition.

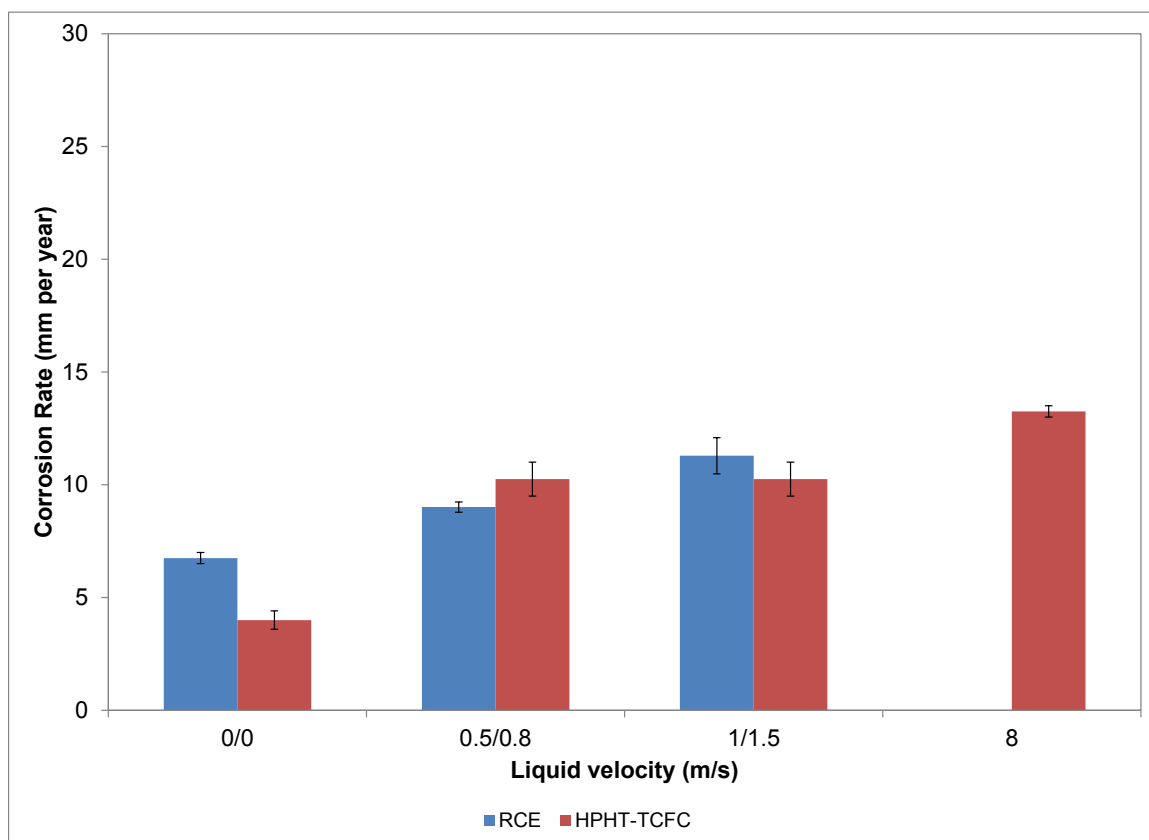


Figure 64: Comparison of the corrosion rates from LPR measurement as a function of liquid velocity between a Rotating Cylinder Electrode (RCE) and a Thin Channel Flow Cell (TCFC) at $p\text{CO}_2$ of 10 bar, 25°C , and pH 3.4 on the basis of equivalent velocity.

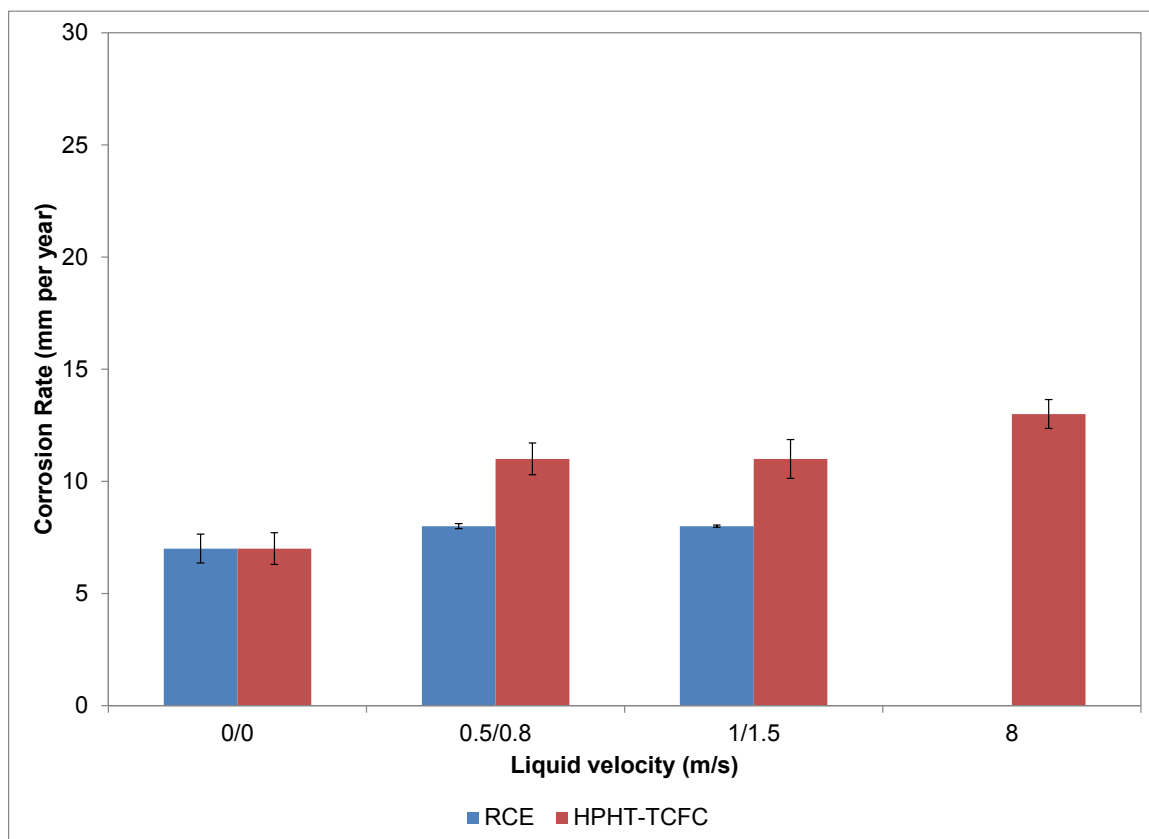


Figure 65: Comparison of the corrosion rates from LPR measurement as a function of liquid velocity between a Rotating Cylinder Electrode (RCE) and a Thin Channel Flow Cell (TCFC) at $p\text{CO}_2$ of 80 bar, 25°C , and pH 3.0 on the basis of equivalent velocity.

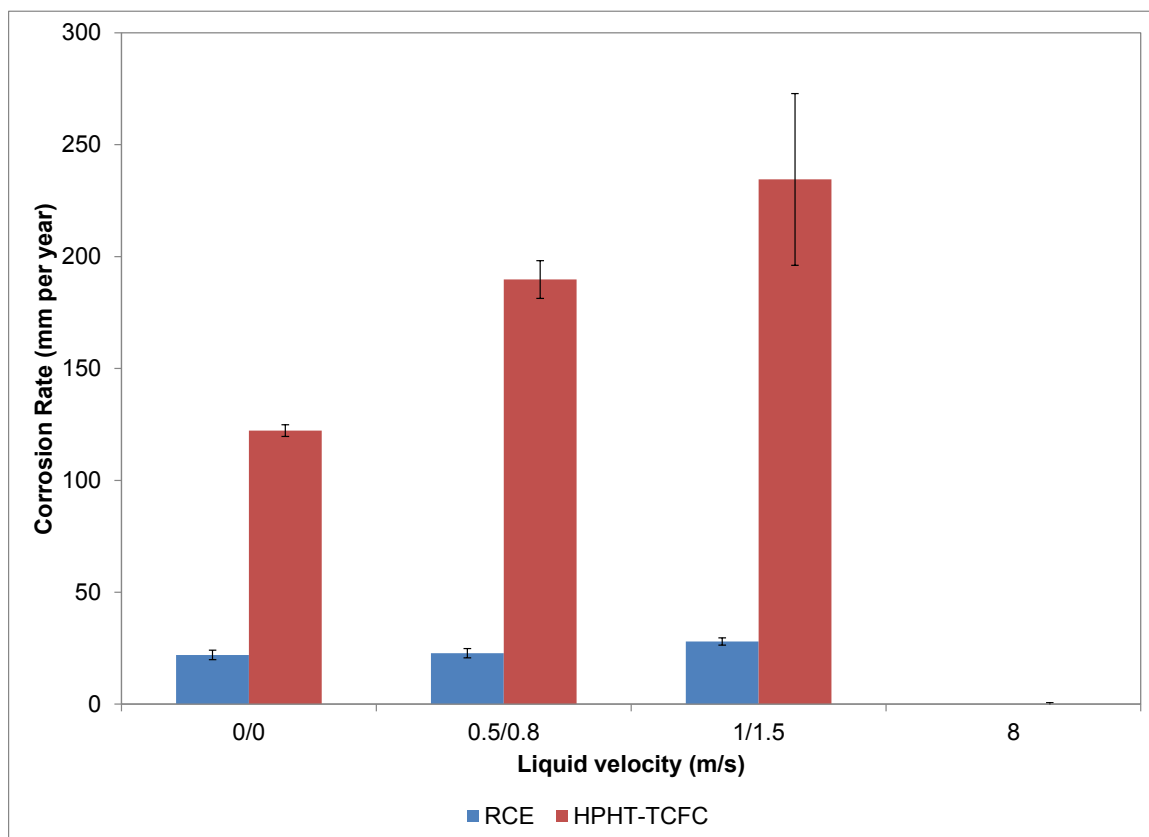


Figure 66: Comparison of the corrosion rates from LPR measurement as a function of liquid velocity between a Rotating Cylinder Electrode (RCE) and a Thin Channel Flow Cell (TCFC) at $p\text{CO}_2$ of 80 bar, 80°C , and pH 3.2 on the basis of equivalent velocity.

The above figures reveal that the corrosion rates measured at high concentrations of carbonic species were very high, especially at 80°C in which the corrosion rate in the TCFC was about one order of magnitude higher than that in the RCE. At 25°C , the corrosion rates in both RCE and TCFC did not vary significantly with liquid velocity even at 80 bar. In fact, their corrosion rates were close to each other. The results then prove the assumption that CO_2 corrosion rate is geometry-independent when the test conditions, including the mass transfer rate, are similar [110, 163]. It is interesting to note that the corrosion rates in both RCE and TCFC at 25°C were only marginally flow-sensitive; this was even true at 8 m/s for the TCFC. This finding then supports the earlier

assumption that the corrosion rate was largely controlled by the reduction of carbonic acid and its subsequent replenishment by hydration of dissolved CO_2 being the rate determining step [67].

However, at 80°C , the corrosion rates in both the RCE and TCFC differed significantly. In fact, in contrast to in the RCE, the corrosion rate in the TCFC exhibited a degree of flow-sensitivity. To determine the reasons for the different corrosion behavior at the two temperatures in the two flow geometries, surface analyses on the corrosion product layers were performed. **Figure 67** and **Figure 68** show that at 25°C , the corrosion product layers in the TCFC consisted mainly of porous cementite with some minor alloying elements. This was similar to what was observed in the earlier RCE experiments (see §5.3.2.3).

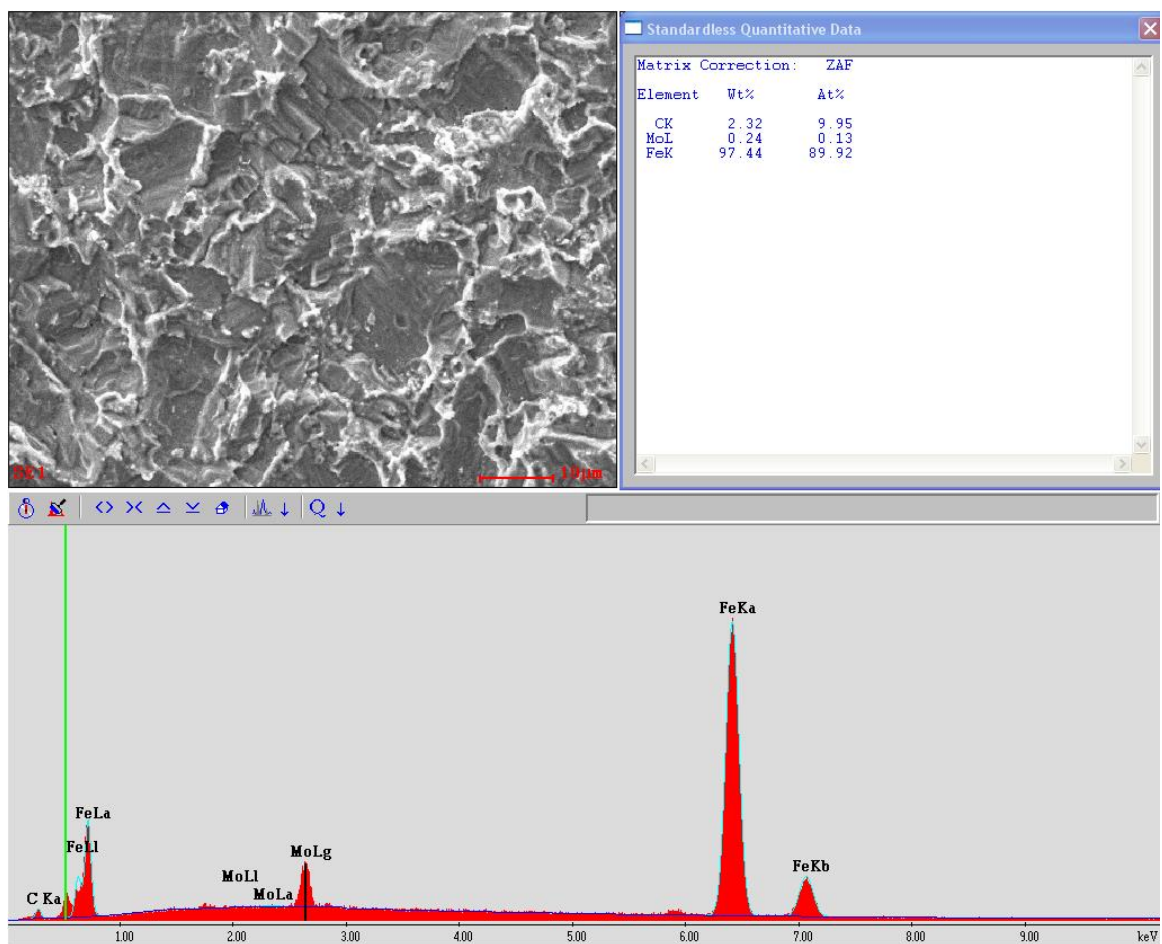


Figure 67: A surface image and elemental analysis of the corrosion product layer obtained using EDX, suggesting the presence of cementite (iron carbide) with some minor alloying elements; steel sample exposed to water saturated with $p\text{CO}_2=10$ bar, at 25°C , and pH 3.4 for 24 h.

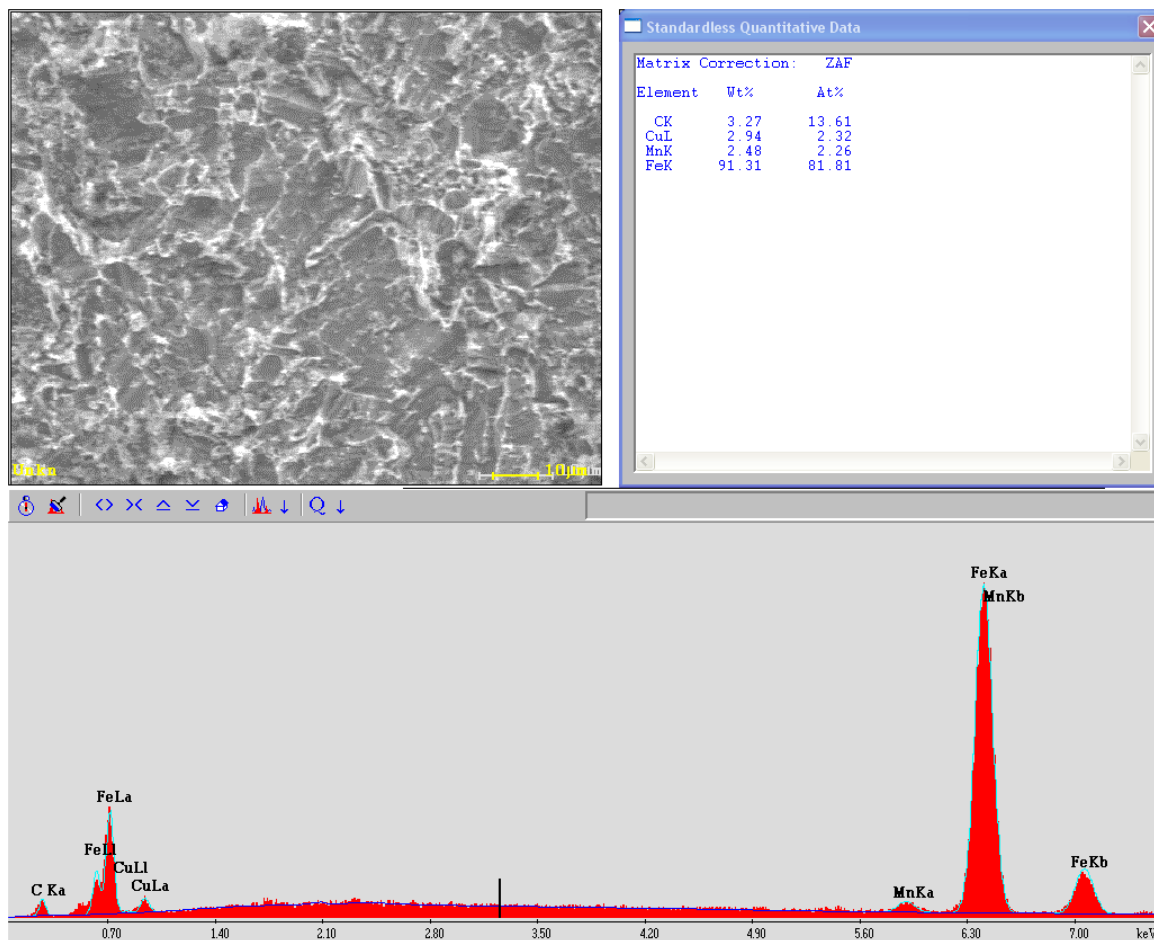


Figure 68: A surface image and elemental analysis of the corrosion product layer obtained using EDX, suggesting the presence of cementite (iron carbide) with some minor alloying elements; steel sample exposed to water saturated with $p\text{CO}_2=80$ bar, at 25°C , and $\text{pH } 3.0$ for 24 h.

On the other hand, as shown by **Figure 69** below, the surface analysis on the specimen exposed at 80°C reveals that the corrosion product layers consisted of cementite mixed with some iron carbonate crystals. This is opposite to what was observed in the RCE at the same test conditions as shown in **Figure 51** and **Figure 59** in which protective iron carbonate layers easily formed.

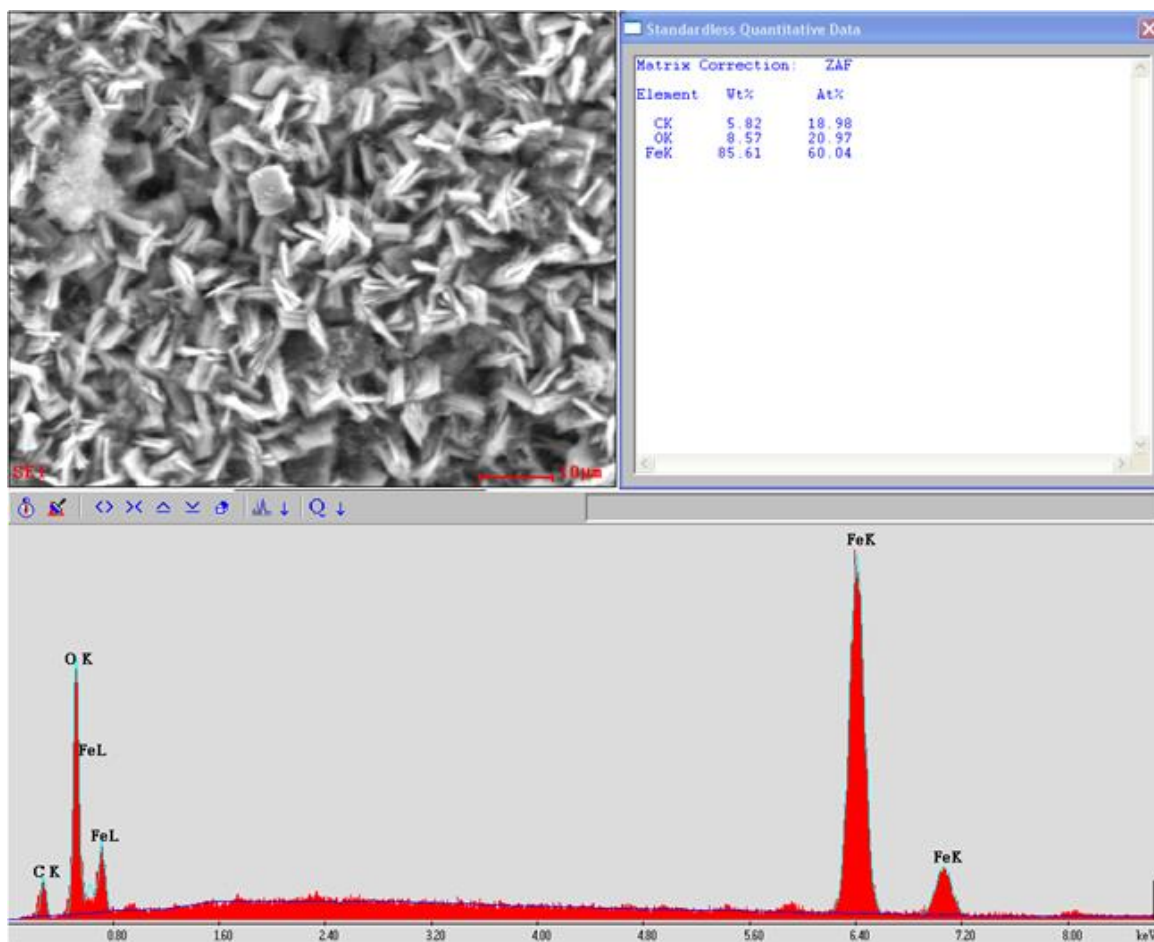


Figure 69: A surface image and elemental analysis of the corrosion product layer obtained using EDX, suggesting the presence of cementite (iron carbide) and siderite (iron carbonate); steel sample exposed to water saturated with $p\text{CO}_2=80$ bar, at 80°C , and pH 3.2 for 24 h.

The difference in corrosion rates at 80°C between TCFC and RCE as shown in **Figure 66** could most probably due to the difference in water chemistry. This was based on the difference in pH and iron count in the two flow geometries. It was observed that while the pH of the test solution in TCFC basically did not change from its autogenous pH 3.2 in the course of the experiment, the pH in the RCE changed from 3.2 to 3.6 for the same period of exposure due to the consumption of hydrogen ions release of ferrous ions by corrosion. This was further evidenced from the iron count data at the end of the

experiment: the TCFC test solution recorded only 13 ppm of ferrous ion concentration while the RCE test solution recorded 330 ppm. The difference in the water chemistry arose from the difference in the volume of test solution in both flow geometries. While the test solution in TCFC was 60 liters, in RCE, the test solution was only 5 liters. This means while the electrolyte volume to corroding surface ratio in TCFC was 600 mL/mm², the ratio in RCE was 3 mL/mm². Consequently, at 80° C in which the corrosion rate was significantly higher as shown by **Figure 66**, the presence of higher concentration of ferrous ions that resulted in the increase in pH in the RCE induced the formation of relatively protective iron carbonate layers, especially at a longer exposure. The drawback with RCE was also observed by Harrop and co-workers who noted a large difference in corrosion rates between RCE and flow loop [164]. They observed a significant decrease in corrosion rate in the RCE while the corrosion rate in the flow loop remained relatively high over the same period of time [164].

The reason the corrosion rates in the TCFC and RCE correlated at 25° C was that at this low temperature, the solubility of iron carbonate was high and the kinetic of film growth was slow. As such, no formation of protective iron carbonate was possible. That was why the specimens in both flow geometries produced the same type of corrosion product layer, namely iron carbide. On the other hand, at 80° C, the solubility of iron carbonate was low and the kinetic of film growth was high. The limited volume of RCE test solution allowed for the increase in saturation as evidenced from high concentration of iron count and pH that led to the formation of iron carbonate. In contrast, the large volume of the TCFC test solution prevented a significant increase in super saturation. In

the absence of iron carbonate layers, the increase in temperature in the TCFC enhanced the charge-transfer rates, making the corrosion rate significantly flow-sensitive. This supports the finding by Eriksrud [52]. Nevertheless, the corrosion rate could not be considered to be purely due to mass transfer control since an approximately twofold increase in linear velocity (0.8 m/s to 1.5 m/s) only led to an increase in corrosion rate by a factor of 1.3 instead of 1.8 as predicted by Sleicher and Rouse's mass transfer correlation. This was probably because the cathodic reduction current was dominated by the direct reduction of carbonic acid which is limited by the slow hydration of dissolved CO_2 . Notwithstanding this fact, when the corrosion product layers were removed, the substrates for all the three cases only experienced uniform corrosion as shown by **Figure 70** to **Figure 72**:

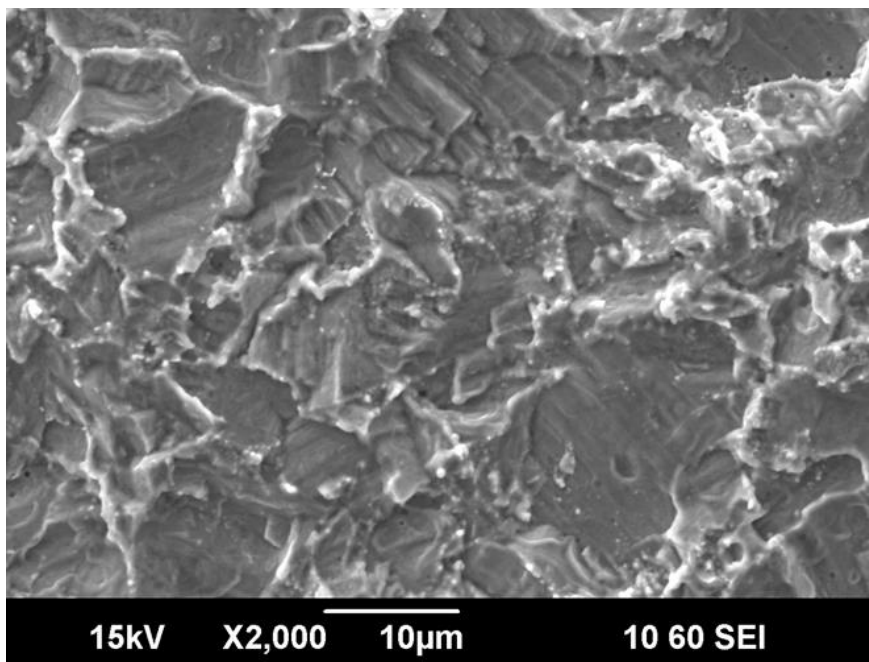


Figure 70: Surface image after the removal of corrosion product layer indicating general corrosion. Steel specimen was exposed to CO_2 -saturated solution with $p\text{CO}_2=10\text{bar}$, at pH3.4 and 25°C .

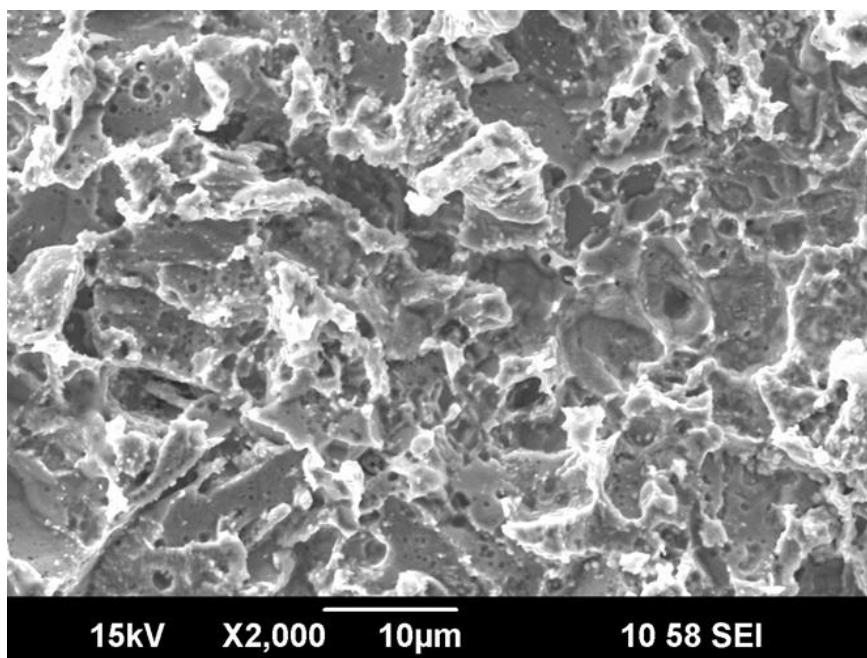


Figure 71: Surface image after the removal of corrosion product layer indicating general corrosion. Steel specimen was exposed to CO₂-saturated solution with pCO₂=80 bar, at pH3.0 and 25° C.

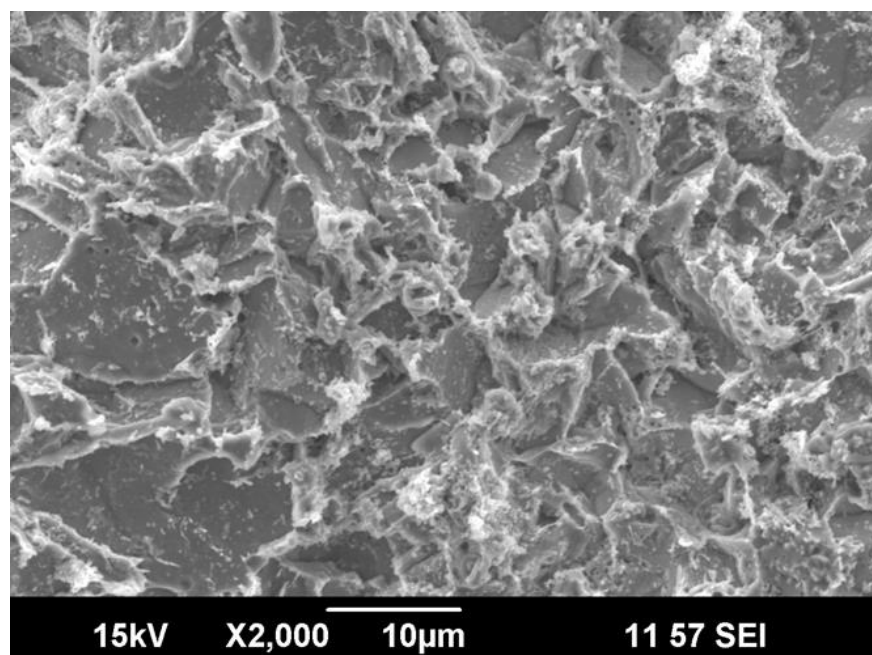


Figure 72: Surface image after the removal of corrosion product layer indicating general corrosion. Steel specimen was exposed to CO₂-saturated solution with pCO₂=80 bar, at pH3.0 and 80° C.

Thus, the comparison of results from the RCE and TCFC indicates that the TCFC produced a more realistic corrosion rate due to its larger volume that could help maintain water chemistry. RCE seems to be more suitable when the test conditions were non-layer forming such as at 25° C. The TCFC results also clarify that under a flowing condition, the formation of protective iron carbonate layer was not possible even at high pressure (80 bar) and high temperature condition (80° C) when the pH was low (pH 3.2). This was despite the fact that a high super-saturation of iron carbonate could be expected as ferrous ions were furnished by a very high corrosion rate and carbonate ions by a high concentration of CO₂. This is because a parallel work [165] carried out in a 20-liter autoclave in stagnant conditions indicated that protective iron carbonate could form at such test condition. Dugstad also observed a similar behavior in which protective iron carbonate layers in an iron carbonate super-saturation environment were unable to form under flowing conditions [99].

CHAPTER 6.0: MODELING

The results from the above experimental work were used to propose a mechanistic model for the effect of flow on CO₂ corrosion rate of carbon steel in CO₂-saturated water system at elevated CO₂ partial pressure environments as a function of pH, temperature, and pCO₂. The model was incorporated into the existing corrosion prediction model, Multicorp[®]; this enhanced model is known as Supercorp[®]. The proposed model is described as follows.

6.1 Effect of CO₂ partial pressure

6.1.1 CO₂ corrosion rate

First of all, the results show that the corrosion rate at high CO₂ partial pressure was very high. This was because of the higher concentration of carbonic acid generated with the increase in CO₂ partial pressure [43]. Consequently, the increase in its concentration increased the magnitude of the direct reduction of carbonic acid, hence increasing the total cathodic current density. This was because of the increase in charge-transfer current density as reflected by **equation (34)** *via* the increase in the exchange current density for carbonic acid reduction [43]:

$$\frac{d(\log i_{C(H_2CO_3)}^o)}{dC_{H_2CO_3}} = 1 \quad (93)$$

The cathodic current density also increased in accordance with **equation (45)**. However, it should be noted that the corrosion rates were expected to be lower than those predicted using the existing prediction models partly due to the lower concentrations of

carbonic acid as predicted by the new water chemistry model developed in this project as displayed in **Figure 73** [15]:

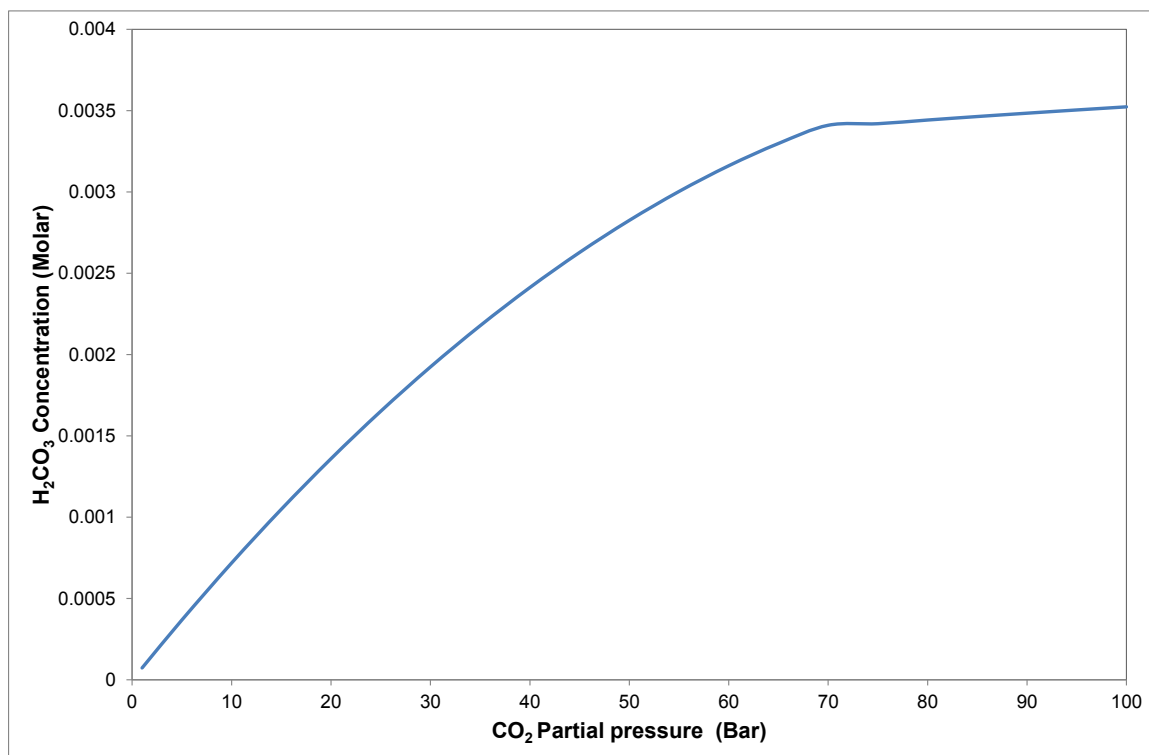


Figure 73: The change in carbonic acid concentration as a function of CO₂ partial pressure at 25° C as modeled by the custom-built water chemistry model [15].

However, the results further suggested that the increase in pCO₂ did not lead to a linear increase in CO₂ corrosion rate, contrary to the prediction by Multicorp (see §6.5 below). This could also be deduced from **Figure 73** that shows a non-linear increase in the concentration of carbonic acid with CO₂ partial pressure. It has been proposed that the reason for such behavior is due to the formation of protective iron carbonate layers [43]. While this was true in RCE experiments where limited volumes of test solution led to the more rapid and increased levels of supersaturation, the TCFC experiments indicate

that no protective iron carbonate layers were formed even at 80° C. It was therefore suggested that the reason for the non-linear increase was due to the increase in the surface adsorption of H₂CO₃. As noted earlier, the mechanism for the direct reduction of carbonic acid mechanism is governed by the adsorption of molecular H₂CO₃ on the steel surface, followed by its dissociation into hydrogen ions and bicarbonate; the hydrogen ions are consequently reduced (see **equation (28)**). As the CO₂ partial pressure increases, the concentration of carbonic acid also increases as governed by the solubility of CO₂ (see **Table 3**). However, at a certain stage, the reactive surface will become saturated with adsorbed carbonic acid. This leads to only a slight increase in corrosion rates. In this regard, to model such effect of CO₂ partial pressure, the following Langmuir isotherm adsorption equation was used [24]:

$$\theta = \frac{K \cdot pCO_2}{1 + K \cdot pCO_2} \quad (94)$$

where θ represents the fractional surface coverage at which CO₂ is adsorbed on the surface and K is the adsorption equilibrium constant. **Figure 74** below shows how the surface coverage varies with CO₂ partial pressure. At $pCO_2 < 20$ bar, the increase in fractional surface coverage was assumed to be linear as corrosion rates at this range increase linearly with CO₂ partial pressure. The fractional surface coverage was then multiplied with the concentration of bicarbonate acid to calculate the concentration at the steel surface. The new concentration was used to calculate the cathodic reduction current contributed by carbonic acid.

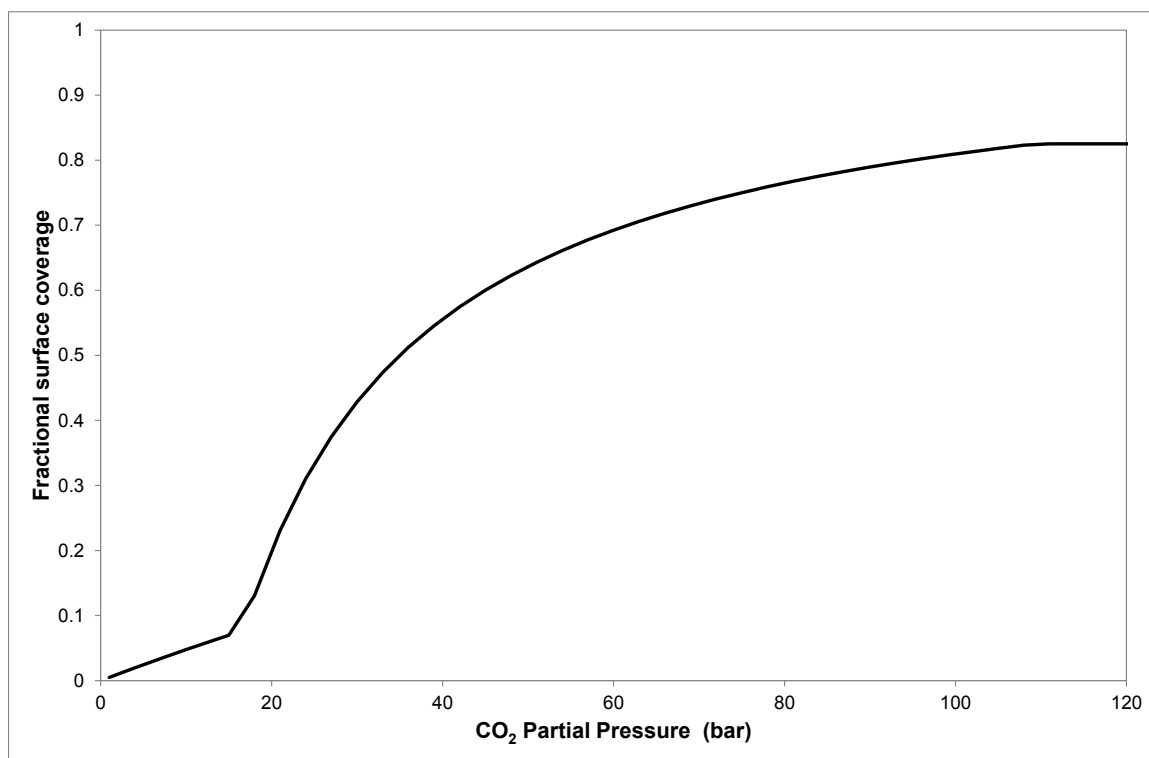


Figure 74: The fractional surface coverage as a function of CO₂ partial pressure to account for the effect of adsorbed carbonic acid on CO₂ corrosion rate.

6.1.2 Flow-sensitivity

The fact that the flow-sensitivity of CO₂ corrosion decreased as CO₂ partial pressure increased suggests that the cathodic reduction reactions involved the direct reduction of carbonic acid. This means that the mechanism first proposed by de Waard is still valid at elevated pCO₂ environments. This was evidenced from the potentiodynamic sweep data that showed the existence of the limiting current density component of cathodic reduction current density which was partially sensitive to flow; that is, its increase did not obey the power law of velocity. This points out that the limiting current density consisted of the diffusion limiting current density and the chemical reaction

limiting current density. The former that arose from the transport of hydrogen ions (see **equation (42)**) gave the flow-sensitivity. On the other hand, the latter (**equation (45)**) showed very limited flow-sensitivity only when the diffusion boundary layer and the chemical reaction boundary layer are about the same [51]. This occurs at a relatively higher velocity and low temperature [51].

In this regard, to model the flow-sensitivity, the cathodic limiting current density was assumed to be dominantly contributed to by the hydration of dissolved CO₂ that precedes the direct reduction of carbonic acid. This chemically dependent limiting current density was therefore calculated as follows [43]:

$$i_{\text{lim}(H_2CO_3)}^c = FC_{CO_2}f_{(H_2CO_3)}\sqrt{D_{(H_2CO_3)}K_{hyd}k_{hyd}^f} \quad (95)$$

where:

F is Faraday constant=96500 C/mol

C_{CO_2} is the concentration of dissolved CO₂ (Molar)

k_{hyd}^f is the forward reaction rate constant (1/s)

$K_{hyd} = \frac{k_{hyd}^f}{k_{hyd}^b}$ is the equilibrium constant

$f_{(H_2CO_3)} = coth(\xi)$ is the flow factor

ξ is the ratio between the diffusion and chemical reaction boundary layers (see **equation (43)**)

$D_{(H_2CO_3)}$ is the diffusion coefficient (m/s²)

6.2 The effect of temperature

Temperature also seems to have had an impact on accelerating the CO₂ corrosion rate (see **Figure 66**). In the RCE experiments, the effect was overshadowed by the formation of protective carbonate layers. On the other hand, in the TCFC, the increase in temperature led to an order of magnitude increase in corrosion rate due to the absence of iron carbonate layers. Dugstad and co-workers also observed that the increase in CO₂ corrosion rate with velocity in non-layer forming conditions was more pronounced at a higher temperature [18]. This effect was reflected in the model via the increase in the cathodic exchange current density (see **equation (35)**) and diffusion coefficient (**equation (69)**), and the decrease in viscosity (**equation (79)**); the decrease in viscosity of water leads to the increase in mass transfer coefficient *via* **equation (69)** by the increase in Reynolds number. The fact that there was a considerable flow-sensitivity when the temperature was increased to 80° C suggests that the charge-transfer rate might have increased much more than the mass-transfer rate [52, 118].

6.3 The effect of pH

Despite the anomaly at pH 4 and 50° C, the model considered the increase in pH as leading to the decrease in corrosion rates. This was based on the fact that the decrease in hydrogen ion concentrations would lead to the decrease in cathodic current density as reflected by **equations (34) and (35)** for the charge transfer portion and by **equation (42)** for the limiting current portion [40, 44]. The exchange current density due to hydrogen ion reduction $i_{C(H^+)}^o$ in **equation (34)** is related to pH by the following relationship [43]:

$$\frac{d(\log i_{c(H^+)})}{dpH} = -0.5 \quad (96)$$

As for the effect of pH on flow-sensitivity, it was governed by the mass transfer rate of hydrogen ions to the steel surface and the concentration of hydrogen ions as reflected by **equation (34)**. At a particular pH, the increase in velocity would increase the transport rate of hydrogen ions ($K_{m(H^+)}$) to the steel by reducing the boundary layer thickness as turbulent eddies penetrated deeper into the diffusion boundary layer [31, 118]. Furthermore, as pH decreased, the concentration of hydrogen ions transported at the same mass transfer rate (for the same velocity and for a constant diffusion coefficient at a given temperature) would be increased, leading to further enhancement of flow sensitivity. However, as noted from the results, in CO₂-saturated solution, the increase in corrosion rate was not proportional to the decrease in pH; nor was it proportional to a power law related to the velocity. This was different from the effect of pH on flow-sensitivity in HCl solution [44] because of the dominance of chemical reaction limiting current density arising from the slow hydration of dissolved CO₂ [51, 65]; that is, there was a competition between the limiting current density that arose due to the transport of hydrogen ions and that which arose from the slow hydration of dissolved CO₂. At elevated CO₂ partial pressure, the cathodic current density came largely from the direct reduction of H₂CO₃ which was limited by the hydration reaction and not largely flow-sensitive. Thus, the chemical reaction limiting current dominated over the diffusion

limiting current from the transport of hydrogen ions, thus overpowering the effect of pH on the flow-sensitivity. This can be mathematically expressed below:

$$i_{lim(Total)} = i_{lim(H^+)} + i_{lim(H_2CO_3)} \quad (97)$$

Thus, the total cathodic limiting reduction current density came largely from the chemical reaction-limiting current density that was largely not sensitive to flow as it was limited by the hydration of aqueous CO₂.

6.4 Anodic reaction

The anodic polarization curves exhibited a Tafel behavior at a potential range of 200 mV nobler than the corrosion potential. In this case, **equations (53) to (57)** were used to model the anodic reaction. With the iron dissolution being under charge-transfer control, the effect of flow was not accounted for in the modeling. The effect of pH and CO₂ partial pressure was captured *via equation (47)*. However, since the effect of pH on the anodic reaction was minimal, its corresponding reaction order could be set to zero. Similarly, the reaction order with respect to CO₂ partial pressure could also be set to zero since its effect on the anodic reaction was negligible. Furthermore, it has been suggested that at CO₂ partial pressure of above 1 bar, the reaction order is zero [45].

6.5 Validation of the model

The changes made on the model platform Multicorp© pertained to water chemistry model and iron carbonate formation in stagnant conditions carried out in parallel research projects [15, 165] as well as the present work. **Figure 75** below shows

the comparison of corrosion rates between Supercor[©] and the TCFC experimental data. The straight line that goes to the origin corresponds to the situation in which the predicted and the experimental corrosion rates perfectly correlate. The other two straight lines correspond to 50 percent error margin between the two.

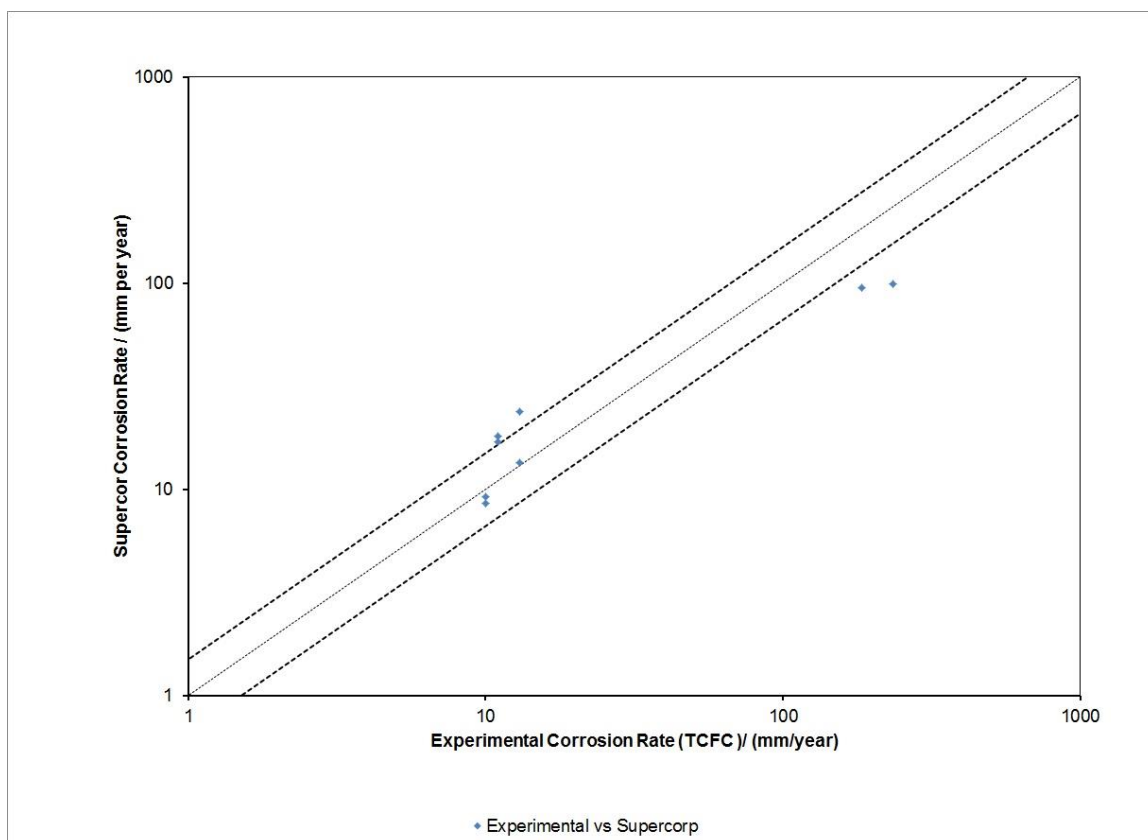


Figure 75: Comparison of corrosion rates between Supercor[©] and the TCFC data

The figure indicates that the correlation at low corrosion rates that corresponded to low temperature cases (25° C) was relatively good while the correlation at high corrosion rates (two data points) that corresponded to higher temperature cases (80° C) was relatively poor. The reason for the poor correlation was probably that Supercor was

also calibrated against the corrosion rates measured in a 20-liter autoclave that took into account the possible formation of iron carbonate layers.

The model was applied in calculating the possible corrosion rate for CO₂ transport pipelines for PETRONAS' high pressure CO₂ environment hydrocarbon gas fields. A comparison with the base model is shown in below:

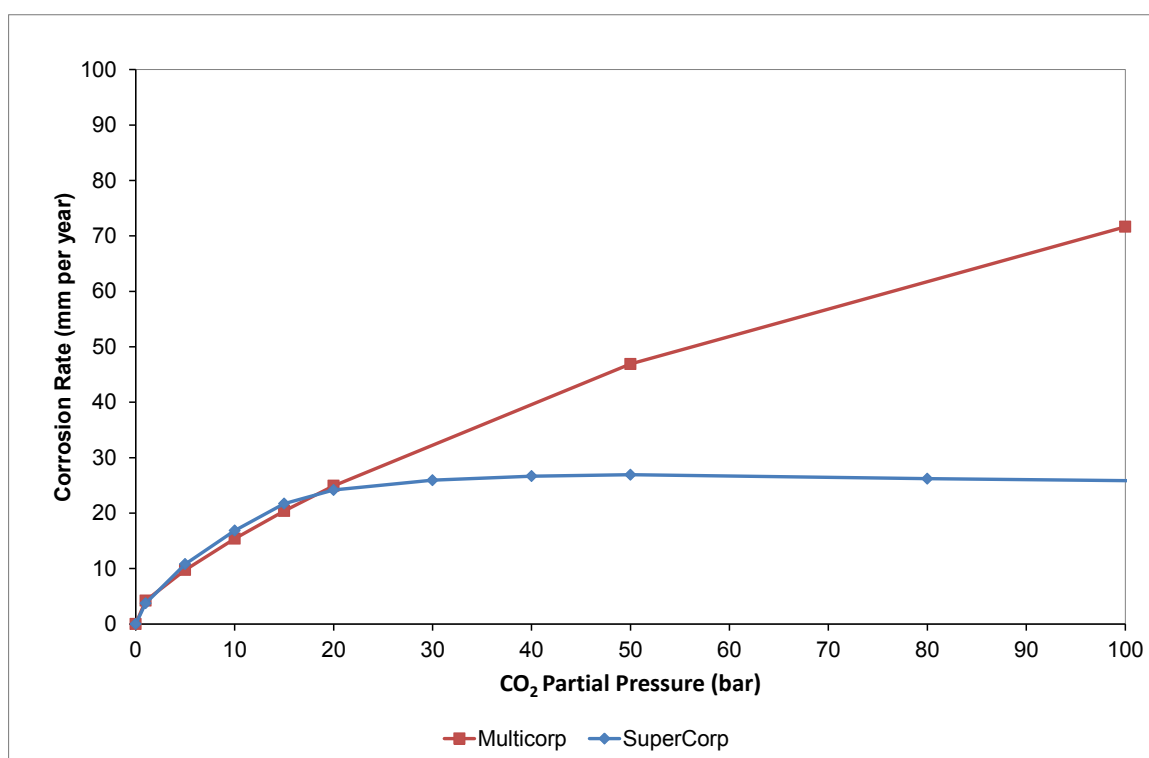


Figure 76: A comparison of Supercorp[®] with Multicorp[®] for PETRONAS CO₂ transport pipeline (32"). The modeling was for 40° C and 2.2 m/s fluid velocity

The above figure indicates that while Multicorp[®] predicted a linear increase in corrosion rate with the increase in CO₂ partial pressure, Supercorp[®] predicted a plateau in corrosion rate due to the surface adsorption effect.

CHAPTER 7.0: CONCLUSIONS AND FUTURE WORK

7.1 Conclusions

Based on the experimental work, the following conclusions were drawn:

1. The hydrodynamic and mass transfer behavior of the thin channel flow cell could be characterized by Sloucher and Rouse's mass transfer correlation. TCFC is therefore suitable for use as an apparatus for flow-sensitive corrosion studies.
2. Given the correct choice of equivalent velocities, the corrosion rates obtained in the RCE autoclave and the TCFC correlated well at low temperature (25° C), indicating a flow geometry-independent corrosion rate.⁴ The poor correlation at high temperature (80° C) was due to the change in water chemistry in the smaller volume RCE autoclave.
3. The TCFC with its larger volume of test solution produced more realistic corrosion rates, particularly at a higher pCO₂ (80 bar) and higher temperature (80° C) as one could avoid a large build-up of corrosion products and an unrealistic change in water chemistry.⁴
4. The increase in temperature seems to have increased the flow-sensitivity of CO₂ corrosion of carbon steel in the absence of protective corrosion product layers.⁴ This could be due to the increase in charge-transfer rate.
5. The effect of pH on the flow-sensitivity of CO₂ corrosion was low even at CO₂ partial pressure of 10 bar due to the dominant effect of chemical-reaction

⁴ Reproduced with permission from NACE International, Houston, TX. All rights reserved. Paper C2012-0001683 presented at CORROSION/2012, Salt Lake, Utah. © NACE International 2012.

controlled limiting current density that came from the slow hydration of dissolved CO₂.

6. The flow-sensitivity of CO₂ corrosion was not clearly observed even at a low pH (pH 3.0). This is opposite to what has normally been observed at a low CO₂ partial pressure.⁵
7. The increase in CO₂ partial pressure led to the decrease in the flow-sensitivity of CO₂ corrosion probably due to the increase in carbonic acid concentration where its reduction is limited by the hydration of dissolved CO₂.⁵
8. The increase in CO₂ partial pressure led to the increase in corrosion rate due to the increase in the cathodic reduction of carbonic acid.
9. The anodic reaction was slightly influenced by pH, CO₂ partial pressure, and temperature.

7.2 Future work

To enhance the model further, it is proposed that:

1. The effect of flow on corrosion product layer formation at elevated CO₂ partial pressure under high super-saturation be studied in the HPHT TCFC. This can help further verify whether flow can interfere with the formation of protective iron carbonate layers.
2. The effect of H₂S in high CO₂ partial pressure environments should be incorporated into the model in non-layer and layer-forming conditions so as to determine whether H₂S will either accelerate or inhibit CO₂ corrosion rates.

⁵ Reproduced with permission from NACE International, Houston, TX. All rights reserved. Paper 11242 presented at CORROSION/2011, Houston, Texas. © NACE International 2011.

3. The effect of multiphase flow on CO₂ corrosion at elevated CO₂ partial pressure should be included. This is relevant to transport of full-well stream containing high CO₂ concentrations.
4. The accuracy of the prediction model should be improved by taking account the more realistic corrosion rate data from the TCFC.

REFERENCES

- [1] M. B. Kermani and L. M. Smith, Eds., *A Working Party Report on CO₂ Corrosion Control in Oil and Gas Production*. London: The Institute of Materials, 1997.
- [2] J. Thrasher and A. J. Fleet, "Predicting the risk of carbon dioxide 'pollution' in petroleum reservoirs," in *Organic Geochemistry: Developments and Applications to Energy, Climate, Environment and Human History*, San Sebastian: AIGOA Donastia, 1995, pp. 1086-1088.
- [3] C. de Waard and C. Lotz, "Prediction of CO₂ corrosion of carbon steel," in *A Working Party Report on Predicting CO₂ Corrosion in the Oil and Gas Industry (European Federation of Corrosion Publications Number 13)*, London: The Institute of Materials, 1994, pp. 30-49.
- [4] J. L. Crolet, "Which CO₂ corrosion, hence which prediction?" in *A Working Party Report on Predicting CO₂ Corrosion in the Oil and Gas Industry*, London: The Institute of Materials, 1994, pp. 1-29.
- [5] G. Schmitt and M. Hörstemeier, "Fundamental aspects of CO₂ metal loss corrosion – Part II: Influence of different parameters on CO₂ corrosion mechanisms," in *Corrosion/2006*, 2006, Paper 06112.
- [6] M. Seiersten and K. O. Kongshaug, "Materials selection for capture, compression, transport and injection of CO₂," in *Carbon Dioxide Capture for Storage in Deep Geologic Formations - Results from the CO₂ Capture Project Capture and Separation of Carbon Dioxide from Combustion Sources*, Amsterdam: Elsevier, 2005, pp. 937.
- [7] M. B. Kermani and A. Morshed, "Carbon dioxide corrosion in oil and gas production - A compendium," *Corrosion*, vol. 59, (8), pp. 659-683, 2003.
- [8] J. Veron, "An overview of the non-developed gas reserves in Southeast Asia," *PetroMin*, (3), pp. 22-28, 2007.
- [9] D. M. Goldin and G. V. Kulikova, "On the dissociation mechanism of carbonates and their isomorphous mixture," *J Therm Anal*, vol. 29, (1), pp. 139-145, 1984.
- [10] Y. Zang, K. Gao and G. Schmitt, "Water effect on steel corrosion under supercritical CO₂ conditions," in *Corrosion/2011*, 2011, Paper 11378.
- [11] M. Davies and P. J. B. Scott, *Oilfield Water Technology*. Houston, Texas: NACE, 2006.

- [12] M. Seiersten, "Material selection for separation, transportation and disposal of CO₂," in *Corrosion/2001*, 2001, Paper No. 01042.
- [13] M. F. Suhor, "High CO₂ corrosion," PETRONAS Advisory Board Meeting. October 26, 2009.
- [14] A. A. Clifford and J. R. Williams, "Introduction to supercritical fluids and their applications," in *Supercritical Fluid Methods and Protocols*, New Jersey: Humana Press, 2000, pp. 1-16.
- [15] M. F. Mohamed, A. Mohammed Nor, M. F. Suhor, M. Singer, Y. S. Choi and S. Nestic, "Water chemistry for corrosion prediction in high-pressure CO₂ environments," in *Corrosion/2011*, 2011, Paper 11375.
- [16] M. F. Suhor, M. F. Mohamed, A. Mohammed Nor, M. Singer and S. Nestic, "Corrosion tests of mild steel in high pressure CO₂ environments," 2011, *Corrosion/2011*.
- [17] T. Y. Chen, A. Moccari and D. D. MacDonald, "The development of controlled hydrodynamic techniques for corrosion testing," *Corrosion*, vol. 48, (3), pp. 239-255, 1992.
- [18] A. Dugstad, L. Lunde and K. Videm, "Parametric study of CO₂ corrosion of carbon steel," in *Corrosion/94*, 1994, Paper No. 99014.
- [19] K. Denpo and K. Ogawa, "Fluid flow effects on CO₂ corrosion resistance of oil well materials," *Corrosion*, vol. 49, (6), pp. 442-449, 1993.
- [20] M. F. Kemmere, "Supercritical carbon dioxide for sustainable polymer processes," in *Supercritical Carbon Dioxide*, Weinheim: Wiley-VCH Verlag GmbH & Co. KGaA, 2005, pp. 1-14.
- [21] S. S. Zumdahl, *Chemistry*. Massachusetts: D. C. Heath and Company, 1986.
- [22] A. S. Padalkar and A. D. Kadam, "Carbon dioxide as natural refrigerant," *Int. J. Appl. Eng. Res.*, vol. 1, (2), pp. 261-272, 2010.
- [23] P. N. Seevam, J. M. Race, M. J. Downie and P. Hopkins, "Transporting the next generation of CO₂ for carbon capture and storage: The impact of impurities on supercritical CO₂ pipelines," in *ASME International Pipeline Conference/2008*, 2009, Paper 64063.
- [24] P. Atkins and J. de Paula, *Elements of Physical Chemistry*. Kuala Lumpur: Oxford University Press, 2007.

- [25] S. Lee, "Special topic in chemical engineering: Supercritical fluid," Ohio University, Fall 2010.
- [26] S. Takenouchi and G. S. Kennedy, "The binary system H₂O-CO₂ at high pressure and temperature," *Amer. J. of Sci*, vol. 262, (11), pp. 1055-1074, 1964.
- [27] N. Spycher, K. Pruess and J. Ennis-King, "CO₂-H₂O mixtures in the geological sequestration of CO₂. I. assessment and calculation of mutual solubilities from 12 to 100 °C and up to 600 bar," *Geochim. Cosmochim. Acta*, vol. 67, (16), pp. 3015-3031, 2003.
- [28] Y. S. Choi and S. Netic, "Effect of water content on the corrosion behavior of carbon steel in supercritical CO₂ phase," in *Corrosion/2011*, 2011, Paper 11377.
- [29] S. Netic and W. Sun, "Corrosion in acid gas solutions," in *Shreir's Corrosion*, Amsterdam: Elsevier, 2009, pp. 1270-1298.
- [30] J. E. Oddo and M. B. Tomson, "Simplified calculation of CaCO₃ saturation at high temperatures and pressures in brine solutions," *J. Petroleum Technol*, vol. 34, (7), pp. 183-190, 1990.
- [31] M. Nordsveen, S. Neic, R. Nyborg and A. Stangeland, "A mechanistic model for carbon dioxide corrosion of mild steel in the presence of protective iron carbonate films - Part 1: Theory and verification," *Corrosion*, vol. 59, (5), pp. 443-456, 2003.
- [32] D. A. Palmer and R. Van Eldik, "The chemistry of metal carbonato and carbon dioxide complexes," *Chem. Rev.*, vol. 83, (6), pp. 651-731, 1983.
- [33] R. Eldik and D. A. Palmer, "Effects of pressure on the kinetics of the dehydration of carbonic acid and the hydrolysis of CO₂ in aqueous solution," *J Sol. Chem.*, vol. 11, (5), pp. 339-346, 1982.
- [34] S. Netic, "Prediction of transport processes in CO₂ corrosion," in *A Working Party Report on Predicting CO₂ Corrosion in the Oil and Gas Industry*, London: The Institute of Materials, 1994, pp. 120-133.
- [35] Y. K. Kharaka, E. H. Perkins, W. D. Gunter, J. D. Debral and C. H. Bamford, *Solmineq 88: A Computer Program for Geochemical Modeling of Water Rock Interactions*. Menlo Park, CA: Alberta Research Council, 1989.
- [36] Z. Duan and D. Li, "Coupled phase and aqueous species equilibrium of the H₂O-CO₂-NaCl-CaCO₃ system from 0 to 250 °C, 1 to 1000bar with NaCl concentrations up to saturation of halite," *Geochim. Cosmochim. Acta*, vol. 72, (20), pp. 5128-5145, 2008.

- [37] G. Schmitt and M. Kriek-Defrain, "pH-static experiments in high pressure CO₂ corrosion of steel: Effect on scale morphology and chemical composition, corrosion rate, pitting susceptibility and inhibitor performance," in *Innovation and Technology Transfer for Corrosion Control*, 1990, Paper 5.
- [38] K. R. Trethewey and J. Chamberlain, *Corrosion for Students of Science and Engineering*. England: Longman Scientific and Technical, 1988.
- [39] S. Nestic, "Metallic corrosion," Ohio University, Fall 2009.
- [40] L. G. S. Gray, B. G. Anderson and M. J. T. Danysh P.R., "Effect of pH and temperature on the mechanism of carbon steel corrosion by aqueous carbon dioxide," in *Corrosion/1990*, 1990, Paper 40.
- [41] L. S. Moiseeva and N. S. Rashevskaya, "Effect of pH value on corrosion behavior of steel in CO₂-containing aqueous media," *Rus. J. Appl. Chem.*, vol. 75, (10), pp. 1625-1633, 2002.
- [42] K. Videm and A. Dugstad, "Corrosion of carbon steel in an aqueous carbon dioxide environment - Part 1: Solution effects," *Mater. Perform.*, vol. 28, (3), pp. 63-67, 1989.
- [43] S. Nestic, "Carbon dioxide corrosion of mild steel," in *Uhlig's Corrosion Handbook*, 3rd ed., New Jersey: A John Wiley and Sons Inc., 2011, pp. 229-245.
- [44] S. Nestic, J. Postlethwaite and S. Olsen, "An electrochemical model for prediction of corrosion of mild steel in aqueous carbon dioxide solutions," *Corrosion*, vol. 52, (4), pp. 280, 1996.
- [45] S. Nestic, N. Thevenot, J. L. Crolet and D. M. Drazic, "Electrochemical properties of iron dissolution in the presence of CO₂ - basics revisited," in *Corrosion/96*, 1996, Paper 9603.
- [46] S. Nestic, "Key issues related to modeling of internal corrosion of oil and gas pipelines - A review," *Corros. Sci.*, vol. 49, (12), pp. 4308-4338, 2007.
- [47] V. Ruzic, M. Veidt and S. Neic, "Protective iron carbonate films -Part 2: Chemical removal by dissolution in single-phase aqueous flow," *Corrosion*, vol. 62, (7), pp. 598-611, 2006.
- [48] C. A. R. Silva, X. Liu and F. J. Millero, "Solubility of siderite (FeCO₃) in NaCl solutions," *J. Sol. Chem.*, vol. 31, (2), pp. 97-108, 2002.
- [49] C. de Waard and D. E. Milliams, "Carbonic acid corrosion of steel," *Corrosion*, vol. 31, (5), pp. 177-181, 1975.

- [50] G. Schmitt and B. Rothmann, "Corrosion mechanism of unalloyed steel in oxygen-free carbon dioxide solutions - Part 1: Kinetics of the liberation of hydrogen," *Werkst. Korros.*, vol. 28, (12), pp. 816-822, 1977.
- [51] S. Nestic, B. F. M. Pots, J. Postlethwaite and N. Thevenot, "Superposition of Diffusion and Chemical Reaction Controlled Limiting Currents-Applications to CO₂ Corrosion." *J. Corro. Sci. and Eng.*, vol. 1, (Paper 3), 1995.
- [52] E. Eriksrud and T. Sontvedt, "Effect of flow on CO₂ corrosion rates in real and synthetic formation waters," in *Corrosion/83*, 1983, Paper 8344.
- [53] A. Dugstad, "Fundamental aspects of CO₂ metal loss corrosion-part I: Mechanism," in *Corrosion/2006*, 2006, Paper 06111.
- [54] E. Remita, B. Tribollet, E. Sutter, V. Vivier, F. Ropital and J. Kittel, "Hydrogen evolution in aqueous solutions containing dissolved CO₂: Quantitative contribution of the buffering effect," *Corros. Sci.*, vol. 50, (5), pp. 1433-1440, 2008.
- [55] B. R. Linter and G. T. Burstein, "Reactions of pipeline steels in carbon dioxide solutions," *Corros. Sci.*, vol. 41, (1), pp. 117-139, 1999.
- [56] M. Stern, "The electrochemical behavior, including hydrogen overvoltage of iron in acid environments," *J. Electrochem. Soc.*, vol. 102, (11), pp. 609-616, 1955.
- [57] B. F. M. Pots. "Mechanistic models for the prediction of CO₂ corrosion rates under multiphase flow conditions," in *Corrosion/1995*, Paper 95137.
- [58] G. Zhang, M. Lu, C. Chai and Y. Wu, "Effect of HCO₃⁻ concentration on CO₂ corrosion in oil and gas fields," *J. Univ. Sci. Technol. Beijing: Min. Metall. Mater. (Eng Ed)*, vol. 13, (1), pp. 44-49, 2006.
- [59] D. A. Jones, *Principles and Prevention of Corrosion*. New Jersey: Prentice-Hall, 1996.
- [60] J. R. Scully, "The influence of mass transport on electrochemical process," in *Electrochemical Techniques in Corrosion Science and Engineering*, New York: Marcel Dekker Inc., 2003, pp. 151-175.
- [61] M. Rahmani and J. E. Strutt, *Hydrodynamic Modeling of Corrosion of Carbon Steels and Cast Irons in Sulfuric Acid*. Houston: NACE, 1992.
- [62] T. Y. Chen, A. Moccari and D. D. MacDonald, *The Development of Controlled Hydrodynamic Techniques for Corrosion Testing*. Houston: NACE, 1992.

- [63] K. Videm, "Fundamental studies aimed at improving models for prediction of CO₂ corrosion," in *Progress in the Understanding and Prevention of Corrosion*, London: Institute of Materials, 1993, pp. 504-512.
- [64] A. Anderko, P. McKenzie and R. D. Young, "Computation of rates of general corrosion using electrochemical and thermodynamic models," in *Corrosion/2000*, 2000, Paper 00479.
- [65] L. G. S. Gray, B. G. Anderson and M. J. T. Danysh P.R., "Mechanisms of carbon steel corrosion in brines containing dissolved carbon dioxide at pH4," in *Corrosion/1989*, 1989, Paper 464.
- [66] G. Schmitt and B. Rothmann, "Studies of the corrosion mechanism of unalloyed steel in oxygen-free carbon dioxide solutions - Part II: Kinetics of iron dissolution," *Werkst. Korros.*, vol. 29, (4), pp. 163-165, 1978.
- [67] S. Wang, K. George and S. Nescic, "High pressure CO₂ corrosion electrochemistry and the effect of acetic acid," in *Corrosion/2004*, 2004, Paper 04375.
- [68] M. F. Mohamed, "Water chemistry model for high CO₂ environments," PETRONAS Advisory Board Meeting, Ohio University, 2010.
- [69] H. S. Folger, *Elements of Chemical Reaction Engineering*. New Jersey: Prentice-Hall, 2005.
- [70] J. Newman and K. E. Thomas-Alyea, *Electrochemical Systems*, 3rd ed. New Jersey: A John Wiley and Sons Inc., 2004.
- [71] A. Dugstad, "The importance of FeCO₃ supersaturation on the CO₂ corrosion of carbon steels," in *Corrosion/1992*, 1992, Paper 14.
- [72] W. Sun, S. Nešić and R. C. Woollam, "The effect of temperature and ionic strength on iron carbonate (FeCO₃) solubility limit," *Corros. Sci.*, vol. 51, (6), pp. 1273-1276, 2009.
- [73] S. Nescic, M. Nordsveen, R. Nyborg and A. Stangeland, "A mechanistic model for carbon dioxide corrosion of mild steel in the presence of protective iron carbonate films - Part 2: A numerical experiment," *Corrosion*, vol. 59, (6), pp. 489-497, 2003.
- [74] S. Nescic and K. J. Lee, "A mechanistic model for carbon dioxide corrosion of mild steel in the presence of protective iron carbonate films - Part 3: Film growth model," *Corrosion*, vol. 59, (7), pp. 616-628, 2003.

- [75] K. Videm and A. Dugstad, "Corrosion of carbon steel in an aqueous carbon dioxide environment - Part 2: Film formation," *Mater. Perform.*, vol. 28, (4), pp. 46-50, 1989.
- [76] M. L. Johnson and M. B. Tomson, "Ferrous carbonate precipitation kinetics," in *Corrosion/1991*, 1991, Paper 268.
- [77] S. L. Wu, Z. D. Cui, G. X. Zhao, M. L. Yan, S. L. Zhu and X. J. Yang, "EIS study of the surface film on the surface of carbon steel from supercritical carbon dioxide corrosion," *Appl. Surf. Sci.*, vol. 228, (1-4), pp. 17-25, 2004.
- [78] I. Stanley, *Chemical, Biochemical, and Engineering Thermodynamics*. New York: John Wiley & Son, 2007.
- [79] G. Schmitt and M. Bakalli, "A critical review of measuring techniques for corrosion rates under flow conditions," in *Corrosion/2006*, 2006, Paper 06593.
- [80] G. Lin, M. Zheng, Z. Bai and X. Zhao, "Effect of temperature and pressure on the morphology of carbon dioxide corrosion scales," *Corrosion*, vol. 62, (6), pp. 501-507, 2006.
- [81] D. A. López, T. Pérez and S. N. Simison, "The influence of microstructure and chemical composition of carbon and low alloy steels in CO₂ corrosion. A state-of-the-art appraisal," *Mater Des*, vol. 24, (8), pp. 561-575, 2003.
- [82] D. V. Edmonds and R. C. Cochrane, "The effect of alloying on the resistance of carbon steel for oilfield applications to CO₂ corrosion," *Mat. Res.*, vol. 8, (4), pp. 377-385, 2005.
- [83] M. B. Kermani, J. C. Gonzales, C. Linne, M. Dougan and R. Cochrane, "Development of low carbon Cr-Mo steels with exceptional corrosion resistance for oilfield applications." in *NACE/2001*, 2001, Paper 01065.
- [84] A. Ikeda and M. Ueda, "CO₂ corrosion behavior of Cr-containing steels," in *Predicting CO₂ Corrosion in the Oil and Gas Industry*, London: The Institute of Materials, 1994, pp. 59-93.
- [85] M. Kimura, Y. Saito and Y. Nakano, "Effects of alloying elements on corrosion resistance of high strength line pipe steel in wet CO₂ environment," in *Corrosion/1994*, 1994, Paper 94018.
- [86] A. Dugstad, H. Hemmer and M. Seiersten, "Effect of steel microstructure on corrosion rate and protective iron carbonate film formation," *Corrosion*, vol. 57, (4), pp. 369-378, 2001.

- [87] L. Hu, L. Zhang, W. Chang, M. Lu and L. Xu, "Compare the corrosion resistance of 3%Cr steel with API X65 pipeline steel in CO₂ corrosion environment," in *Corrosion/2011*, 2011, Paper 11073.
- [88] P. S. Jackman and L. M. Smith, Eds., *Advances in Corrosion Control and Materials in Oil and Gas Production*. London: The Institute of Materials, 1999.
- [89] A. Dugstad and L. Lunde, "Influences of low alloying elements upon the CO₂ corrosion rate," in *NACE Corrosion/1991*, 1991, Paper 473.
- [90] L. D. Paolinelli, T. Pérez and S. N. Simison, "The incidence of chromium-rich corrosion products on the efficiency of an imidazoline-based inhibitor used for CO₂ corrosion prevention," *Mater. Chem. Phys.*, vol. 126, (3), pp. 938-947, 2011.
- [91] D. A. Brandt, *Metallurgy Fundamentals*. Illinois: The Goodheart-Willcox Company, 1985.
- [92] S. Vaynman, M. E. Fine, R. I. Asfahani, D. M. Bormet and C. Hahin, "High performance copper-precipitation-hardened steel," in *Microalloyed Steels/2002*, 2002, .
- [93] D. W. Stegmann, R. H. Hausler, C. I. Cruz and H. Sutanto, "Laboratory studies on flow-induced localized corrosion in CO₂/H₂S environment, 1. Development of test methodology," in *Corrosion/90*, 1990, Paper 5.
- [94] C. A. Palacios and J. R. Shadley, "Characteristics of corrosion scales on steels in a CO₂-saturated NaCl brine," *Corrosion*, vol. 47, (2), pp. 122-127, 1991.
- [95] J. L. Mora-Mendoza and S. Turgoose, "Fe₃C influence on the corrosion rate of mild steel in aqueous CO₂ systems under turbulent flow conditions," *Corros. Sci.*, vol. 44, (6), pp. 1223-1246, 2002.
- [96] S. Nescic and L. Lunde, "Carbon dioxide corrosion of carbon steel in two-phase flow," *Corrosion*, vol. 50, (9), pp. 717-727, 1994.
- [97] D. A. López, W. H. Schreiner, S. R. De Sánchez and S. N. Simison, "The influence of carbon steel microstructure on corrosion layers: An XPS and SEM characterization," *Appl. Surf. Sci.*, vol. 207, (1-4), pp. 69-85, 2003.
- [98] J. L. Crolet, S. Olsen and W. Wilhelmsem. "Influence of a layer of undissolved cementite on the rate of the CO₂ corrosion of carbon steel," in *Corrosion/1994*, Paper 94004.
- [99] A. Dugstad, "Mechanism of protective film formation during CO₂ corrosion of carbon steel," in *Corrosion/1998*, 1998, Paper 9831.

- [100] F. D. de Moraes , J. R. Shadley, J. Chen and E. F. Rybicki, "Characterization of CO₂ corrosion product scales related to environmental conditions," in *Corrosion/2000*, 2000, Paper 0030.
- [101] R. Jasinski, "Corrosion of N80-type steel by CO₂ water mixtures," *Corrosion*, vol. 43, (4), pp. 214-218, 1987.
- [102] G. Schmitt, "Fundamental aspects of CO₂ corrosion," in *Proceedings of the corrosion/83 Symposium in CO₂ Corrosion in Oil and Gas Industry*, 1983, Paper 43.
- [103] A. Muñoz, J. Genesca, R. Duran and J. Mendoza, "Mechanism of FeCO₃ formation on API X70 pipeline steel in brine solutions containing CO₂," in *Corrosion/2005*, 2005, Paper 05297.
- [104] H. Malik, "Influence of C16 quaternary amine on surface films and polarization resistance of mild steel in carbon dioxide-saturated 5% sodium chloride," *Corrosion*, vol. 51, (4), pp. 321-328, 1995.
- [105] T. Tanupabrunsun, "CO₂ corrosion at elevated temperature," Corrosion Center Joint Industry Project, Advisory Board Meeting, Ohio University, Nov. 2010.
- [106] J. Han, Y. Yang, S. Netic and B. N. Brown, "Roles of passivation and galvanic effects in localized CO₂ corrosion of mild steel," in *Corrosion/2008*, 2008, Paper 08332.
- [107] J. Han, D. Young and S. Netic, "Characterization of the passive film on mild steel in CO₂ environments," in *17th International Corrosion Congress 2008: Corrosion Control in the Service of Society*, 2008, Paper 2511.
- [108] V. Ruzic, M. Veidt and S. Netic, "Protective iron carbonate films - Part 1: Mechanical removal in single-phase aqueous flow," *Corrosion*, vol. 62, (5), pp. 419-432, 2006.
- [109] R. Nyborg, "Initiation and growth of mesa corrosion attack during CO₂ corrosion of carbon steel," in *Corrosion/1998*, 1998, Paper 9848.
- [110] S. Netic, G. T. Solvi and J. Enerhaug, "Comparison of the rotating cylinder and pipe flow tests for flow sensitive CO₂ corrosion," *Corrosion*, vol. 51, (10), pp. 773-787, 1995.
- [111] K. D. Efirid, "Flow-induced corrosion," in *Uhlig's Corrosion Handbook*, New York: John Wileys & Sons Inc., 2000, pp. 233-247.
- [112] E. Heitz, "Chemo-mechanical effects of flow on corrosion," *Corrosion*, vol. 47, (2), pp. 135-145, 1991.

- [113] S. Nestic, J. Postlethwaite and M. Vrhovac, "CO₂ corrosion of carbon steel-from mechanistic to empirical modeling," *Corros. Rev.*, vol. 15, (1-2), pp. 211-240, 1997.
- [114] J. T. Davies, *Turbulence Phenomena: An Introduction to the Eddy Transfer of Momentum, Mass, and Heat, Particularly at Interfaces*. New York: Academic Press, 1972.
- [115] D. C. Silverman, "Rotating cylinder electrode-geometry relationships for prediction of velocity-sensitive corrosion," *Corrosion*, vol. 44, (1), pp. 42-49, 1988.
- [116] M. Eisenberg, C. W. Tobias and C. R. Wilke, "Ionic mass transfer and concentration polarization at rotating electrodes," *J. Electrochem. Soc.*, vol. 101, (6), pp. 306-320, 1954.
- [117] D. C. Silverman, "State-of-the-art report on controlled-flow laboratory corrosion tests," *NACE Publication 5A195*, pp. 1-22, 1995.
- [118] P. J. Boden, "Effect of concentration, velocity and temperature," in *Corrosion*, Oxford: Butterworth-Heinemann, 2000, pp. 2.1-2.30.
- [119] V. Ruzic, "Mechanism of protective FeCO₃ film removal in single-phase flow-accelerated CO₂ corrosion of mild steel," PhD Thesis, Dept. Mech. Eng., Queensland Univ., Queensland, Australia, 2005.
- [120] S. Nestic, "Effects of multiphase flow on internal CO₂ corrosion of mild steel pipelines," *Energy Fuels*, vol. 26, (7), pp. 4098-4111, 2012.
- [121] R. B. Bird, W. E. Stewart and E. N. Lightfoot, *Transport Phenomena*. New York: John Wiley & Sons, Inc., 2007.
- [122] K. D. Efirid, "Effect of fluid dynamics on the corrosion of copper-base alloys in seawater," *Corrosion*, vol. 33, (1), pp. 3-8, 1977.
- [123] Y. Yang, B. Brown, S. Neic, M. E. Gennaro and B. Molinas, "Mechanical strength and removal of a protective iron carbonate layer formed on mild steel in CO₂ corrosion," in *Corrosion/2010*, 2010, Paper 10383.
- [124] C. de Waard and D. E. Williams, "Prediction of carbonic acid corrosion in natural gas pipelines," *Ind. Finish. Surf. Coatings*, vol. 28, (340), pp. 24-26, 28, 1976.
- [125] C. de Waard, U. Lotz and A. Dugstad, "Influence of liquid flow velocity on CO₂ corrosion: A semi-empirical model," in *Corrosion/1995*, 1995, Paper 95128.

- [126] S. Turgoose, R. A. Cottis and K. Lawson, "Modeling of electrode processes and surface chemistry in carbon dioxide containing solutions," in *ASTM Special Technical Publication*, 1992, .
- [127] J. L. Dawson, C. C. Shih and P. K. N. Bartlett, "Models and prediction of CO₂ corrosion and erosion-corrosion under flowing conditions," in *A Working Party Report on Predicting CO₂ Corrosion in the Oil and Gas Industry*, London: The Institute of Materials, 1994, pp. 120-133.
- [128] I. A. Herce, E. I. Wright, K. D. Efirid, I. A. Boros and T. G. Hailey, "Effects of solution chemistry and flow on the corrosion of carbon steel in sweet production," in *Corrosion/1995*, 1995, Paper 95111.
- [129] J. Kvarekvål, "Flow loop studies of the relationship between limiting currents and CO₂/H₂S corrosion of carbon steel," in *Corrosion/1998*, 1998, Paper 9844.
- [130] L. M. Silva, J. Hernandez, J. Genesca, R. Duran and J. Mendoza, "Effect of flow on the corrosion mechanism of different API pipeline steels grades in NaCl solutions containing CO₂," in *Corrosion/2004*, 2004, Paper 04651.
- [131] J. Postlethwaite and S. Netic, "*Erosion-corrosion in single and multiphase flow*," in *Uhlig's Corrosion Handbook*, 2nd ed. New Jersey: John Wiley and Sons, 2000, pp. 249-272.
- [132] F. W. Schremp and G. R. Roberson, "Effect of supercritical carbon dioxide (CO₂) on construction materials," *SPE of AIME Journal*, vol. 15, (3), pp. 227-233, 1975.
- [133] E. M. Russick, G. A. Poulter, C. L. J. Adkins and N. R. Sorensen, "Corrosive effects of supercritical carbon dioxide and cosolvents on metals," *J. Supercrit. Fluids*, vol. 9, (1), pp. 43-43, 1996.
- [134] S. Huang, K. Daehling, T. E. Carleston and A. Propp, "Construction and calibration of an internal silver/silver chloride reference electrode for supercritical fluid studies," *Corrosion*, vol. 47, (3), pp. 185-188, 1991.
- [135] Z. F. Yin, Y. R. Feng, W. Z. Zhao, Z. Q. Bai and G. F. Lin, "Effect of temperature on CO₂ corrosion of carbon steel," *Surf. Interface Anal.*, vol. 41, (6), pp. 517-523, 2009.
- [136] Y. Choi and S. Netic, "Corrosion behavior of carbon steel in supercritical CO₂ - water environments," in *Corrosion/2009*, 2009, Paper 09256.
- [137] Z. D. Cui, S. L. Wu, C. F. Li, S. L. Zhu and X. J. Yang, "Corrosion behavior of oil tube steels under conditions of multiphase flow saturated with super-critical carbon dioxide," *Mater Lett*, vol. 58, (6), pp. 1035-1040, 2004.

- [138] T. Hara, H. Asahi, Y. Suehiro and H. Kaneta, "Effect of flow velocity on carbon dioxide corrosion behavior in oil and gas environments," *Corrosion*, vol. 56, (8), pp. 860-866, 2000.
- [139] Y. Wu, W. Liu, J. Dai, X. Fan, J. Zhang and M. Lu, "Comparison of corrosion behavior of X65 pipeline steel in CO₂-H₂S and CO₂ environment at different flow velocities," in *NACE Corrosion/2012*, 2012, Paper C2012-0001238.
- [140] R. Nyborg. "Overview of CO₂ corrosion models for wells and pipelines," in *Corrosion/2002*, Paper 02233.
- [141] R. Nyborg. "CO₂ corrosion models for oil and gas production systems," in *Corrosion/2010*, Paper 10371.
- [142] R. Nyborg. "Field data collection, evaluation and use for corrosivity prediction and validation of models," in *Corrosion/2006*, Paper 06118.
- [143] S. Netic and M. Vrhovac, "A neural network model for CO₂ corrosion of carbon steel," *J. Corros. Sci. Eng.*, vol. 1, (4), pp. 1-13, 1999.
- [144] M. Nordsveen, S. Nešić, R. Nyborg and A. Stangeland, "A mechanistic model for carbon dioxide corrosion of mild steel in the presence of protective iron carbonate films - Part 1: Theory and verification," *Corrosion*, vol. 59, (5), pp. 443-456, 2003.
- [145] E. Dayalan, G. Vani, J. R. Shadley, S. A. Shirazi and E. F. Rybicki, "Modeling CO₂ corrosion of carbon steel in pipe flow," in *Corrosion/1995*, 1995, Paper 95118.
- [146] C. de Waard and D. E. Williams, "Prediction of carbonic acid corrosion in natural gas pipelines," *Ind. Finish. Surf. Coat*, vol. 28, (340), pp. 24-28, 1976.
- [147] F. Farelas, M. Galicia, B. Brown, S. Netic and H. Castaneda, "Evolution of dissolution processes at the interface of carbon steel corroding in a CO₂ environment studied by EIS," *Corros. Sci.*, vol. 52, (2), pp. 509-517, 2010.
- [148] Y. Yang, "Progress of the thin channel flow cell," Corrosion Center Joint Industry Project, Advisory Board Meeting, Ohio University, October 2007.
- [149] A. J. Keating , "Large eddy simulation of heat transfer in turbulent channel flow and in the turbulent flow downstream of backward facing step," PhD dissertation, Dept. Mech. Eng., Queensland Univ., Queensland, Australia, 2004.
- [150] GAMRY Instruments, "*Electrochemical Measurement Systems Hardware Operator's Manuals*," October 2006., Rev. 5.11.

- [151] C. A. Sleicher and M. W. Rouse, "Convenient correlation for heat transfer to constant and variable property fluids in turbulent pipe flow," *Int. J. Heat Mass Transfer*, vol. 18, (5), pp. 677-683, 1975.
- [152] F. P. Berger and K. F. F. L. Hau, "Mass transfer in turbulent pipe flow measured by the electrochemical method," *Int. J. Heat Mass Transfer*, vol. 20, (11), pp. 1185-1194, 1977.
- [153] B. Poulson and R. Robinson, "The use of corrosion process to obtain mass transfer data," *Corros. Sci.*, vol. 26, (4), pp. 265-280, 1986.
- [154] A. Dugstad, B. Morland and S. Clausen, "Corrosion of transport pipelines for CO₂—Effect of water ingress," *Energy Proc.*, vol. 4, (0), pp. 3063-3070, 2011.
- [155] B. Kinsella, "Progress review," PETRONAS High Partial Pressure CO₂ Project, Ohio University, July 2010.
- [156] *Standard practice for laboratory immersion corrosion testing of metals*, ASTM G31, 2004.
- [157] *Standard practice for preparing, cleaning, and evaluating corrosion test specimens*, ASTM G1, 2003.
- [158] S. Papavinasam, "Electrochemical techniques for measuring corrosion rates in operating oil and gas pipelines," in *NACE 2010/097X*, 2010, Technical Information Exchange.
- [159] S. Papavinasam, "Electrochemical polarization techniques for corrosion monitoring," in *Techniques for Corrosion Monitoring*, 2008, pp. 49-85.
- [160] J. R. Scully, "The polarization method for determination of instantaneous corrosion rates," in *Electrochemical Techniques in Corrosion Science and Engineering*, New York: Marcel Dekker Inc., 2003, pp. 125-150.
- [161] J. N. Tilton, "Fluid and particle dynamics," in *Perry's Chemical Engineers' Handbook*, Columbus, OH: McGraw-Hill, 1999, pp. 6-1-6-54.
- [162] D. C. Silverman, "Technical note: On estimating conditions for simulating velocity-sensitive corrosion in the rotating cylinder electrode," *Corrosion*, vol. 55, (12), pp. 1115-1118, 1999.
- [163] D. C. Silverman, "Technical note: Conditions for similarity of mass-transfer coefficients and fluid shear stresses between the rotating cylinder electrode and pipe," *Corrosion*, vol. 61, (6), pp. 515-518, 2005.

[164] D. Harrop, "CO₂ corrosion: A testing problem with a predictive solution," in *European Federation of Corrosion Publications no. 13*, London: The Institute of Materials, 1994, pp. 50-58.

[165] M. F. Suhor, M. F. Mohamed, A. Muhammad Nor, M. Singer and S. Nestic, "Corrosion of mild steel in high CO₂ environment: Effect of the FeCO₃ layer," in *Corrosion/2012*, 2012, Paper C2012-0001434.

[166] A. Mohammed Nor, M. F. Suhor, M. F. Mohamed, M. Singer and S. Nestic, "Corrosion of carbon steel in high CO₂ environment: Flow effect," in *Corrosion/2011*, 2011, Paper 11245.

[167] A. Mohammed Nor, M. F. Suhor, M. F. Mohamed, M. Singer and S. Nestic, "Corrosion of carbon steel in high CO₂ containing environments: The effect of high flow rate," in *Corrosion/2012*, 2012, Paper C2012-0001683.



OHIO
UNIVERSITY

Thesis and Dissertation Services